



## ***Welcome to the RII Symposium!***

On behalf of Louisiana EPSCoR, I would like to welcome you to the 2014 LA EPSCoR RII LA-SiGMA Symposium. This is a great opportunity for everyone to become engaged in this trend-setting research/education initiative supported under the auspices of the National Science Foundation and the Louisiana Board of Regents. The objective of the project is to build the next generation of experimentally validated formalisms, algorithms, and codes for multiscale materials simulations; implementing them on present and next-generation supercomputers; and educating the next generation of a highly skilled workforce of materials scientists and engineers.

We are very proud of this multidisciplinary initiative, in which undergraduate/graduate students, post-doctoral researchers, and university research faculty from seven institutions across the State participate. I also welcome our distinguished participants and guests—NSF program officer, individuals serving on our External Review Board, the Diversity Advisory Committee, EPSCoR Committee members, and university research administrators.

This Symposium features presentations on LA-SiGMA's achievements, a poster competition, and plenty of opportunities to network with your colleagues.

Thank you for participating in this Symposium, and I wish you all a productive and enjoyable meeting.

Michael Khonsari,  
Louisiana EPSCoR Project Director and  
Associate Commissioner for Sponsored Programs R&D, Louisiana Board of Regents

*The research featured in this Symposium is supported by the National Science Foundation's Experimental Program to Stimulate Competitive Research (EPSCoR) under Grant No. EPS-1003897 and the Louisiana Board of Regents through its Board of Regents Support Fund.*

Louisiana Board of Regents  
Post Office Box 3677  
Baton Rouge LA 70821-3677  
225-342-4253  
[www.laregents.org](http://www.laregents.org)

**NSF EPSCoR Research Infrastructure Improvement (RII) Award**  
**2014 LA-SiGMA RII Symposium**

August 18, 2014  
 Marriott Hotel, 5500 Hilton Avenue, Baton Rouge, Louisiana 70808

Agenda

7:00 – 8:00	Registration, Coffee & Bagels
8:00–8:20	Welcoming Remarks (Michael Khonsari)
8:20–8:40	Sean Kennan, NSF Program Director
<b>Science Drivers (SD) and CyberTools and CyberInfrastructure Group (CTCI)</b>	
8:40–9:00	<i>Project Overview</i> (Mark Jarrell)
9:00–9:10	Q&A
9:10–9:30	<i>Electronic and Magnetic Materials</i> (Juana Moreno)
9:30–9:40	Q&A
<b>9:40–10:00</b>	<b>Break</b>
10:00–10:20	<i>Materials for Energy storage and Generation</i> (Ramu Ramachandran)
10:20–10:30	Q&A
10:30-10:50	<i>Biomolecular Materials</i> (Michal Brylinski)
10:50 – 11:00	Q&A
11:00-11:20	<i>Computational Tools for Multiscale Simulations</i> (David Koppelman)
11:20 –11:30	Q&A
11:30-11:45	<i>Sustainability</i> (Lawrence Pratt)
11:45-11:55	Q&A
<b>11:55 – 2:00</b>	<b>Lunch and poster session</b>
<b>Assessment and Broader Impacts</b>	
2:00 – 2:15	<i>Diversity and Workforce Development</i> (Pedro Derosa)
2:15 – 2:25	Q&A
2:25 – 2:40	<i>External Engagement</i> (Noshir Pesika and Jessica Patton)
2:40 – 2:50	Q&A
2:50 – 3:20	Presentations by invited recipients of EPSCoR awards, and Q&A
3:20 – 3:35	<i>Graduate Student Retreat</i> (Fernando Soto and Ayo Hassan)
3:35 – 3:55	<i>Evaluation and Assessment</i> (Cindi Dunn)
3:55 – 4:10	Break
<b>Planning Session</b>	
4:10– 5:15	<b>Simultaneous sessions:</b> ERB Deliberations DAC Deliberations
5:15 – 5:30	DAC and ERB debriefing to LA-SiGMA
5:30	Concluding Remarks (Michael Khonsari)

## Table of Contents

Foreword .....	i
Agenda.....	ii
LA EPSCoR .....	vi
A Need for NO <sub>x</sub> Exhaust Sensor: Computational Study of Gaseous Reaction over Au/YSZ Substrate by S. Killa and D. Mainardi.....	1
<i>Ab-initio</i> DFT Prediction of Electronic Properties and Effective Masses of Li <sub>2</sub> S by Y. Malozovsky, E.C. Ekuma and D. Bagayoko .....	5
Achieving High Efficiency in Serial and at Extreme Scale by Md Hasan, M. Sujon and C. Whaley.....	9
Aligned Carbon Nanotube Forest as Supercapacitor Electrodes by M. Oguntoye, L. Pratt and N. Pesika .....	13
Aligning Metagenomic Short Read Sequences using GPGPUs and Expectation-Maximization Algorithm by M. Karnik, D. Anderson, P. Chowriappa and S. Dua .....	17
Anderson Localization in Systems with Off-Diagonal Disorder by H. Terletska, C.E. Ekuma, C. Moore, K.M. Tam, J. Moreno and M. Jarrell .....	21
Attosecond Transient Absorption with Time Dependent Hartree-Fock by A. Sissay and K. Lopata .....	25
Coarse-grained Biomolecule-Wall Interactions for Implementation into Multi-scale MD- Continuum Simulations by K. Hesary, B. Novak, D. Moldovan and D.E. Nikitopoulos .....	29
Computational Studies of Oxido-Reductases for Improved Biofuel Cell Design by E. Gomez, T. Tran, N. Tran and D. Chakravorty .....	33
Computational Study of the Self-Assembly of Surfactant Molecules by C. Whicker, S. Joseph, E. Gomez, S. Tumulime and D. Chakravorty .....	37
Crystallization and the Dimensionality Effect by T. Loeffler, A. Galatas, and B. Chen .....	41
Design of Tailored Polymer via Molecular Dynamics Simulations by L. Liu, S. Parameswaren, A. Sharma, H. Ashbaugh, S. Rick and S. Grayson.....	45
Direct Dynamical Simulation of Filling of Carbon Nanotube Forests by X. You and L.R. Pratt.....	49
Dynamical Cluster Approximation Study of the Two-Dimensional Anderson-Hubbard Model by S. Yang, P. Haase, H. Terletska, T. Pruschke, J. Moreno and M. Jarrell .....	53
Effect of Nanoparticle Size, Shape and Orientation on Effective Dielectric Constant in Polymer- Nanocomposites by S. C. Sklare, S. Adireddy, V. Puli, J. Shipman and D. Chrisey .....	57
Electrical and Thermal Transport Properties of Superconducting Ca <sub>10</sub> Pt <sub>4</sub> As <sub>8</sub> ((Fe <sub>1-x</sub> Pt <sub>x</sub> ) <sub>2</sub> As <sub>2</sub> ) <sub>5</sub> Single Crystals by B. Karki, J.Y. Pan, P. Watkins-Curry, G.T. McCandless, J.Y. Chan, E.W. Plummer and R. Jin .....	61
Equation of Motion Coupled Cluster Methods for Electron Attachment and Ionization Potential: Implementation and Applications by K. Bhaskaran-Nair, K. Kowalski, J. Moreno, M. Jarrell and W. Shelton .....	65
Exploiting Sparse Matrix Structure in a Monte-Carlo Arnoldi Iteration on Many-Core Architectures by R. Karimi and D. Koppelman .....	69

GeauxDock: A Novel Approach for Ligand Molecular Docking Using a Hybrid Force Field by Y. Ding, Y. Fang, W. Feinstein, D.M. Koppelman, J. Moreno, J. Ramanujam, M. Brylinski and M. Jarrell .....	73
Heterogeneous Computing Aided Material Science Research by Y. Fang, S. Feng, Y. Ding, K.M. Tam, W. Feinstein, Z. Yun, M. Brylinski, D. Koppelman, J. Moreno, M. Jarrell and J. Ramanujam.....	77
Homogeneous Nucleation of Crystals of Ionic Liquids from the Melt by Y. Shen, X. He, E. Santiso and F. Hung .....	81
In Situ Polymerization of Thiol-acrylate Nanocomposite Foam for Bone Defects by A. Forghani, L. Garber, C. Chen, R. Devireddy and D. Hayes .....	85
Investigation of the Molecular Mechanism of Tin Sulfide (SnS <sub>2</sub> ) as a Lithium Ion Battery Electrode Material by K. Moyer, A. Hassan, C. Wick and R. Ramachandran.....	89
Ionic liquids in the Ordered Mesoporous Carbon CMK-5: Pore-pore Correlation Effects by X. He, J. Monk, R. Singh, L. Lorio and F. Hung .....	93
Lithiation Mechanism of RuO <sub>2</sub> , and its Potential Use as Lithium-Ion Battery Anode Material by A. Hassan, R. Ramachandran, C. Wick, A. Navulla and L. Meda.....	97
Magnetic Structure of Metamagnetic Fe <sub>3</sub> Ga <sub>4</sub> by Y. Wu, H. Cao, A. Karki, J.C. Prestigiacomo, B. Fulfer, R. Jin, J. Chan and J.F. DiTusa.....	101
Metal Organic Frameworks as Vehicles for Drug Delivery by K. Taylor-Edinbyrd, T. Li and R. Kumar .....	105
Micellization of Cationic Linear Peptide Analogs Studied Using Molecular Dynamics Simulations by B. Novak and D. Moldovan.....	109
Molecular Dynamics Simulation Study of the Transport of DNA through Mononucleotides through Nanoslits Driven by Electric Fields by K. Xia, B. Novak, D. Nikitopoulos, S. Soper and D. Moldovan.....	113
Monte Carlo Study of a Spin Glass Model with a Correlated Disorder by K.M. Tam, J. Willard, J. Moreno and M. Jarrell .....	117
Multi-scale Theory in the Molecular Simulation of Electrolyte Solutions by W. Zhang, X. You and L.R. Pratt.....	121
Optimizing Growth Conditions of Zinc Sacrificial Layer for Micro-Origami Technology by R. Eskandari, B. Buchanan and L. Malkinski .....	125
Parallelizing Protein Docking Code to Accelerate Drug Discovery by B. Burkman, M. Brylinski and W. Feinstein.....	129
Periodic Anderson Model with Electron Phonon Interaction and its Antiferromagnetic Susceptibility by E. Li, P. Zhang, K.M. Tam, S. Yang, J. Moreno and M. Jarrell.....	133
Quantum Chemistry Studies of Zn <sup>2+</sup> and Mg <sup>2+</sup> Ions in Aqueous Environments by L. Hartman, M. Soniat and S. Rick.....	137
Quantum Coherent Manipulation of Two-Level Systems in Superconducting Circuits by A. Burin, A. Maksymov and K. Osborn.....	141

Quantum Confinement Effect on Electron-phonon Interaction in Atomically Thin Nb <sub>3</sub> SiTe <sub>6</sub> by J. Hu, X. Liu, C.L. Yue, J.Y. Liu, H.W. Zhu, J. Wei, Z.Q. Mao, L. Antipina, Z.I. Popov, P.B. Sorokin, T.J. Liu, P.W. Adams, J. Heng and D. Natelson.....	145
Redeveloping and Optimizing the Interactive Chromatin Modeling Web Server Kernel by G. Kankanala, I. Sondh and T.C. Bishop .....	149
Sign-Learning Kink-Based Path Integral Calculations of Molecules H <sub>2</sub> O, N <sub>2</sub> , and F <sub>2</sub> by J. Baylis, X. Ma, F. Loffler, R. Hall, K. Kowalski, M. Jarrell and J. Moreno .....	153
Simulation of the Controlled Release of Molecules from Halloysite Nanotubes by D. Elumalai, M. McCoy, Y. Lvov, J. Tully and P. Derosa.....	157
Simulations of Ions in Non-Aqueous Solvents by A. Vuong, S. Wagstaff and S. Rick.....	161
Study of CO Adsorption and Dissociation on Metal clusters using DFT by S. Gyawali and D. Mainardi .....	165
Study of the Three-Dimensional Edwards-Anderson Model in an External Field with a Multi-spin Coding Parallel Tempering Monte Carlo Simulation by S. Feng, Y. Fang, K.M. Tam, J. Moreno, J. Ramanujam and M. Jarrell.....	169
Synthesis and Characterization of Dendronized Polymers based on Poly(Ethylene Glycol) by B. Myers and S. Grayson .....	173
Synthesis of Novel Amphiphilic Capping Ligands as an Organic Coating for Nanoparticulate Iron Oxide Imaging and Delivery Agents by D. Nilov, P. Kucheryavy, R. Komati, C. Mitchell, A. LeBeaud, A. Burin, V. Kolesnichenko and G. Goloverda .....	177
The Role of Defects in the Metal-Nonmetal Transition in SrVO <sub>3</sub> Thin Films by G. Wang and J. Zhang.....	181
Towards Online Comparative Genomics of Mononucleosomes by V. Pereddy, P. Mahadasyam, M. Badar and T.C. Bishop.....	185
Typical Medium Dynamical Cluster Approximation Study of Disordered Superconductors by E. Siddiqui, C.E. Ekuma, H. Terletska, N.S. Vidyadhiraja, J. Moreno and M. Jarrell .....	189
Ultraviolet Radiation Effects on the Electrical Resistivity of some La(Ca/Sr)MnO Materials by W. Raziano, J. Franklin and L. Henry .....	193
Unifying Interactive Chromatin Model and Genome Browsing by K. Chitturi and T.C. Bishop.....	197
What is the Valence of Mn in (Ga, Mn)N? by R. Nelson, T. Berlijn, W. Ku, J. Moreno and M. Jarrell.....	201
Workflow Software for Keck & CAMD Tomography Systems by J. Yuan, B. Cormier and L. Butler .....	205
LA SIGMA Poster Session.....	209
Registered Attendee List .....	211

## **What is EPSCoR?**

The Experimental Program to Stimulate Competitive Research (EPSCoR) is a federal/state partnership established in 1978 by the National Science Foundation (NSF) with the goal of stimulating sustainable improvements in the research & development (R&D) capacity of states—like Louisiana—that historically have not received significant federal R&D funding. Since its initial establishment, EPSCoR programs are now supported by seven federal agencies.



**LA EPSCoR**

Louisiana has participated in NSF EPSCoR since 1987, and has been the recipient of several competitively awarded Research Infrastructure Improvement (RII) awards. LA EPSCoR has served as the catalyst for transforming the way large-scale collaborative research is conducted in the State—from individual campuses competing for limited federal resources to one in which increased collaboration has enabled Louisiana to become more competitive for major R&D funding at the national level.

The major research component of the current RII award is the Louisiana Alliance for Simulation-Guided Materials Applications (LA-SiGMA). This ambitious initiative brings together seven academic institutions with the vision to make transformative advances in materials science research and education through a sustained multidisciplinary and multi-institutional alliance of researchers. LA-SiGMA research and education activities involve three areas of materials science, tied together with a common computational framework. The specific goals are:

**Electronic and Magnetic Materials:** To transform the field by extending many-body formalisms and first principles methods to much larger length scales than currently possible.

**Materials for Energy Storage and Conversion:** To develop and apply multi-scale computational tools to study materials for energy generation, storage, and conversion.

**Biomolecular Materials:** To develop, apply, and validate experimentally multi-scale computational tools for the design of novel vehicles for drug delivery and other applications.

**Shared Computational Strategies:** To develop multi-scale formalisms, algorithms, and codes for materials simulations and modeling; leverage existing tools and make optimum use of the next generation computing environments.

Tightly integrated with LA-SiGMA are a suite of programs offered by LA EPSCoR to the entire State's higher education and K-12 community. These programs are designed to improve Louisiana's research competitiveness, train a highly-education workforce, and promote greater public awareness and participation in science, technology, engineering, and mathematics (STEM). These programs include:

- Opportunities for Partnerships in Technology with Industry (OPT-IN)
- Supervised Undergraduate Research Experience (SURE)
- Pilot Funding for New Research (Pfund)
- Links with Industry, Research Centers, and National Labs (LINK)
- Travel Grants for Emerging Faculty (TGEF)
- Preliminary Planning Grants for Major Initiatives
- Planning Grants for Major Initiatives
- Grantwriting Workshops
- Faculty Expertise Database (SPINPlus, LA GENIUS, SMARTS)
- Speaking of Science (SOS) speakers' bureau

## **Participating Institutions**

- **Grambling State University**
- **Louisiana State University**
- **Louisiana Tech University**
- **Southern University**
- **Tulane University**
- **University of New Orleans**
- **Xavier University**

## National Science Foundation EPSCoR

- **Sean Kennan**, NSF EPSCoR Program Director, Arlington, VA

### External Review Board (ERB) members

- **B. Vincent McKoy**, Professor of Chemistry, California Institute of Technology (ERB Chair)
- **James Hoehn**, Formerly of the EPSCoR/IDeA Foundation, Washington, DC
- **William A. Lester Jr.**, Professor of the Graduate School, University of California, Berkeley
- **Susan B. Sinnott**, Professor of Materials Science and Engineering, University of Florida
- **Harold Silverman**, Senior Vice Provost, State University of New York System (retired)

### Diversity Advisory Council (DAC) members

- **William A. Lester Jr.**, Professor, Department of Chemistry, University of California, Berkeley
- **Stephanie Adams**, Department Head and Professor, Virginia Polytechnic Institute and State University
- **Jenna Carpenter**, Associate Dean for Administration & Strategic Initiatives, Louisiana Tech University
- **DiOnetta Jones Crayton**, Associate Dean and Director, Office of the Dean for Undergraduate Education, Massachusetts Institute of Technology
- **Shelia Edwards Lange**, Vice President for Minority Affairs and Vice Provost for Diversity, University of Washington
- **Janet B. Ruscher**, Associate Dean for Graduate Programs, School of Science and Engineering, Tulane University
- **Zakiya Wilson**, Office of Strategic Initiatives, Executive Assistant and Director from STEM Education, Louisiana State University

## Louisiana EPSCoR Committee members

- **Les Guice** (Chair), President, Louisiana Tech University
- **Thomas Klei** (Vice Chair), Boyd Professor, School of Veterinary Medicine, Louisiana State University
- **Nicholas Altiero**, Dean, College of Science and Engineering and Professor of Biomedical Engineering, Tulane University
- **Diola Bagayoko**, Southern University System Distinguished Professor and Chair of Physics, Southern University - Baton Rouge, Chancellor's fellow, Director (Timbuktu Academy and M.S. Program), Associate Director (LaSPACE)
- **Geoffrey Cazes**, Vice President, Cyber Innovation Center
- **Henry Chu**, Director, School of Computing and Informatics, College of Sciences and Professor, Laboratory for Internet Computing, University of Louisiana at Lafayette (DEPSCoR Representative)
- **Gene D'Amour**, Senior Vice President for Resource Development, Xavier University of Louisiana
- **Kerry Davidson**, Deputy Commissioner for Sponsored Programs, Louisiana Board of Regents
- **Connie Fabré**, Executive Director, Greater Baton Rouge Industry Alliance
- **Robert Godke**, Boyd Professor, School of Animal Sciences, LSU Agricultural Center
- **Michael Khonsari**, Associate Commissioner for Sponsored Programs R&D and LA EPSCoR Project Director and Dow Chemical Endowed Chair Professor of Mechanical Engineering, Louisiana State University
- **Ramesh Kolluru**, Interim Vice President for Research, University of Louisiana at Lafayette
- **Barry LeBlanc**, President, CEO, PamLab, L.L.C.
- **Laura Levy**, Associate Senior Vice President for Research and Professor of Microbiology and Immunology, Tulane University Health Sciences Center
- **Quentin Messer**, Director of LED's State Economic Competiveness group, Louisiana Economic Development
- **Sandra Roerig**, Dean for Graduate Studies and Research, LSU Health Sciences Center – Shreveport
- **Jacqueline Stephens**, Director of Basic Science, Pennington Biomedical Research Center
- **Hilary Thompson**, Adjunct Professor of Ophthalmology, Biometry, and Neuroscience, Director, Clinical Trials and Biometry Unit, School of Public Health, LSU Health Sciences Center – New Orleans
- **John Wefel**, Professor of Physics, Louisiana State University, (NASA EPSCoR Representative)

## Project Evaluators

- **Cindi Dunn**, Office of Educational Innovation and Evaluation - Kansas State University (external evaluator)
- **Wendi Stark**, Office of Educational Innovation and Evaluation - Kansas State University (external evaluator)

## LA-SiGMA Project Execution Team

- **Gene D'Amour**, Senior Vice President for Resource Development, Xavier University
- **Diola Bagayoko**, Distinguished Professor and Chair of Physics, Director (Timbuktu Academy and M.S. Program) Southern University – Baton Rouge
- **Pedro Derosa**, Associate Professor, Larson Professor, Grambling University/Louisiana Tech University
- **Cindi Dunn**, Office of Educational Innovation and Evaluation – Kansas State University (member-at-large)
- **Leslie Guice**, President, Louisiana Tech University
- **Mark Jarrell**, Professor, Department of Physics and Astronomy, CCT, Louisiana State University
- **Michael Khonsari**, Louisiana EPSCoR Project Director, Louisiana State University
- **Juana Moreno**, Assistant Professor, Department of Physics and Astronomy, CCT, Louisiana State University
- **Noshir Pesika**, Assistant Professor, Tulane University
- **Lawrence Pratt**, Professor and Brown Chair of Chemical Engineering, Tulane University
- **Ramu Ramachandran**, Professor Chemistry, Associate Dean for Research College, Louisiana Tech University
- **J. Ram Ramanujam**, Distinguished Professor of Electrical Engineering, Louisiana State University
- **Steven Rick**, Professor of Chemistry, University of New Orleans
- **William Shelton**, Professor, Louisiana State University

## **EPSCoR Staff**

- **Michael Khonsari**, Project Director
- **Jim Gershey**, Project Administrator
- **Amber King**, Communication Manager
- **Alysia Delone**, Grants and Contracts Coordinator
- **Susan Jernigan**, EPSCoR Associate
- **Jessica Patton**, EPSCoR Associate, Faculty Development Coordinator
- **Karthik Poobalashubramanian**, IT Coordinator

## A Need for NO<sub>x</sub> exhaust sensor: Computational study of gaseous reaction over Au/YSZ substrate

Sajin Killa<sup>1</sup>, Daniela S. Mainardi<sup>1</sup>

<sup>1</sup>Institute for Manufacturing, Louisiana Tech University

<sup>1</sup>Chemical Engineering, Louisiana Tech University

**Abstract:** The density functional theory approach is used to determine the transition state for the gaseous reaction over Au/YSZ model cluster. During this process, different theory levels available in DFT are used to find the Gibbs free energy barrier,  $\Delta G$  (T). We show that the Gibbs free energy barrier,  $\Delta G$  (T) obtained from PWC/DNP theory level is overestimated and the better kinetic results are obtained through the single point energy calculations at PBE/DNP and RPBE/DNP theory levels. These studies will help in understanding the reaction mechanism and in developing a reliable NO<sub>x</sub> sensor.

**Keywords:** density functional theory, cluster, LDA/PWC, GGA/PBE, gaseous reactions, adsorption, internal energy of activation, Gibbs free energy barrier

### 1. Introduction

NO<sub>x</sub> exhaust sensors are the high temperature devices especially designed to control the expulsion of NO<sub>x</sub> derivatives into the environment. NO<sub>x</sub> derivatives compose of different oxides of nitrogen gas mostly NO and NO<sub>2</sub>. These gases create acid rain and smog and can cause possible health hazards due to which proper measures must be carried out to prevent their effects. Several automobile companies like Toyota, Ford and Chrysler have put forward an effort on researches to develop more efficient NO<sub>x</sub> sensors.<sup>1</sup> The NO<sub>x</sub> exhaust sensors currently available in the market can detect NO<sub>x</sub> of about 10 ppm.<sup>2</sup> The ceramic oxide based electrochemical NO<sub>x</sub> sensors are mostly popular and they use Yttria-Stabilized Zirconia (YSZ) as the electrolyte due to its reliability with lean and rich exhaust environment. YSZ has a high oxygen ion conductivity which enhances the ability of the sensor response.<sup>3,4</sup> Typically, the NO<sub>x</sub> sensor is made up of porous Pt electrodes and YSZ electrolyte but recent studies have found that the sensor should be fabricated with dense electrode and porous electrolyte since the sensitivity increased due to allowance for gas diffusion.<sup>5</sup> Catalytic studies by Yang et al. confirmed that there are strong molecular interactions between NO<sub>x</sub> species and YSZ.<sup>6</sup> The interaction mechanisms between the porous YSZ and NO<sub>x</sub> need to be well understood to contribute in optimization of NO<sub>x</sub> exhaust gas sensors. In order to get the deeper understanding, the possible intermediate species and reaction pathways are studied using computational method by implementation of different theory level to determine the binding energy.

### 2. Methodology

In this computational method, a 40-atom model cluster of YSZ supported on a 16-atom Au cluster was studied with density functional theory (DFT) method by using DMOL<sup>3</sup> module of the Materials Studio<sup>®</sup> 6.0

software by Accelrys, Inc. The  $\delta$ -YSZ crystal structure<sup>7</sup> was built using the crystal builder option of this software. The first-principles calculations were then carried out to investigate the gas-phase internal energy of activation and free energy barrier of the reaction in the presence of 56 atom Au/YSZ cluster model. The cluster was initially optimized using Local Density Approximation (LDA)<sup>8</sup> method within the Density functional Theory formalism<sup>7</sup>, as implemented in the DMOL<sup>3</sup> module of the Materials Studio<sup>®</sup> 6.0 software. All geometry optimization of the model was performed using Perdew-Wang (PWC) theory level with the double numerical with polarization (DNP) basis set as it was the best set available<sup>8</sup> in DMOL<sup>3</sup>. The errors in energies using PWC/DNP theory level are expected to be in the order of 8-20 kJ/mol; similar to those expected when using the Becke-3 hybrid functionals in combination with the 6-31G\*\* basis set.<sup>7, 9</sup> Harmonic vibrational frequency calculations were performed to determine the stationary point on the potential energy surface which is local minima (all real frequencies) or transition states (only one imaginary frequency). Zero point energy corrections were applied with spin multiplicity checked. To perform the accurate ground state conformations, energies obtained at different minima were compared which were obtained by diverse arrangement of reactant, intermediates and product of the molecular system.

For the reaction kinetics modeling, a 3D trajectory file representing the reaction path preview generated with Reaction Preview tool of the software is used as inputs to obtain the transition states, using the linear synchronous transit and quadratic synchronous transit (LST/QST) calculation with conjugate gradient minimization<sup>11</sup> within Transition State Search tool. The maximum obtained in reaction pathway was used to perform LST/optimization and the transition state obtained further went through QST/optimization for finer search. The final result provides a single stationary point with only one imaginary frequency (transition state). The transition state obtained is further verified using the Transition State Optimization tool.<sup>8</sup> The Transition State Confirmation tool is further used in which the intrinsic reaction coordinate (IRC) analysis performed confirms the minimum energy path that starts from transition state to presumed reactant and product. In this work, the Gibbs Free energy barrier (internal energy of activation with the thermal corrections to the Gibbs Free energy at different temperatures included),  $\Delta G(T)$ , for the forward reaction are included as these energies are not affected by temperature. The improved calculations are further performed using Generalized Gradient Approximation (GGA) methods using same single point energy calculations at DNP basis set. The GGA functionals used include the Perdew-Burke-Ernzerhof (PBE) functional<sup>12</sup> and the revised PBE functional (RPBE)<sup>13</sup>. The RPBE functional is found to be superior in the description of the energetics of atomic and molecular bonding to surfaces. The results from LDA PWC/DNP theory and three GGA functionals will be further compared and discussed in section below.

### 3. Results

#### 3.1. Kinetic Modeling on LDA PWC functional:

The 56 atom Au/YSZ cluster was used as an input after geometry optimization. The reactant consisted of two molecules of NO and one molecule of oxygen while the product consisted of two molecules of NO<sub>2</sub>. Both the reactant and product are geometrically optimized and through the vibrational frequency analysis, the reaction pathway is determined to find the transition state. The reaction path for the Au/YSZ cluster at the PWC/DNP theory level is shown in Figure 1. The path shows oxygen surface reactions that begin with adsorbed NO association with adsorbed O<sub>2</sub> on a Zr surface site followed by the O<sub>2</sub> dissociative adsorption, atomic oxygen diffusion and migration to free NO molecules resulting in the formation of NO<sub>2</sub>. The calculated internal energy of

activation at absolute zero,  $\Delta U$ , and the Gibbs Free energy barrier,  $\Delta G(T)$  for the forward reaction  $2NO + O_2 \leftrightarrow 2NO_2$  at the PWC/DNP theory level is  $\Delta G(650^\circ\text{C}) = 912.77$  kJ/mol (averaged for the 600-700 °C temperature of the experimental work) respectively. The  $\Delta G$  is calculated by applying the following formula:

$$\Delta G = (E_{\text{Total}} + G_{\text{Total}})_{\text{TS}} - (E_{\text{Total}} + G_{\text{Total}})_{\text{Reactant}} \text{ or } \Delta G = (E_{\text{TCorr}})_{\text{TS}} - (E_{\text{TCorr}})_{\text{Reactant}}$$

The correction is applied by interpolating the Gibbs energy at two different temperature i.e. 626.85 °C and 651.85 °C from the computational results.

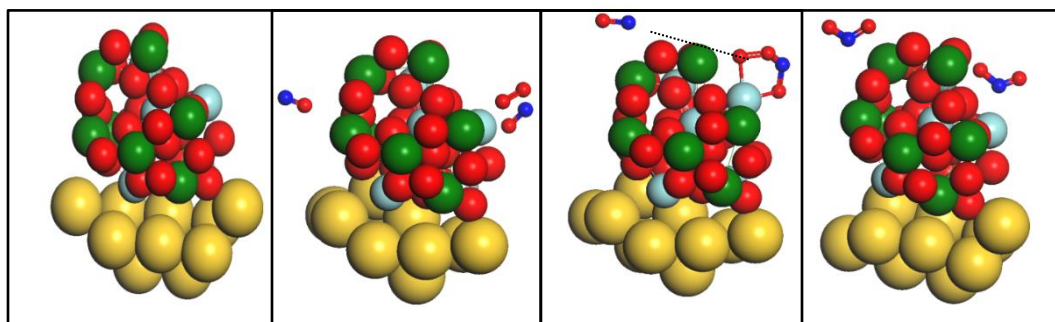


**Figure 1.** Ground state conformations of the (a) YSZ/Au model cluster, (b) reactant of Eqn.3 (YSZ/Au cluster with 2NO and  $O_2$ ), transition state structure, and product of Eqn.3 (YSZ/Au cluster with 2NO<sub>2</sub> molecules). ●: Y, ●: Zr, ●: O, ●: N, and ●: Au.

### 3.2. Kinetic Modeling on GGA PBE functional:

The calculated free energy barrier obtained from LDA functionals are overestimated so the structures optimized at this level were used to conduct the single point energy calculations at the PBE/DNP theory level. Similar mechanisms were followed and various combinations of reactant, intermediates and product were matched to get the feasible internal energy and Gibbs free energy barrier. At this theory level, we obtained the Gibbs free energy,  $\Delta G(650^\circ\text{C}) = 400.65$  kJ/mol which is lower than the one obtained from PWC/DNP theory level.

### 3.3. Kinetic Modeling on GGA RPBE functional:

The revised PBE is the improvised version of PBE functional. It improves the atomization energy and chemisorption energy than prior functionals. The optimized cluster model from PBE/DNP functional is further optimized using this theory level and the transition state was found according to similar methods. The free energy of barrier obtained in this case is  $\Delta G(650^\circ\text{C}) = 519.3$  kJ/mol. In this case, the energy was estimated to be lower than that of PBE/DNP theory level. The intermediate found from RPBE/DNP theory level is shown in the Figure 2 above.

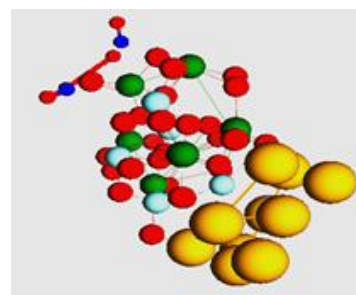


**Figure 2.** Intermediate for RPBE/DNP theory level ●: Y, ●: Zr, ●: O, ●: N, and ●: Au

#### 4. Conclusion

The reaction mechanism due to adsorption of NO and O<sub>2</sub> over the Au/YSZ surface to form NO<sub>2</sub> is studied using different functionals of density functional theory. The DFT calculations performed to determine the Gibbs free energy of barrier;  $\Delta G$  clearly states that the value changes drastically from primitive theory level to the advanced theory level. The calculations were made taking the average at the temperature of 600-700 °C as the exhaust sensor is supposed to function at this temperature range. The kinetic studies provided more accurate results but the difference in energy values between PBE/DNP and RPBE/DNP functionals were also seen which needs to be further verified. Thus, to understand the reaction mechanism within the NO<sub>x</sub> sensor, this study will be helpful and will generate more results towards the development of reliable sensor.

#### 5. Acknowledgments

The current work is funded by the NSF EPSCoR LA-SiGMA project under award #EPS-1003897.

#### 6. References

- [1] Mukundan, R.; Teranishi, K.; Brosha, E. L.; Garzona, F. H., Nitrogen Oxide Sensors Based on Yttria-Stabilized Zirconia Electrolyte and Oxide Electrodes. *Electrochemical and Solid-State Letters* **2007**, 10, (2), J26-J29.
- [2] 2008 Progress Report: Vehicle and Engine Compliance Activities. *United States Environmental Protection Agency, EPA-420-R-10-022* (August 2010).
- [3] Martin, L. P.; Woo, L. Y.; Glass, R. S., Impedancemetric NO<sub>x</sub> Sensing Using YSZ Electrolyte and YSZ/Cr<sub>2</sub>O<sub>3</sub> Composite Electrodes. *Journal of The Electrochemical Society* **2007**, 154, (3), J97-J104.
- [4] Menil, F.; Coillard, V.; Lucat, C., Critical Review of Nitrogen Monoxide Sensors for Exhaust Gases of Lean Burn Engines. *Sens. Actuators B* **2000**, 67, (1).
- [5] Striker, T.; Ramaswamy, V.; Armstrong, E. N.; Willson, P. D.; Wachsmann, E. D.; Ruud, J. A., Effect of nanocomposite Au-YSZ Electrodes on Potentiometric Sensor Response to NO<sub>x</sub> and CO. *Sens. Actuators B* **2013**, 181, 313.
- [6] Yang, J. C.; Dutta, P. K., Promoting Selectivity and Sensitivity for a High Temperature YSZ-based Electrochemical Total NO<sub>x</sub> Sensor by Using a Pt-loaded Zeolite Y Filter. *Sens. Actuators B* **2007**, 125, (1), 30-39.
- [7] Peredith, A.; Ceder, G.; Wolverton, C.; Persson, K.; Mueller, T., Ab Initio Prediction of Ordered Ground-state Structures in ZrO<sub>2</sub>-Y<sub>2</sub>O<sub>3</sub>. *Phys. Rev. B* **2008**, 77, (1-7).
- [8] Accelrys *Materials Studio*, 2006.
- [9] Becke, A. D., Density-functional thermochemistry III. The role of exact exchange. *J. Chem. Phys.* **1988**, 88, 2547.
- [10] N. Govind; M. Petersen; G. Fitzgerald; D. King-Smith; Andzelm, J., A generalized synchronous transit method for transition state location *Computational Material Science* **2003**, 28, (2), 250-258.
- [11] Jones, R. O.; Gunnarsson, O., The Density Functional Formalism, Its Applications and Prospects. *Rev. Mod. Phys.* **1989**, 61, 689.
- [12] Perdew, J. P.; Burke, K.; Ernzerhof, M., Generalized Gradient Approximation Made Simple. *Phys. Rev. Lett.* **1996**, 77, 3865.
- [13] Hammer, B.; Hansen, L. B.; Norskov, J. K., Improved Adsorption Energetics within Density-functional Theory Using Revised Perdew-Burke-Ernzerhof Functionals. *Phys. Rev. B* **1999**, 59, (11), 7413-7421.

## ***Ab-initio* DFT Prediction of Electronic Properties and Effective Masses of Li<sub>2</sub>S**

Y. Malozovsky <sup>1</sup>, E. C. Ekuma <sup>2</sup>, and D. Bagayoko<sup>1</sup>

<sup>1</sup>Department of Physics, Southern University and A&M College, Baton Rouge, LA 70813, USA

<sup>2</sup>Department of Physics and Astronomy, Louisiana State University, Baton Rouge, LA 70803, USA

**Abstract:** We present results from *ab-initio*, self consistent local density approximation (LDA) calculations of electronic and related properties of cubic antiferite (anti-CaF<sub>2</sub>) lithium sulfide (Li<sub>2</sub>S). To obtain results, we applied Density Function Theory (DFT) enhanced by Bagayoko, Zhao, and Williams (BZW) method in *ab-initio* self-consistent calculations. We also employed Local Density Approximation (LDA) and Linear Combination of Atomic Orbitals (LCAO). Our predicted an indirect LDA gap of 3.723 eV at the X-point (and predicted GGA gap of 3.935 eV), for Li<sub>2</sub>S. We have also calculated the total (DOS) and partial (pDOS) densities of states and electron and hole effective masses for Li<sub>2</sub>S, as well as total energy versus lattice constant, and bulk modulus.

**Keywords:** Ab-initio calculations, Band gap energy, DFT, LDA, LCAO

### **1. Introduction**

The Lithium Sulfide (Li<sub>2</sub>S) is the one of the member of Alkali-Metal Sulfides is found to crystallize in the face centered cubic (FCC) antiflorite (anti-CaF<sub>2</sub>) structure with space group Fm $\bar{3}$ m. <sup>1</sup> The Lithium Sulfide has recently attracted considerable attention due to its high ionic conductivity. <sup>2</sup> Theoretical calculations of the band gap of Li<sub>2</sub>S have been mainly performed within local density approximation (LDA) in terms of the density functional theory (DFT). The calculations of Li<sub>2</sub>S indirect band gap using the various ab-initio computer packages varies in quite wide range of values between 3.1 eV and 4.55 eV. <sup>3</sup> This is main motivation of this study of electronic properties of the cubic antiferite Li<sub>2</sub>S. Our predicted an indirect LDA gap of 3.723 eV at the X-point (and predicted GGA gap of 3.935 eV), for Li<sub>2</sub>S. We have also calculated the total (DOS) and partial (pDOS) densities of states and electron and hole effective masses for Li<sub>2</sub>S, as well as total energy versus lattice constant, and bulk modulus. The main feature of the calculations are based on the implementation of the LCAO formalism followed the Bagayoko, Zhao, and Williams method as enhanced by Ekuma and Franklin (BZW-EF) which is described in details in Ref. 4.

### **2. Method**

Our calculations employ the local density functional potential of Ceperly and Alder, <sup>5</sup> obtained by the quantum Monte Carlo techniques, and parameterized by Vosko et al. <sup>6</sup> and the linear combination of atomic orbitals (LCAO). The radial parts of these atomic orbitals are approximated in terms of the Gaussian functions. We

utilized a computational program package developed at the Department of Energy, Ames Laboratory, Iowa.<sup>7</sup> Our *ab-initio*, self-consistent calculations are non-relativistic and are performed at experimental lattice constant of 5.6890Å (10°K). The distinctive feature of our approach resides in implementation of the Bagayoko-Zhao-Williams (BZW) method, as enhanced by Ekuma and Franklin (BZW-EF),<sup>8</sup> based on the search for the optimal basis set that yields the minima of the occupied energies.<sup>9</sup> The BZW-EF method<sup>10</sup> consists of implementing the LCAO procedure in such a manner that the basis set is methodically increased from a small one (no smaller than the minimum basis set) to that of the optimal basis set. The minimum basis set is the smallest one that accounts for all the electrons in the solid under study, i.e., those from Li and S. In the BZW-EF method,<sup>10</sup> the optimal basis set is the smallest basis set that yields the minima of all the occupied energies. The use of basis sets greater than the optimal one, and that contain it, does not change or lower the occupied energies. However, by virtue of the Rayleigh theorem for eigenvalue equations, such larger basis sets do lead to the lowering of some unoccupied energies. The theorem states that when the same eigenvalue equation is solved self consistently with N and (N+1) functions, such that the (N+1) functions include the N functions, then the eigenvalues from the calculation with (N+1) functions are lower or equal to their corresponding ones from the calculation with N functions. We should underscore the fact that the increase of the size of the basis set is accompanied by its enrichment in angular symmetry and radial functions. Hence, the optimal basis set is capable of accounting for the redistribution of the electronic cloud in the solid environment as compared to that of free ions. The successive sizes of the basis sets for the description of the valence states, for Li<sub>2</sub>S, are given farther below in Table 1. Computational details relevant to the replication of this work follow. Cubic antiferroite (anti-CaF<sub>2</sub>) lithium sulfide (Li<sub>2</sub>S) possessing a face-centered cubic structure in the  $O_h^5 - Fm\bar{3}m$  space group, with a space group number of 225 and Patterson symmetry  $Fm\bar{3}m$ .<sup>11</sup> The Li<sub>2</sub>S unit cells contain two atoms: two cation (Li<sup>1+</sup>) and one anion (S<sup>2-</sup>) at the positions indicated between parentheses: S: (0, 0, 0), Li: ( $\pm 1/4, \pm 1/4, \pm 1/4$ ).<sup>1,11</sup>

### 3. Results

A total of six (6) different basis sets of atomic orbitals were utilized for cubic Li<sub>2</sub>S in the search for their optimal basis sets. Our calculated, *ab-initio*, self-consistent band structure for cubic-Li<sub>2</sub>S (Calculation IV) is shown in Fig. 1. Fig.1 shows Calculation IV and V and which are identical corresponding occupied ground state energies and are equal at any k-point. We conclude that the Calculation IV represents the optimal basis set corresponding to the lowest ground state energy. As noted above, the optimal basis set is identified by the fact that the occupied energies are at their minima. Hence, larger basis sets do not lead to any lowering of these energies. As per the contents of Table 1 and of Figure 1, the basis set of Calculations IV is the optimal ones for cubic-Li<sub>2</sub>S.

The calculated electron effective mass at the  $\Gamma$  point is nearly isotropic and equal to 0.426  $m_0$ . The calculated electron effective mass at X<sub>1</sub><sup>c</sup> is anisotropic with the longitudinal value in the X to  $\Gamma$  direction of 0.686  $m_0$  and a transverse effective mass in the X to K direction of 0.355  $m_0$ . The light hole effective mass at the  $\Gamma$  point is anisotropic with 0.298, 0.490, and 0.385 in the [111], [100], and [110] directions respectively, with an average effective mass of 0.39  $m_0$ . The heavy hole effective mass is essentially anisotropic, with 2.139, 0.938, and 1.501 in the [111], [100], and [110] directions respectively, and with 1.04 for the second heavy hole effective mass in

the [110] (from  $\Gamma$  to K) direction. To the best of our knowledge, we are first whoever performed calculations of effective masses for  $\text{Li}_2\text{S}$  in terms of *ab-initio* LDA calculations.

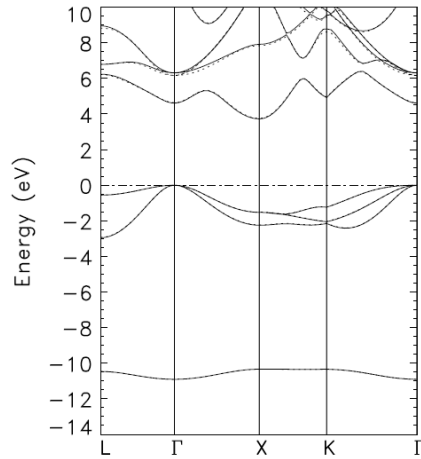


Fig.1. Calculated, electronic energy bands structure of cubic antifluorite (anti- $\text{CaF}_2$ ) lithium sulfide ( $\text{Li}_2\text{S}$ ) from Calculation IV (solid lines) and V (dashed lines). The corresponding occupied ground state energies from Calculation IV and V are equal at any k-point. Calculation IV corresponds to the optimal basis set.

**Table 1.** Successive basis sets for the self consistent calculations for cubic- $\text{Li}_2\text{S}$ . The three last columns show the calculated band gaps, in eV. The optimal basis set is that for Calculation IV and the calculated, preliminary, indirect gap of cubic- $\text{Li}_2\text{S}$  is 3.723 eV and GGA gap is 3.935 eV.

Nº	Trial Functions for valence states of $\text{Li}^{+1}$	Trial Functions for valence states of $\text{S}^{2-}$	Total Nº of Funct.(Dimen. of Hamilton.)	Band Gap at $\Gamma$ in eV	Band Gap $\Gamma$ - X, eV	Band Gap $\Gamma$ - K, eV
I	$1s^2 2s^0 2p^0$	$2p^6 3s^2 3p^6$	34	<b>4.7267</b>	<b>4.8263</b>	<b>5.9419</b>
II	$1s^2 2s^0 2p^0$	$2p^6 3s^2 3p^6 3d^0$	44	<b>4.7261</b>	<b>4.0246</b>	<b>5.1857</b>
III	$1s^2 2s^0 2p^0 3p^0$	$2p^6 3s^2 3p^6 3d^0$	56	<b>4.6690</b>	<b>3.8423</b>	<b>5.0377</b>
IV	$1s^2 2s^0 2p^0 3p^0$	$2p^6 3s^2 3p^6 3d^0 4p^0$	62	<b>4.6102</b>	<b>3.7231</b>	<b>4.9215</b>
V	$1s^2 2s^0 2p^0 3p^0 3d^0$	$2p^6 3s^2 3p^6 3d^0 4p^0$	82	<b>4.6360</b>	<b>3.7555</b>	<b>4.9531</b>
VI	$1s^2 2s^0 2p^0 3p^0 3d^0$	$2p^6 3s^2 3p^6 3d^0 4p^0 4d^0$	92	<b>4.6415</b>	<b>3.5391</b>	<b>4.7103</b>

We have also calculated the total energy versus lattice constant. The data fit well to the Murnaghan equation of state (EOS).<sup>5</sup> The calculated bulk modulus,  $B_0$ , is 45.57 GPa, in close agreement with experimental value of 45.7 GPa.<sup>3</sup> We have also calculated the equilibrium lattice constant from the total energy minimization. The calculated equilibrium lattice constant is 5.651 Å.

#### 4. Conclusion

We performed first principle, self consistent, computational studies of the electronic and related properties of cubic antiferroite (anti-CaF<sub>2</sub>) lithium sulfide (Li<sub>2</sub>S), using a local density approximation (LDA) potential. We utilized the linear combination of atomic orbitals (LCAO) and the Bagayoko, Zhao, and Williams (BZW) method as enhanced by Ekuma and Franklin (BZW-EF).<sup>10</sup> Our results for cubic antiferroite (anti-CaF<sub>2</sub>) lithium sulfide (Li<sub>2</sub>S) are guideline for future experiments and theoretical calculations on electronic properties of Li<sub>2</sub>S. This work illustrates the potential of the BZW-EF method in providing accurate, calculated electronic and related properties of materials. Therefore our findings show that first principle calculations when employed with BZW-EF<sup>10</sup> have enormous predictability and could aid in the search for novel materials with desired properties, including binary to quaternary systems for various materials. The BZW method in the self-consistent calculations of the electronic properties of materials is must to warranty the convergence of the ground state. The nature of the BZW-EF method is supported and lies on the Rayleigh theorem. It is necessary for materials where an energy or band gap exists between occupied and unoccupied higher states- bands. With BZW-EF method, the prospects seem great for DFT within LDA to inform and to guide the design and fabrication of semiconductor based devices. Further, the *ab-initio* theory from first principles has enormous predictability and could aid in the search for novel materials with desired properties, including binary to quaternary systems.

**5. Acknowledgments:** This work was funded in part by the National Science Foundation and the Louisiana Board of Regents [EPS-1003897, No. NSF(2010-15)-RII-SUBR , and HRD-1002541], NASA and the Louisiana Board of Regents, through the Louisiana Space Consortium (LaSPACE) [NASA Coop. Agree. NNG05GH22H and Sub-Contract No. **37861**], and the Louisiana Optical Network Initiative [LONI].

#### 6. References

- [1] E. Zintl, A. Harder, and B. Dauth, *Z. Electrochem*, **40**, 588 (1934).
- [2] S. Kim, Y. Jung, S-J. Park, *Journ. of Power Sources* **152**, 272 (2005).
- [3] H. Khachai, R. Khenata, A. Bouhemadou, A. Haddou, A. H. Reshak, B. Amrani, D. Rached and B. Soudini, *J. Phys.: Condens. Matter* **21**, 095404 (2009).
- [4] D. Bagayoko, in: Proceedings of the first International Seminar on Theoretical Physics and National Development (ISOTPAND), August 2008, Abuja, Nigeria. Available in the African Journal of Physics [http://sirius-c.ncat.edu/asn//ajp/allissue/ajp\\_ISOTPAND/index.html](http://sirius-c.ncat.edu/asn//ajp/allissue/ajp_ISOTPAND/index.html).
- [5] D. M. Ceperly, B. J. Alder, *Phys. Rev. Lett.* **45**, 566 (1980).
- [6] S. H. Vosko, L. Wilk, M. Nusair, *Can. J. Phys.* **58**, 1200 (1980).
- [7] B. N. Harmon, W. Weber, D. R. Harmann, *Phys. Rev.* **B25**, 1109 (1982).
- [8] L. Franklin, C. E. Ekuma, G. L. Zhao, and D. Bagayoko, *J. Phys. and Chem. Solids* **74**, 729 (2013).
- [9] E. C. Ekuma, L. Franklin, G. L. Zhao, J. T. Wang, D. Bagayoko, *Physica B* **406**, 1477 (2011).
- [10] E. C. Ekuma, M. Jarrell, J. Moreno, and D. Bagayoko, *AIP Advances* **2**, 012189 (2012).
- [11] Theo Hahn (Ed. ), *International Tables for Crystallography, Vol. A: Space Group Symmetry*, 5<sup>th</sup> ed. Springer, 2005.

## Achieving High Efficiency in Serial and at Extreme Scale

Md Rakib Hasan<sup>1</sup>, Majedul Haque Sujon<sup>2</sup>, R. Clint Whaley<sup>3</sup>

<sup>123</sup>Computer Science and Engineering Division / Center for Computation and Technology  
Louisiana State University  
{<sup>1</sup>rhasan, <sup>2</sup>msujon}@cct.lsu.edu, <sup>3</sup>rcwhaley@lsu.edu

**Abstract:** This paper discusses our research on computational optimization for LA-SiGMA. It provides a motivation for the importance of this work, an introduction to the software projects that embody the work, and a brief summary of our current progress. Citations are provided for further details.

**Keywords:** Optimization, empirical tuning, BLAS, LAPACK, linear algebra, LU factorization, compilers, iFKO.

### 1. Introduction

Our research group moved to LSU and joined the LA-SiGMA project in August of 2013. Our research is primarily concentrated on improving the performance of kernels used by computational scientists. Section 1.1 motivates this line of investigation, while Section 2 introduces our main areas of research. Sections 2.1 and 2.2 will then discuss some of our recent progress, with Section 3 concluding the report.

#### 1.1 Motivation

In high performance computing (HPC), time-to-solution at a given level of accuracy is the overwhelming fitness criteria by which algorithms and solutions are constantly being judged. Typically, when time-to-solution decreases (due to algorithmic, tuning, or hardware advance), the community simply increases the accuracy of the model or simulation; this dynamic explains HPC's voracious and essentially unsatisfiable appetite for extremely efficient applications. Outside of HPC, adequate performance is seen using compilers, which have a long history of producing extremely important speedups on everyday code. Within HPC, however, compiler-optimized kernels (a kernel is any relatively small routine that when strongly optimized, has a major impact on application performance) are routinely outperformed (often by multiple orders of magnitude) by code which has been hand-tuned by experts in both the target architecture and the problem domain. Hand-tuners with the necessary expertise are always in critically short supply, which both drastically slows the pace of HPC research and strongly distorts its outcome. Obviously, when the computational scientist is unable to interest a hand-tuner in tuning kernels for the machines he/she has access to, they are forced to rely on inefficient kernels, and can therefore do less science in a given amount of time (not uncommonly, they may not be able to do some work at all due to inefficient use of scarce resources). Research outcomes are also distorted because only a few kernels (e.g., the Basic Linear Algebra

Subprogram, or BLAS [1]) have a large enough pre-existing audience to command the attention of these experts, and so algorithms that can use such supported kernels receive a dominating performance advantage, which almost guarantees that alternative approaches to the problem cannot compete, and therefore never gain the widespread usage and development necessary for their full potential to be reached.

Automated empirical tuning [2], where a search driver finds high performance solutions by iteratively applying code transformations, compiling and measuring the performance of the transformed code on the actual target architecture, is today the main means by which researchers are attempting to provide kernels that remain highly efficient even in the face of platform (OS & architecture) churn. Our ATLAS (Automatically Tuned Linear Algebra Software) package was one of the pioneering empirical tuning projects which demonstrated just how successful this approach can be, not only at producing high quality research, but also in generating tools that are extremely useful for computational scientists across the globe. If the produced tools are actually going to solve the kernel optimization problem, it is necessary to combine extremely meticulous engineering with the research insights that determine the course of the work.

## 2. Our main research areas

Our work in computational efficiency is concentrated in two primary areas. The most well established is ATLAS [2]–[5], where we develop new optimization techniques, and study extreme-scale parallel computing. ATLAS is our original empirical-tuning framework which provides tuned linear algebra kernels; specifically, it provides tuned versions of the entire BLAS [1] API, and a subset of the LAPACK [6] API. These two APIs are the main libraries used for dense linear algebra in HPC. ATLAS has been enormously successful in empirically tuning these libraries, and is currently used by hundreds of thousands of scientists and engineers all across the globe. Since it provides tuning in a well-understood domain, ATLAS provides us with an ideal test bed for developing new optimizations, getting experience with their real-world application and system effects, as well as performing required numerical analysis research. The ATLAS open-source project can be downloaded at its homepage (<http://math-atlas.sourceforge.net>).

The linear algebra supported by ATLAS underlies a tremendous number of computational approaches, but no domain-specific library can help with arbitrary computation. Handling arbitrary calculation requires a *compiler*. The problem is that compilation frameworks are extremely complicated software projects, with existing compilers targeting generality over performance, which results in their failing to deliver the extreme efficiency required by computational scientists. Therefore, in our second area of research we have developed our own compilation framework, iFKO (iterative Floating Point Kernel Optimizer).

iFKO [7], [8] is an empirical compilation framework specialized for optimizing compute kernels to extreme levels of efficiency. In order to achieve extreme optimization, the framework actually performs timings to measure the impact of proposed optimizations, and in this way can automatically discover the unique set of code transformations necessary to tune a particular input computational kernel the user's unique hardware and software

platform. In order to reach the required levels of performance, iFKO must exploit hardware-specific features of the target platform, and so the framework must be ported to new ISAs (Instruction Set Architecture, essentially the native language of the actual hardware). Our current ISA focus is modern x86 (e.g., mainline Intel and AMD architectures).

## **2.1 Recent iFKO research**

Modern computer architectures overwhelmingly rely on SIMD vectorization to provide highly efficient computation. Unfortunately, branches can inhibit vectorization, and this was a real problem in our original iFKO work [7]. Just before our group's move to LSU, we completed research that enabled us to overcome this problem completely for the kernels studied in [7]. To do so, we invented a new compilation technique known as speculative vectorization; the results of this research were published in [9].

An HPC compiler can only be effective if it can achieve extreme levels of performance, which required us to start with very simple kernels. We are presently extending the iFKO so that it can automatically tune more complicated routines. Our current efforts are in supporting multidimensional arrays, increasing register effectiveness, and better handling of nested loops. When this work is complete, iFKO should be able to fully tune the entire suite of kernels used by ATLAS. At this stage, iFKO should also have enough functionality to tune other non-ATLAS kernels used by LA-SiGMA researchers, which will be our next phase of research.

## **2.2 Recent ATLAS research**

Our current research is mainly concentrated on effectively exploiting extreme-scale (i.e. large numbers of cores) in shared memory architectures. Our first paper as part of the LA-SiGMA effort was [10], where we introduced a new approach to parallel LU factorization that provided the best-known performance for all problem sizes. LU factorization is used to solve linear systems of equations, and the lessons learned in this research can be applied to most dense linear algebra.

We have also undertaken study of new architectures being used for LA-SiGMA computations, including the Intel Xeon PHI, which provides unparalleled scale for modest price. We are currently performing research on effectively exploiting this scale, and lessons learned so far are already informing a complete rewrite of ATLAS's shared memory approach.

## **3. Conclusion**

In conclusion, we are making good progress on handling extreme-scale computing, and are still expanding our suite of techniques to better utilize the Intel Xeon PHI. We are also increasing the capabilities of our compilation framework, and are looking for compute-bound kernels to auto-optimized with iFKO. LA-SiGMA researchers are therefore encouraged to contact us to discuss optimizing their kernels (starting with the simplest).

#### 4. Acknowledgments

This work was supported by the National Science Foundation grant no. OCI-1149303 and the NSF EPSCoR Cooperative Agreement no. EPS-1003897, with additional support from the Louisiana Board of Regents.

#### 5. References

- [1] J. Dongarra, J. Du Croz, I. Duff, and S. Hammarling, “A Set of Level 3 Basic Linear Algebra Subprograms,” *{ACM} Trans. Math. Softw.*, vol. 16, no. 1, pp. 1–17, 1990.
- [2] R. C. Whaley and J. Dongarra, “Automatically Tuned Linear Algebra Software,” in *SuperComputing 1998: High Performance Networking and Computing*, 1998.
- [3] R. C. Whaley, A. Petitet, and J. J. Dongarra, “Automated Empirical Optimization of Software and the {ATLAS} Project,” *Parallel Comput.*, vol. 27, no. 1–2, pp. 3–35, 2001.
- [4] A. M. Castaldo, R. C. Whaley, and A. T. Chronopoulos, “Reducing Floating Point Error in Dot Product Using the Superblock Family of Algorithms,” *SIAM J. Sci. Comput.*, vol. 31, no. 2, pp. 1156–1174, 2008.
- [5] A. M. Castaldo and R. C. Whaley, “Achieving Scalable Parallelization For The Hessenberg Factorization,” in *Proceedings of IEEE Cluster*, 2011, pp. 65–73.
- [6] E. Anderson, Z. Bai, C. Bischof, J. Demmel, J. Dongarra, J. Du Croz, A. Greenbaum, S. Hammarling, A. McKenney, S. Ostrouchov, and D. Sorensen, *{LAPACK} Users' Guide*, 3rd ed. Philadelphia, PA: SIAM, 1999.
- [7] R. C. Whaley and D. B. Whalley, “Tuning High Performance Kernels through Empirical Compilation,” in *The 2005 International Conference on Parallel Processing*, 2005, pp. 89–98.
- [8] R. C. Whaley, “Automated Empirical Optimization of High Performance Floating Point Kernels,” Florida State University, 2004.
- [9] M. H. Sujon, R. C. Whaley, and Q. Yi, “Vectorization Past Dependent Branches Through Speculation,” in *Proceedings of the 22nd International Conference on Parallel Architectures and Compilation Techniques*, 2013, pp. 353–362.
- [10] M. R. Hasan and R. C. Whaley, “Effectively exploiting parallel scale for all problem sizes in LU factorization,” in *Proceedings of the 28th International Parallel and Distributed Processing Symposium (IPDPS2014)*, 2014, pp. 1039–1048.

## **Aligned Carbon Nanotube Forest as Supercapacitor Electrodes**

**Moses Oguntoye, Lawrence Pratt and Noshir Pesika**

Department of Chemical and Biomolecular Engineering, Tulane University, New Orleans, LA 70118

**Abstract:** This ongoing study investigates the potential use of aligned carbon nanotube forest arrays as supercapacitor electrodes in ionic liquid electrolytes. Carbon nanotubes have been touted as viable materials for use as electrodes in supercapacitors because of their unique properties. Here, we have studied the effects of their alignment and plasma pretreatment in improving capacitance. Aligned carbon nanotubes were grown, treated and electrochemically tested in a three electrode system as electrodes and showed high capacitance with the potential of replacing current supercapacitor technology.

**Keywords:** Carbon nanotubes, Supercapacitor, Double layer capacitance, Pseudocapacitance, Ionic Liquids

### **1. Introduction**

Supercapacitors offer an advantage over conventional capacitors in solving energy storage problems because of the larger power and energy densities they offer [1] as well as the larger electrochemical operating window obtainable when ionic liquids are used as electrolytes [2]. From a research perspective, proper material selection and design together with proper electrolyte choice can further enhance the storage capabilities of supercapacitors. Target material properties known to enhance measured capacitance in supercapacitors include porosity, surface area and electrical conductivity [3]. The known means of charge storage in capacitive materials are in the formation of a Helmholtz double layer at the electrode-electrolyte interface (Electric double layer capacitance) or in the advancement of redox reactions during charge-discharge processes (pseudocapacitance) or a combination of both. Carbon nanotubes can be designed to encapsulate all these properties as well as store charge using a combination of both charge storage mechanisms with a view to increasing the overall capacitance and that is the objective of this study [4, 5]. So far, very little focus has been placed on the alignment of carbon nanotubes and how this affects capacitance, as well as the physical (non-chemical) treatment that introduces pseudocapacitance to the electrodes. Here, we have used aligned carbon nanotube forests, known to have sufficient porosity, high electrical conductivity and high surface area (due to their alignment); as supercapacitor electrodes. In addition, we have subjected the nanotube forests to physical treatments that introduce some pseudocapacitive ability to the electrodes. Prepared electrodes were tested electrochemically in an ionic liquid electrolyte and the results obtained were discussed.

## 2 Experimental

Aligned carbon nanotube forests were prepared using water assisted super growth [6]. Substrates were prepared by electron beam deposition of successive layers of Al (10nm) and Fe (1.5nm) on a 300nm SiO<sub>2</sub> coated silicon wafer. Carbon nanotube growth was carried out in a quartz tube furnace at 775°C for 15 minutes under a gas flow mixture containing 1.3slm of Ar-H<sub>2</sub> mixture (15% H<sub>2</sub>), 100sccm of C<sub>2</sub>H<sub>4</sub> and water vapor generated by flowing 100sccm of the same Ar-H<sub>2</sub> mixture through a water bubbler. The as-grown nanotubes were characterized using Scanning and Transmission electron microscopy imaging techniques. The BET surface area for N<sub>2</sub> adsorption was measured and Thermogravimetric analysis (TGA) was used to confirm the graphitic nature of the nanotubes

Aligned carbon nanotube forest electrodes were prepared by contact transfer [5]. Double sided conducting copper tape was placed on a plain silicon wafer and the nanotube forest was transferred to one side of the tape using adhesives. The electrical contact between the conducting tape and the nanotube forest was further enhanced by sputtering an ultrathin gold layer (~5nm) on the transferred forest. The prepared electrodes are treated with air plasma; 18W RF for 3 minutes, before electrochemical analysis. Electrochemical characterization was done on the prepared electrodes by using them as the working electrode in a three electrode electrochemical cell system with platinum gauze (~1cm<sup>2</sup>) as counter electrode and Ag/AgCl reference electrode. The electrolyte used was 1M Tetraethylammonium Tetrafluoroborate in propylene carbonate. Electrochemical measurements were done using a Potentiostat/Galvanostat.

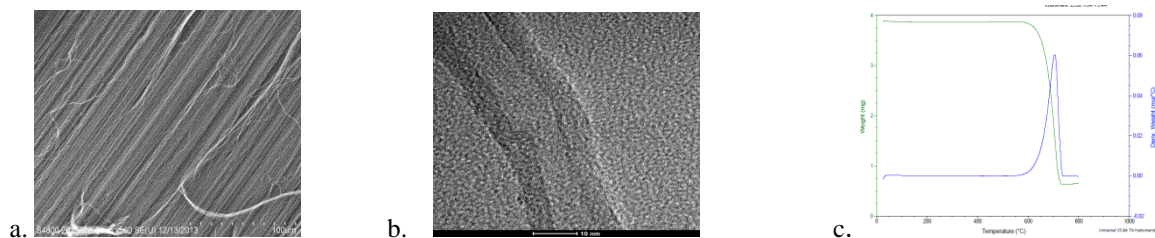


Figure 1 (a) SEM micrograph showing alignment of grown carbon nanotubes. (b) TEM micrograph showing multi-walled nature of grown carbon nanotubes. (c) Results of TGA of carbon nanotubes

## 3 Results and Discussion

A scanning electron micrograph showing alignment of as-grown nanotubes is shown in Figure 1a and the nanotubes grown are multi-walled as seen in the TEM micrograph (Figure 1b). The thermogravimetric analysis result shown in Figure 1c reveals that the nanotubes are graphitic by reason of their sharp combustion in air at

about 700°C. The BET surface area was determined to be about 693m<sup>2</sup>/g which is higher than the 400m<sup>2</sup>/g surface area proposed by the Peigney et al model for plasma treated multiwalled carbon nanotubes [7]. The mass of the active portion of each electrode was determined by weighing the wafers before contact transfer and after plasma treatment using a high precision scale and was determined to be about 0.16mg. The carbon nanotubes had a height of about 200 microns after 15 minutes of growth. Electrochemical analysis of the characteristics of the electrodes included cyclic voltammograms (CV scans) and charge-discharge experiments. CV scans were carried out at varying scan speeds of 5, 20, 50 and 100mV/s between -1 and 1V and the resulting curves are shown in Figure 2a. The steep sloped curves at the voltage boundaries of the electrochemical window show that the formation of an electric double layer is the major contributor to the capacitance of the electrodes [5] and is more pronounced in scans of slower speeds which is believed to be as a result of the ions having enough time to diffuse through the pores of the electrodes to form a double layer during charging, and diffuse out during discharging. The peaks observed also reflect the contribution of a small amount of pseudocapacitance [8]. This is thought to be as a result of the treatment of the nanotube electrodes with air plasma. As previously reported, treatment of carbon nanotubes with air plasma can give rise to the attachment of oxygen containing groups on the surface of the nanotubes which can undergo redox reactions during electrode charge and discharge, in addition to enhancing the wettability of the nanotubes [9]. The capacitance of the electrode is determined from the CV scans using the formula [10]: “Capacitance = Current per unit mass/scan rate”. The estimated capacitance from the CV scans at 20mV/s (which is an estimated realistic charge-discharge rate [10]) is estimated to be about 156F/g. Figure 2a (inset) also shows the reduction of capacitance with increasing scan rate showing that only about 30% of the capacitance is retained as scan rate is increased from 5mV/s to 100mV/s. Future work directed towards optimizing the height of the aligned carbon nanotubes is expected to increase the percentage of retained capacitance. The galvanostatic charge-discharge curves for a 1.5V range at 1mA, 2mA and 3mA currents are also shown in Figure 2b. Here, we observe that the interfacial resistance drop is as little as less than 0.5V for a charging current of 1mA which indicates a fast ion transport between the electrode and the electrolyte [5].

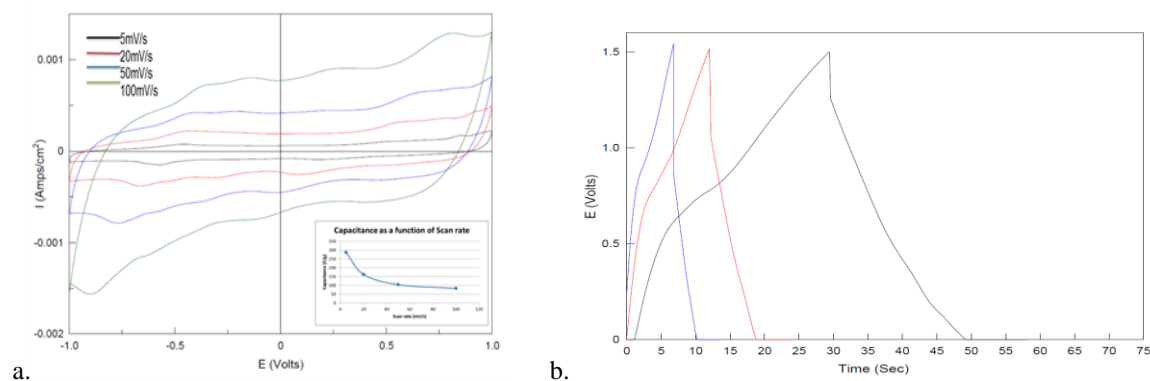


Figure 2. (a) CV curves of scans carried out at 5,20,50 and 100mV/s. (b) Charge-Discharge curves.

#### 4. Conclusions and Future Work

Aligned multiwalled carbon nanotubes were successfully grown and were used to assemble electrodes. So far, the obtained high charge storage capability of the aligned carbon nanotube electrode in ionic liquid electrolyte shows that there is enormous potential in exploring the unique properties of carbon nanotubes for the fabrication of energy storage materials. Future work on this project will be aimed at optimizing the carbon nanotube forest height and introducing more pseudocapacitance to the forest by fabricating a 3D carbon nanotube-metal oxide structure while studying the interplay between the resultant changing pore size and the overall capacitance.

#### 5. Acknowledgments

The current work is funded by the NSF EPSCoR LA-SiGMA project under award #EPS-1003897. The authors gratefully acknowledge Rahmatollah Eskandari and Dr. Leszek Malkinski for helping to prepare the catalysts used.

#### 6. References

- [1] Wen Lu and Liming Dai. *Carbon Nanotube Supercapacitors (2010)*, Jose Mauricio Marulanda (Ed.), ISBN: 978-953-307-054-4, InTech.
- [2] Takaya Sato, Gen Masuda, Kentaro Takagi. *Electrochimica Acta* 49 (2004), 3603
- [3] Hui Pan, Jianyi Li, Yuan Ping Feng. *Nanoscale Res. Lett.* (2010). 5. 654
- [4] Robert A. Fisher, Morgan R. Watt, W. Jud Ready. *ECS Journal of Solid State Science and Technology* (2013), 2 (10) M3170-M3177
- [5] Wen Lu, Liangti Qu, Kent Henry, Liming Dai. *Journal of Power Sources* 189 (2009) 1270-1277.
- [6] Kenji Hata, Don N. Futaba, Kohei Mizuno, Tatsunori Namai, Motoo Yumura, Sumio Iijima. *Science* 306 (2004)
- [7] A. Peigney, Ch. Laurent, E. Flahaut, R.R. Bacsa, A. Rousset. *Carbon* 39 (2001) 507
- [8] Joseph N. Barisci, Gordon G. Wallace, Ray H. Baughman. *J. Electrochem. Soc.* (2000) volume 147, issue 12, 4580-4583
- [9] S. Huang, L. Dai. *J. Phys. Chem. B* 106 (2002) 3543
- [10] Meryl D. Stoller, Rodney S. Ruoff. *Energy Environ. Sci.*, 2010, 3, 1294–1301

## **Aligning Metagenomic Short Read Sequences using GPGPUs and Expectation-Maximization Algorithm**

**Mihir Karnik<sup>1</sup>, David Anderson<sup>2</sup>, Pradeep Chowriappa<sup>1</sup> and Sumeet Dua<sup>1</sup>**

<sup>1</sup>Computer Science, Louisiana Tech University, Ruston, LA

<sup>2</sup>Mathematics and Computer Science Department, Louisiana School for Math, Science, and the Arts, Natchitoches, LA

**Abstract:** Metagenomic analysis has allowed the study of many organisms that were unculturable in a laboratory, and has enabled us to determine the composition of a community of organisms using short reads. We hypothesize that there is an expectation that any given short read would map to more than one reference sequence as well as to multiple variable regions of the same reference sequence with varying degrees of probability. We use a semi-supervised approach to calculate the conditional probabilities of reads occurring in different variable regions across various reference sequences. However, such a process is computationally expensive and is limited by the CPU power. To circumvent this, we have employed GPGPUs with CUDA programming to convert the short reads to a feature vector that will improve efficiency and accuracy of the mapping. The results of running the EM algorithm demonstrate the unique reads that map to various organisms in the metagenome sample.

**Keywords:** Metagenomic analysis, next-generation sequencing, short reads, assembly, mapping

### **1. Introduction**

Metagenomics as a method for analyzing genomes is providing a new and striking insight into the environmental surroundings of different microbial communities [1]. As defined by [2] metagenomics is the sequence analysis of genomic data taken directly from the environment. Using short reads to assemble the community of multiple organisms that are present in the metagenome sample generally fails. Characterization of microbial community composition is often done with a phylogenetic marker gene, most commonly the small subunit ribosomal RNA (SSU rRNA) gene [3]. Earlier, rRNA sequences were generated by amplification, cloning, and Sanger sequencing. Nowadays, technologies such as pyro tag sequencing of short hyper-variable regions [4], Illumina sequencing of variable tags [5], and hybridization to specialized high-density microarrays [6] are used to calculate the throughput of SSU-based microbial community characterization. Due to this, there is a need to create a mechanism, which could be used to find out and quantify unique sequences that mapped to different organisms that were present in the sample taken from the environment.

## 2. Related Research

The ‘read mapping’ problem is one of the important challenges presented by the application of new sequencing technology. Sequencing machines made by Illumina of San Diego, Applied Biosystems (ABI) of Carlsbad, California, and Helicos of Cambridge, Massachusetts, produce short sequences of 25–100 base pairs (bp), which are sequence fragments read from a longer DNA molecule present in the sample that is fed into the machine [7]. The short read lengths and high conservation of sequence in some regions of the SSU gene produce ambiguous assignments of many reads among closely related strains, creating complex situations in a simple mapping strategy [8]. The current methods rely on aligning reads to a single reference genome which leads to inherent biases and lower accuracy [9]. The algorithms written to handle the data structures for reads can also cause bottlenecks in metagenome analysis [10]. Quantification of species abundance can be reduced to a read mapping problem if the community composition of the reference sequences was known ahead of time and all reference SSU sequences were available. The composition of environmental samples is rarely known ahead of time. [8].

Variable regions are the ones that can have a large amount of differences from the reference sequence of an organism. The presence of a large number of repeats or substitutions is characteristic of these regions. The problem of read mapping is solved by [9] by using compressed representation of a collection of genomes, which explicitly tackles the genomic variation observed at every position and designing an algorithm based on the Burrows–Wheeler transform that maps short reads from a newly sequenced genome to an arbitrary collection of two or more genomes. There has been an increase in the machines computationally intensive alignment problems due to the advent of next generation gene sequencing that can take many hours on a modern computer [11]. The complexity of the problem arises from the fact that we have to compare the given order of sequences and consider the fact that the sequences present in the original reference sequence can be in any order. The objective here is to carry out the mapping of the reads to the variable regions of the reference sequence in an accurate manner.

## 3. Methodology

The methodology used in this this paper has been divided into three sections as depicted in the diagram below.

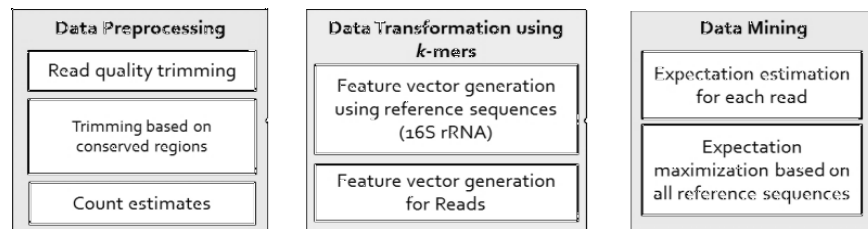


**Figure 1 Framework for Methodology**

The Feature Vector has been stored into a newly designed file called the ‘PMD’ file which is based on the BAM and SAM formats which are used to store genome data. The procedure to create this file involves breaking down the short reads into sequences of 21 bp length called  $n$ -mers and then representing each of those 21 bp sequence as a function of 64 codons. The naïve Bayes algorithm is then applied to these  $n$ -mers to calculate the posterior probability which is the expectation that a given read maps to a variable region in a reference sequence.

For a given read  $R$  and a reference sequence  $S_{ref}$ ,  $P(R|S_{ref}) = P(S_{ref}|R) \times P(S_{ref}) / P(R)$  where,  $P(S_{ref}|R)$  is calculated using the number of  $n$ -mers that map to a given reference sequence  $S_{ref}$ . The maximization step is used to reduce the number of possible choices that a read can map to. It is calculated using the average of the probability for a given variable region across all the reference sequences.

Figure 2 below shows the comparison of performance of the GPU using CUDA vs the CPU when creating the feature vectors for the reads. The second part of figure 2 is a read profile, which demonstrates the mapping of all the  $n$ -mers in a read vs all the reference sequences. Figure 3 is a histogram that has been produced after we have used the average posterior probability to determine which read will map to which reference sequence.

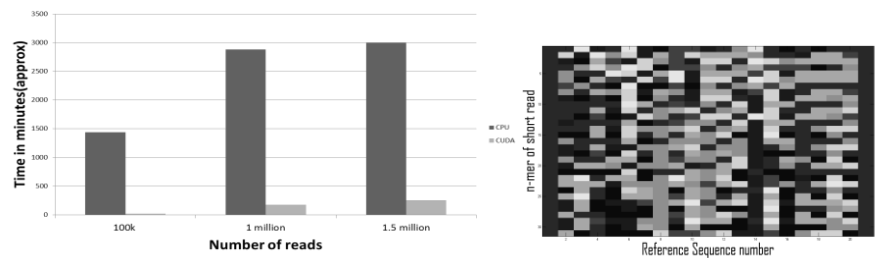


Figure 2 CPU vs CUDA and Read mapping

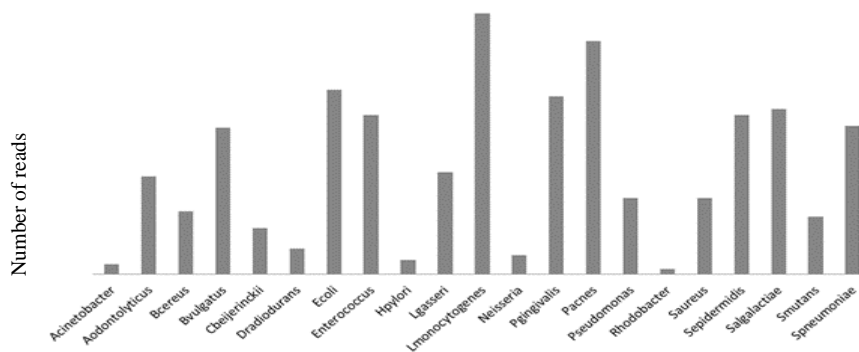


Figure 3 Number of reads mapping based on average posterior probability

#### **4. Conclusion**

The results demonstrate that there is a considerable improvement in the efficiency of the mapping of the short reads to reference sequences when we used the GPU enabled CUDA as opposed to using traditional CPUs. The read quality trimming helps to increase the accuracy of the mapping as it deletes the reads that can possibly have errors in them. The read profile calculated during the expectation step helps to confirm our hypothesis that a given short read maps to more than one reference sequence as well as to multiple variable regions of the same reference sequence. The maximization step is used to calculate the average posterior probability, which provides the distribution of the organisms with respect to the number of short reads that mapped to them.

#### **5. Acknowledgments**

The current work is funded by the NSF EPSCoR LA-SiGMA project under award #EPS-1003897.

#### **6. References**

- [1] L. Krause, N. N. Diaz, A. Goesmann, S. Kelley, T. W. Nattkemper, F. Rohwer, R. A. Edwards, and J. Stoye, "Phylogenetic classification of short environmental DNA fragments," *Nucleic Acids Res.*, vol. 36, no. 7, pp. 2230–2239, Feb. 2008.
- [2] "PHD-2010-06.pdf."
- [3] N. R. Pace, "A molecular view of microbial diversity and the biosphere," *Science*, vol. 276, no. 5313, pp. 734–740, May 1997.
- [4] M. L. Sogin, H. G. Morrison, J. A. Huber, D. Mark Welch, S. M. Huse, P. R. Neal, J. M. Arrieta, and G. J. Herndl, "Microbial diversity in the deep sea and the underexplored 'rare biosphere,'" *Proc. Natl. Acad. Sci. U. S. A.*, vol. 103, no. 32, pp. 12115–12120, Aug. 2006.
- [5] H.-W. Zhou, D.-F. Li, N. F.-Y. Tam, X.-T. Jiang, H. Zhang, H.-F. Sheng, J. Qin, X. Liu, and F. Zou, "BIPES, a cost-effective high-throughput method for assessing microbial diversity," *ISME J.*, vol. 5, no. 4, pp. 741–749, Apr. 2011.
- [6] E. L. Brodie, T. Z. DeSantis, J. P. M. Parker, I. X. Zubietta, Y. M. Piceno, and G. L. Andersen, "Urban aerosols harbor diverse and dynamic bacterial populations," *Proc. Natl. Acad. Sci. U. S. A.*, vol. 104, no. 1, pp. 299–304, Jan. 2007.
- [7] C. Trapnell and S. L. Salzberg, "How to map billions of short reads onto genomes," *Nat. Biotechnol.*, vol. 27, no. 5, pp. 455–457, May 2009.
- [8] C. S. Miller, B. J. Baker, B. C. Thomas, S. W. Singer, and J. F. Banfield, "EMIRGE: reconstruction of full-length ribosomal genes from microbial community short read sequencing data," *Genome Biol.*, vol. 12, no. 5, p. R44, 2011.
- [9] L. Huang, V. Popic, and S. Batzoglou, "Short read alignment with populations of genomes," *Bioinformatics*, vol. 29, no. 13, pp. i361–i370, Jul. 2013.
- [10] E. Drezen, G. Rizk, R. Chikhi, C. Deltel, C. Lemaître, P. Peterlongo, and D. Lavenier, "GATB: Genome Assembly & Analysis Tool Box," *Bioinformatics*, p. btu406, Jul. 2014.
- [11] R. Fariyar, S. Venkataraman, Y. Li, E. M. Chan, A. Verma, and R. Campbell, "Accurate Sequence Alignment using Distributed Filtering on GPU Clusters," 2011.

## Anderson localization in systems with off-diagonal disorder

H. Terletska<sup>1,2</sup>, C. E. Ekuma<sup>1,2</sup>, C. Moore<sup>1,2</sup>, K. M. Tam<sup>1,2</sup>, J. Moreno<sup>1,2</sup>, and M. Jarrell<sup>1,2</sup>

<sup>1</sup>Center for Computation & Technology, Louisiana State University, Baton Rouge, LA 70803, USA

<sup>2</sup>Department of Physics & Astronomy, Louisiana State University, Baton Rouge, LA 70803, USA

**Abstract:** We generalize the Blackmann *et al.* [1] coherent-potential-approximation-like mean-field method of electron localization in systems with both diagonal and off-diagonal disorder to incorporate the important non-local quantum coherent effects, by employing the dynamical cluster approximation scheme. To study the effect of off-diagonal disorder on electron localization we generalized the recently developed typical medium dynamical cluster approximation to incorporate both diagonal and off-diagonal randomness. We find strong evidence that non-local effects can induce pronounced changes on the density of states and the mobility edge. These results point to the importance of the cluster generalization of mean-field methods.

**Keywords:** Anderson localization, diagonal disorder, off-diagonal disorder, TMDCA

### 1. Introduction

Disorder which is ubiquitous in most materials can have a dramatic effect on their properties [2]. Scattering of charge carriers off random potentials can lead to their spatial confinement, known as Anderson localization [3]. Such spatial confinement of carriers is a quantum effect, which arises from the quantum interference between various carrier trajectories and has strong dependence on the dimensionality of the system.

There has been considerable progress on the development of the formalism to understand the Anderson localization induced for diagonal disorder, where randomness is modeled by the change in the local potential in the tight-binding model. However, for a proper study of many real materials, it is often important to include both diagonal and off-diagonal disorder. In this case, the disorder is modeled not only by the randomness of the local potential but also by randomness in the hopping amplitudes.

A single-site self-consistent mean field approximation for systems with off-diagonal disorder was constructed by Blackman, Esterling and Berk (BEB) [3]. However, by its construction, the BEB formalism is a single-site approximation, and hence cannot include multi-site quantum coherent effects. To address such shortcoming of the BEB, we have recently extended it by using the dynamical cluster approximation (DCA) [4].

In order to identify the Anderson localized states, one has to employ the ideas of the typical medium theory (TMT) [5] where the typical density of states (TDOS) serves as an order parameter. Up to now, the typical medium analysis, has been used to study the diagonal disorder only. However, since off-diagonal disorder can cause quite a different behavior, it is necessary to have a tool which would account for Anderson localization in systems with both diagonal and off-diagonal disorder on equal footing. To accomplish this, we generalized our recently developed typical medium dynamical cluster approximation (TMDCA) [6] to treat systems with off-diagonal disorder. In this work, by performing a systematic comparison of the single site and finite cluster results for the TDOS, we find a pronounced difference between the local and non-local results, which demonstrate the

necessity of including the non-local multi-site effects for a proper and quantitative characterization of the localization transition in systems with off-diagonal disorder.

## 2. Model Hamiltonian

The single band tight binding model is the simplest model which is commonly used to study disordered systems

$$H = -\sum_{\langle i,j \rangle} t_{ij} (c_i^\dagger c_j + h. c.) + \sum_i V_i n_i \quad (1)$$

where  $V_i$  is a local random potential and  $t_{ij}$  is the nearest-neighbor hopping matrix. In this paper, we focus on the binary disorder case, where some host  $A$  atoms are substituted with  $B$  impurities with a probability distribution function of the form  $P(V_i) = c_A \delta(V_i - V_A) + c_B \delta(V_i - V_B)$ . For the diagonal disorder case, it is assumed that substitution of impurity atoms on average has no effect on hopping amplitudes to the neighboring atoms and hence, the hopping probability  $t_{ij} = t$  is the same for each site. For systems with off-diagonal disorder, the randomness is introduced not only locally in the random potential but also in the hopping matrix

$$t_{ij} = \begin{cases} t_{ij}^{AA}, & i \in A, j \in A \\ t_{ij}^{BB}, & i \in B, j \in B \\ t_{ij}^{AB}, & i \in A, j \in B \\ t_{ij}^{BA}, & i \in B, j \in A \end{cases} \quad (2)$$

where hopping  $t_{ij}$  depends on the type of impurity occupying sites  $i$  and  $j$ . For the off-diagonal disorder, Eq. (1) becomes a  $2 \times 2$  matrix equation, with corresponding AA, AB, BA, and BB matrix elements [1].

## 3. Results and Discussions

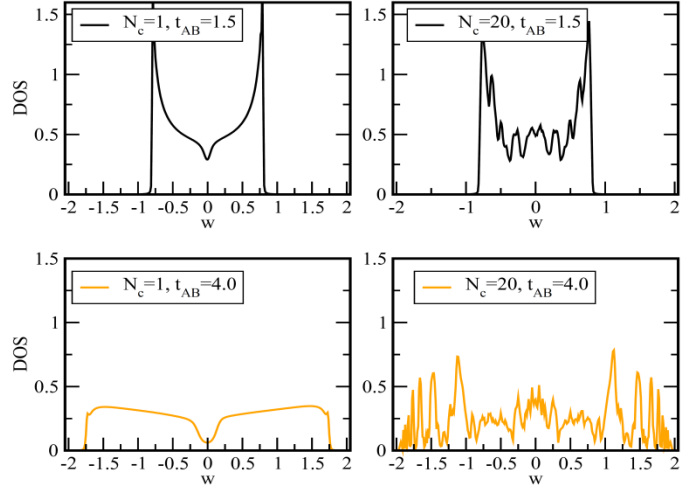
### (A) The Dynamical Cluster Approximation for off-diagonal disorder

The existing BEB [1] scheme for off-diagonal disorder is a local, single-site mean-field approximation. Therefore, by its construction, the BEB formalism is unable to capture non-local multi-site disorder-induced correlations [3]. To overcome the shortcomings of the BEB theory, we utilize the DCA and extended the BEB to a finite cluster. A detail discussion of our DCA extension of BEB is presented in Ref. [7].

It is known that the non-local quantum coherent effects are more pronounced in lower dimensions [2,3]. To test this, we apply our generalized off-diagonal disorder DCA scheme of Ref. [7] to a one-dimensional (1D) Anderson Hamiltonian of Eq. (1). To see the effect of the off-diagonal randomness with  $t_{AA} \neq t_{BB} \neq t_{AB}$ , we present in Fig.1 the local average density of states (DOS) for a fixed diagonal disorder potential  $V_A = -V_B = 0.3$  calculated for several values of the off-diagonal disorder. In particular, the off-diagonal randomness is modelled by the change in the  $t_{AB}$  hopping amplitudes with  $t_{AA} = t_{BB} = 1$  being fixed. Our DCA results are obtained for a cluster size  $N_c = 20$ , the concentration of  $A$  ions is fixed to  $c_A = 0.5$ . To demonstrate the effect of non-local inter-site correlations, we compare the  $N_c = 1$  and finite cluster  $N_c = 20$  results. The  $N_c = 1$  results correspond to the local BEB analysis. As can be seen from Fig.1 for  $N_c = 1$  the change in  $t_{AB}$  has a very similar effect to the change of the local diagonal disorder, i.e. increasing  $t_{AB}$  leads to the broadening of the bands

and gradual opening of the gap at  $\omega = 0$ . On the other hand, the finite cluster  $N_c = 20$  data show a rather different behavior. The DOS acquires a finite structures and most importantly the  $N_c = 20$  data show accumulation of the states near the band center. Fig. 1 demonstrates, that single site BEB overestimates the gap at the band center [8], as it cannot account for the non-local effects.

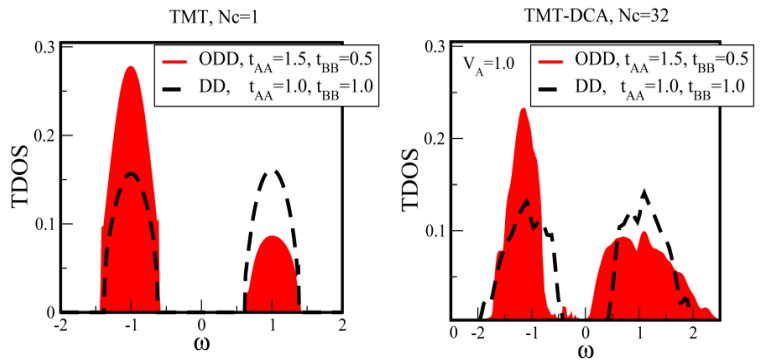
**Fig.1:** Parameters: One-dimension,  $t_{AA} = t_{BB} = 1$ ,  $t_{AB} = 1.5, 4$  and  $c_A = 0.5$ . The average DOS calculated within the local  $N_c = 1$  (left panel) and non-local DCA (left panel) for  $N_c = 20$  schemes at different values of the off-diagonal disorder modelled by changes in the  $t_{AB}$  hopping. Varying the mixed off-diagonal parameter  $t_{AB}$  for  $N_c = 1$  leads to a gradual opening of the gap at  $w = 0$  which is the same behavior as for the pure diagonal disorder. The non-local finite cluster  $N_c = 20$  results not only introduce the finite structures in the DOS but also fill up the  $w = 0$  gap that is overemphasizes in  $N_c = 1$  data. Our findings also agree with results of [8].



### (B) The typical medium finite cluster analysis of off-diagonal disorder

Next, we consider the effect of the off-diagonal randomness on the Anderson localization in three dimensions. The Anderson transition depends strongly on the dimensionality of the systems [9], with metal-insulator transition occurring at finite disorder strength in only three-dimension ( in 1D and 2D all states are localized for any amount of disorder).

**Fig.2:** The typical density of states for the diagonal and off-diagonal disorder for  $N_c = 1$  (left panel) and  $N_c = 32$  (right panel). For the diagonal disorder, the TDOS is symmetric, with finite cluster  $N_c = 32$  mobility edge (defined within the finite TDOS) being wider as compared to the  $N_c = 1$  results. For the off-diagonal disorder, while the local  $N_c = 1$  captures some effects of the off-diagonal randomness with a pronounced asymmetry in the TDOS, it fails to capture vivid changes in the mobility edge boundaries.



Hence, in this section, we decide to focus on the effect of the off-diagonal disorder on the 3D Anderson model with the configuration-dependent hopping. The tool that we use to quantify the localized states is our generalized TMDCA scheme [7]. Again, detailed discussion on the TMDCA can be found at [7]. Within the typical medium analysis, the TDOS serves as an order parameter for the Anderson transition [5, 6, 7]; i.e., the TDOS is finite for the extended states, and vanishes when electrons become localized. In Fig.2, we present our results for the TDOS for the diagonal (with  $t_{AA} = t_{BB} = t_{AB} = 1$ ) and the off-diagonal disorder (with  $t_{AA} = 1.5, t_{BB} = 0.5, t_{AB} = 1$ ) at  $N_c = 1$  (left panel) and  $N_c = 32$  (right panel) for  $V_A = 1.0$  and  $c_A = 0.5$ . Our results strongly indicate that  $N_c = 1$  is insufficient for a proper description of the Anderson localized states as it neglects the non-local disorder-induced correlations.

#### 4. Conclusion

In this work, to study the off-diagonal disorder we have extended the local single-site BEB [1] to a finite DCA cluster that incorporates the missing non-local inter-site correlation effects. Applying the generalized DCA method to the Anderson model in 1D, we found that non-local disorder correlation cause the development of finite structures in the DOS and the closure of the gap (overemphasized in a single site approach) at the band center.

To consider the effect of the off-diagonal randomness on the Anderson localized states, we have also generalized our recent TMDCA [6] method to include both diagonal and off-diagonal disorder. To benchmark our TMDCA results, in [7] we compared them with other well-established methods, such as transfer matrix method and kernel polynomial method. We also find that a local  $N_c=1$  scheme by neglecting the inter-site correlations is not able to describe properly the effect of the off-diagonal disorder. It strongly underestimates the extended states regimes and also cannot capture the transformation of the mobility edge trajectories [7]. Our results show a strong evidence of the necessity to include non-local quantum coherence affects for the proper description of Anderson localization.

#### 5. Acknowledgments

The current work is funded by the NSF EPSCoR LA-SiGMA project under award #EPS-1003897. Also, this work is supported by DOE SciDac grant DE-FC02-10ER25916 and by NSF OISE-09552300 grants.

#### 6. References

- [1] J. A. Blackman, D. M. Esterling, and N. F. Berk, Phys. Rev. B 4, 2412 (1971).
- [2] P. A. Lee and T.V. Ramakrishnan, Rev. Mod. Phys. 57, 287 (1985).
- [3] P. W. Anderson, Phys. Rev. 109, 1492 (1958).
- [4] M. Jarrell and H. R. Krishnamurthy, Phys. Rev. B 63, 125102 (2001).
- [5] V. Dobrosavljevic, A. A. Pastor, and B. K. Nikolic EPL 62 (1), 76 (2003).
- [6] C. E. Ekuma, H. Terletska, K.-M. Tam, Z.-Y. Meng, J. Moreno, and M. Jarrell, Phys. Rev. B 89, 081107 (2014).
- [7] H. Terletska, C. E. Ekuma, C.Moore, K.-M. Tam, J. Moreno, and M. Jarrell, arxiv (2014).
- [8] K. Kopernik and B. Velicky, Phys. Rev. B. 58, 11 (1998).
- [9] E. Abrahams, P.W. Anderson, D. C. Liccardello and T. V. Ramakrishnan, Phys. Rev. Lett. 42, 673 (1979).

## **Attosecond Transient Absorption with Time Dependent Hartree-Fock**

Adonay Sissay and Kenneth Lopata

Department of Chemistry, Louisiana State University

**Abstract:** In order to study the transient absorption of hydrogen atom and molecule we used a real-time dependent density functional theory (TDDFT). We employed NWchem package that is capable of doing real-time TDDFT. A weak electric field in the infrared (IR) region was applied to hydrogen atom and then probed by an extreme ultra violet (XUV) pulse. These pump probe technique data that is generated is Fourier transformed to get the absorption spectra. In order to get a clear spectra of H-atom we employed a hann window function [1]. The results for hydrogen atom was generated by developing a time dependent Hartree-Fock (TDHF) code and compared to an already published paper that studies Stark shifts and Autler –Townes effect [2]. The comparison yielded similar results by doing calculations using the same specifications in the paper.

**Keywords:** transient absorption, time dependent Hartree-Fock (TDHF)

### **1. Introduction:**

Transient absorption spectra is a time dependent spectroscopy, in which a sample's absorbance is measured as a function of time. These kind of spectroscopy is used to study excitations of molecules and atoms. A pump probe technique is used to study a sample by using two different types of pulses, IR and XUV. The pump pulse is a weak IR electric field that is used to excite the electrons in the sample and see some change in the dipole moment. Then a very short time later, usually in the femtosecond range, XUV pulse with a higher energy and frequency probes the sample to measure the absorbance. This technique was used to study the absorption spectra of hydrogen atom. The time delay between the two pulses is fixed at the time when the XUV pulse is at the peak of the IR envelope.

Hydrogen atom is perfect for studying an absorption spectra using time dependent Hartree-Fock (HF) because it does not introduce a self-interaction problem which is encountered in density functional theory (DFT). In this case, DFT is better at studying systems with multiple electrons than HF because density functional computes for electron-electron interaction energy which doesn't exist in hydrogen atom with its one electron. Moreover, the results and the implemented techniques used in studying hydrogen's absorption spectra will be used for studying bigger systems. DFT is a good approach for studying bigger systems because it is computationally cheap since it deals with density of electrons to determine the total energy of the system; unlike HF which directly deals with N-body wave function.

### **2. Time Dependent Hartree-Fock (TDHF)**

In order to study large molecules with many interacting electrons, one has to circumvent the electron-electron repulsion (interaction) complexity. One approach is the Hartree-Fock approximation, which gets rid of the multiple electron repulsion and replaces it with a single electron interaction with other electrons in a sample.

In other words, it is like dealing with one electron-electron interaction at a time but one electron communicating with many other electrons. Instead of having many of electrons communicating with each other in a system, we introduce a mean field  $V_{HF}$  that computes the potential of i-th electron as it interacts with the presence of other electrons.

$$H = T + V$$

$$f(i) = -\frac{1}{2}\nabla_i^2 - \sum_{A=1}^M \frac{Z_A}{r_{iA}} + v_{HF}(i)$$

Where T is the kinetic energy operator term that corresponds to the first term in the effective Hamiltonian  $f(i)$  equation, while V is the potential operator that corresponds to the second term of the Hamiltonian.

Light molecule interaction could be modeled by utilizing TDHF. The electron dynamics of molecules once a system has been perturbed by an external field gives lots of information [3]. The Schrodinger equation could be solved numerically when computing the total energy for small molecule like hydrogen. However, for large molecules, it is virtually impossible to solve for the TDSE because of aforementioned reason relating to the electron- electron repulsion. The TDHF equations are:

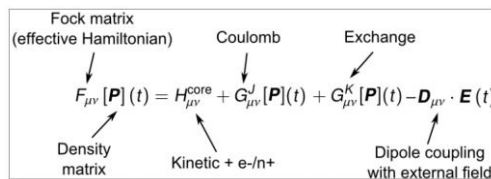
$$i\frac{\partial|\psi_i(t)\rangle}{\partial t} = F(t)|\psi_i(t)\rangle$$

Using density matrix  $\rho(t)$ , where  $P_i$  is the guess density matrix for i-th electron and  $\psi_i(t)$  is wave function for which we use Gaussian basis functions to describe it.

$$\rho(t) = \sum_i P_i |\psi_i(t)\rangle \langle \psi_i(t)|$$

To solve for the above density matrix, we employ the Von-Neumann eq. as shown below.

$$i\frac{\partial\rho(t)}{\partial t} = [F(t), \rho(t)]$$



### 3. Results:

#### Hydrogen Molecule TDHF Simulation

In order to check whether the code is working or not, we compare our result to a similar work done on hydrogen molecule [4]. The comparison looks very promising when using the same parameters as the authors used. The electric field and dipole propagation in time results were similar using the basis set aug-cc-pvtz. The electric field used to perturb the hydrogen molecule is shown below.

$$E = E_{max} \sin(\omega t)$$

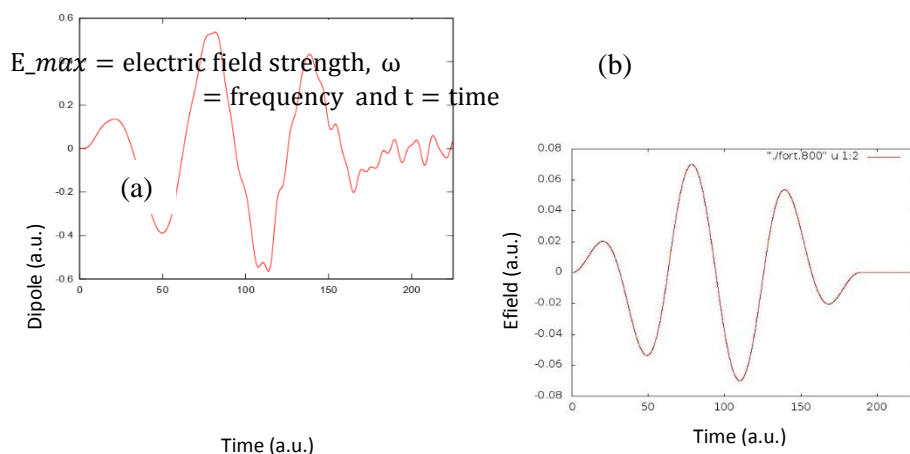


Fig 1. The charts are TDHF simulation for  $H_2$  in an oscillating electric field ( $E_{max} = 0.07$  a.u. and  $\omega = 0.10$  a.u.) using aug-cc-pvtz basis set. (a) Dipole profile and (b) electric field profile.

### Hydrogen Atom Transient Absorption Spectra

The envelope function of IR and XUV pulses are given by  $E_{IR}(t) = E_{IR-max}(t) \sin(\omega t)$  and  $E_{XUV}(t) = E_{XUV-max}(t) \sin(\omega t)$ , respectively, where  $E_{XUV-max}$  and  $E_{IR-max}$  are the field strengths of the respective pulses. The total electric field is given by  $E(t, \tau_d) = E_{IR}(t) + E_{XUV}(t - \tau_d)$ , where  $\tau_d$  is the time delay between the IR and the XUV pulses.

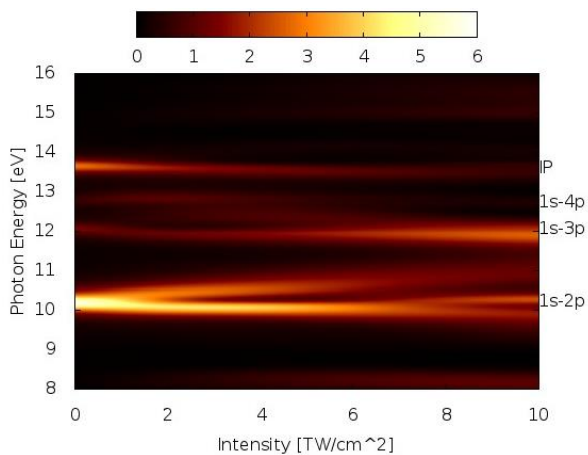


Fig. 2. The above figure shows the absorption spectra of hydrogen atom generated using TDDFT using aug-cc-pv6z basis set. As the intensity increases, a doublet splitting caused by Stark shifts are observed.

It could clearly be seen in Fig. 2 above that the absorption has Stark effect, which is splitting of the spectral lines of atoms and molecules due an external electric field. These are alternating current (ac) Stark shifts since they are time dependent. The way these splitting occur is through dressed states that describe the atom and the perturbing light (coupled case), and the uncoupled case. The difference between these two states (coupled – uncoupled) is Stark effect or Stark shift. Whenever a photon is ejected from an electron, it goes to a higher level orbital. In doing so it could do two things: it could either go to a higher level orbital, or it could just couple degenerate states. Both cases obey the selection rule. The latter case of photon movement is when the Stark shift is observed. The first case of movement is called Autler-Townes effect (AT). In a similar fashion as in Stark shift, AT effect could be studied since it is a dynamical type of ac-Stark shift. This effect is noticed when the external electric field perturbing the atom, which is the IR field, is in resonance with a photon transition frequency. In accordance with reference [2], the intensities are related to the field by  $E_{\text{IR}} = I_{\text{IR}}^{1/2}$ . As mentioned earlier, the time delay is at  $\tau_d = 0$ . Also, the wavelength for the driving IR field is at 656 nm and the function used to generate this field's envelope is a  $\sin^2$  hann function. In Fig. 2, it could also be noticed that there is a doublet with a strong splitting in the transition of a photon from 1s-2p due to AT effect. The amount of separation is about 0.5 eV at IR intensity  $I = 2 \text{ TW cm}^{-2}$  and gradually increase to  $\sim 1 \text{ eV}$  at  $10 \text{ TW cm}^{-2}$ . There are also fairly strong absorption lines at 8 and 12 eV caused by ac-Stark shift.

#### **4. Conclusion:**

The technique used to generate the absorption of H-atom using pump probe technique worked. The AT splitting and Stark effect were observed in the absorption spectra due to an increase in intensity of the IR envelope. In comparison of this work with Ref. [2] showed similar results which is promising for future work in studying bigger molecules and atoms using pump probe technique but by utilizing DFT this time. Using big basis sets in our calculation we were able to generate the absorption spectrum of  $\text{H}_2$  and H-atom, however, this was computationally expensive. There were errors in the absorption plots which were due to the size basis set used. For example, quadruple augmented cc-pv6z basis set had issues with predicting accurately the absorption of H-atom at higher excitations ( $> 12 \text{ eV}$ ).

#### **5. Acknowledgements:**

The current work is funded by the NSF EPSCoR LA-SiGMA project under award #EPS-1003897. I would like to thank my research advisor, Dr. Kenneth Lopata, Assistant Professor of Chemistry, Louisiana State University.

#### **6. References:**

- [1] M.B. Gaarde, C. Buth, J.L. Tate, and K. J. Schafer. *Phys. Review A* **83**, 013419 (2011)
- [2] M. Murakami and S. Chu. *Phys. Review A* **88**, 043428 (2013)
- [3] Kenneth Lopata, Niranjan Govind. *J. Chem. Theory Comput.* **9** (11), pp 4939–4946 (2013)
- [4] Xiaosong Li, Stanley M. Smith, Alexei N. Markevitch, Dmitri A. Romanov, Robert J. Levis and H. Bernhard Schlegel. *Phys. Chem. Chem. Phys.* **7**, 233-239 (2005)

## Coarse-grained Biomolecule-Wall Interactions for Implementation into Multi-scale MD-Continuum Simulations

K. Fattah-Hesary<sup>1,2</sup>, B. Novak<sup>1,2</sup>, D. Moldovan<sup>1,2</sup>, and D. E. Nikitopoulos<sup>1,2</sup>

<sup>1</sup>Mechanical Engineering Department, LSU

<sup>2</sup>Center for Computation and Technology, LSU

**Abstract:** The interactions of Fullerene,  $C_{60}$ , with a PMMA,  $(C_5O_2H_8)_n$ , wall within water as solvent, is investigated using advanced free energy calculations method via molecular dynamics simulation. Experimental observations show that Fullerene can be taken as a nonpolarizable entity, PMMA is pretty hydrophobic (contact angle of  $72^\circ$ ) too. Therefore, the typical tendency of Fullerene is to evade the water and sticks to the wall, however, with the aid of free energy methods the Fullerene can explore and sample the configurational space adequately. Eventually at least a 3-dimensional (eliminating the rotational preferences) free energy calculation is crucial to capture the interaction of nano-particles with rough walls, therefore, ABF is chosen since computationally is highly efficient and suitable for handling of reaction coordinates of higher than one dimension. The results show that the solvation forces caused by fluid layers formed near the wall cause an oscillatory force on the particle which is not negligible. This work is the ground work to obtain a detailed force analysis on the nanoparticle, which will subsequently be substituted by a bio-molecule, for two purposes. One is the development of hierarchical models of bio-molecule interaction with walls of various materials used in bio-analytical devices. These hierarchical models will then be introduced into continuum models of transport in such devices. The second purpose is to incorporate the methodology to the developed hybrid MD-continuum simulation framework, which simultaneously bridges molecular-level scales to continuum scales, so as to address the physically meaningful transition of the particle (bio-molecule) from the continuum domain to the atomistic near wall domain (and vice versa) as well as its interaction with the wall. This work will leverage force-field development efforts also under the LA-SiGMA grant to enable multi-scale simulations involving interactions between biomaterials for which such force-fields are unknown.

**Keywords:** Molecular dynamics, Free energy calculation, ABF, PMF, Hybrid.

### 1. Introduction

Transport of particles in liquids involves fundamental phenomena which have led to renewed interest in molecular hydrodynamics, with many applications in engineering and biology. Bio-molecules, such as mononucleotides or DNA fragments, interacting with natural, or functionalized/chemically modified wall surfaces in bio-analytical mixed-scale (micro/nano) fluidic instruments is a relevant example involving both bio and non-

bio materials. To design such systems one must understand and resolve molecular interaction processes while developing hybrid multiscale modeling which bridges molecular-level scales to continuum scales. The hybrid continuum and molecular dynamics (MD) approach is a simulation method which adopts the continuum hypothesis in capturing macroscopic features of transport and details atomistic inter-molecular interactions on interfaces of different materials by using the MD approach [1]. This type of multiscale methods should have both the efficiency of the continuum model and the accuracy of the molecular model when necessary. For understanding the interaction of nanoparticles on molecular level, calculation of free energy is of great importance. However, different states of the system are separated by high barriers which impede the exploration of phase space to obtain a valid average force on the particles. There exist various methods which have been proposed for efficient calculations of free energy by applying different strategy trying to better sample the phase space. In this paper, the interactions of Fullerene,  $C_{60}$ , with a PMMA,  $(C_5O_2H_8)_n$ , wall within water as solvent, is investigated. Experimental observations show that Fullerene can be taken as a nonpolarizable entity, PMMA is pretty hydrophobic (contact angle of  $72^\circ$ ) too. Therefore, the typical tendency of Fullerene is to evade the water and sticks to the wall. However, we can subjugate this impeding force by using adaptive biasing force (ABF) method which negates the impeding forces on Fullerene and let it explore and sample the configurational space adequately to obtain potential of mean force (PMF).

## 2. Simulation Method

The Fullerene ( $C_{60}$ ) interaction with surrounding is studied in our simulations. Simulation box consist of 8 PMMA polymer chains as wall and 6384 water molecules. The simulation details are shown in Table 1. We use CHARMM force field parameters for PMMA and the potential parameter for water is taken from TIP3P model [2]. The interaction parameters between water molecules and rigid fullerene are taken from [3]. We use geometric mean for  $\epsilon$  and arithmetic mean for  $\sigma$  in Lennard-Jones interactions of unlike atoms. SHAKE algorithm is used to constraint stiff degrees of freedom in water to facilitate larger time steps to be taken. The Verlet scheme with a time step of  $\Delta t = 2$  fs is used for time integration of the interacting particles equation of motion to find the particles trajectories. Following equilibration of the solutions at atmospheric pressure using  $NPT$  ensemble, sampling is carried out with an  $NVT$  ensemble. Adaptive biasing force (ABF) is used for free energy calculations where the mean force on the desired reaction coordinate is calculated and then it's removed to enhance the sampling in regions that are rarely sampled otherwise. It doesn't require running a constrained simulation and can be performed entirely with a single molecular dynamics run [4].

Table 1: Simulation details,  $N_{water}$ ,  $N_{PMMA}$  and  $N_{Fullerene}$  are number of particles in water, PMMA wall and Fullerene nanoparticle, respectively.  $T$  is the temperature and  $P$  is the system average pressure.

Simulation Box ( $\text{\AA}^3$ )	$N_{water}$	$N_{PMMA}$	$N_{Fullerene}$	$T(K)$	$P(\text{bar})$
$50 \times 50 \times 97$	19152	5285	60	298	1.0

## 3. Results and Discussion

We apply ABF method for the calculation of PMF in Fullerene interaction with the PMMA wall and water along a reaction coordinate that is defined as: the distance separating the center of mass the nanoparticle from the center of mass of the wall. Figs. 1(a), through (d) show the simulation box with  $\xi$  symbolizing the reaction coordinate.

Figs. 1(a) and (b) show a side view of the box while Fig. 1(c) depicts a top view of the PMMA wall with periodic images shown in Fig. 1(d).

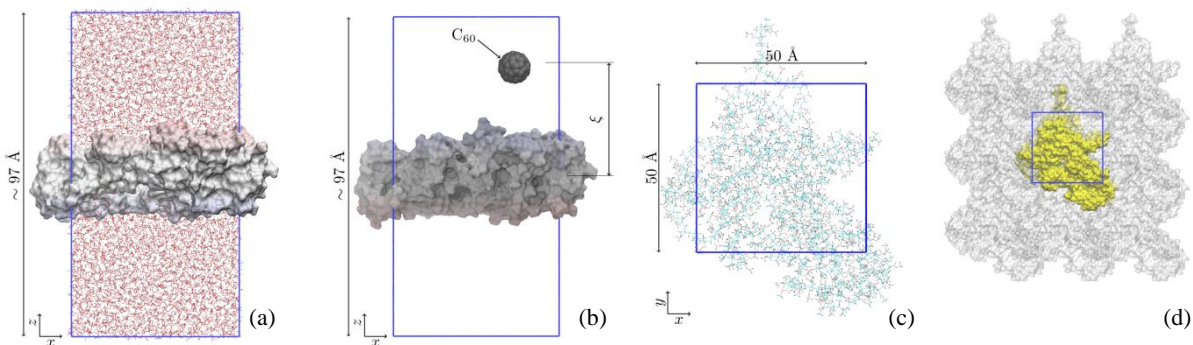


Fig 1: Snapshots from MD simulation for interaction of Fullerene ( $C_{60}$ ), PMMA and water. (a) and (b) show side view of the simulation box while (c) and (d) depict a top view. The periodic images of the PMMA wall are shown in gray with the original piece in yellow.

The highly hydrophobic nature of Fullerene makes it to avoid water and goes towards the hydrophobic PMMA wall. Thus, an adequate sampling of configurational space by Fullerene is not achieved as it's shown in 5 ns  $z$ -direction trajectory of Fullerene shown in Fig 2(b) while a snapshot of the stuck Fullerene on the wall is depicted in Fig. 2(a). An improved sampling was attained by exploiting the ABF method. Fig. 2(c), shows the Fullerene trajectory after using ABF. The sampling of configurational space is ameliorated due to negation of the forces that

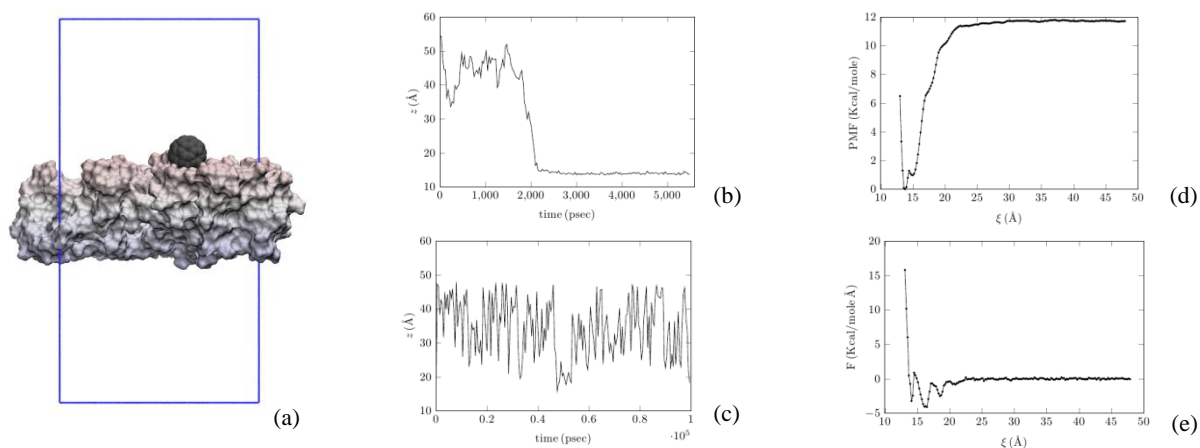


Fig 2: (a) Snapshot from the unbiased MD simulation showing adsorption of Fullerene ( $C_{60}$ ), to PMMA wall (b) Shows trajectory of Fullerene along the  $z$ -axis in unbiased simulation while in (c) trajectory is shown in biased simulation using ABF. (d) and (e) are showing PMF and averaged force on Fullerene along the reaction coordinate.

were stopping Fullerene to adequately sample along the reaction coordinate. Figs. 2(d) and (e) are showing potential of mean force and the mean force itself, respectively. The energy well near the wall surface ( $z \sim 13 \text{ \AA}$ ) is almost 25 times of  $k_B T \approx 0.6 \text{ Kcal/mole}$ , which is a very deep well and explains the sticking of Fullerene to the wall.

#### **4. Conclusion and Future Work**

We presented a molecular dynamics investigation of the interactions of a Fullerene ( $C_{60}$ ) nanoparticle in water as solvent and a PMMA wall. Adaptive biasing force (ABF) was exploited for investigation of the force applied on the nanoparticle along the reaction coordinate. Because of the hydrophobic nature of Fullerene it prefers to evade water and be situated on the PMMA wall. In addition, to sample the effect of the wall, we need at least 3-dimensional reaction coordinates, and ABF method is the prominent option in dimension greater than one. This work is the ground work to obtain a detailed force analysis on a nanoparticle, which will subsequently be substituted by a bio-molecule, for two purposes: One is the development of hierarchical models of bio-molecule interaction with walls of various materials used in bio-analytical devices. These hierarchical models will then be introduced into continuum models of transport in such devices. The second purpose is to incorporate the methodology to the developed hybrid MD-continuum simulation framework, which simultaneously bridges molecular-level scales to continuum scales, so as to address the physically meaningful transition of the particle (bio-molecule) from the continuum domain to the atomistic near wall domain (and vice versa) as well as its interaction with the wall. Next we will implement this in a continuum wall-bounded transport simulations of such bio-molecules and comparisons will be made with full atomistic results for validation. In tandem the work will be extended to address the particle entry/exit problem in-to/out-of a fully atomistic wall layer in our hybrid multi-scale (MD/Continuum) simulation framework.

#### **5. Acknowledgments**

This work is supported in part by LA-SIGMA, National Science Foundation (NSF) Award Number #EPS-1003897.

#### **6. References**

- [1] X. Nie, S. Chen, W. E and M. O. Robbins, A Continuum and Molecular Dynamics Hybrid Method for Micro- and Nano-Fluid Flow, *J. Fluid Mech.* 500, 55 (2004)
- [2] W. L. Jorgensen, J. Chandrasekhar, J. D. Madura, R. W. Impey, M. L. Klein, Comparison of simple potential fluctuations for simulating liquid water, *J. Chem. Phys.* 79, 926 (1983)
- [3] D. Bedrov, G. D. Smith, H. Davande, L. Li, Passive transport of  $C_{60}$  fullerenes through a lipid membrane: a molecular dynamics simulation study, *J. Phys. Chem.* 112, 7 (2008).
- [4] C. Chipot and A. Pohorille. *Free Energy Calculations: Theory and Applications in Chemistry and Biology.* Springer Berlin Heidelberg, 2007.

## Computational studies of oxido-reductases for improved biofuel cell design

<sup>1</sup>Edwin F. Gomez, <sup>1</sup>Trang T. Tran, <sup>1,2</sup>Nguyen Q. Tran and <sup>1</sup>Dhruva K. Chakravorty

<sup>1</sup>Department of Chemistry, <sup>2</sup>Department of Computer Science, University of New Orleans

**Abstract:** Glucose Oxidase (GOx) is a redox enzyme that uses flavin adenine dinucleotide (FAD) as a cofactor to reduce  $\beta$ -D-glucose into  $\delta$ -gluconolactone via a ping-pong steady-state kinetic mechanism. While GOx remains a primer candidate for developing enzymatic biofuel cells and sensor based devices much remains unknown about the conformational ensembles sampled by GOx and the interactions between the enzyme with its cofactor, sugar molecules and the electrode surface. In this study, we find significant differences between conformations sampled by the monomer and the dimer assemblies of GOx. Our molecular dynamics (MD) simulations of the dimer assembly of GOx determine a previously uncharacterized conformational state that provides sugar molecules from solution access to the active site. Such a conformational change have been previously hypothesized are in agreement with experiments. We further find that these structural changes are conserved over both *Aspergillus niger* and *Penicillium amagaskiense* species of GOx that are commonly used in commercial applications.

**Keywords:** biofuel cell, graphene, molecular dynamics, redox chemistry, glucose oxidase, bio-materials, sugars, glycosylation, glycoprotein, sugar-graphene interactions, oxido-reductases

### 1. Introduction

Glucose oxidase (GOx) is an oxido-reductase that catalyzes the oxidation of  $\beta$ -D-glucose in order to produce  $\delta$ -gluconolactone and hydrogen peroxide (Figure 1).<sup>1-4</sup> It is widely used in commercially produced biosensors that measure the amount of blood in glucose. While it is challenging for sensors to directly detect glucose in the blood, but it is easy to detect the byproduct of GOx, which is hydrogen peroxide. In addition to being used in biosensors GOx has found numerous applications in applications such as biofuel cells, tandem catalysis and molecular motors.<sup>3</sup> Most of these applications use GOx extracted from *Aspergillus niger* and *Penicillium amagaskiense*.<sup>3</sup> Both species of GOx share a similar fold and are known to catalyze the reaction in their dimer assembly with one flavin adenine dinucleotide (FAD) cofactor per monomer. *P. amagaskiense* GOx (PGOx) contains 587 amino acids per monomer while *A. niger* GOx (AGOx) contains 581 amino acids per monomer. Furthermore, both proteins have multiple glycosylation sites and may be glycosylated by up to 15% of their weight. Owing to their large sizes, relatively little is known about the conformational dynamics of these proteins and previously theoretical studies have solely focused on the monomer.<sup>4</sup> In this study, we present the results from our study of the conformational dynamics of PGOx and AGOx in their monomer and dimer assemblies both in the

presence and absence of the cofactor. Understanding the nature of conformational sampling in GOx will help us identify mutations that will help improve the stability and catalytic efficiency of the enzyme.

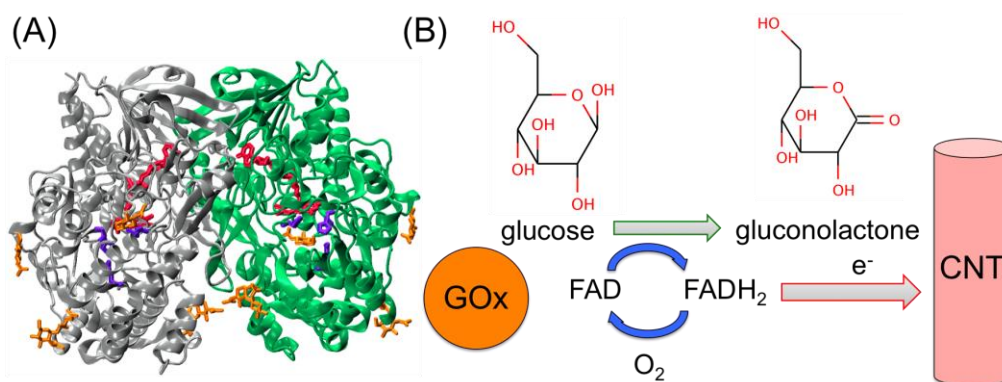


**Figure 1.** (A) Cartoon representation of GOx (PDB code: 1GPE) from *Penicillium amagaskiense*. FADH (red), active site residues (purple) and sugar molecules (yellow) are depicted in stick notation. (B) Schematic of a glucose oxidase based biofuel cell involving a carbon nano tube (CNT) electrode.

## 2. Methods

All MD simulations were performed using the assisted model building with energy refinement (AMBER) 12 suite of programs in this study.<sup>5</sup> MD simulations of PGOx and AGOx proteins were started from their high-resolution crystal structure conformations obtained from the protein data bank (PDB). While the crystal structure of PGOx (PDB code: 1GPE) found the protein in the dimer assembly, the crystal structure of AGOx (PDB code: 3QVR) was available for the monomer state of the protein. Starting from these crystal structures, the monomer, dimer, and FADH-bound monomer and dimer assemblies were generated. Charged amino acids were modeled in protonation determined using the H++ protonation state server. Each protein structure was immersed in a box of explicit SPC/E water molecules and ions. The solvated protein was then prepared for production MD using a well-established procedure.<sup>6</sup> In this process, the solvated system was first energy-minimized over five steps in which parts of the system were sequentially released from positional restraints. Following this, the energy-minimized system was gradually heated to 300K over 200 ps of MD for a canonical ensemble (NVT) followed by 1 ns of MD performed for an isobaric and isothermal ensemble (NPT).<sup>7</sup> Following the equilibration phase, each system was propagated for hundreds of nano seconds of MD simulation at 300K for an isobaric and isothermal ensemble using standard MD protocols.<sup>6</sup> In addition to the simulation presented in this study, we have also simulated these proteins in sugar solutions with varying degrees of glycosylation both in the presence and absence of mono-layer graphene. The AMBERTools suite of programs was utilized to analyze the results from these simulations.<sup>5</sup>

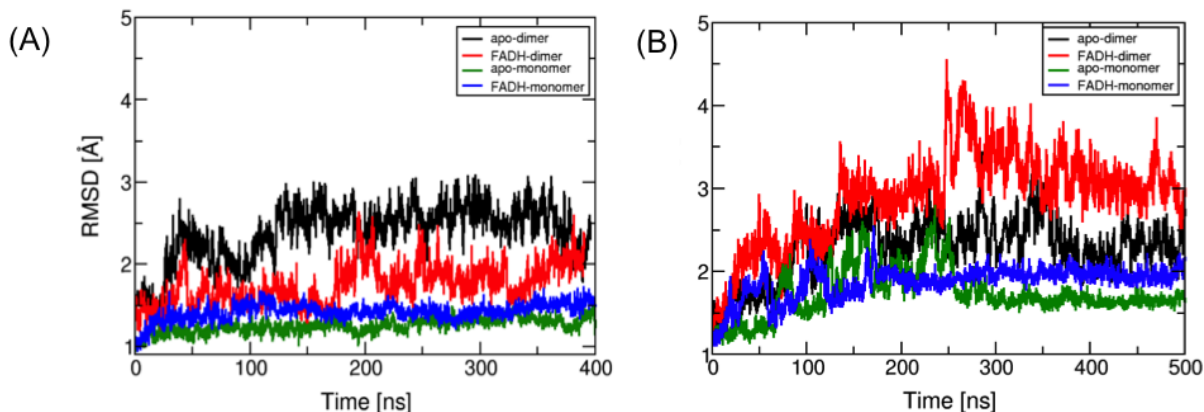


**Figure 2.** Structural changes observed in apo and FADH-bound monomer and dimer assemblies of (A) AGOx and (B) PGOx over the course of MD simulations.

### 3. Results and Discussion

We have collected over 10  $\mu$ s of MD production data from our simulations of various forms of PGOx and AGOx. As mentioned above, we only present the results obtained from from 3.6  $\mu$ s of MD data collected for the apo and FADH-bound monomer and dimer assemblies of PGOx and AGOx. All protein structures were found to maintain their fold over the course of these simulations. Crystal structures along with kinetics and mutagenesis experiments find the active site of glucose oxidase to contain an FADH molecule and two positively charged histidine amino acids that are involved in the reaction with  $\beta$ -D-glucose.<sup>1-3</sup> These structures are, however, unable to provide a pathway for sugar molecules to enter the active site of the protein. An analysis of the root mean square deviation (RMSD) of protein backbone atoms over the course of these trajectories surprising revealed that the dimer assemblies of both proteins were more likely to undergo conformational changes as compared to the monomer assemblies (Figure 2). Furthermore, an analysis of the root mean square fluctuations (RMSF) calculated for backbone C $\alpha$  atoms once again found the dimer assemblies of both proteins to be more mobile in comparison to the monomer assembly (Figure 3). These calculations further reveal that a large number of residues near the active site of the protein are flexible in the dimer assembly. While these data initially suggested that the dimer assemblies was less stable than the monomer assemblies, a closer analysis of our simulations revealed that the dimer assemblies of both AGOx and PGOx undergo a significant secondary structural change similar to a breathing motion that drives the protein from the crystallographically observed “closed” conformation and a previously uncharacterized transient “open” conformation that provides access to the active site. Furthermore, our simulations of the monomer assembly of AGOx find the protein sample an open conformation in which an  $\alpha$ -helix region of 22 amino acids swings aside to provide direct access to the active site of the protein.

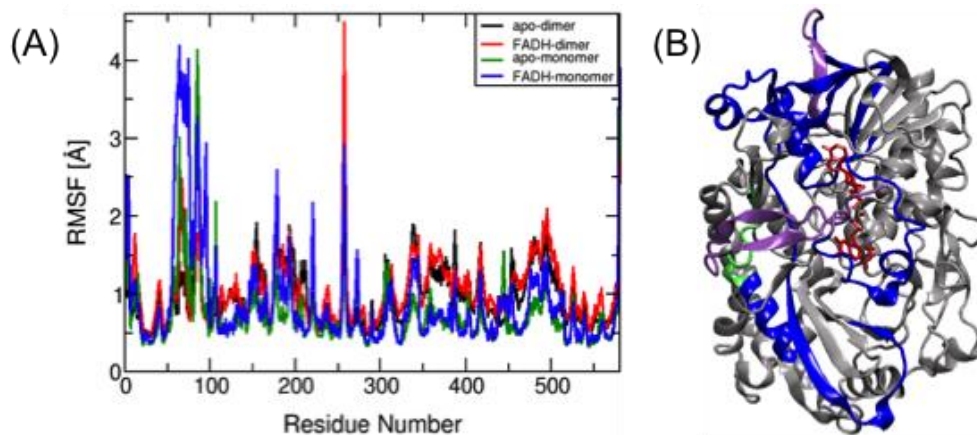


**Figure 3.** (A) Plot of backbone Ca atoms' RMSF values from simulations of apo and FADH-bound monomer and dimer assemblies of PGOx. A similar residue mobility profile was obtained from our simulation of AGOx. (B) Color coded depiction of protein mobility of FADH-monomer PGOx on a cartoon image of FADH-bound monomer assembly of PGOx. The FADH molecule is shown in stick notation (red). Residues are color-coded based on their RMSF values - 0 Å to 1.5 Å (silver), 1.6 Å to 2.5 Å (blue), 2.6 Å to 3.5 Å (purple) and 3.6 Å to 4.0 Å (green).

#### 4. Conclusions

We find that the dimer dimer assembly of GOx accesses a previously unobserved open conformation that will help in the design of more active and stable GOx species for commercial applications.

#### 5. Acknowledgments

The current work is funded by the NSF EPSCoR LA-SiGMA project under award #EPS-1003897, NSF research experiences for undergraduate program (DMR-1262904), the UNO SCoRE award and the CoSURP program at UNO. The authors gratefully acknowledge LONI and LSU-HPC for providing computational support.

#### 6. References

- [1] Holland, J.T.; Harper, J.C.; Dolan, P.L.; Manginell, M.M.; Arango, D.C.; Rawlings, J.A.; Apblett, C.A.; Brozik, S.M. *PLoS ONE* **2012**, *7*, 37924.
- [2] Kohen, A.; Jonsson, T.; Klinman, J.P. *Biochemistry* **1997**, *36*, 2603.
- [3] Bankar, S.P.; Bule, M.V.; Singhal, R.S.; Ananthanaryan, L. *Biotech. Adv.* **2009**, *27*, 489.
- [4] Prabhakar, R.; Siegbahn, P.E.M.; Minaev, B.F.; *Biochim. Biophys. Acta.* **2003** *1647*, 173.
- [5] Case, D.A.; Chetham, T.E.; Darden, T.; Gohlke, H.; Luo, R.; Merz, K.M. Jr.; Onufriev, A.; Simmerling, C.; Wang, B.; Woods, R.J. *J. Comput. Chem.* **2005**, *26*, 1668.
- [6] Chakravorty, D.K.; Wang, B.; Ucisik, M.N.; Merz, K.M. Jr. *J. Amer. Chem. Soc.* **2011** *133*, 19330.
- [7] Allen, M.P.; Tildesley, D.J. *Computer Simulations of Liquids*; Clarendon Press: Oxford, 1987.

## Computational study of the self-assembly of surfactant molecules

Camera Whicker<sup>1</sup>, Seneca M. Joseph<sup>2</sup>, Edwin F. Gomez<sup>3</sup>, Sylvester Tumulime<sup>3</sup> and Dhruva K. Chakravorty<sup>3</sup>

<sup>1</sup>Department of Mathematics, <sup>3</sup>Department of Chemistry, University of New Orleans, New Orleans, LA  
<sup>2</sup>Westgate High School, New Iberia, LA

**Abstract:** Understanding the nature of interactions between surfactant molecules will provide molecular insight into the structure-property relationships that are responsible for surfactant action. In this study, we present an analysis of the conformational dynamics study of surfactant molecules in different solvent models and salinity conditions using molecular dynamics (MD) simulations. Towards this, we performed MD simulations on the well-characterized dodecyldiphosphocholine (DPC) surfactant. Our simulations provide atomistic insights into the conformational ensembles sampled by the surfactant molecules in the commonly used SPC/E, TIP3P, TIP4P-Ew and TIP5P water models. We further study the influence of Na<sup>+</sup>Cl<sup>-</sup> and K<sup>+</sup>Cl<sup>-</sup> ions on the conformational dynamics of surfactants molecules. We are currently expanding our studies to investigate the self-assembly of 54 randomly dispersed monomers in similar conditions. Determining the self-assembly pathways will help us understand inter-monomer interactions and provide a means to develop a theoretical surfactant model for prediction of solubility of large molecules.

**Keywords:** self-assembly, dodecyldiphosphocholine, molecular dynamics, surfactant action, conformational dynamics, metal ions.

### 1. Introduction

DPC is a polar surfactant that is extensively used for membrane solubilization and purification (Figure 1). It is a structural analog of lauroyl lysophosphatidylcholine that is more stable to hydrolytic cleavage. A vast amount of available kinetic and spectroscopic data make it an ideal system to validate various MD water models and understand the influence of metal ions on the self-assembly of surfactants.<sup>1-3</sup> Prior MD studies have studied similar properties with a few water models and force fields.<sup>2,3</sup> In this study, we investigate the influence of the commonly used TIP3P, SPC/E, TIP4PEw and TIP5P water models on the conformational dynamics of a single surfactant molecule before leading to studies of the self-assembly of the surfactant molecules in solution.<sup>5</sup> We further investigate the influence of monovalent metal ion salts (Na<sup>+</sup>/Cl<sup>-</sup> and K<sup>+</sup>/Cl<sup>-</sup>) on these properties.

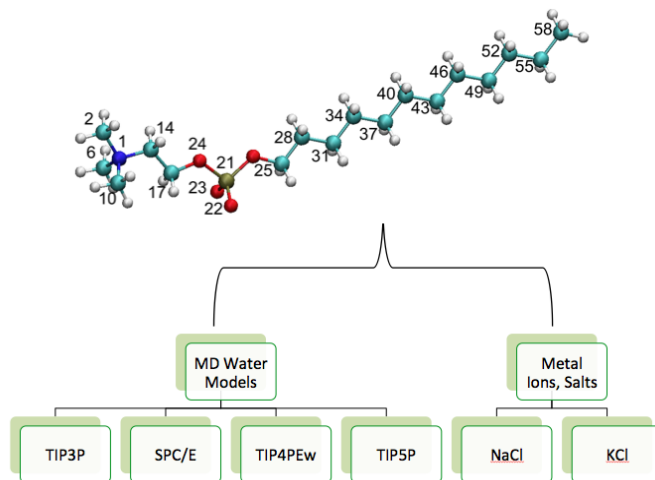


**Figure 1.** Scheme used in this study to investigate the influence of water models and metal ions on surfactant conformational dynamics.

## 2. Methods

All MD simulations were performed using the assisted model building with energy refinement (AMBER) 12 suite of programs in this study. AMBER parameters for the ff99SB and GAFF along with the structural input coordinates for a DPC molecule were adopted from the repository from the study of the conformational dynamics of DPC in TIP3P water model by Abel *et al.* A surfactant molecule was immersed in a box of explicit water molecules for each of the SPC/E, TIP3P, TIP4P-Ew and TIP5P water models. In addition to simulations performed in pure water, the monomer was solvated in 0.4 M solutions of NaCl and KCl for each water model as well. The solvated DPC molecule was then prepared for production MD using a well-established procedure.<sup>4</sup> In this process, the solvated monomer was first energy-minimized over three steps in which parts of the system were sequentially released from positional restraints. Following this, the energy-minimized system was gradually heated to 300K over 200 ps of MD for a canonical ensemble (NVT) followed by 1 ns of MD performed for an isobaric and isothermal ensemble (NPT).<sup>7</sup> Following the equilibration phase, each system was propagated for multiple nano seconds of MD simulation at 300K for an isobaric and isothermal ensemble using standard MD protocols.<sup>5</sup> The AMBERTools suite of programs was utilized to analyze the results from these simulations.<sup>4</sup>

## 3. Results and Discussion

We have collected over 100 ns of MD production data for each simulated system. We measured the structural change in each surfactant molecule by calculating the root mean square deviation (RSMD) of DPC main chain heavy atoms over the course of these trajectories for all water models. Our analysis revealed that the surfactant

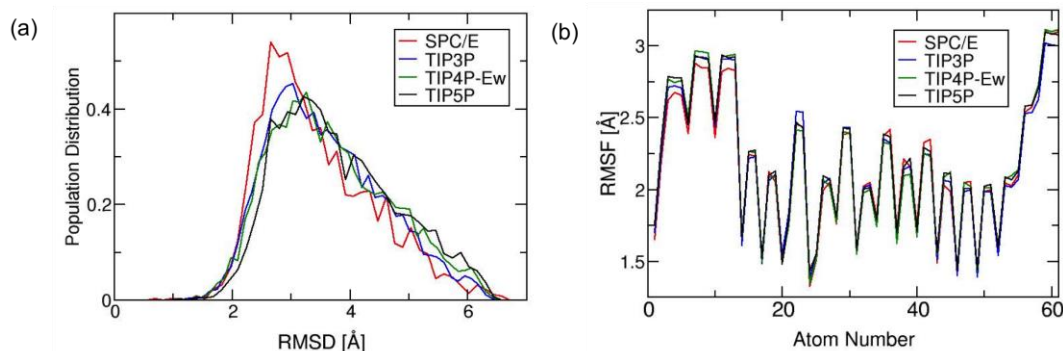


**Figure 2.** (A) Normalized population distribution of RMSD values and (B) RMSF values for atoms in DPC molecules calculated for every water model for DPC MD simulations performed in pure water.

molecule sampled similar conformational ensembles in the various environments. We further calculated the root mean square fluctuations (RMSF) values for each DPC atom from these simulations in order to understand the influence of metal ions and water models on the flexibility of specific residues. Our analyses found the head and tail regions of the surfactant to be more mobile, while the charged regions remained relatively rigid by comparison in all simulated systems. Finally, in an effort to distinguish the influence of water models, we performed a water shell analysis that calculated the number of water molecules in the first and second hydration

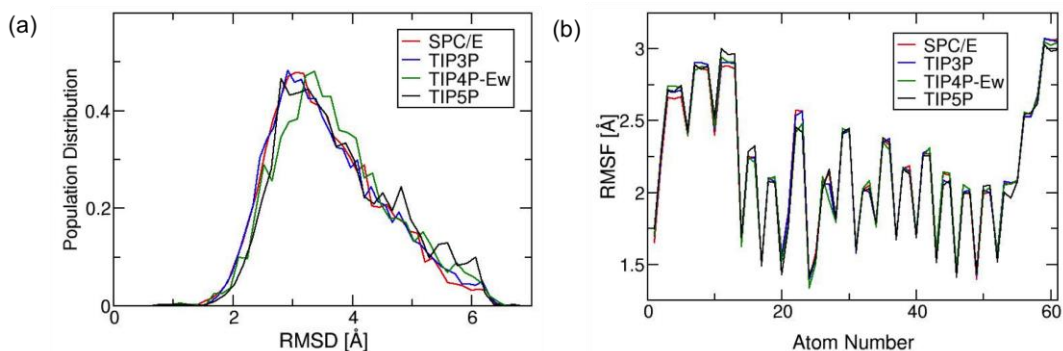


**Figure 3.** (A) Normalized population distribution of RMSD values and (B) RMSF values for atoms in DPC molecules calculated for every water model for DPC MD simulations performed in 0.4 M NaCl.

shells of DPC. In contrast to our previous results, we found sharp distributions for the number of water molecules surrounding DPC in 0.4 M KCl-SPC/E. This effect was not observed in our simulations of DPC in 0.4 M KCl-TIP3P and 0.4M-TIP4P-Ew water models. While the  $K^+$  ion may have influence the water shell around the DPC

molecule while using the SPC/E water model, these simulations need to be extended to the microsecond time scale to in order to rule out errors brought about by insufficient sampling.

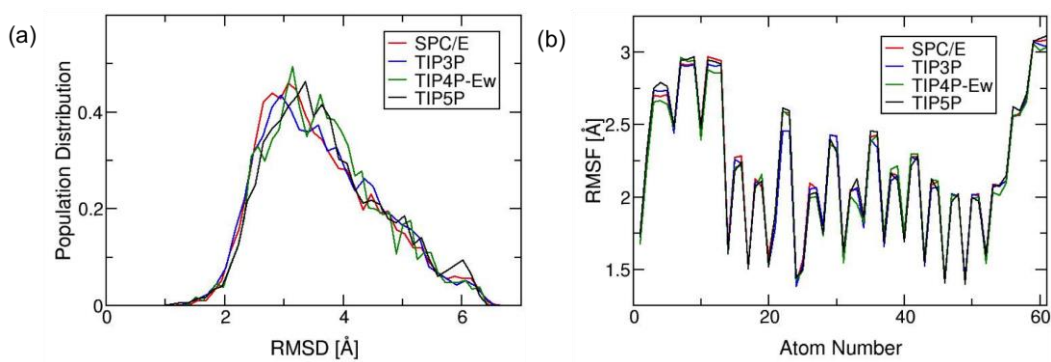


**Figure 4.** (A) Normalized population distribution of RMSD values and (B) RMSF values for atoms in DPC molecules calculated for every water model for DPC MD simulations performed in 0.4 M KCl.

#### 4. Conclusions

We find that the choice of water models and presence of monovalent metal ions has a minimal impact on the conformational sampling of the DPC surfactant. It is quite likely that the effect of these water models will become obvious in simulations involving multiple monomers in solution.

#### 5. Acknowledgments

The current work is funded by the NSF EPSCoR LA-SiGMA project under award #EPS-1003897. The authors gratefully acknowledge LONI and LSU-HPC for providing computational support.

#### 6. References

- [1] Nagarajan, R.; *Surfactant Science and Technology: Retrospects and Prospects*; Romsted, L.; Taylor and Francis: New York, 2013, 1-57.
- [2] Tieleman, D. P.; van der Spoel, D.; Berendsen, H. J. C. *J. Phys. Chem.* **2000**, *104*, 6380.
- [3] Abel, S.; Dupradeau, F.; Marchi, M. Molecular Dynamics Simulations of a Characteristic DPC Micelle in Water. *Journal of Chemical Theory and Composition*, **2012**, *8*, 4610.
- [4] Case, D.A.; Chetham, T.E.; Darden, T.; Gohlke, H.; Luo, R.; Merz, K.M. Jr.; Onufriev, A.; Simmerling, C.; Wang, B.; Woods, R.J. *J. Comput. Chem.* **2005**, *26*, 1668.
- [5] Allen, M.P.; Tildesley, D.J. *Computer Simulations of Liquids*; Clarendon Press: Oxford, 1987.

## **Crystallization and the Dimensionality Effect**

**Troy D. Loeffler, Andrew Galatas, Bin Chen**

Louisiana State University

**Abstract:** We present the results of the aggregation-volume-bias Monte Carlo simulation of a two dimensional and three dimensional Lennard-Jonesium well below the freezing point. We show that the presence of non-crystalline structures at small sizes can directly hinder the formation of an ideal FCC lattice in a three dimensional system. Conversely in the two dimensional system shows a direct crystalline transition due to the absence of these energy traps.

**Keywords:** Nucleation, Crystallization

### **1. Introduction**

The formation of a single crystal has been important for a host of applications such protein sequencing, material science, atmospheric nucleation, etc.<sup>1-5</sup> For simple materials it is often easy to obtain single crystals by growing the materials slowly under controlled conditions. However, for larger and more chemically complicated materials this can be one of the most challenging tasks a researcher can perform. The underlying cause of this difficulty can be linked to a variety of situations that may arise during the nucleation process. For instance, under homogenous nucleation it is not uncommon to see ordered structures form that is not the most thermodynamically stable in the bulk. For instance with water, it has been observed that when nucleating ice in the upper atmosphere that the structure that forms is not the hexagonal ice configuration which is the most stable, but rather cubic ice.<sup>6</sup> In the case of water the cubic ice configuration is the kinetically favorable product because of the surface effects. Often these systems will initially nucleate via the kinetically favorable structure until the cluster reaches sufficient size upon which the cluster will attempt to transition to the more thermodynamically stable structure. However, at lower temperatures this transition can have a large free energy barrier which can prohibit this from happening. As a consequence the system can form all manners of globally disordered solids. This of course can be

detrimental to a researcher's desired application. Thus it is important to understand the underlying mechanics to improve crystallization techniques.

## **2. Simulation Details**

These simulations were performed using the aggregation-volume-bias Monte Carlo method coupled with umbrella sampling.<sup>2,7,8</sup> The simulation was performed for clusters containing up to 300 LJ particles at a reduced temperature of 0.30. In one system the particles were simulated in a normal three dimensional framework while in the other system the particles were confined onto a two dimensional plane.

## **3. 2D vs 3D Lennard-Jones Crystallization**

Shown in Fig. 1 are the calculated free energy obtained for the 2D and 3D Lennard-Jonesium in addition to several snapshots taken from the simulation. The 3D Lennard-Jonesium displays small "dips" at cluster sizes of 13, 55, and 140. The sudden change in slope is indicative of the formation of icosahedral geometries (as shown along with the figure.) These clusters have been shown previously to have unusually high stability at these "magic" cluster sizes.<sup>9</sup> These non-crystalline geometries are highly stable at low cluster sizes, but they are not as stable in the bulk. In order for the system to form the ideal FCC lattice that is stable for the Lennard-Jones, the system will have to reorder from the icosahedral structure into the FCC lattice. However, this is not observed in this simulation due to the low temperatures involved. In direct contrast the 2D system shows no such dips. Instead there is a smooth curve and upon visualization of the clusters it is clear that the clusters even at small sizes can immediately begin forming bulk like structures. As a result there is a direct phase transition in the 2D system that is not present in the 3D system. This result demonstrates that the formation of these non-crystalline clusters serve to trap the system in non-ideal configurations.

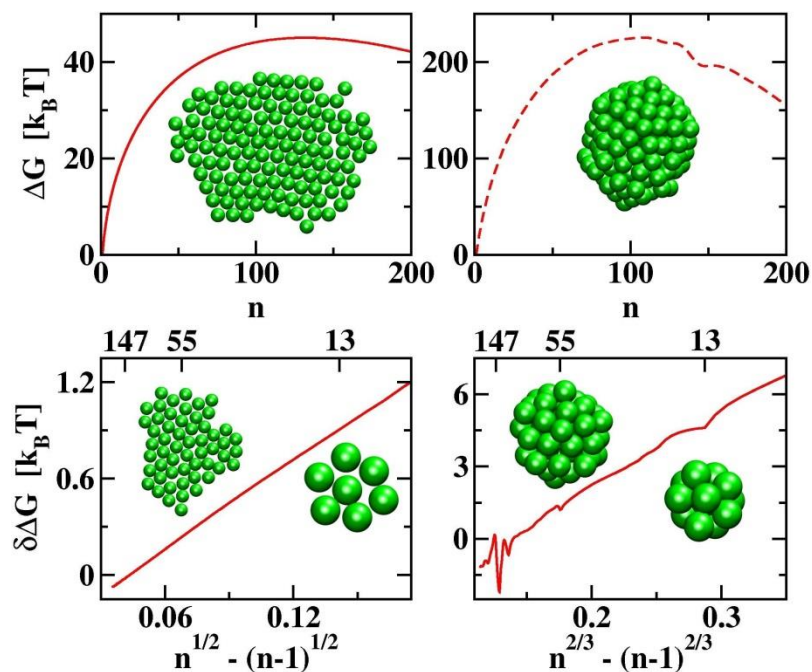


**Fig 1: Free Energy plotted as a function of the number of particles in a cluster. Shown here are the results for the 2D (top-left panels) and 3D (top-right panels) LJ systems. Also shown are the differential plots for the free energy of the respective systems.**

#### 4. Conclusion

By reducing the degrees of freedom in a Lennard-Jonesium, we have shown that the crystalline phase transition and proceed directly from the gas phase in the 2D while in the 3D the formation of icosahedral geometries will greatly hinder the formation of ideal FCC lattices.

#### 5. Acknowledgments

Financial support from the National Science Foundation (CHE-1052015 and EPS-1003897) is gratefully acknowledged. The calculations were carried out using the resources from the Louisiana Optical Network Initiative (LONI), the Center for Computation and Technology, and the Office of Computing Services at LSU.

**6. References**

- [1] D.W. Oxtoby, *Nature* **406**, 464 (2000).
- [2] G.M. Torrie and J.P. Valleau, *Journal of Computational Physics* **23**, 187 (1977).
- [3] H. Wei, et al, *Nat Nano* **6**, 93 (2011).
- [4] P.R.t. Wolde and D. Frenkel, *Science* **277**, 1975 (1997).
- [5] S.T. Yau and P.G. Vekilov, *Nature* **406**, 494 (2000).
- [6] B.J. Murray, D.A. Knopf, and A.K. Bertram, *Nature* **434**, 202 (2005).
- [7] B. Chen and J.I. Siepmann, *The Journal of Physical Chemistry B* **104**, 8725 (2000).
- [8] B. Chen and J.I. Siepmann, *The Journal of Physical Chemistry B* **105**, 11275 (2001).
- [9] X.G. Gong and V. Kumar, *Physical Review Letters* **70**, 2078 (1993).

## Design of Tailored Polymer via Molecular Dynamics Simulations

Lixin Liu<sup>†</sup>, Sreeja Parameswaren<sup>‡</sup>, Arjun Sharma<sup>‡</sup>, Henry S. Ashbaugh<sup>†</sup>, Steve W. Rick<sup>‡</sup>, Scott Grayson<sup>†</sup>

<sup>†</sup>Department of Chemical and Biomolecular Engineering, Tulane University, New Orleans, LA

<sup>‡</sup>Department of Chemistry, University of New Orleans, New Orleans, LA

**Abstract:** Based on previous work investigating to novel amphiphilic cyclic and linear polymers' structural changes upon transferring them between the varying polarity environments, we use Molecular Dynamics (MD) simulation studies to design the cyclic polymers in strengthening their amphiphilic arms' segregations. Among several proposed schemes, one that terminated hydrophilic arms with a charged amine group ( $\text{NH}_3^+$ ) was chosen. This addition increased the polymer's size in both water and toluene, subsequently resulting in deeper and higher amount penetration both of the polar and non-polar solvents. Instantaneous liquid surface analysis revealed stronger segregation of amphiphilic arms comparing with the original polymers. Even though the polymer did not exhibit complete inversion, the charged groups indeed enhanced the incompatibility of amphiphilic blocks which basically achieved our proposed design. Through combining with other polymer designs, we would deliver a complete plan of next-stage improvements of interested polymeric materials.

### Keywords:

#### 1. Introduction

Within previous work reported by Liu et.al<sup>1</sup>, we already mapped out an effective strategy that using the REDS2 technique to exploit a polymer's ability of carrying moieties, rational design of polymer can be employed by alternating existing molecules' functional groups accordingly. One of the main issues about the PHS-yns macrocyclic polymer was the amphiphilic arms did not undergo complete inversion. Shown in Figure 1, the amphiphilic arms tended to tangle with each other due to the natural affinity of non-polar parts existing in both hydrophilic and hydrophobic arms. The causes of such structures can be explained according to the unified weak or strong segregation block co-polymer theories developed by Matsen and Bates<sup>2</sup>. Potentially immiscible Diblock copolymer would like to undergo phase transition and induced self-assembly of polymeric solvents to form various ordered morphologies. Diblock co-oligomer of PEO and dodecane may co-exist at disordered phase or approached to the separation boundary since the oligomer length is quite short (6 units).

First, according to the polarity being capable to tune the Flory-Huggins interacting parameter, we plan to introduce a bio-compatible charged amine group to terminate the hydrophilic arms (Figure1). For the current phase, the effect of alternating terminating group from methyl group to  $\text{NH}_3^+$  group are being studied.

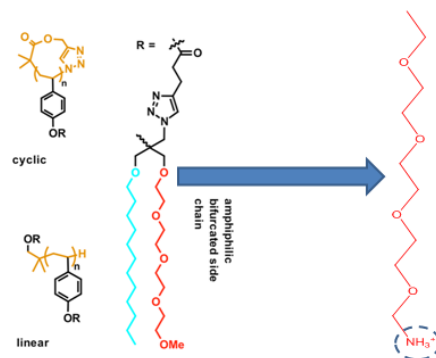


Figure 1 Designate polymer in strengthening arms' self-assembly structure: terminated the PEO oligomer with a charged group.

## 2. Methodology

Followed up with techniques' statements of previous work, we built up an initial configuration using LEaP module in AMBER 12. Since cyclic polymer exhibited more consistent results for analyzing, this time the only architecture we focused on is macro-cycle. The amphiphilic units still constituted a hydrophobic dodecane chain and polystyrene based backbone. Whereas a tetra (ethylene glycol) chain attached to tris-alcohol core was terminated with a  $\text{NH}_3^+$  charged group. Correspondingly, 32 chloride ions were solvated into our system to keep electrostatic balance and the force field of  $\text{Cl}^-$  was updated according Molinero's work<sup>3</sup> using frcmod format file. QM calculations were also performed to obtain RESP charges of the modified group ( $\text{NH}_3^+\text{CH}_2\text{OCH}_2\text{CH}_3$ ) using GAUSSIAN 09 packages at the MP2 level with cc-pvtz basis sets as the left figure showed. To get consistent results with previous studies, we still used GAFF to describe organic groups and solvent as well as TIP4P2005<sup>4</sup> to describe water model. Also 8000 water and 1500 toluene were solvated into the system.

## 3. Results and Discussion

As table 1 indicates, overall cyclic polymer sizes were increased after alternating the end of the group. Backbones'  $R_g$ s were increased too, but the observation of snapshots (Figure 2) indicated the backbone was stretched into an elliptical shape. The actual area of central space probably was smaller compared with original polymer. Alkyl arms in toluene solution displayed the slight difference between modified and original polymers within only 0.1 Å. Those arms in aqueous solution manifested expansion about 2.4 Å which is not surprising due to overall structural inflation. On the other hand, PEO arms'  $R_g$  of modified polymer in both toluene and water solution were about 21 Å. Compared with the original polymer's results, the radii-of-gyration stretches about 2 Å.

However, the structural change trend regarding varying polarity actually did not exhibit any difference within the modified and original polymer. Demonstrated by Table 1, what drew a difference was the extent of arms' retreating and advancing.

	polymer (Å)	backbone (Å)	alkyl arm (Å)	PEO arms (Å)
cyclic in water (mod.)	18.4	10.3	18.8	21.9
cyclic in toluene (mod.)	19.7	10.2	23.7	21.3
cyclic in water	16.5	9.1	16.4	19.2
cyclic in toluene	18.9	9.2	23.8	19.4

Table 1 Average Radii of Gyration of the Modified and Original Cyclic Amphiphilic Polymers, Their Backbones, the Hydrophobic Alkyl Arms, and the Hydrophilic PEO Arms in water and Toluene at 300 K

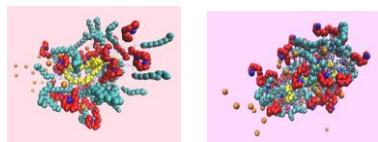


Figure 2 Demonstrating snapshots of modified cyclic polymer in toluene (left) and in water (right). The polymer backbone, alkyl side chains, and oligomeric PEO side chains are illustrated as the yellow, cyan, and red van der Waals surface. The modified heavy atom of  $\text{NH}_3^+$  is illustrated with blue surface.

To discern interior molecular structure details clearly, density distribution function was further implemented to study interested components of polymers. Compared with previous studies, there were several obvious structural changes: Firstly, backbone's distribution was narrowed to sharper distribution toward the inner place, suggesting backbone loop actually became smaller comparing with original distribution. Secondly, there was no distribution of alkyl arms and PEO arms nearby the center of polymer, resulting denser distribution of alkyl arms outside the backbone. Thirdly, PEO arms' exterior distribution was prolonged to 28~30 Å after modification with the original PEO arms' distribution only reaching at 25 ~28 Å. Fourthly both polar and non-polar solvents penetrated deeper. Especially the water penetration could reach to 5 Å which is quite departing from the original phenomenon that cyclic polymer blocked the water penetrating at about 15 Å. Fifthly, chloride ions' distribution superimposed with PEO arms' and most of the ions were absorbed onto the polymer side. Under  $\text{NH}_3^+$  strong attraction to chloride, Chlorides' distribution was influenced by  $\text{NH}_3^+$ 's dynamics majorly, but it was still perturbed under other atoms' influence such as oxygen of water, oxygen of Tris-alcohol groups or nitrogen atoms in trials groups.

As demonstrated by Figure 3, further comparative analysis between the instantaneous liquid surface of modified cyclic polymers and the original cyclic polymer were implemented. In non-polar environment, the original distribution rendered significant overlapping between PEO and alkyl arms. However, such overlapping distributions were replaced by the separated ones for the modified polymer. Especially the PEO arms were faded further from the liquid surface through the alkyl arms still occluded the same position nearby the liquid interface. It's a remarking validation of our initial design idea that charged groups pended on the hydrophilic arms will lead stronger segregation of amphiphilic chains and affect the chemistry utterly with a minor change of structure.

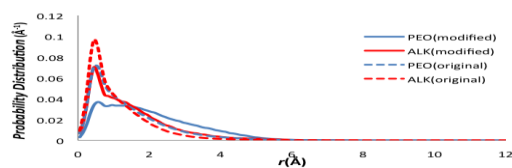


Figure 3 Comparison of the probability distribution of distance for PEO (blue) and ALK (red) between modified and original polymer in a toluene solution

#### 4. Conclusion

We performed simulations with adding terminated charged group  $\text{NH}_3^+$  onto the hydrophilic arms of cyclic polymer as well as chloride ions into the existed system. Indicated by radius-of-gyration analysis, overall size of polymer as well as amphiphilic arms were all increased, but the modified polymers' preferences to various polarities beared no differneces. Density distribution function revealed several molecular details distinct from the original template, indicating relatively loose structure after introducing new charged group. The instantaneous liquid surface analysis also revealed that minor difference of backbone didn't affect the basic orientation preference of amphiphilic arms. Distributions of instantaneous liquid surface distance were faded to flatter upon modifying the polymer. Especially PEO arms' distribution shrouded more under the instantaneous toluene surface, indicating the occurrence of stronger segregation. According to our expectation, stronger segregation should result a more thorough inversion, however, complete inversion was not observed. One of the current problems is still that the backbone's flexibility is limited due to the geometry constraints. High stiffness of hydrocarbon backbone as well as shorter chain length may lead such consequence. In the future, combining the present results with previous studies, a complete design scheme for improving the performance of interested polymeric micelles can be established.

#### 5. Acknowledgments

The current work is funded by the NSF EPSCoR LA-SiGMA project under award #EPS-1003897.

#### 6. Reference

- [1] Liu, L.; Parameswaran, S.; Sharma, A.; Grayson, S. M.; Ashbaugh, H. S.; Rick, S. W., *J Phys Chem B*.
- [2] Matsen, M. W.; Bates, F. S., *Macromolecules* **1996**, *29* (4), 1091-1098.
- [3] DeMille, R. C.; Molinero, V., *Journal of Chemical Physics* **2009**, *131* (3).
- [4] Abascal, J. L. F.; Vega, C., *Journal of Chemical Physics* **2005**, *123* (23).

## Direct Dynamical Simulation of Filling of Carbon Nanotube Forests

X. You and L. R. Pratt<sup>1</sup>

<sup>1</sup>Department of Chemical & Biomolecular Engineering, Tulane University

**Abstract:** Charging and discharging processes for electrochemical double-layer capacitors (EDLCs) are studied by direct simulating of the filling of a nanotube forest (CNT) with propylene carbonate (PC) tetraethylammonium-tetrafluoroborate (TEABF<sub>4</sub>) solutions. Demixing was observed in the bulk reservoir as the forest becomes strongly charged. In both filling and emptying, equilibration of the charge balance was reached within one nanosecond. Kinetic characteristics are compared between bulk solution reservoir and the interstitial spaces of the CNT forest.

**Keywords:** carbon nanotube forests (CNT forests), electrochemical double-layer capacitors (EDLCs), propylene carbonate (PC), molecular dynamics simulation

### 1. Introduction

The transport parameters can be substantially different in nanoporous materials such as these, *e.g.*, viscosities might differ substantially with nanoscale confinement from their value for macroscopic (bulk) systems. A recent work [1] has shown that more general interactions must be included in the numerical simulation data to resolve these questions conclusively.

In our previous study [2], we exhaustively studied propylene carbonate as a solvent for EDLCs, reported experimental and molecular simulation results on PC interfaces. PC wets graphite with a contact angle of 31° at ambient conditions. Molecular dynamics simulations agree with this contact angle after 40% reduction of the strength of graphite-C atom Lennard-Jones interactions with the solvent. This validation paves the way to direct simulation of dynamical filling and performance of CNT-based EDLCs.

Here, we present all-atom molecular dynamics simulations of electrochemical double-layer capacitors based on CNT forests with propylene carbonate tetraethylammonium-tetrafluoroborate (PC: TEA-BF<sub>4</sub>) solutions. We explicitly characterize the charging and discharging process, including electrolyte composition in the pores, and the rates that charging responses equilibrate and pore size dependence. Also, we consider the kinetic characteristics associated with the confinement and the anisotropic environment.

### 2. Methods

Simulations were carried out by GROMACS packages [3] with periodic boundary conditions in an isothermal-isobaric ensemble (NPT) at 300K. System sizes ranged from 18,000 to 35,000 atoms. For each charge level, 50ns production equilibrium run was performed after a 50ns-aging period.

### 3. Results

Preliminary simulation with 8 nanotubes, 85 pairs of TEABF<sub>4</sub> ions and 1000 PC molecules was carried out (Figure 1). Upon step-change of the CNT charge, ions transfer into the interstitial pores. That is, negative ions (BF<sub>4</sub><sup>-</sup>) experience an attraction from the positively charged lower nanotubes and move into the lower layer, whereas positive ions (TEA<sup>+</sup>) go into the upper layer. This transport accomplishes a de-mixing of the reservoir solution.

For each charge level, the ionic charge difference matched the charge difference between nanotubes (Figure 1, lower panel). The rate of charging responses relates to the power density of EDLC. In our simulation, sub-nanosecond equilibration was observed during both charging and discharging processes.

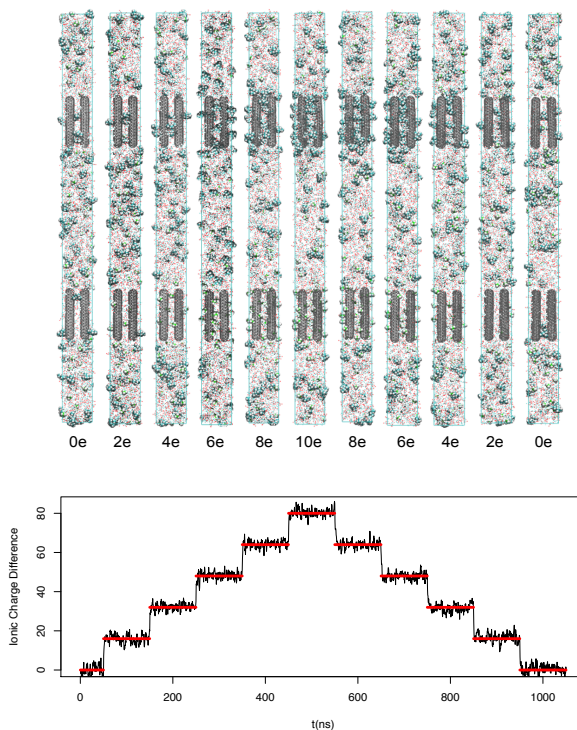
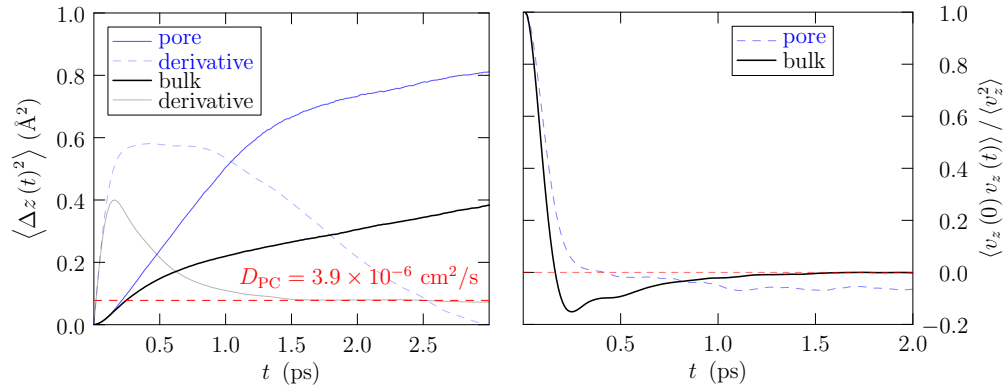


Figure 1: Upper panel: Snapshots, separated by 100 ns, of the molecular dynamical filling of CNT forests, as the electronic charge on the nanotubes is incremented. The label below each frame is the electronic charge/CNT. Upper layer has negatively charged CNTs, and the lower layer has positively charged CNTs. Here four CNTs above and below, for a total of eight (8) tubes altogether. The solvent is propylene carbonate, and the electrolyte is tetra-ethylammonium tetra-fluoroborate. T = 300K. Lower panel: Difference in ionic charge (black) above and below the mid-plane of simulation cells in FIG.2. Notice the sub-nanosecond equilibration of the charge balance, in both filling and emptying.

Transport properties for PC molecule in above simulations are showed in Figure 2, compared between bulk solution reservoir and the interstitial spaces of the CNT forest. The intermediate time differences --- the negative peak in the velocity autocorrelation function (vacf) --- are probably consequences of long-range interactions with the two media, which are different over long distances scales. At much longer times, the vacf for the PC molecules in the pore displays a negative correlation tail. This may be due to the one-dimensional (single-file) character of the motions within the pore. The long-term diffusivity of a PC molecule in this channel is then substantially lower than in the bulk solution.



**Figure 2: (left) Mean-square z-displacement of a propylene carbonate (PC) molecule in the interstitial spaces of the CNT forest, compared to a PC molecule in the bulk solution reservoir. (right) Comparison of the z-velocity autocorrelation function for a PC molecule in the two cases, bulk vs pore. (T,p) = (300K,1atm) and the electrolyte concentration is about 1M. In this case, the CNTs are discharged (neutral) so that differences reflect just the confinement. The pores have a nominal diameter of 1nm.**

We considered a memory function  $\gamma(t)$  defined [4] as

$$M \left( \frac{dC(t)}{dt} \right) = - \int_0^t \gamma(t - \tau) C(\tau) d\tau, \quad (1)$$

with  $M$  the mass of the PC molecule,  $C(t)$  the velocity autocorrelation function (Figure 2, right).  $\gamma(t)$  is the autocorrelation function of the random forces on a PC molecule.

We obtained  $\gamma(t)$  by solving the linear equation (Eq. 1), after discretization. We also utilized a specialized Fourier transform method to extract  $\gamma(t)$  from  $C(t)$  on the basis of the one-sided Fourier (Laplace) transform  $\tilde{\gamma}(z) \equiv \int_0^\infty e^{izt} \gamma(t) dt$ . Results are shown in Figure 3.

The two numerical methods gave similar results for  $\gamma(t)$ , which decays approximately exponentially for the largest times shown. The long-time behavior was suggested in considering dielectric friction on ion mobility. [5] Here, the PC molecules are not ions, so this long-time decay has to be understood in more

general terms. Since this longer time decay interesting for the basic theory of liquids, we have studied the corresponding long-time decay in ethylene carbonate, acetonitrile, and water in collaboration with the LA-SiGMA group at UNO (S. Rick).

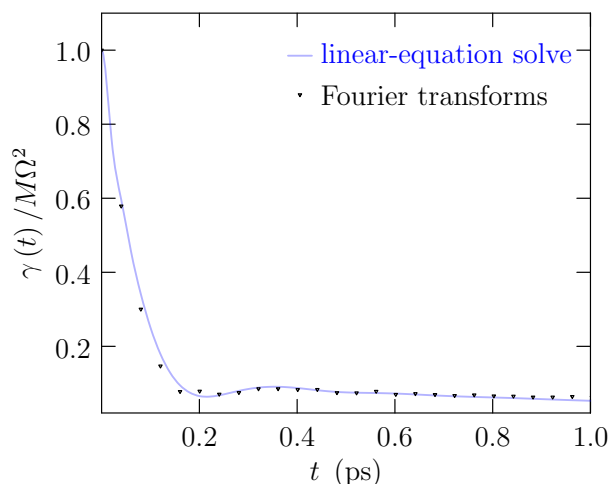


Figure 3: The autocorrelation function of the random forces on PC molecules, normalized by utilizing the Einstein frequency  $\Omega$ .  $\gamma(t)$  is extracted here from  $C(t)$  (Eq.1) by discretized linear-equation solving or by a specialized Fourier transform method.

#### 4. Conclusions

Here we characterize the charging and discharging processes for EDLCs by direct simulating of PC:TEABF<sub>4</sub> solution filling of CNT forests. Recent studies of interfacial properties of PC have laid the basis for this simulation model. Explicating the rates of charging responses and the kinetic characteristics associated with the confinement and the anisotropic environment. The memory function kernel for the vacf is obtained utilizing linear-equation solving after discretization, or specialized Fourier transform method.

#### 5. Acknowledgments

The current work is funded by the NSF EPSCoR LA-SiGMA project under award #EPS-1003897.

#### 6. References

- [1] P. Zhu, *et al.*, *J. Chem. Phys.* **137**, 17 (2012): “Pairing of 1-hexyl-3-methylimidazolium and tetrafluoroborate ions in n-pentanol.”
- [2] X. You, *et al.*, *J. Chem. Phys.* **138**, 114708 (2013): “Interfaces of propylene carbonate.”
- [3] Van der Spoel, D., Lindahl, E., Hess, B., Groenhof, G., Mark, A. E., Berendsen, H. J. C. (2005) GROMACS: Fast, Flexible and Free. *J. Comp. Chem.* **26**, 1701-1718.
- [4] R. Zwanzig, *Nonequilibrium Statistical Mechanics* (Oxford, 2001)
- [5] P. G. Wolynes, *J. Chem. Phys.* **68**, 473 (2012).

## Dynamical cluster approximation study of the two-dimensional Anderson-Hubbard model

Shuxiang Yang<sup>1,2</sup>, Patrick Haase<sup>3</sup>, Terletska<sup>1,2</sup>, Thomas Pruschke<sup>3</sup>, Juana Moreno<sup>1,2</sup>, Mark Jarrell<sup>1,2</sup>

<sup>1</sup>Department of Physics & Astronomy, Louisiana State University

<sup>2</sup>Center for Computation & Technology, Louisiana State University

<sup>3</sup>Department of Physics, University of Goettingen

**Abstract:** The dynamical cluster approximation (DCA) is used to study the Mott-Hubbard metal-insulator transition. With both the Coulomb interaction and disorder treated on the same footing, the numerical results for a two-dimensional eight-site cluster reveal how the disorder affect the metal-insulator transition. For small disorder, the system does not show major changes neither the critical  $U$  change much. Starting from a disorder strength around 0.2 (the bandwidth is 2), the critical  $U$  increases approximately linearly on increasing disorder strength.

**Keywords:** Anderson-Hubbard model, disorder, metal-insulator transition, dynamical cluster approximation.

### 1. Introduction

There are two well-known routes to the metal-insulator transition (MIT): one is the Mott-Hubbard MIT [1] where the driving force is the Coulomb interaction, while the other is the Anderson MIT [2] due to disorder scattering. In realistic materials, the charge carriers experience scattering from both Coulomb interactions and disorder. In this situation, one needs to treat both the Coulomb interaction and the disorder on the same footing, and this imposes a great challenge for the theoretical study of the underlying physics. For quite a long time, people rely on single-site approximations, such as the dynamical mean-field theory (DMFT) [3] and the coherent potential approximation (CPA) [4], to deal with interacting disordered systems. They are powerful methods and reveal a lot of interesting physics. However, such methods are exact only in the infinite dimensional system. For any real system, three-dimensional, two-dimensional or even one-dimensional for some materials, it provides only a rough approximation, and might even miss the essential physics, such as the d-wave superconductivity and the pseudo-gap physics, due to the absence of the non-local correlations. Cluster extensions of the single-site approximation are therefore needed. The so-called dynamical cluster approximation (DCA) [5,6] and the cellular DMFT [5] are the two most well-known methods along this direction.

### 2. Method

Instead of a single-site, the DCA [5] employs a cluster as the reference, and embeds the cluster in a self-consistently determined mean-field. Therefore, in addition to the local correlations, the short correlations within the cluster size are also taken into account and thus the DCA represents a much improved approach to explore the physics of strongly-correlated system, where correlations at different length-scales all contribute to the underlying physics.

In the following, we will use the DCA to study the interacting disordered system which is nicely modeled by the Anderson-Hubbard model described by the Hamiltonian

$$\mathcal{H} = \sum_{\mathbf{k},\sigma} (\epsilon_{\mathbf{k}} - \mu) c_{\mathbf{k}\sigma}^\dagger c_{\mathbf{k}\sigma} - \sum_{i\sigma} v_i n_{i\sigma} + U \sum_i n_{i\uparrow} n_{i\downarrow} \quad (1)$$

where the first term is the non-interacting contribution, the second is the disorder contribution with  $v_i$  is the on-site disorder potential, and the third, the Coulomb interaction contribution with the  $U$  the interaction strength. In this paper we will focus on the box disorder distribution case with the on-site disorder potential uniformly distributed within  $[-V/2, V/2]$  with  $V$  the disorder strength.

For all the results shown in this paper, we use the unit fixed by setting  $4t=1$  ( $t$  is the hopping constant), choose an  $N_c=8A$  cluster, and focus on the half-filled two-dimensional Anderson-Hubbard model.

### 3. Results

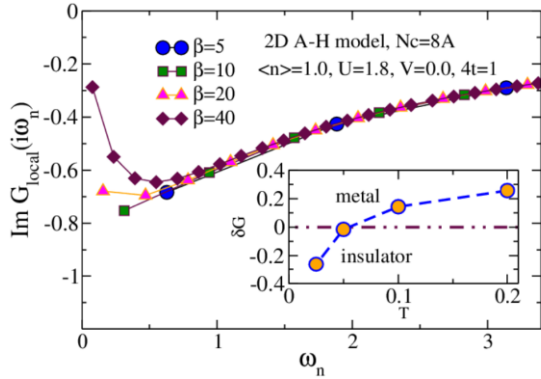


Fig. 1 The frequency dependence of the local Green function for different temperatures. At high temperature, the system is in the metallic state due to the thermal fluctuations. As the temperature is reduced, the thermal fluctuations are quenched and the spectral weight at the zero frequency is thus depleted, signaling the forming of an insulating state. The inset shows the temperature dependence of  $dG$  defined in Eq. (2).

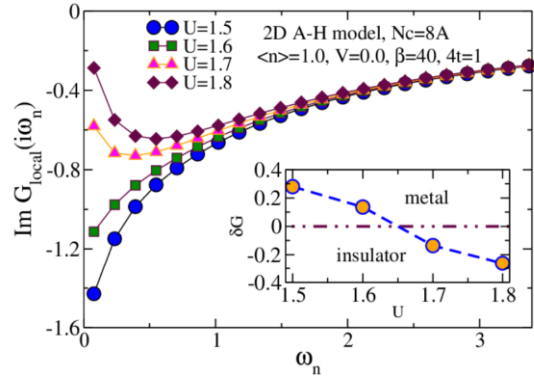


Fig. 2 The frequency dependence of the local Green function for different Coulomb interactions. The Coulomb interaction  $U$  is the driving force of the Mott-Hubbard metal-insulator transition. By increasing  $U$ , one can observe this transition at  $U_c \sim 1.65$ .

To gain some insight on how an insulator is developed, we first analyze how the local Green function evolves as the temperature is reduced. The frequency dependence of the local Green function for different temperatures is shown in Fig. 1. At high temperature (small  $\beta$  since  $\beta=1/T$ ,  $T$  is the temperature), the system is in the metallic state since the charge carriers are activated by thermal fluctuations. As the temperature is reduced ( $\beta$  is increased),

the thermal fluctuations are quenched and the spectral weight at zero frequency is thus depleted, signaling the forming of an insulating state. To quantify how this happens, we define the quantity

$$\delta G \equiv \text{Im} [G_{local}(3i\pi T) - G_{local}(i\pi T)] \quad (2)$$

using information at the lowest two Matsubara frequencies. The spectral function at the chemical potential (zero frequency) is related to the low-frequency information of the local Matsubara Green function. A positive  $\delta G$  suggests that the spectral function is finite at zero frequency and thus is in a metallic state, while a negative  $\delta G$  tells that the spectral weight is reduced and the system possibly becomes insulating. So we can detect the metal-insulator transition by identifying the sign change of  $\delta G$ . We expect this method of identifying the metal-insulating transition to underestimate the critical  $U$ , especially for high-temperature. However, for the temperature as low as  $\beta=40$ , the error would be relatively small. The inset of Fig. 1 shows the temperature dependence of this quantity. Note that the MIT transition occurs at  $\beta \sim 20$  where the  $\delta G$  changes its sign. For  $\beta=40$ , the insulating state is well-developed. We will use this temperature in the following analysis.

Next we look into how the local Green function evolves depending on the interaction by fixing the disorder strength at  $V=0$ . The result is shown in Fig. 2. From the small interaction side, the system is in the Fermi liquid regime and shows a metallic behavior with a positive  $\delta G$ . When approaching the critical  $U$  around 1.65, the gap is gradually formed and  $\delta G$  is reduced to zero. It becomes negative when  $U > 1.65$  and the system becomes insulating.

To see how disorder changes the MIT, we fix  $U=1.7$  and vary the disorder strength. The result is shown in Fig. 3. The system is in the insulating state with no disorder initially. After the disorder is turned on, the low frequency contribution of the local Green function is enhanced by the disorder scatterings. It becomes metallic around the disorder strength 0.35. To see how the critical  $U$  is modified by the disorder, in Fig. 4 we show the  $U$ -dependence of  $\delta G$  for different fixed disorder strength. With such data, we extract the critical  $U$  for different  $V$ , and in the inset, we show disorder dependence of the critical  $U$ . For small  $V$ , the system is not affected by the disorder scattering and the critical  $U$  does not change much until the disorder strength is around 0.2. Beyond  $V=0.2$ , the critical  $U$  increases almost linearly with the disorder.

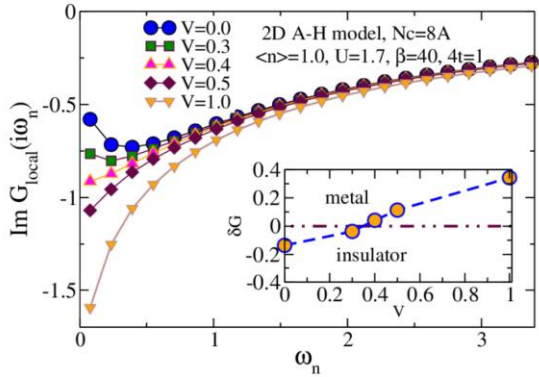


Fig. 3 The frequency dependence of the local Green function for different disorder strength. The scattering processes due to weak disorder increase the electron mobility, and drive the system out of the insulating state. For the  $U=1.7$  case, the system is originally in an insulating system due to the Coulomb interaction. When turning on the disorder, it becomes a metal at  $V \approx 0.35$ .

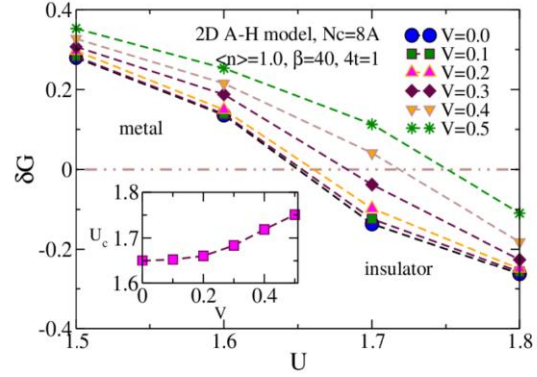


Fig. 4 The Coulomb interaction dependence of the difference between the values of the local Green function for the two lowest Matsubara frequencies for different disorder strength. In the inset, the disorder dependence of the extracted critical  $U$  is shown. For small  $V$ ,  $U$  does not change much until the disorder strength is around 0.2. Beyond  $V=0.2$ , the critical  $U$  increases almost linearly on the disorder.

#### 4. Conclusion

We have used the dynamical cluster approximation (DCA) method, which enables us to take into account the contributions from both the Coulomb interaction and disorder on the same footing, to study the Mott-Hubbard metal-insulator transition (MIT). The numerical results on a two-dimensional eight-site cluster reveal how the disorder scattering affects the MIT. For small disorder, the system is not affected by the disorder scattering and the critical  $U$  does not change much. Starting from disorder strength around 0.2, the critical  $U$  increases approximately linearly on increasing disorder strength.

#### 5. Acknowledgments

The current work is funded by the NSF EPSCoR LA-SiGMA project under award #EPS-1003897.

#### 6. References

- [1] N. F. Mott, Metal - Insulator Transitions, 2nd ed. (Taylor and Francis, London, 1990).
- [2] P. W. Anderson, Phys. Rev. 109, 1492 (1958).
- [3] A. Georges, G. Kotliar, W. Krauth, and M. Rozenberg, Rev. Mod. Phys. 68, 13 (1996).
- [4] P. L. Leath and B. Goodman, Phys. Rev. 148, 968 (1966).
- [5] Th. Maier, M. Jarrell, Th. Pruschke, and M. Hettler, Rev. of Mod. Phys., 77, 1027 (2005).
- [6] M. Jarrell and H. R. Krishnamurthy, Phys. Rev. B 63, 125102 (2001).

# Effect of Nanoparticle Size, Shape and Orientation on Effective Dielectric Constant in Polymer-Nanocomposites

S.C. Sklare<sup>1</sup>, Shiva Adireddy<sup>1</sup>, Venkata S. Puli<sup>1</sup>, J. Shipman<sup>1</sup>, and Douglas B. Chrisey<sup>1</sup>

<sup>1</sup>Department of Physics and Engineering Physics, Tulane University

## Abstract:

Polymer-nanocomposites are being investigated as a possible material for dielectric capacitors. Polymer-nanocomposites offer enhanced electrical and mechanical properties; these include high breakdown strength ( $E_b$ ), relative permittivity ( $\epsilon$ ) and mechanical flexibility. Despite enhancing the properties of individual constituents, current polymer-ceramic nanocomposites do not have the durability or energy density to address industrial or commercial peak usage applications. As such, new nanoparticles (NPs) and nano-composites must be developed to better take advantage of NPs with high dielectric constants and polymers with high break down fields.

Energy density is proportional to the product of the square of the applied electric field and permittivity ( $\propto E_b^2 \epsilon$ ). In turn, the relative permittivity and effective dielectric constant are affected by how NPs are oriented, and their shape and size. Fortunately, we have the ability to tune the size and shape of ceramic NPs and produce almost monodispersed NPs with narrow size distributions. To optimize our polymer-nanocomposite we have modeled the effective dielectric constant in a composite film with NPs of varying orientation for a range of percent volume mixings and the effective dielectric constant of polymer-nanocomposite films utilizing different mixing models.

**Keywords:** Nanoparticles, Nanocomposites, polymer-nanocomposites, capacitor devices and dielectric optimization

## 1. Introduction

Modeling nanocomposite material properties enables researchers to predict important composite bulk dielectric properties and optimize filler nanostructure parameters for further composite enhancement. Numerical models can predict dielectric permittivity using simple mixing models, combinations of existing mixing models and *ad hoc* mixing models. These models can also be used to approximate properties of constituents from bulk composite measurements.

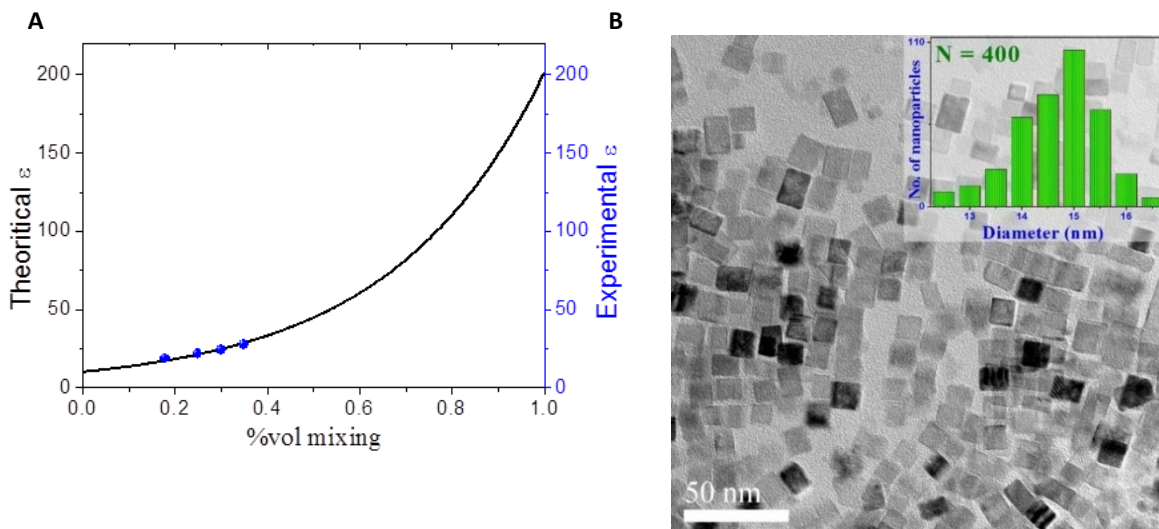
Dielectric characteristics of polymer nanocomposite systems are affected by changes in parameters of the individual phases of the composite. Accurate theoretical predictions of dielectric properties require careful consideration of important material parameters and are beyond the volume-fraction average (Equation 1). This proceedings paper serves as a progress update to accompany other presented material.

$$\epsilon_{eff} = v_1\epsilon_1 + v_2\epsilon_2 \quad (\text{Equation 1})$$

$\epsilon_{eff}$  is the effective dielectric constant of the composite material,  $\epsilon_n$  is the dielectric constant of each constituent and  $v_n$  is the associated volume fraction.

## 2. Mixing Models and Calculating Constituent Dielectric Constants from Composite Data

In general, mixing models approximate the filler and matrix as equivalent circuits composed of either two repeating components (filler and matrix) or three such components (filler, matrix and interface) repeating components. Particularly important parameters include the filler nanostructure's morphology (e.g. shape, size, orientation, core size, shell size), composite parameters (e.g. volume loading, thickness, interface), and permittivity and conductivity of individual phases and constituents.[1] Finding and appropriately utilizing existing standard and *ad hoc* models requires matching and/or compensating for assumptions and performing empirical



tests.

Figure 1 (A) Theoretical and experimental dielectric constant values versus volume loading of BST. Black line indicates the theoretical prediction of dielectric as a function of volume percent of ceramic component in the polymer matrix. Filled blue circular dots indicate the experimental dielectric constants. (B) TEM images of BST nanoparticles obtained via solvothermal synthesis at 150°C, with inset showing particle size distribution.

Direct measurement of effective dielectric constants of NPs is difficult and often impossible. Models used to predict composite dielectric constants can also be used to predict constituent properties. To approximate the dielectric constant of pure BST NPs, data for different compositions (18%, 25%, 30%, 35%) was fit to the Lichtenecker logarithmic law (Equation 3). The Lichtenecker logarithmic law, or the “logarithmic mixing rule” is frequently used when investigating the effects of composition on effective dielectric permittivity ( $\epsilon_{eff}$ ).[2]

$$\ln \epsilon_{eff} = v_1 \ln \epsilon_1 + v_2 \ln \epsilon_2 \quad \text{Equation 2}$$

Groups using sigmoidal curves and other ad-hoc empirical models, have shown higher accuracy than the basic Lichtenecker law when modeling dielectric constants of polymer nanocomposites at various volume compositions. However for the range of compositions, the method described gives a reasonable working approximation.

Equation 3 was minimized by varying  $\epsilon_{BST}$ , effectively performing an un-weighted least squares fit. Dielectric permittivity of PVDF ( $\epsilon_{PVDF}$ ) was taken to be 10 in all calculations.

$$\Delta^2 = \sum (e^{v_f \log \epsilon_{BST} + v_m \log \epsilon_{PVDF}} - \epsilon_{measured})^2 \quad \text{Equation 3}$$

Via the described approximation method, dielectric permittivity of BST NPs was found to be 195.61. This number is interpreted as a lower bound approximation for the dielectric permittivity of pure BST NPs, because the model does not account for loss due to the composite film fabrication. Figure 1 A plots the theoretical dielectric constant of the composite films versus BST volume percent and experimental values observed.

### 3. Nanoparticle Orientation

The solvothermal NP synthesis method offers several advantages, NP shape and size control is among the most critical. Figure 1 B shows images of uniform BST crystals taken using transmission electron microscopy (TEM). Figure 1 B Inset shows the size distribution of the BST NPs shown.

$$E_d = \left(\frac{1}{2}\right) \epsilon_0 \epsilon_r E_b^2 \quad \text{Equation 4}$$

The energy density ( $E_d$ ) associated with a storage device is proportional to effective dielectric constant ( $\epsilon_r$ ) (eq. 4). In turn the effective dielectric constant, also known as the relative permittivity, is a function of the cross section of dielectric material perpendicular to an applied electric field. To perform a qualitative analysis on the effect of NP orientation, we associated proportional coefficients cross sections of cube orientations and associated cross sectional coefficients with each. Orientations and coefficients are shown in the table below.

Orientation	Flat	Random	Diamond
Associated Coefficient	1	.5(1 + $\sqrt{2}$ )	$\sqrt{2}$

#### 4. Conclusion

Theoretically, maximizing the cross section perpendicular to applied electric field has been shown to have a large effect on the effective dielectric constant of composite films. In a comparison of different cross section for an arbitrary filler-matrix composite, the effective dielectric constant of the filler constituent, when maximized, was approximately 50% greater than when minimized, as shown in Figure 2.

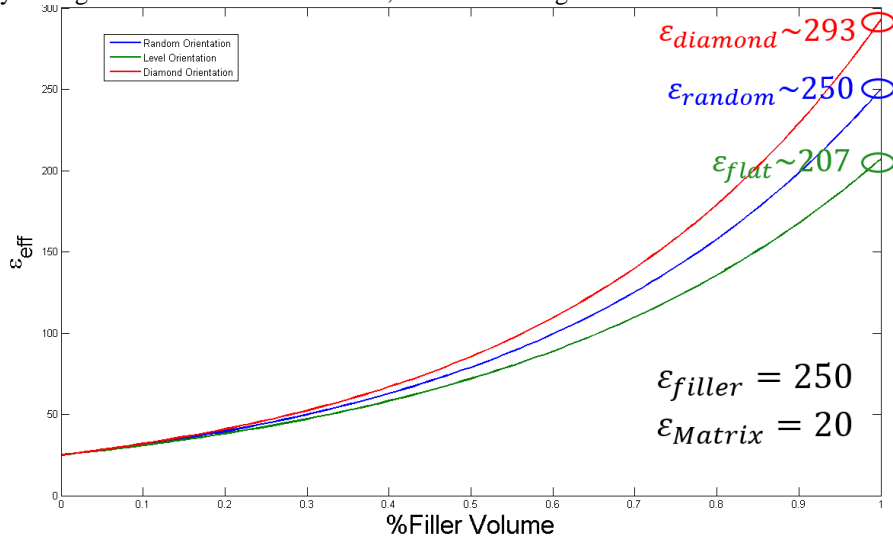


Figure 2 Effect of Filler Orientation: Dielectric Constant vs. Volume % Filler for an arbitrary system

The Logarithmic Mixing Rule was applied to a PVDF-BST composite film to approximate the effective dielectric constant of the filler NP constituent using an *ad-hoc* least squares fitting method. This method yielded a theoretical dielectric constant of 195.61, which was considered a lower bound estimate. Experimentally measured dielectric constant of a fabricated bulk BST NP pellet was 250, which is considered an upper bound estimate for embedded NPs.

#### 5. Acknowledgments

The current work is funded by the NSF EPSCoR LA-SiGMA project under award #EPS-1003897.

#### 6. References

- [1] N. Harfield, "Bulk permittivity of a composite with coated spheroidal filler particles," *J. Mater. Sci.*, vol. 5, pp. 5809–5816, 2000.
- [2] R. Simpkin, "Derivation of Lichtenecker's Logarithmic Mixture Formula From Maxwell's Equations.," *IEEE Trans. Microw. Theory Tech.*, vol. 58, no. 3, pp. 545–550, 2010.

## Electrical and Thermal Transport Properties of Superconducting $\text{Ca}_{10}\text{Pt}_4\text{As}_8((\text{Fe}_{1-x}\text{Pt}_x)_2\text{As}_2)_5$ Single Crystals

A. B. Karki<sup>1</sup>, J. Y. Pan<sup>1</sup>, P. Watkins-Curry<sup>2</sup>, G. T. McCandless<sup>2,3</sup>, J. Y. Chan<sup>2,3</sup>, E. W. Plummer<sup>1</sup>, R. Jin<sup>1</sup>

<sup>1</sup>Department of Physics and Astronomy, Louisiana State University, Baton Rouge, LA 70803

<sup>2</sup>Department of Chemistry, Louisiana State University, Baton Rouge, LA 70803

<sup>3</sup>Department of Chemistry, University of Texas at Dallas, Richardson, TX 75080

**Abstract:** We report experimental investigation of the electrical and thermal transport properties of superconducting  $\text{Ca}_{10}\text{Pt}_4\text{As}_8((\text{Fe}_{1-x}\text{Pt}_x)_2\text{As}_2)_5$  ( $x \sim 0.05$ ) single crystals with  $T_c = 34$  K. While the normal-state in-plane resistivity is metallic, the normal-state  $c$ -axis resistivity shows non-metallic behavior, sharing the same characteristic as underdoped high- $T_c$  cuprates. Large anisotropy is observed in both normal- and superconducting-state with anisotropy parameter  $\gamma \sim 6 - 7$  near  $T_c$ , making it one of the most anisotropic Fe-based superconductors. The negative Hall coefficient and thermopower indicate that charge carriers are dominantly electrons in this multiband system. Both in-plane electrical resistivity and thermal conductivity suggest that electron-phonon scattering plays a key role in transport properties. Furthermore, low phonon thermal conductivity is observed, making this material attractive for thermoelectric applications as well.

**Keywords:** transport properties, new layered superconductor, high anisotropy

### 1. Introduction

The discovery of high-temperature ( $T_c$ ) superconductivity in Fe-based compounds has generated tremendous interest in the condensed matter and materials science community. The new class of materials offers the opportunity not only for studying superconducting mechanism but also for exploring structure-property relationship. As in high- $T_c$  cuprates, Fe-based superconductors form layered crystallographic structure, consisting of FeAs or Fe(Te/Se) building blocks separated by interlayer spacers. The relationship between  $T_c$  and spacers is complicated, as the spacers change not only interlayer coupling strength but also structural parameters within the superconducting plane. Furthermore, the spacers act as charge reservoirs, thereby influencing the electronic properties. A fundamental question is how the nature of spacers affects superconducting transition temperature. Empirically,  $T_c$  correlates with the interlayer distance ( $d$ ) in a cusp-shaped curvature in both cuprates and Fe-based superconductors. This suggests that the selection of spacers is important in order to achieve high  $T_c$  value. However, the recently discovered superconducting  $\text{Ca}_{10}\text{Pt}_n\text{As}_8(\text{Fe}_2\text{As}_2)_5$  seem to violate this empirical rule, where  $T_{c,\text{max}} \sim 13$  K for  $n = 3$  with  $d \sim 10.5 - 10.7$  Å, and  $T_{c,\text{max}} \sim 38$  K for  $n = 4$  with  $d \sim 10.5 - 11.2$  Å [1-3]. Given similar  $d$  value for both  $n = 3$  and  $n = 4$ , the large difference in  $T_c$  ought to be attributed to the interlayer spacer:  $\text{Ca}_{10}\text{Pt}_n\text{As}_8$ .

## 2 Experiment

To grow single crystals of  $\text{Ca}_{10}\text{Pt}_4\text{As}_8(\text{Fe}_2\text{As}_2)_5$ , stoichiometric amounts of high purity calcium shot, platinum powder, iron powder, and arsenic powder are mixed in a ratio of 10:4:10:18, as reported previously [5]. The mixture is placed in an alumina crucible and sealed in a quartz tube under vacuum. The whole assembly is heated in a box furnace to 700 °C at a rate of 150 °C/h, and is held at this temperature for 5 h. It is then heated to 1100 °C at a rate of 80 °C/h. After holding at 1100 °C for 50 h, it is cooled to 1050 °C at a rate of 1.25 °C/h. It is then cooled to 500 °C at a rate of 5.5 °C/h, and finally cooled down to room temperature by turning off power. As shown in the inset of Fig.1a, shiny plate-like single crystals with typical dimensions of  $4 \times 4 \times 0.2 \text{ mm}^3$  are obtained without requiring any additional process.

Single crystal x-ray diffraction results confirm that the sample crystallizes in a triclinic structure with space group symmetry  $P_{-1}$ . Due to the mosaicity ( $\sim 6^\circ$ ) of crystals, full structure refinement was not possible. However, the cell dimensions are obtained from indexing the reflections on the precession images (see Figs. 1b-1d). At room temperature, the lattice parameters are  $a = 8.7640(11) \text{ \AA}$ ,  $b = 8.7550(13) \text{ \AA}$ , and  $c = 10.69001(7) \text{ \AA}$ , and angles are  $\alpha = 94.672(8)^\circ$ ,  $\beta = 104.398(9)^\circ$ , and  $\gamma = 90.038(10)^\circ$ . These parameters are fairly close to that for  $\text{Ca}_{10}(\text{Pt}_3\text{As}_8)((\text{Fe}_{1-x}\text{Pt}_x)_2\text{As}_2)_5$  [5-6]. The chemical composition of our crystal determined by EDX analysis is  $\text{Ca}_{10.3}\text{Pt}_{4.5}\text{Fe}_{9.5}\text{As}_{18}$ , after an average of 6 scans at different locations. This corresponds to  $\text{Ca}_{10}(\text{Pt}_{4-\delta}\text{As}_8)((\text{Fe}_{1-x}\text{Pt}_x)_2\text{As}_2)_5$  with  $\delta \sim 0$  and  $x \sim 0.05$ .

## 3 Results and Discussion

Figure 1a shows the temperature dependence of  $\rho_{ab}$  and  $\rho_c$  of our  $\text{Ca}_{10}\text{Pt}_{4.5}\text{Fe}_{9.5}\text{As}_{18}$  single crystals between 2 and 300 K. The overall profile of  $\rho_{ab}(T)$  is similar to previous report for the  $n = 4$  phase [1-4], i.e.,  $\rho_{ab}(T)$  decreases with decreasing  $T$  in the entire temperature range measured with  $d\rho_{ab}/dT > 0$ . It shows a sharp superconducting transition with onset  $T_c = 34 \text{ K}$  and zero resistivity  $T_{c0} = 32 \text{ K}$ . The transition temperature is slightly lower than that reported in Ref. [1] but higher than that in Refs. [2-4] all for the  $n = 4$  phase. Note that  $\rho_c$  also drops at  $T_c$ , indicating three-dimensional (3D) superconductivity in this material. Strikingly,  $\rho_c$  in the normal state increases with decreasing  $T$ , i.e.,  $d\rho_c/dT < 0$ . This results in variable resistivity anisotropy  $\gamma_p^2 = \rho_c/\rho_{ab}$  from 17 at 300 K to 55 at 40 K (see inset of Fig. 1a), the highest anisotropy among Fe-based superconductors.

The disparity in sign of  $d\rho_{ab}/dT$  and  $d\rho_c/dT$  suggests different transport mechanisms between the  $ab$  plane and the  $c$  axis. As shown in Fig. 1b,  $\rho_{ab}$  exhibits almost linear- $T$  dependence

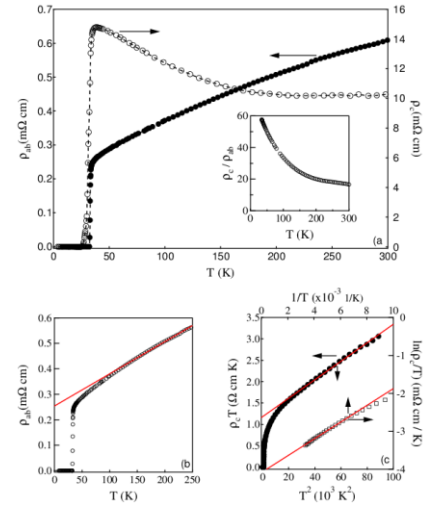


FIG. 1: (a) Temperature dependence of  $\rho_{ab}$  and  $\rho_c$  of  $\text{Ca}_{10}\text{Pt}_4\text{As}_8((\text{Fe}_{1-0.05}\text{Pt}_{0.05})_2\text{As}_2)_5$  single crystals. Inset is the temperature dependence of electrical resistivity anisotropy  $\rho_c/\rho_{ab}$  at variable temperatures. (b) Highlight of linear  $T$  dependence of  $\rho_{ab}(T)$  with the fitting line (see text). (c)  $\rho_c(T)$  data replotted as  $\rho_c(T)$  vs.  $T^2$  and  $\ln(\rho_c/T)$  vs.  $1/T$ .

between  $\sim 100$  K to 250 K. The straight line is the fit to experimental data in this temperature range. While it usually suggests electron-phonon scattering mechanism, the linear T-dependence of  $\rho_{ab}$  is also regarded as the signature of quantum critical behavior, as it occurs in the normal state of optimally-doped superconducting cuprates and Fe-based superconductors. At present, it is unclear if our sample is under- or over-doped, but surely not optimally doped as its  $T_c$  is not the highest among reported results. Therefore, the linear T dependence of  $\rho_{ab}(T)$  is likely the result of the electron-phonon scattering. On the other hand, the non-metallic  $\rho_c(T)$  ( $d\rho_c/dT < 0$ ) is observed for the first time in a Fe-based superconductor, although it is a common feature in underdoped cuprates. Thus,  $\text{Ca}_{10}(\text{Pt}_{4.8}\text{As}_8)((\text{Fe}_{1-x}\text{Pt}_x)_2\text{As}_2)_5$  is an ideal system for a comparative study between Fe- and Cu-based superconductors. Quantitatively, several attempts are made to fit  $\rho_c(T)$  using models developed for describing the  $c$ -axis transport of high- $T_c$  cuprates. According to Anderson's model [19], the  $c$ -axis transport of underdoped cuprates is incoherent and  $\rho_c(T) = AT + B/T$  (where  $A$  and  $B$  are T-independent constants). In the linear regime between 140 K and 300 K, the data apparently can be fit well by the formula with  $A = 21.6$  m $\Omega$  cm/K, and  $B = 1.18$   $\Omega$  cm K (Fig. 1c). In the other model, the non-metallic  $\rho_c(T)$  is considered to be due to the opening of pseudogap  $\Delta$ , and  $\rho_c(T)$  can be described by  $\rho_c(T) = \frac{\alpha_c T}{\Delta} \exp\left(\frac{\Delta}{T}\right)$  for  $T_c \ll T \ll \Delta$  (where  $\alpha_c$  is a

constant). In either case, the disparity in  $\rho_{ab}(T)$  and  $\rho_c(T)$  of  $\text{Ca}_{10}\text{Pt}_4\text{As}_8((\text{Fe}_{1-x}\text{Pt}_x)_2\text{As}_2)_5$  is unexpected within the conventional Fermi-liquid theory, and the fact that  $\rho_c(T) \gg \rho_{ab}(T)$  implies that hopping time along the  $c$  direction is much longer than the in-plane scattering time.

According to first-principles calculations, the electronic structure of  $\text{Ca}_{10}(\text{Pt}_{n-8}\text{As}_8)((\text{Fe}_{1-x}\text{Pt}_x)_2\text{As}_2)_5$  is similar to the rest of Fe-based superconductors with three electron-like and two hole-like bands. While Hall coefficient shows monotonic T dependence in the normal state, the multiband nature is reflected in thermopower. Shown in Fig. 2a is

the temperature dependence of in-plane thermopower,  $S_{ab}$ , between 2 and 300 K. The negative  $S_{ab}$  is consistent with negative  $R_H$ , confirming that the system is indeed electron dominant. However, different from  $R_H$ ,  $S_{ab}$  exhibits non-monotonic behavior with temperature – its magnitude initially increases with decreasing T and then decreases below  $\sim 150$  K before reaching zero at  $T_c$ . The non-monotonic behavior ought to be the consequence of multiband nature of electronic structure mixed with both electron- and hole-type with different mobilities. At  $T_c$ , the magnitude of  $S_{ab}$  quickly drops to zero, indication of electron condensation due to the formation of superconducting gap. The sharp transition again reflects high quality of our single crystals.

In contrast to the sharp drop of  $S_{ab}$ , the in-plane thermal conductivity,  $\kappa_{ab}$ , increases below  $T_c$ , as shown in Fig. 2b. In a non-magnetic system, thermal conductivity consists of contributions from both electrons ( $\kappa_{el}$ ) and phonons ( $\kappa_{ph}$ ), i.e.,  $\kappa_{ab} = \kappa_{el} + \kappa_{ph}$ . Electron condensation below  $T_c$  gives rise to reduced  $\kappa_{el}$  but enhanced  $\kappa_{ph}$

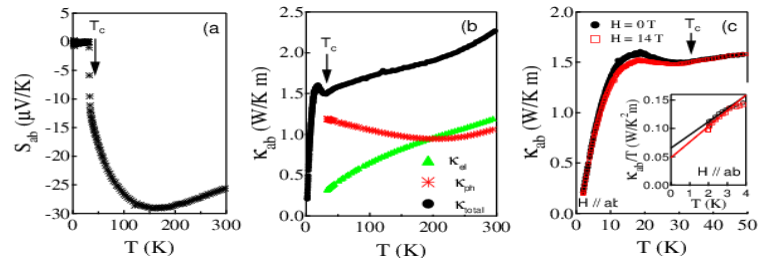


FIG.2: (a) Temperature dependence of in-plane Seebeck coefficient; (b) T dependence of in-plane thermal conductivities as indicated; (c) In-plane thermal conductivity at zero field and 14 T at low temperatures. Inset in c: Thermal conductivity plotted as  $\kappa_{ab}/T$  vs. T.

because of reduced electron-phonon scattering. Therefore, the upturn  $\kappa_{ab}$  below  $T_c$  indicates the importance of electron-phonon scattering in this material. Overall, the normal-state  $\kappa_{ab}$  is small for a single-crystal solid. We may estimate normal-state  $\kappa_{el}$  via Wiedemann-Franz law with  $\kappa_{el} = L_0 T / \rho_{ab}$  ( $L_0 = 2.44 \times 10^{-8} \text{ V}^2/\text{K}^2$ ). As plotted in Fig. 2b,  $\kappa_{el}$  decreases with decreasing temperature. As a result,  $\kappa_{ph}$  increases with decreasing temperature below  $\sim 250 \text{ K}$ , as expected for a single-crystal solid. Remarkably,  $\kappa_{ph}$  is only around  $1.0 \text{ W/K-m}$  at room temperature. This value is much lower than other Fe-based layered compounds. We believe that the low phonon thermal conductivity is due to its unique crystal structure, similar to cobaltates with misfit layered structures. Both low thermal conductivity and low electrical resistivity make this compound potentially useful for thermoelectric applications.

Figure 2c shows the temperature dependence of  $\kappa_{ab}$  at  $H = 0$  and 14 Tesla, which is applied in parallel to the  $ab$  plane ( $H//ab$ ). While there is little effect above  $T_c$ , magnetic field ( $H$ ) suppresses thermal conductivity below  $T_c$ . This is because of the suppression of superconductivity, which leads to less electron condensation. This further confirms the dominance of electron-phonon scattering in transport properties of  $\text{Ca}_{10}(\text{Pt}_4\text{As}_8)(\text{Fe}_{1-x}\text{Pt}_x)_2\text{As}_2)_5$ . If replot  $\kappa_{ab}(T)$  at  $T \ll T_c$  as  $\kappa_{ab}(T)/T$  versus  $T$  as shown in the inset of Figure 5c, it may be found that  $\kappa_{ab}/T$  exhibits more or less linear  $T$  dependence for both  $H = 0$  and 14 Tesla. Linear extrapolation to  $T = 0 \text{ K}$  leads that  $\kappa_{ab}(0)/T \neq 0$ . Such a residual term appears in superconductors with node(s) in pairing symmetry.

#### 4. Conclusion

In summary, we have experimentally investigated the electrical and thermal transport properties of superconducting  $\text{Ca}_{10}\text{Pt}_{4.5}\text{Fe}_{9.5}\text{As}_{18}$  single crystals with  $T_c = 34 \text{ K}$ . For the first time, we observe metallic in-plane resistivity but non-metallic-like  $c$ -axis resistivity, similar to that seen in underdoped high- $T_c$  cuprates. Anisotropy is observed in both normal- and superconducting-state with anisotropy parameter 6 – 7, making it one of the most anisotropic Fe-based superconductors. This will help us understand structure-property relationship among layered superconductors. The negative Hall coefficient and thermopower confirm that the dominant carriers are electrons, while involving multiple bands. Both electrical resistivity and thermal conductivity suggest that electron-phonon scattering plays a key role in transport properties. Furthermore, we observe low phonon thermal conductivity, making this material attractive for thermoelectric applications as well.

#### 5. Acknowledgments

The current work is funded by the NSF EPSCoR LA-SiGMA project under award #EPS-1003897 (JYP, RJ), NSF DMR-1002622 (EWP), and NSF DMR-1063735 (PWC, GTM, JYC).

#### 6. References

- [1] S. Kakiya, et al., Journal of the Physical Society of Japan **80**, 093704 (2011).
- [2] N. Ni, J. M. Allreda, B. C. Chanb, and R. J. Cava, PNAS **108**, E1019 (2011).
- [3] C. Löhnert, et al., Angew. Chem. Int. Ed. **50**, 9195 (2011).
- [4] Q.-P. Ding, Y. Tsuchiya, S. Mohan, T. Taen, Y. Nakajima, and T. Tamegai, Phys. Rev. B **85**, 104512 (2012).

## Equation of motion coupled cluster methods for electron attachment and ionization potential: implementation and applications

Kiran Bhaskaran-Nair<sup>1,3,4</sup>, Karol Kowalski<sup>2</sup>, Juana Moreno<sup>1,3</sup>, Mark Jarrell<sup>1,3</sup>, and William A. Shelton<sup>1,4</sup>

<sup>1</sup>Center for Computation and Technology, Louisiana State University, Baton Rouge, LA 70803, USA

<sup>2</sup>William R. Wiley Environmental Molecular Sciences Laboratory, Battelle,

Pacific Northwest National Laboratory, K8-91, P.O.Box 999, Richland, WA 99352, USA

<sup>3</sup>Department of Physics & Astronomy, Louisiana State University, Baton Rouge, LA 70803, USA

<sup>4</sup>Cain Department of Chemical Engineering, Louisiana State University, Baton Rouge, LA 70803, USA

**Abstract:** We have developed an accurate and parallel efficient approach to calculate the ionization potential (IP) and the electron affinity (EA) based on the equation of motion (EOM)-CC technique. To demonstrate the accuracy and efficiency of this implementation we have calculated the ionization potential (IP) and electron affinity (EA) of C<sub>60</sub> and C<sub>70</sub>.

**Keywords:** ionization potential, electron affinity, equation of motion coupled cluster method, fullerenes

### 1. Introduction

For systems ranging from light harvesting polymers and photo-catalytic compounds to semiconductors there is a need for the accurate determination of the ionization potential (IP) and the electron affinity (EA). The equation of motion coupled cluster (EOMCC) methodologies provides an proper description of excited states characterized by complicated collective electron excitations. EA/IP are often approximated by simple HOMO-LUMO energy does not provide sufficient accuracy. Our goal is to fill this gap by enabling IP/EA-EOM-CCSD methods for large systems.

### 2. Theory

A brief introduction to IP/EA-EOM-CCSD method is given below. At the heart of the CC method is the exponential ansatz.<sup>[1-4]</sup> where wavefunction is expressed as,

$$|\Psi\rangle = e^T|\phi\rangle,$$

where  $|\Phi\rangle$  is the reference wavefunction and  $T$  is the cluster operator. Similarly, in the EA/IP-EOM-CC formalism, the wavefunction is obtained by the application of the  $R(k)$  operator on the ground state CC wavefunction,

$$|\Psi_k\rangle = R(k)|\Psi_0\rangle.$$

The  $R(k)$  operator in the IP method<sup>[5]</sup> is given by

$$R(k) = \sum_i r_i(k)i + \frac{1}{2} \sum_a \sum_{ij} r_{ij}^a a^+ j i$$

and likewise for the EA<sup>[6]</sup>

$$R(k) = \sum_a r^a(k)a^+ + \frac{1}{2} \sum_{ab} \sum_i r_i^{ab} a^+ b^+ i$$

The IP/EA are obtained by solving the following matrix equation,

$$\bar{\mathbf{H}}_N \mathbf{R}(\mathbf{k}) = \mathbf{R}(\mathbf{k}) \omega_{\mathbf{k}}$$

where  $\omega_k = \Delta E_k - \Delta E_0$  is the energy difference associated with the EA or IP process. The EA/IP-EOM-CCSD implementation was done in the NWChem program package<sup>[7]</sup> using the Tensor Contraction Engine (TCE)<sup>[8]</sup> and Global Arrays (GA) capabilities.

### 3. Results

We performed a series of benchmark calculations for  $F_2$  and  $C_2$  and comparing the results with the literature. The ionization potential and electron affinity for  $C_{60}$  and  $C_{70}$  was performed employing 6-311G<sup>[10]</sup> and Dunning's correlation consistent spherical Gaussian cc-pVDZ<sup>[9]</sup> basis sets. In addition, the core electrons were excluded from the correlation treatment in these calculations.

Method/Basis set	cc-pV5Z	cc-pV6Z	Method/Basis set	cc-pV5Z	cc-pV6Z
IP-EOM-CCSD <sup>1</sup>	15.74	15.77	EA-EOM-CCSD <sup>1</sup>	3.32	3.35
IP-EOM-CCSD <sup>2</sup>	15.78	15.81	EA-EOM-CCSD <sup>2</sup>	3.36	3.40
Method/Basis set	aug-cc-pV5Z	aug-cc-pV6Z	Method/Basis set	aug-cc-pV5Z	aug-cc-pV6Z
IP-EOM-CCSD <sup>1</sup>	15.76	15.78	EA-EOM-CCSD <sup>1</sup>	3.36	3.37
IP-EOM-CCSD <sup>2</sup>	15.80	15.82	EA-EOM-CCSD <sup>2</sup>	3.41	3.42
Expt. <sup>[11]</sup>		15.83	Expt. <sup>[12]</sup>		3.30±0.1

Table 1: IP for F<sub>2</sub> molecule (R=1.41193Å) and EA for C<sub>2</sub> molecule (R=1.243Å). The labels <sup>1</sup> and <sup>2</sup> refers to results without and with core electrons in the correlation treatment, respectively. All the results shown here are in eV.

The ionization potential for F<sub>2</sub> and the electron affinity for C<sub>2</sub> obtained using EA-EOM-CCSD as a function of increasing basis set size are shown in Table 1. As can be seen, as the basis set size increases the IP increases. The including core electrons in the correlation treatment also increases the IP energies. Moving from aug-cc-pV5Z to aug-cc-pV6Z basis set the IP increases by 0.02 eV. The result obtained from aug-cc-pV6Z is close to the experimental value of 15.83 eV.

Similar to F<sub>2</sub>, increasing the size of the basis set or including the core electrons for C<sub>2</sub> increases the EA energies. The EA results obtained using aug-cc-pV6Z basis set with core electrons included in the correlation treatment is 3.42 eV which is closer to the experimental value of 3.30±0.1 eV.

Basis	Method	C <sub>60</sub>	Basis	C <sub>70</sub>
6-31++G**	IP-EOM-CCSD	7.65	6-31++G	7.41
aug-cc-pVDZ	IP-EOM-CCSD	7.64	cc-pVDZ	7.40
Expt.		7.6±0.2 <sup>[13]</sup>	Expt.	7.47±0.02 <sup>[14]</sup>
6-31++G**	EA-EOM-CCSD	2.28	6-31++G	2.03
aug-cc-pVDZ	EA-EOM-CCSD	2.38	cc-pVDZ	2.12
Expt.		2.689±0.008 <sup>[15]</sup>	Expt.	2.765±0.01 <sup>[16]</sup>

Table 2: Ionization potential and Electron Affinity for C<sub>60</sub> and C<sub>70</sub> molecule. All the results shown here are in eV.

The ionization potential and electron affinity obtained for C<sub>60</sub> and C<sub>70</sub> are shown in Table 2. For C<sub>60</sub> and C<sub>70</sub> the IP results obtained are also in very good agreement with the experimental values. The deviation for experimental value for C<sub>60</sub> and C<sub>70</sub> in aug-cc-pVDZ and cc-pVDZ basis sets are only 0.04 and 0.07 eV. In the case of EA the same basis sets produce a 0.3 eV and 0.6 eV deviation from the experimental values.

#### 4. Conclusion

We have implemented a highly accurate parallel IP/EA-EOM-CCSD approach in NWChem for determining electron affinity and ionization potential accurately. This highly parallel efficient implementation allowed for the investigation of large molecular systems, such as fullerenes, using highly accurate large basis sets. For both C<sub>60</sub>

and  $C_{70}$ , the IP results are less sensitive to the choice of basis set as compared to EA. For accurate IP/EA results requires at least triple zeta (TZ) quality basis set. This parallel efficient implementation can take advantage of the aggregate power of a range of computer architectures spanning from small to mid-size clusters to leadership-class systems, thereby enabling the study of a variety of systems from small molecules to moderately large nano scale systems where the electron affinity and ionization potential play an important role on determining the system properties.

## 5. Acknowledgments

This work is supported by the National Science Foundation under the NSF EPSCoR Cooperative Agreement No. EPS-1003897 with additional support from the Louisiana Board of Regents. The calculations have been performed using the Environmental Molecular Sciences Laboratory and Pacific Northwest National Laboratory (PNNL) Institutional Computing both resources located at PNNL, which is sponsored by the Department of Energy Office of Biological and Environmental Research. The PNNL is operated for the US Department of Energy by the Battelle Memorial Institute under Contract DE-AC06.76RLO-1830. A small portion of this research has used the high performance computational resources provided by Louisiana State University (<http://www.hpc.lsu.edu>).

## 6. References

- [1] F. Coester, *Nucl. Phys.* 7, 421 (1958).
- [2] F. Coester and H. Kummel, *Nucl. Phys.* 17, 477 (1960).
- [3] J. Čížek, *J. Chem. Phys.* 45, 4256 (1966).
- [4] J. Paldus, I. Shavitt, and J. Čížek, *Phys. Rev. A* 5, 50 (1972).
- [5] J. Stanton and J. Gauss, *J. Chem. Phys.* 103, 1064 (1995).
- [6] M. Nooijen and R. J. Bartlett, *J. Chem. Phys.* 102, 3629 (1995).
- [7] M. Valiev and E.J. Bylaska and N. Govind and K. Kowalski and T.P. Straatsma and H.J.J. Van Dam and D. Wang and J. Nieplocha and E. Apra and T.L. Windus and W.A. de Jong, *Comput. Phys. Commun.* 181, 1477 (2010).
- [8] S. Hirata, *J. Phys. Chem. A* 107, 9887 (2003).
- [9] T. H. Dunning, *J. Chem. Phys.* 90, 1007 (1989).
- [10] W. Hehre, R. Ditchfield, and J. Pople, *J. Chem. Phys.* 56, 2257 (1972).
- [11] K. Kimura, S. Katsumata, Y. Achiba, T. Yamazaki, and, S. Iwata, *Handbook of He I Photoelectron Spectra of Fundamental Organic Molecules* (Japan Scientific Societies Press, Tokyo,(1981), .
- [12] S. Yang, K.J. Taylor, M.J. Craycraft, J. Conceicao, C.L. Pettiette, O. Cheshnovsky and R.E. Smalley *Chem. Phys. Lett.* 144, 431 (1988).
- [13] X.-B. Wang, C.-F. Ding, and L.-S. Wang, *J. Chem. Phys.* 110, 8217 (1999).
- [14] X-B Wang, H.-K. Woo, X. Huang, M. M. Kappes, and L.-S. Wang, *Phys. Rev. Lett.* 96 143002 (2006).
- [15] D. L. Lichtenberger, K. W. Nebesny, C. D. Ray, D. R. Huffman, L. D. Lamb *Chem. Phys. Lett.* 173, 203 (1991).
- [16] D. L. Lichtenberger, M. E. Rempe, and S. B. Gogosha, *Chem. Phys. Lett.* 198, 454 (1992).

# Exploiting Sparse Matrix Structure in a Monte-Carlo Arnoldi iteration on Many-Core Architectures

Roozbeh Karimi<sup>1</sup>, David M. Koppelman<sup>1</sup>

<sup>1</sup>Division of Electrical and Computer Engineering, Louisiana State University, Baton Rouge, Louisiana

**Abstract:** A common solution to Matrix Exponential of a sparse matrix uses the Krylov subspace approximation; this involves an Arnoldi iteration on that sparse matrix which involves a sparse matrix-vector multiplication (SpMV). Different sparse representations such as ELL, HYB, and SELL are popular choices for GPU and Phi. Such representations for our sparse matrix would require 84, 60, and 63 kiB of storage space respectively. A careful analysis of the matrix for this problem reveals structure that can reduce storage required and reduce scatter/gather overhead using a custom representation. For example, there are only two distinct values for non-zero off diagonal elements, and these represent about 2/3 of the total values. Also, these elements follow a self-repeating pattern along diagonals of the sparse matrix (except the main diagonal). With specialized storage formats, we can reduce the memory requirements to about 9kiB; furthermore, we can reduce the gather/scatter overheads.

**Keywords:** SpMV, Intel Xeon Phi, CUDA, GPU, ESB, CSR, ELL, SELL, COO, DIA

## 1. Introduction

Sparse matrix structures are common in various scientific applications; thus, it is often desirable in to manipulate them in different ways. One such kernel is the sparse matrix-vector multiplication (SpMV). SpMV is a common operation in various scientific and engineering applications, e.g. eigenvalue problems and large scale linear systems. Our interest in SpMV rises from a Monte-Carlo simulation of a code which involves Krylov subspace approximations to the matrix exponential operation on a relatively large (1024-by-1024) highly structured sparse matrix. A common approach to this is the Arnoldi iteration [1]. The most costly computation in the Arnoldi iteration on a sparse matrix is a SpMV operation repeated in all iterations.

Different approaches have been proposed for SpMV, each tailored for specific architectures and/or sparsity patterns. Recent years have seen the rise of many-core architectures such as the GPU and the Intel Xeon Phi. Thus, it is desirable to have SpMV implementations targeting such architectures. Most of the methods proposed for many-cores are derived from older schemes originally designed for CPUs and multi-cores. As we will show, extra care is needed to choose an appropriate method depending on the application and sparsity pattern. However, in the case of our problem, none of the conventional methods are able to exploit the specific characteristics of our sparse matrix. We propose a “blocked stridden diagonal” format to fit our specific problem.

We’ll start by providing some characteristics about our sparse matrix in section 2. In section 3 we discuss some possible conventional formats and discuss their applicability to our problem. Next we will try to come up with a format that can exploit our problem characteristics in section 4. Finally we will conclude in section 5.

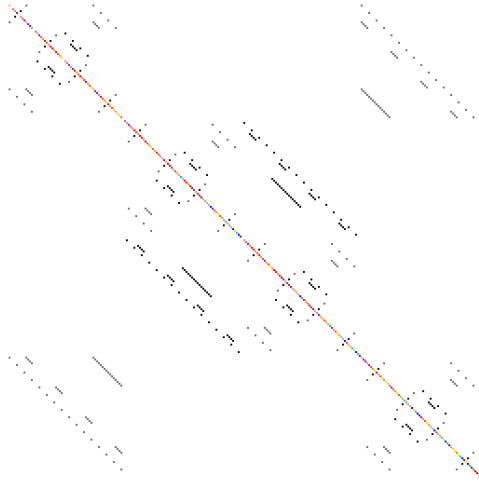


Figure 1: a 256-by-256 crop of our sparse matrix.

## 2. Sparse matrix characteristics

The sparse matrix we're interested in has a size of 1024-by-1024 with only 3574 nonzeros. Fig. 1 shows a crop of the matrix we're interested in. The image is color coded based on the values. Some interesting characteristics can be observed there. E.g. all the non-zero elements outside of the main diagonal (which are over 2/3 of all the nonzeros in this matrix) have either of two values (0.1 and -0.1), also they are all restricted to one of 40 different diagonals. The main diagonal is almost entirely nonzero. Also we should note that the matrix is symmetrical.

## 3. Conventional Sparse Matrix Formats

Sparse matrix operations in the conventional dense format are very inefficient. So, the first step for sparse operations is to use some compression format to store them. There are two different categories of sparse matrix storage formats, dynamic ones which are suitable for modifying the sparse matrix (e.g. rapid insertion and deletion of elements), and static formats where the main goal is lowering storage requirements. SpMV does not involve modification of the sparse matrix so we are only interested in static formats. Perhaps the four most commonly used sparse matrix formats are: coordinates (COO), compressed sparse Row (CSR), diagonal (DIA) and ELLPACK (ELL). DIA relies on the non-zero elements being concentrated and restricted to only a few diagonals, while ELL is most suitable with matrices that have a consistent number of nonzeros per row; it packs nonzero elements from each row into a dense array. There are also various modifications of these formats that try to reduce memory requirements and/or improve performance. For example, SELL, ESB and Hybrid formats.

In GPUs as well as Phi, it is best to access aligned and consecutive memory locations in each warp/vector using coalesced operations to increase memory efficiency. It is possible to access scattered locations from the memory; however, memory divergence results in performance drop due to slow scatter and gather operations.

Results on GPU taken from Bell and Nathan's work [2], show that DIA and ELL formats are best suited for structured and semi-structured sparsity patterns, since they both guarantee contiguous access to the matrix elements (DIA also has contiguous access to vector elements. The scalar CSR kernel generally shows poor

performance; the vector CSR shows considerable improvement, though still not competitive to other formats. The COO manages to give a relatively steady (but low) performance across a broad range of matrices making it a reliable complement in hybrid formats. The HYB format (ELL+COO) proved to have the best overall performance across all sparsity patterns. As for the Phi; ESB kernel's performance implemented by Liu et.al [3], has proven to give good results; beating both CPU's and GPU's performance.

For our application, Phi is the primary target platform. Our plan is for every Phi thread to handle one instance of the Arnoldi iteration; So, L2 utilization is crucial for our application. One approach would be to use an ELL variant format, e.g. the ELL, ESB, SELL, or HYB. Initial analysis of the sparse matrix we're interested in shows that, the rows have an average of 3.49 nonzeros with a variance of 1.94, a minimum of 0 and a maximum of 7. Hence, a direct ELL approach would require about double the needed space due to padding. However, a closer look shows that only 40 rows (out of 1024) have 7 nonzeros per row; and curiously, none of the rows has 6 nonzeros per row. This means that by using the HYB format, we could store those 40 rows in COO format while handling the rest of the rows in ELL format (with a row depth of 5). Examining SELL (with slice height of 8), on the matrix shows that it can reduce the average row-depth down to 5.21 (note that even though the memory efficiency is lower than HYB format, it could perform faster). More complex schemes like the ESB might also be considered, we expect ESB to be able to bring down memory requirements significantly lower, however at this point we're concerned about how the extra complexity would affect performance in comparison to other formats. Taking a quick look at fig. 1 shows that the matrix has some diagonal characteristics; however there are large streaks of zeros on the nonzero diagonals (except for the main diagonal). So a direct diagonal approach is not very attractive as it would require excessive zero padding. Also considering that non-zero elements outside the main diagonal amount to over two thirds of the nonzeros, a blocked hybrid DIA/COO is not a good approach either.

It is important to mention that Phi has 512kiB L2 per core. Assuming we want the four threads on phi to run the same MC chains, this would be more than enough for the entire Arnoldi iteration's variables to fit in. however, all ELL based formats suffer from memory divergence in accesses to the vectors which means we have to rely on slow scatter/gather instructions. Also, the memory requirements are too large to make any use of L1.

#### **4. Stridden Diagonal format**

Taking a closer look at the sparse matrix, you can see that the nonzero elements on any of the non-zero diagonals (except the main diagonal) follow distinct periodic. What's interesting about these patterns is that they follow strides of 1, 4, 16, 64, and 256. Looking at the big picture a fractal behavior is obvious. PBR [4] is a format designed to exploit patterns. However, PBR only accounts for periodic patterns, and is incapable of handling self-similar patterns. Also, PBR cannot exploit the fact that nonzero elements outside the main diagonal hold only two distinct values. Thus, we believe that a format specifically designed for our system will perform better

We believe it's best to decompose the sparse matrix into 3 parts, a diagonal matrix, and two structures composed of the -0.1 and +0.1 values. Handling the diagonal matrix is easy and efficient. For the two off-diagonal matrices, we only need to store the structure since value is uniform across the non-zero elements, reducing memory requirements. Due to the fractal (self repeating) behavior, we can formulate these diagonal patterns using a multi level stride format. For example on diagonal with offset -60 we have nonzeros in the following locations [71, 72, 73, 74, 87, 88, 89, 90, 103, 104, 105, 106, 119, 120, 121, 122, 327, 328, 329, 330, 343, 344, 345, 346, ...]. This can be represented with a two level stride; at the outer level we have a stride of 256, while at the inner level we have a stride of 16. Also each of the nonzero segments has a length 4. So we only need 7 values to store the

structure for this entire row; diagonal offset (-60), number of levels (3), stride values of each level (256, 16 and 1), base (71) and segment lengths (4 and 4). Using this format for all the 40 different diagonals (even without accounting for the symmetry), we would require about 1kiB. This method ensures that everything will fit on L2.

Phi has 32kiB of L1 cache. each of the input and output vectors have a size of 8kiB; furthermore, the main diagonal also has 1024 elements which corresponds to 8kiB, add to this the rest of the elements and the total memory requirements of the SpMV kernel is somewhere close to 25kiB which is less than the L1 cache. We expect that being able to take full use of L1 would increase our performance significantly. This is why we're suggesting that the threads within the same core share the same MC sample.

The stridden storage format as we discussed so far allows us to fully utilize L1 cache for the SpMV kernel; however, the kernel would still need to use slow gather/scatter instructions to and from the x and y vectors ( $y=Ax+y$ ). Taking into account that the most often stride value in our structure is 4, it might be feasible to use a skewed storage format for these vectors (as well as the main diagonal vector). We expect this to reduce the amount of necessary gather/scatter instructions significantly, further improving our performance.

## **5. Conclusion**

Sparse operations tend to have varied and individual behaviors depending on the structure and characteristics of the sparse matrix. For our MC application the more conventional formats proved to be unable to exploit the natural characteristics of our sparse matrix. We proposed a special storage format based on those features in order to reduce the memory requirements of our code to enhance our cache utilization. Furthermore, our method can enhance the memory access pattern in order to reduce slow gather/scatter operations on many-core architectures.

## **6. Acknowledgments**

The current work is funded by the NSF EPSCoR LA-SiGMA project under award #EPS-1003897.

We would also like to thank Mark Jarrell, Juana Moreno, Ka Ming Tam, Jian Tao, and Wei Feinstein.

## **7. References**

- [1] Saad, Yousef. "Analysis of some Krylov subspace approximations to the matrix exponential operator." *SIAM Journal on Numerical Analysis* 29.1 (1992): 209-228.
- [2] Bell, Nathan, and Michael Garland. Efficient sparse matrix-vector multiplication on CUDA. Vol. 2. No. 5. Nvidia Technical Report NVR-2008-004, Nvidia Corporation, 2008.
- [3] Liu, Xing, et al. "Efficient sparse matrix-vector multiplication on x86-based many-core processors." *Proceedings of the 27th international ACM conference on International conference on supercomputing*. ACM, 2013.
- [4] Belgin, Mehmet, Godmar Back, and Calvin J. Ribbens. "Pattern-based sparse matrix representation for memory-efficient SMVM kernels." *Proceedings of the 23rd international conference on Supercomputing*. ACM, 2009.

## **GeauxDock: A novel approach for ligand molecular docking using a hybrid force field**

**Y. Ding<sup>1</sup>, Y. Fang<sup>2,4</sup>, W. Feinstein<sup>3,4</sup>, D.M. Koppelman<sup>2,4</sup>, J. Moreno<sup>1,4</sup>,  
J. Ramanujam<sup>2,4</sup>, M. Brylinski<sup>3,4</sup>, M. Jarrell<sup>1,4</sup>**

<sup>1</sup>Department of Physics and Astronomy, Louisiana State University

<sup>2</sup>School of Electrical Engineering and Computer Science, Louisiana State University

<sup>3</sup>Department of Biological Sciences, Louisiana State University

<sup>4</sup>Center for Computation & Technology, Louisiana State University

**Abstract:** Conventional high-throughput screening used in drug discovery suffers from the high costs of experiments and low hit rates, therefore, virtual screening techniques have been developed to provide a faster and cheaper solution. At the core of structure-based virtual screening is molecular docking that predicts the conformation of a ligand when bound to the target protein. In this communication, we present a novel hybrid force field for ligand docking, which shows a remarkable accuracy compared with other widely used scoring functions. Furthermore, we propose a new Contact Topology Score to access the accuracy of docking approaches.

**Keywords:** ligand molecular docking, contact topology score, force field optimization

### **1. Introduction**

Computational modeling of drug binding to proteins has become an integral component of modern drug discovery pipelines<sup>1</sup>. A typical application is structure-based virtual screening, which involves a large-scale modeling of pharmacologically relevant associations between small molecules and their macromolecular targets. This approach can dramatically reduce the overall costs of discovering lead compounds by limiting the size of a screening library. At the core of virtual screening are ligand docking algorithms, which search for the global minimum of the drug-target protein conformational space.

The desire to improve state-of-the-art motivated us to develop GeauxDock, an ultra-fast ligand docking approach that uses Monte Carlo as the sampling method and features computations on graphics processing units (GPU). Combined with an effective hybrid scoring function, this new algorithm will provide accurate predictions at a high performance/cost ratio, which is a critical factor for large-scale virtual screening applications. In this communication, we focus on the details of the docking algorithm used in GeauxDock and its comparative benchmarking results.

### **2. Materials and methods**

First, we developed a Contact Topology Score (CTS) to quantify the similarity between different conformations of a ligand-protein complex. CTS uses Matthew's correlation coefficient<sup>2</sup> calculated for atomic contacts at the

ligand-protein interface. CTS ranges from -1 to 1 with the higher values indicating similar ligand-protein conformations. In contrast to a widely used root-mean-square deviation (RMSD), CTS is size-independent, therefore it can be used to compare even different ligand-protein systems.

Next, we developed a novel hybrid force field for the modeling of ligand-protein complexes that combines classical physics-based potentials with statistical and knowledge-based scoring terms. Physics-based terms include soft electrostatic and Lennard-Jones (LJ) potentials. Knowledge-based potentials are used for hydrogen bonds in the form of single Gaussian restraints, as well as for protein-ligand contacts with the parameters derived from the Protein Small Molecule Database (PSMDB). In addition to these generic knowledge-based potentials, a series of target-specific restraints derived from evolutionarily related complexes, a pocket specific potential, and a new pseudo-pharmacophore model is also incorporated. We also impose explicit harmonic restraints on family-conserved anchor substructures, which were shown to be effective in ligand docking.

The energy weight factors were optimized against an ensemble of decoy conformations. For each protein-ligand complex, a non-redundant set of decoy conformations was constructed as follows: first,  $10^5$  different conformations were created through a Monte Carlo (MC) simulation; here, we included only LJ interactions and harmonic restraints on the binding pocket center to prevent steric clashes and confine ligand conformations to the binding site. Next, pairwise CTS values were calculated for each two ligand conformations to create a  $10^5 \times 10^5$  CTS matrix. To remove redundancy, this matrix was subjected to clustering using CLUTO<sup>3</sup> resulting in 5,000 clusters; a cluster centroid was selected to represent each group. The final training dataset comprises 102,000 ligand-protein conformations constructed for 204 complexes from the Astex/CCDC set<sup>4</sup>.

The native-like recognition capability of the force field was optimized by maximizing the Z-score calculated across the training dataset. The Z-score is defined as:

$$Z - score = \frac{\bar{E}_d - \bar{E}_n}{S_n^2 + S_d^2} \quad (1)$$

where  $\bar{E}_n$  and  $\bar{E}_d$  are the mean values of energy calculated for decoy and native-like conformations, and  $S_n^2$  and  $S_d^2$  are the corresponding standard deviations. We employed an Evolution Strategies (ESs) algorithm to solve the parameter optimization problem. Specifically, the weight factors that maximize the Z-score were identified by imitating the principles of natural evolution using the *Math::Evol* package<sup>5</sup>. In order to avoid any bias, the optimization was performed 10 times starting from a random initial set of weight factors; the final weights taken as the consensus of 10 simulations.

### 3. Results and Discussion

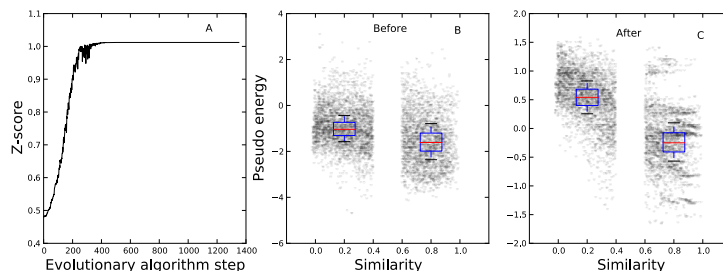


**Figure 1.** Optimization of the force field by an Evolution Strategies algorithm. (A) Z-score as a function of the evolutionary algorithm step. Distribution of energy values (B) before and (C) after the force field optimization; the similarity of 0.0-0.4 and 0.6-1.0 corresponds to decoy and native-like conformations, respectively. Boxes end at the quartiles  $Q_1$  and  $Q_3$ ; horizontal red lines are the medians.

Figure 1A shows a trajectory of Z-score recorded during one complete optimization process. The simulation converges within ~400 generations, indicating an efficient update of weight factors using the ESs algorithm. Note that all 10 simulations seeded with random initial weight factors resulted in the same weight factors, which shows that the optimized values are stable and robust. Figures 1B and 1C show the distribution of energy values calculated using the random and optimized weight factors, respectively. In Figure 1B, there is no clear separation between decoy and native-like conformations based on the energy score; however, Figure 1C shows that the optimized weight factors yield significantly lower energy for native-like conformations. It suggests that the energy calculated using the optimized weights should efficiently distinguish misdocked ligands.

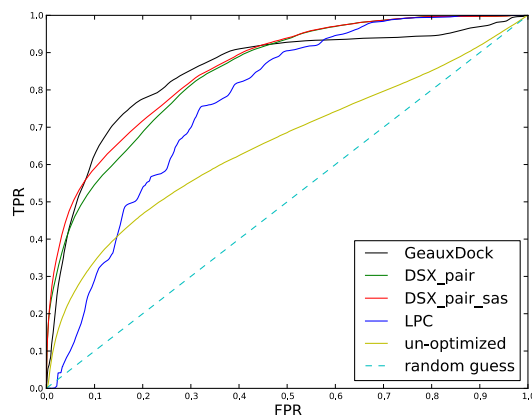


**Figure 2.** ROC plot for the recognition of native-like conformations in docking ensembles by GeauxDock compared to other scoring functions. TPR - true positive rate, FPR - false positive rate.

A strong capacity to identify native-like ligand poses among a vast number of generated configurations is pivotal to a successful docking approach. Figure 2 shows the Receiver Operating Characteristic (ROC) analysis<sup>2</sup> for the separation of native-like conformations from misdocked decoys across MC trajectories generated for the training set. Here, we compare GeauxDock to two other scoring functions: DSX<sup>6</sup> and LPC<sup>7</sup>. In general, all scoring functions identify native-like poses better than a purely random guess. The area under the curve (AUC) for the un-optimized GeauxDock force field (all weight factors set to 1.0) is 0.654; when the optimized set of weights is used, the AUC increases to 0.851. For comparison, DSX<sub>pair</sub>, DSX<sub>pair\_sas</sub> and LPC yield the AUC of 0.847, 0.858 and 0.765, respectively. Despite a slightly lower AUC, GeauxDock gives ~5% higher true positive rate than DSX<sub>pair\_sas</sub> at relatively small false positive rates of 0.1-0.2. Note that the results for DSX are in good agreement with those reported previously by Cheng *et al.*<sup>8</sup> using RMSD and different ligand-protein complexes, suggesting that our dataset is of high quality and the CTS indeed provides an effective assessment metric.

#### 4. Conclusion

We developed a novel hybrid scoring function for ligand docking that has a high capability to recognize native-like ligand-protein conformations within docking ensembles generated by Monte Carlo simulations. Moreover, we introduced Contact Topology Score as a new size-independent metric to quantify the similarity between ligand-protein conformations. Future directions include the re-optimization of the force field using a non-linear Bayesian approach to improve the accuracy of ligand docking, and the development of a new statistical framework to reliably predict binding affinities in virtual screening applications.

#### 5. Acknowledgments

This work is supported by the NSF EPSCoR LA-SiGMA project under award #EPS-1003897 and the Louisiana Board of Regents through the Board of Regents Support Fund [contract LEQSF(2012-15)-RD-A-05].

#### 6. References

- [1] B. Waszkowycz, D. E. Clark, and E. Gancia, *Wiley Interdiscip. Rev. Comput. Mol. Sci.* **1**, 229–259 (2011).
- [2] Powers, D. M. Evaluation: from precision, recall and F-measure to ROC, informedness, markedness and correlation. (2011).
- [3] Steinbach, M., Karypis, G. & Kumar, V. A comparison of document clustering techniques. in *KDD Work. text Min.* **400**, 525–526 (Boston, 2000).
- [4] Hartshorn, M. J. *et al.* Diverse, high-quality test set for the validation of protein-ligand docking performance. *J. Med. Chem.* **50**, 726–741 (2007).
- [5] Schwefel, H.-P. *Numerical optimization of computer models.* (John Wiley & Sons, Inc., 1981).
- [6] G. Neudert and G. Klebe, *J. Chem. Inf. Model.* **51**, 2731–45 (2011).
- [7] V. Sobolev, a Sorokine, J. Prilusky, E. E. Abola, and M. Edelman, *Bioinformatics* **15**, 327–32 (1999).
- [8] T. Cheng, X. Li, Y. Li, Z. Liu, and R. Wang, *J. Chem. Inf. Model.* **49**, 1079–93 (2009).

## Heterogeneous Computing Aided Material Science Research

Ye Fang<sup>1,2</sup>, Sheng Feng<sup>4</sup>, Yun Ding<sup>4</sup>  
Ka-Ming Tam<sup>1,4</sup>, Wei Feinstein<sup>3</sup>, Zhifeng Yun<sup>5</sup>  
M. Brylinski<sup>1,3</sup>, D. Koppelman<sup>1,2</sup>, J. Moreno<sup>1,4</sup>, M. Jarrell<sup>1,4</sup>, J. Ramanujam<sup>1,2</sup>

<sup>1</sup>Center for Computation and Technology, Louisiana State University

<sup>2</sup>Department of Electrical and Computer Engineering, Louisiana State University

<sup>3</sup>Department of Biological Sciences, Louisiana State University

<sup>4</sup>Department of Physics and Astronomy, Louisiana State University

<sup>5</sup>Center for Advanced Computing and Data System, University of Houston

**Abstract:** A recent trend in computational science is that the raw performance of general purpose multi-core processors is overshadowed by heterogeneous systems. The efficiency of heterogeneous systems are attributed to massive quantities of light-weight cores and multiple levels of memories, which add burdens to the programmers. This paper provides a brief introduction to our successful experience of adapting two dominant heterogeneous systems, namely, the CPU plus NVIDIA GPU, and the CPU plus MIC, for accelerating the Monte Carlo simulations in material science. We demonstrate our programming techniques for building robust, portable and high performance applications. The performance improvements from our developments have helped us collecting data in a significantly faster rate and gain new insight into scientific problems.

**Keywords:** heterogeneous computing, GPU, MIC, spin glass, molecular docking

### 1. Introduction

Simulation is one of the most important method in today's scientific discoveries and stochastic or Monte Carlo (MC) simulation plays an important role of studying the complex interacting systems. However, even with the huge success of Monte Carlo methods, many systems remain very difficult to simulate primarily due to the demand of extreme scale of computational power. To satisfy the demand of computational scientists, the computer science community has transited from homogeneous multi-core architecture to heterogeneous architecture, starting with the revolution of GPU computing<sup>1</sup> in 2007. Another successful example is MIC (Many Integrated Core Architecture)<sup>2</sup> from the traditional CPU vendor Intel. Today, heterogeneous computing has been established as a pillar in computational science and related field. According to the July 2014 list of Top500<sup>3</sup>, the top two HPC systems in the world are heterogeneous systems consisting of general-purpose multicores and accelerators. More interestingly, in term of the power efficiency that has started to become the gold standard for measuring computer systems, heterogeneous systems completely dominate the Green500<sup>4</sup> list.

A heterogeneous computer has two major components, the conventional CPUs and the accelerators. The general purpose CPUs are fast but costly resources, while light weight accelerator cost significantly less per unit (core). Though the performance of a single accelerator unit is reduced, the duplication of cheap units enables extremely efficient parallel processing on suitable workload. Therefore, the strategy of programming heterogeneous system

is to detect or construct regular parallel workload, and manage the CPU-accelerator offloading traffic. Although the heterogeneous system from different vendors share conceptual architectural ideas, the programming practice differs quite significantly. The GPU embraces CUDA or OpenCL. Both APIs provide C interface, and adopt a low level of programming model. Everything is explicit, including task identification, task mapping, data distribution, communication mapping, and synchronization. The memory hierarchy of the GPU is also exposed to the programmer with very little automatic support. While GPU programming with CUDA/OpenCL implies manual tuning, the programming model of MIC stands on the other side of the balance. Like the GPU, MIC's parallel architecture has two level. The inner level of vectorization is detected and implemented by the compiler; the outer lever is semi-automatically handled by the OpenMP run time. MIC also employs smart cache mechanisms in contrast with the GPU. Despite these implementation differences, designing efficient programs for GPU or MIC involves the laborious construction and scheduling for multiple levels of parallel workloads. MIC's automatic tools may relieve programmers from low-level implementations, but are certainly not silver bullets.

In the later sections of this paper, we initiate two case studies of programming GPU or MIC for scientific Monte Carlo Simulations. Conclusions are discussed in section 4.

## 2. Simulating Edward-Anderson Model

### 2.1 Algorithms

The Edward-Anderson (EA) model has been intensively simulated over the past few decades. Its inherent randomness and frustration lead to very long relaxation time. The algorithm is simply the single spin flip Monte Carlo Metropolis update. The system is a three-dimensional cubic lattice with a dimension of  $L$ , therefore the lattice has  $L^3$  sites. On each site, there is a +1 or -1 spin, and the spins interact with the following Hamiltonian:  $H = \sum_{\langle i,j \rangle} J_{ij} S_i S_j + \sum_i h S_i$ , where  $J_{ij}$  is a random interaction energy and  $\langle i,j \rangle$  stands for nearest neighbors. In order to help the system explore the phase space more efficiently, the parallel tempering or replica exchange method is used.

### 2.2 Implementation

The Edward-Anderson simulation program is implemented for cluster computers with NVIDIA GPUs. We expose the inherent parallelism of the algorithm to the GPU accelerator, including parallel computation on multiple sites, multiple temperature replicas and multiple disorder realizations. The memory requests are efficiently handled through memory tiling. In addition, the computation is simplified and vectorized using table look-ups and the Compact Asynchronous Multispin Coding (CAMSC). We also substitute all floating point arithmetic with integer or bit string computations while preserve the same precision. Details are discussed in our paper<sup>5</sup>.

### 2.3 Results

We verified our code with both the simple ferromagnetic Ising model and the Edwards-Anderson spin glass model. We find that the results with and without parallel tempering swap are consistent with each other. More of

our scientific research can be found at paper<sup>6</sup>. Performance wise, our code substantially faster than any other GPU implementation<sup>5</sup> and around fifty percent of the speed achieved by special-purpose FPGA implementations<sup>5</sup>. See Fig. 1 for a comparison of the performance of different implementations. Detailed references and explanations are available in our paper<sup>5</sup>.

### **3. Simulating Ligand-Protein Docking**

#### **3.1 Algorithms**

Computational modeling of drug binding to proteins has become an integral component of modern drug discovery pipelines. A typical application is structure-based virtual screening, which involves a large-scale modeling of pharmacological relevant associations between small molecules and their macromolecular targets. At the core of virtual screening are ligand docking algorithms<sup>7</sup>, which search for the global minimum of the drug-target protein conformational space.

#### **3.2 Implementation**

We maintain fairly similar codes for three platforms: multicore-CPU, MIC accelerator, NVIDIA GPU with CUDA. The code is modularized to allow switching to the suitable data structure. CPU platform use array of structure (AoS) for better cache locality, and GPU/MIC use structure of array (SoA) to better suit data parallelisms. See Fig. 2 for the SoA data layout. We model all three platforms as offload computing, which involves four steps of (1) data allocation, (2) copy-in, (3) kernel computation, and (4) copy-back. We implement these operations in a set of unified APIs for three platforms, thus allow CPU/MIC/GPU code share the common high level infrastructure. Although the kernel code have to be written separately, the clear structured two-dimensional loops of ligand-protein interactions is pleasant to handle during our manual code transformations. The compilation and linking also benefit from the modularization. By changing two flags in the sources and the makefile, the code can be compiled for any of the supported platforms.

#### **3.3 Results**

The performance evaluations are conducted on the following systems: CPU system: 6 cores 12 threads Xeon E5-2620; MIC system: 57 cores Xeon Phi 3120; GPU system: 2 GPUs of Geforce GTX 580. Our single threaded CPU code outperform the C++ prototype by 3.64 time, primarily due to hand tunings of strength reductions. The OpenMP multi-threading CPU code further improves the performance by a factor of 6.75. We consider this the full potential of homogeneous CPU systems, and set it as the reference (1.00X). When we launch the kernels on heterogeneous accelerators, we observe the speedups of 2.13, 4.63, and 8.78 on MIC, 1 GPU and 2 GPUs respectively.

#### 4. Conclusion

The parallel implementations of our two scientific simulation programs, EA model and ligand-protein docking, have shown significant performance benefit on GPU and MIC heterogeneous accelerators. To our experience, the complexity of programming heterogeneous system with explicit model (such as GPUs) can be managed via a top-down programming approach, however, with great effort on tunings. Implicit heterogeneous programming model (such as that of MIC) ease the programming interface, but still need much engineering for decent performance.

The source code of our simulation programs are publically available from our website<sup>8</sup>.

#### 5. Acknowledgments

The current work is funded by the NSF EPSCoR LA-SiGMA project under award #EPS-1003897. Portions of this research were conducted with high performance computational resources provided by Louisiana State University (<http://www.hpc.lsu.edu>). Part of this work was done on the Oakley system at the Ohio Supercomputer Center.

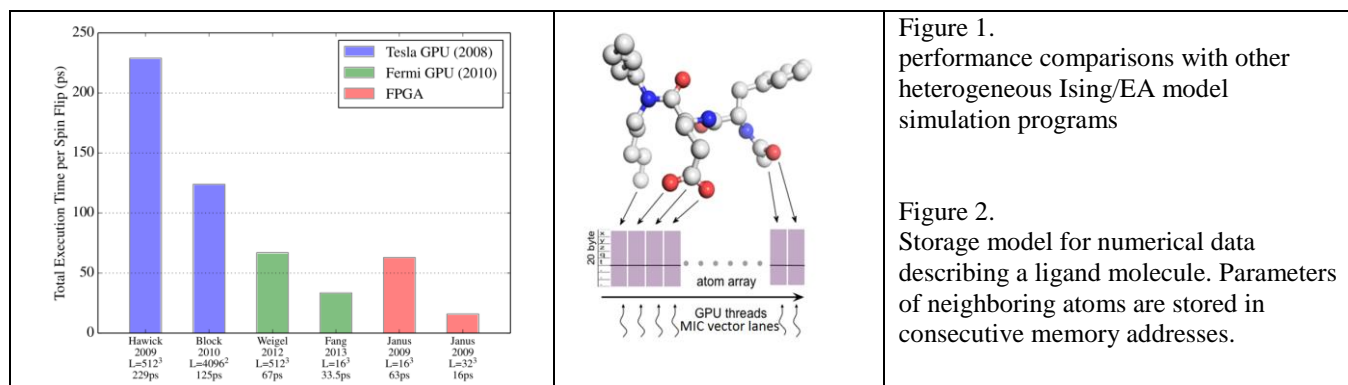


Figure 1. performance comparisons with other heterogeneous Ising/EA model simulation programs

Figure 2. Storage model for numerical data describing a ligand molecule. Parameters of neighboring atoms are stored in consecutive memory addresses.

#### 6. References

- [1] NVIDIA. NVIDIA CUDA, <http://www.nvidia.com/cuda>
- [2] Intel, Intel Xeon Phi Coprocessor, <https://software.intel.com/en-us/mic-developer>
- [3] The Top 500 list, <http://www.top500.org/>
- [4] The Green 500 list, <http://www.green500.org/lists/green201406>
- [5] Y. Fang, S. Feng, et al., Computer Physics Communications, Parallel tempering simulation of the three-dimensional Edwards–Anderson model with compact asynchronous multispin coding on GPU (2014)
- [6] S. Feng, Y. Fang, et al., ArXiv 1403.4560, Three Dimensional Edwards-Anderson Spin Glass Model in an External Field (2014)
- [7] M. Brylinski, J. Skolnick. Q-Dock(LHM): Low-resolution refinement for ligand comparative modeling. J Comput Chem. (2010)
- [8] LASiGMA Developed Packages, <http://www.institute.loni.org/lasigma/package/>

## Homogeneous Nucleation of Crystals of Ionic Liquids from the Melt

Yan Shen,<sup>1</sup> Xiaoxia He,<sup>1</sup> Erik E. Santiso,<sup>2</sup> and Francisco R. Hung<sup>1,3</sup>

<sup>1</sup>Cain Department of Chemical Engineering, Louisiana State University, Baton Rouge, LA 70803

<sup>2</sup>Department of Chemical and Biomolecular Engineering, North Carolina State University, Raleigh, NC 27695

<sup>3</sup>Center for Computation and Technology, Louisiana State University, Baton Rouge, LA 70803

**Abstract:** Crystallization of ionic liquids (ILs) is relevant for the synthesis of optically-active and magnetic nanomaterials. However, very little is understood about the actual mechanism of the crystallization of the ILs. The string method in collective variables (SMCV) and the Voronoi tessellated milestone method were used with order parameters for molecular crystals to study the homogeneous nucleation of crystals of the ILs 1,3-dimethylimidazolium chloride, [dmim<sup>+</sup>][Cl<sup>-</sup>], and 1-butyl-3-methylimidazolium chloride, [bmim<sup>+</sup>][Cl<sup>-</sup>], from their supercooled liquid phase. The transformation between the liquid and crystal structures were characterized by order parameters (OPs) for molecular crystals, which allow us to distinguish between different crystal polymorphs and liquid/amorphous phases, as well as permit the detection of local order in nm-sized regions. Properties such as minimum free energy paths for the nucleation process, free energy barriers, mechanisms of nucleation, and size of the critical nuclei for these ILs are briefly discussed.

**Keywords:** MD simulations; ionic liquids; crystallization; string method; Voronoi tessellation

### 1. Introduction

Ionic liquids (ILs) are “organic salts with a melting temperature below the boiling point of water”.<sup>1</sup> The properties of ILs are highly tunable, and ILs have various applications as green solvents for chemical synthesis, catalysis and separations, and as electrolytes for electrochemistry and photovoltaics, among others.<sup>2,3</sup> In recent work, nanomaterials based on ILs, dubbed GUMBOS (Group of Uniform Materials Based on Organic Salts)<sup>4-9</sup> have shown potential applications in fields such as biomedical, analytical, optoelectronics, photovoltaics and separations. In order to rationally design nanoGUMBOS with optimal properties, a fundamental understanding of the crystallization of ILs is needed. However, it is very difficult to study nucleation of crystals using experiments alone or conventional molecular dynamics simulations. The string method in collective variables (SMCV),<sup>10-12</sup> combined with the Voronoi tessellated milestone method<sup>12-15</sup> have proven to be a robust and efficient combination of techniques to determine the minimum free energy path (MFEP) for nucleation of crystals from supercooled liquid phases. The relative stability of different states, as well as the configurations of high-energy and metastable states along the MFEP can be identified using these methods. In this study, we applied the SMCV and the Voronoi tessellated milestone method to gain mechanistic insights into the homogeneous nucleation of ILs 1,3-dimethylimidazolium chloride ([dmim<sup>+</sup>][Cl<sup>-</sup>]) and 1-butyl-3-methylimidazolium chloride ([bmim<sup>+</sup>][Cl<sup>-</sup>]) from the liquid phase respectively. We coupled these methods with recently developed order parameters<sup>16</sup> (OPs) for molecular crystals, in order to detect local order in nm-sized regions and to characterize the structure of the different states found along the MFEP. Properties such as minimum free energy paths for the nucleation process, free energy barriers, mechanisms of nucleation, and size of the critical nuclei for these ILs are discussed.

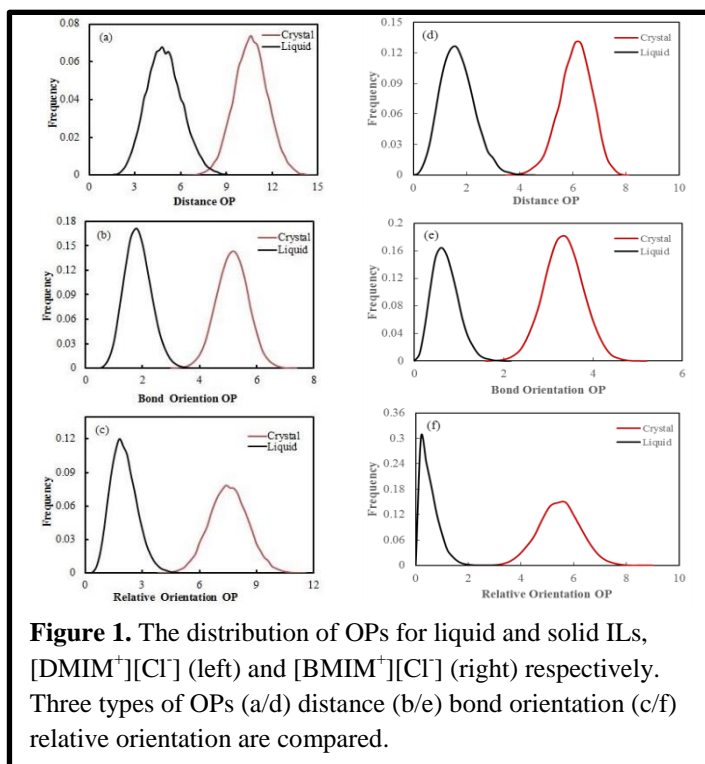
## 2. Computational details

Molecular simulations involving 1372 ion pairs of [dmim<sup>+</sup>][Cl<sup>-</sup>] bulk in the NPT ensemble were performed at 1 bar and 340 K, which is 58 K lower than its melting point. For [bmim<sup>+</sup>][Cl<sup>-</sup>], we considered 840 ion pairs at 1 bar and 273 K, 65 K lower than its bulk melting point. Our molecular simulations were performed using a modified version of the NAMD software package<sup>17</sup>, where the SMCV, Voronoi tessellated milestone method and the OPs were implemented in C++ libraries. We first generated a string of states connecting the supercooled liquid phase with its bulk crystal, by melting the crystal at a high temperature. This initial string of states was then relaxed using the SMCV,<sup>10-12</sup> where the string of states relaxes in the direction of the negative gradient of the free energy. Once the SMCV gives a converged string of states, we have an initial estimate of the minimum free energy path connecting the supercooled liquid and the crystal phases. Afterwards, we used this converged string of states to run a Markovian milestone with Voronoi tessellations,<sup>12-15</sup> to obtain the free energy along a ‘reaction coordinate’ parameterizing the transition. Central to these methods is to select a set of collective variables (OPs)<sup>16</sup> that are appropriate for describing this transition. Additional details of these methodologies can be found in the original papers. From these methods we can determine the minimum free energy paths for the nucleation process, free energy barriers, mechanisms of nucleation, and size of the critical nuclei for these ILs.

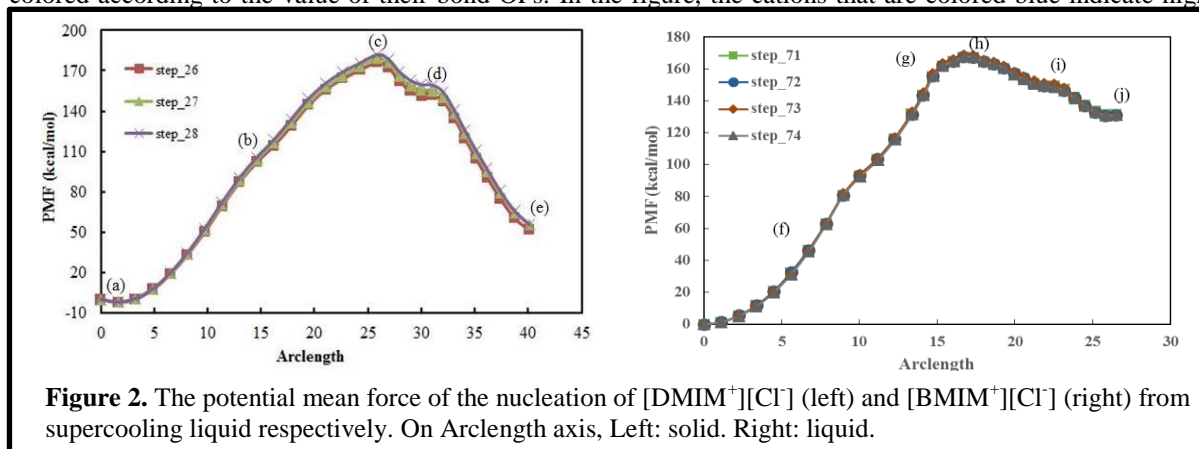
## 3. Results and Discussion

In Figure 1, we plot the distribution of local OPs of [dmim<sup>+</sup>][Cl<sup>-</sup>] and [bmim<sup>+</sup>][Cl<sup>-</sup>]. Distance, bond orientation, and relative orientation OPs values for the liquid and solid phases of these ILs are depicted. The three types of OPs give distinct peaks for the liquid and solid phases, and therefore any of those can be used to distinguish among these phases. We chose the bond orientation OPs because they have no clear overlap between the liquid and solid peaks. In Figure 2 we show the potential of mean force as a function of the arclength between the bond OPs, as determined from our converged SMCV simulations for both ILs. From the figure, we can observe that the PMF profiles for the last steps of the SMCV are very close to each other, strongly suggesting that the strings of states for each IL have converged.

The profiles also show the solid IL has lower free energy than the liquid IL, as expected because the crystalline phase is the thermodynamically-stable state at the degrees of supercooling we considered. In Figure 3



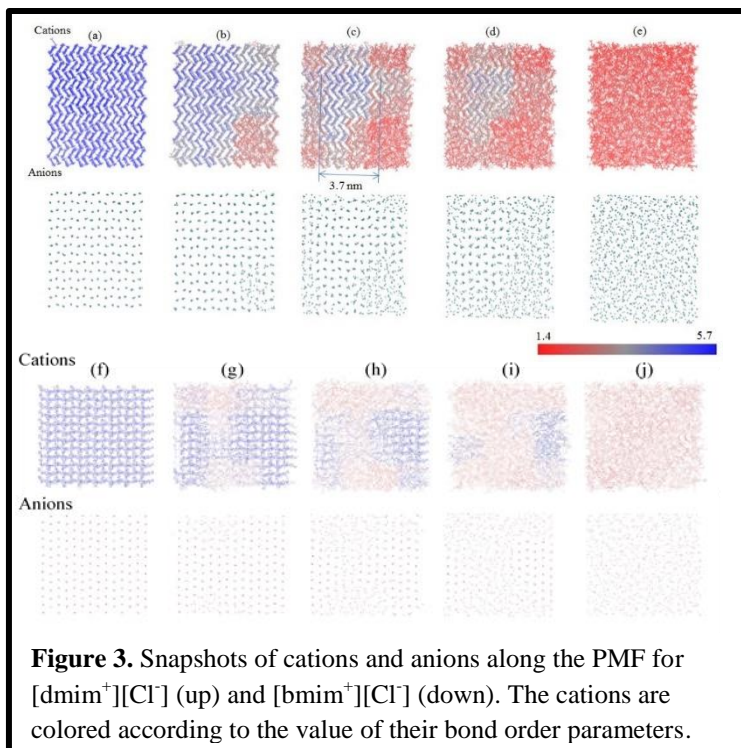
we show representative snapshots of the cations and anions in the states labeled in Figure 2. The cations are colored according to the value of their bond OPs. In the figure, the cations that are colored blue indicate highly



ordered local structure (solid-like); and the cations that are colored red indicate disordered structure (liquid-like). From this figure, we can observe the nucleation mechanism of IL from supercooling liquid. For [dmim<sup>+</sup>][Cl<sup>-</sup>], from (e) to (d), there is a small nucleus appearing from the disordered liquid. The nucleus is not stable since the system has some supersaturation at 340 K. From (d) to (c), the nucleus has grown and becomes more ordered and reaches to a critical cluster size. The critical cluster size is about 3.7 nm, which is an important parameter for many theoretical and experimental studies. From (c) to (a), the nucleus keeps growing until the whole system becomes solid. For the anions, we got consistent results as cations. Similar trends are observed for [bmim<sup>+</sup>][Cl<sup>-</sup>]. In summary, our simulations suggest two main steps for the crystallization of IL: the nucleation process, from (e) to (c), where the molecules dispersed liquid IL start to gather together into a stable nucleus and the subsequent growth of the nucleus, from (c) to (a).

#### 4. Conclusions

The present results demonstrate the utility of the SMCV and Voronoi milestone



method, which were used in combination with OPs for molecular crystals to study the homogeneous nucleation of crystals of the ILs [dmim<sup>+</sup>][Cl<sup>-</sup>] and [bmim<sup>+</sup>][Cl<sup>-</sup>], from their supercooled liquid phases in the bulk. Our preliminary results give insights about the minimum free energy path for the nucleation process, free energy barriers, mechanisms of nucleation, and size of the critical nuclei for the crystallization process of these two ILs. Our results suggest that these two ILs form a metastable state before forming a critical nucleus in the transition state at the top of the PMF curve. Calculations are still in progress to calculate the rate of nucleation of the crystal phases from their supercooled liquid states.

## 5. Acknowledgements

This work was partially supported by the NSF (EPSCoR Cooperative Agreement EPS-1003897 and CAREER Award CBET-1253075), and by the Louisiana Board of Regents. High-performance computational resources were provided by HPC at LSU (<http://www.hpc.lsu.edu>) and LONI (<http://www.loni.org>).

## 6. References

- [1] Thomas, W. P. W. *Ionic liquids in Synthesis*; Wiley-VCH: Weinheim, 2008.
- [2] Welton, T. *Chemical Reviews* **1999**, *99*, 2071.
- [3] Plechkova, N. V.; Seddon, K. R. *Chemical Society Reviews* **2008**, *37*, 123.
- [4] Tesfai, A.; El-Zahab, B.; Bwambok, D. K.; Baker, G. A.; Fakayode, S. O.; Lowry, M.; Warner, I. M. *Nano Letters* **2008**, *8*, 897.
- [5] Tesfai, A.; El-Zahab, B.; Kelley, A. T.; Li, M.; Garno, J. C.; Baker, G. A.; Warner, I. M. *ACS Nano* **2009**, *3*, 3244.
- [6] Bwambok, D. K.; El-Zahab, B.; Challa, S. K.; Li, M.; Chandler, L.; Baker, G. A.; Warner, I. M. *ACS Nano* **2009**, *3*, 3854.
- [7] Das, S.; Bwambok, D.; El-Zahab, B.; Monk, J.; de Rooy, S. L.; Challa, S.; Li, M.; Hung, F. R.; Baker, G. A.; Warner, I. M. *Langmuir* **2010**, *26*, 12867.
- [8] Dumke, J. C.; El-Zahab, B.; Challa, S.; Das, S.; Chandler, L.; Tolocka, M.; Hayes, D. J.; Warner, I. M. *Langmuir* **2010**, *26*, 15599.
- [9] de Rooy, S. L.; Li, M.; Bwambok, D. K.; El-Zahab, B.; Challa, S.; Warner, I. M. *Chirality* **2011**, *23*, 54.
- [10] Maragliano, L.; Fischer, A.; Vanden-Eijnden, E.; Ciccotti, G. *Journal of Chemical Physics* **2006**, *125*.
- [11] Maragliano, L.; Vanden-Eijnden, E. *Chemical Physics Letters* **2007**, *446*, 182.
- [12] Ovchinnikov, V.; Karplus, M.; Vanden-Eijnden, E. *The Journal of Chemical Physics* **2011**, *134*.
- [13] Vanden-Eijnden, E.; Venturoli, M. *Journal of Chemical Physics* **2009**, *130*.
- [14] Vanden-Eijnden, E.; Venturoli, M. *Journal of Chemical Physics* **2009**, *130*.
- [15] Maragliano, L.; Vanden-Eijnden, E.; Roux, B. *Journal of Chemical Theory and Computation* **2009**, *5*, 2589.
- [16] Santiso, E. E.; Trout, B. L. *Journal of Chemical Physics* **2011**, *134*.
- [17] Phillips, J. C.; Braun, R.; Wang, W.; Gumbart, J.; Tajkhorshid, E.; Villa, E.; Chipot, C.; Skeel, R. D.; Kale, L.; Schulten, K. *Journal of Computational Chemistry* **2005**, *26*, 1781.

## **In situ polymerization of Thiol-acrylate nanocomposite foam for bone defects** **Anoosha Forghani<sup>1</sup>, Leah Garber<sup>2</sup>, Cong Chen<sup>2</sup>, Ram Devireddy<sup>1</sup>, Daniel Hayes<sup>2</sup>**

<sup>1</sup> Department of Mechanical Engineering, Louisiana State University, Louisiana 70803

<sup>2</sup> Department of Biological and Agricultural Engineering, Louisiana State University Agricultural Center, Louisiana 70803

**Abstract:** The purpose of this study is to develop a novel bone substitute using in situ polymerization of thiol-acrylate or co-polymers with adipose tissue derived adult stem cells (ASCs). Specifically, Poly(ethylene glycol) diacrylate -co-trimethylolpropane tris (3-mercaptopropionate) (PEGDA -co- TMPTMP) was synthesized with 10% Hydroxy Apatite (HA) foam by an amine-catalyzed Michael addition reaction. Initial characterization studies were performed to determine the temperature profile during the exothermic reaction. These studies showed a temperature of 50°C. To prevent hyperthermic cell damage and death during the exothermic polymerization procedure, the ASCs were encapsulated in agarose gel. Characterization of the 3-D structure and the interconnectivity of pores in the polymeric foam scaffolds were performed using Micro-CT. The results showed that HA particles were distributed uniformly in the polymer matrix. Additional cell viability experiments within the polymeric scaffold were performed using Alamar blue dye exclusion method, as well as fluorescent dyes: Calcein-AM (live) and Ethidium homodimer-1 (dead) which shows viability of cells inside the samples.

**Keywords:** PEGDA, Bone Tissue Engineering, Hydrogel

### **1. Introduction**

Tissue engineering is a combination of art and science which has been gaining notable attention lately because of many advantages over conventional methods such as autografting and allografting procedures [1]. Scaffolds which are one of the most important factors in Tissue engineering, use as extracellular matrix (ECM) to stimulate cell adhesion, proliferate, and differentiate [2]. An ideal scaffold should have good mechanical properties, porous structure, adequate pore size and interconnectivity to be used in tissue engineering.[3] Considerable interest has been drawn in in situ generated implants because of eliminating the need for making ex-vivo scaffolds and the ability to fill defects with critical size and shape. In situ injectable polymers also show better adhesion to the native bone [4]. Thiol Acrylate based polymers are potential candidates as in situ forming scaffolds for bone tissue engineering applications. Photopolymerization is a method to form injectable thiol acrylate polymer which provides the ability of spatial and temporal control of polymerization and is followed by chain growth reaction. Despite the advantages of this method, it has some drawbacks which the most important one could be residual initiator molecules which are toxic and they could damage cells. The alternative method is Michael addition reaction in which general reaction proceeds by a step-growth polymerization of the thiol and acrylate groups, eliminates the danger of unreacted monomers and radicals compared to photopolymerization.[5,6]. The purpose of this study is to develop a novel bone substitute using in situ polymerization of thiol-acrylate 10% HA composite polymers with (hASC) cells using Michael addition reaction. Initial characterization studies were performed to determine the temperature profile during the exothermic reaction. These studies showed a temperature of 50°C. To prevent hyperthermic cell damage and death during the exothermic polymerization procedure, we encapsulated the ASCs in agarose gel. The results showed viability of cells inside the foam.

## **2. Materials and Methods**

### **Preparation of thiol-acrylate composites**

All chemicals were used as received. Trimethylolpropane tris(3-mercaptopropionate) (TMPTMP) were obtained from Aldrich. Diethylamine (DEA) was obtained with 99% purity from AGROS organics, and Poly(ethylene glycol) diacrylate (PEGDA) was obtained from Alfa Aesar. The foam was prepared by adding TMPTMP in a 1:1 molar functionality to 16.1% PETA/DEA stock solution after 12h of mixing. Then HA (10% wt/wt) was added to the PETA-co TMPTMP solution and then this mixture was poured into a 250 mL pressurized spray canister using 7 g-compressed nitrous oxide as a gaseous porogen. The foamed composite copolymer was sprayed out of the canister into laboratory weigh boats and got fully polymerized after 5-7 minutes.

### **Preparation of the composite polymer with cells**

Agarose (UltraPure Agarose, invitrogen) 2% by weight was dissolved in standard stromal media solution. Approximately,  $2 \times 10^6$  ASCs were then combined with 100 ml of agarose-stromal media solution at 37°C for 3 to 4 mins, resulting in ASCs encapsulated with agarose. Approximately, 40 grams of the ASCs encapsulated in the agarose gel were combined with approximately 60 grams of the extruded polymeric foam to complete the polymerization process

### **hASC isolation and culture**

Liposuction aspirates from subcutaneous adipose tissue were obtained from three donors. All tissues were obtained with informed consent under a clinical protocol reviewed and approved by the Institutional Review Board at the Pennington Biomedical Research Center. Isolation of hASC was performed as described elsewhere.<sup>13</sup> The initial passage of the primary cell culture was referred to as “Passage 0” (p0). The cells were passaged after trypsinization and plated at a density of 5000 cells/cm<sup>2</sup> (“Passage 1”) for expansion on T125 flasks to attain 80%. Passage 2 of each individual was used for cell viability test after acute exposure to the scaffold medium.

### **In vitro hASC viability on scaffolds**

#### **Live/Dead stain**

Live/dead staining (Cell viability®, Invitrogen – using a Leica DM RXA2 Deconvolution System) were performed at to assess hASC attachment and viability inside the scaffolds.

#### **Alamar Blue assay**

AlamarBlue® metabolic activity assay was used to study the cytotoxicity of the ASCs in PEGDA(700)-co TMPTMP polymer. The metabolic activity of cells were measured at an excitation wavelength of 530 nm and an emission wavelength of 595 nm using a fluorescence plate reader

#### **Micro-CT analysis**

Characterization of the 3-D structure and the interconnectivity of pores in the polymeric foam scaffolds were performed using Micro-CT (SkyScan 1074).

#### **SEM analysis**

SEM analysis performed using field emission scanning electron microscopy (Quanta3D FEG, FEI Company, USA). Pore sizes were measured using ImageJ.

### 3. Results

Live/dead stain assay shows live cells as green dots and dead cells as red dots. Fig 1 shows viability of cells trapped inside the agarose gel as positive control. Existing green dots shows that cells are still alive after mixing with agarose gel. Viability of cells inside the polymer has been shown in Fig2. Again these pictures show that left acrylate monomers didn't kill cells and live cells could be observed inside the samples. The results of Alamarblue assay after 22, 23 and 24 hrs is demonstrated in Fig3. As one can see this figure confirms metabolic activity inside the foam samples.

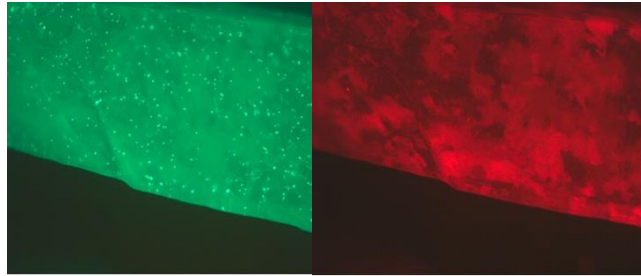


Fig1. Fluorescent Microscope images of positive control after running live/dead stain assay

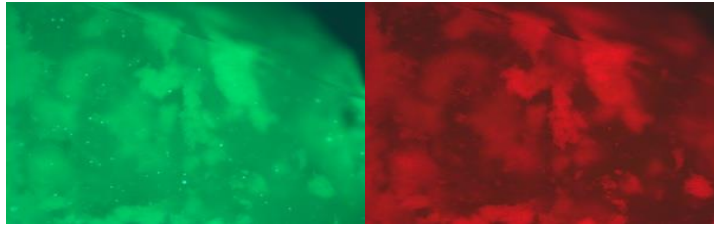


Fig2. Fluorescent Microscope images of composite samples after running live/dead stain assay

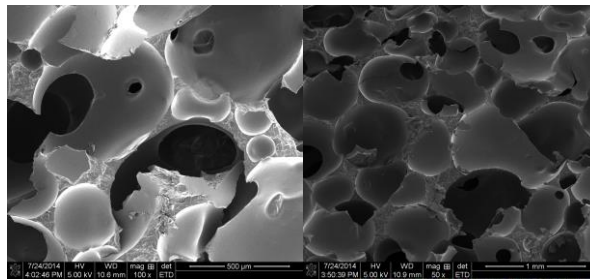


Fig4 SEM image of PEGDA –TMPTMP 10%HA composite in two different magnifications

SEM images of the samples show that foams have porous structure with pore sizes ranging from 500 to 600  $\mu\text{m}$  (fig4). This fig also shows interconnectivity of pores inside the foam.

Micro CT analysis of the samples demonstrates interconnectivity of the samples. fig 5 shows ceramic and polymeric phase of the sample. As can be seen in this picture HA are distributed in the polymeric phase which is shown with blue color.

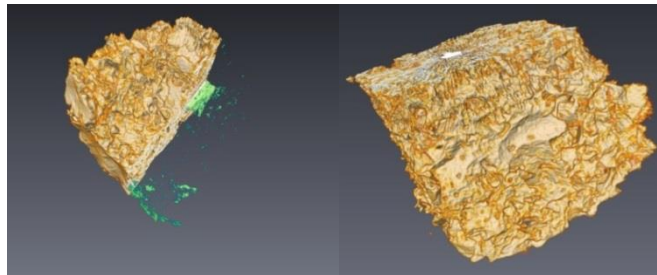


Fig5. Micro- CT images of the samples

#### 4. Conclusion

PEGDA-TMPTMP copolymer is a novel material which could be used as biomaterial. This polymer can be obtained by Michael addition reaction method which gives less unreacted toxic monomers. Thus this polymerization could be a good candidate for in situ polymerization. The effect of high temperature of the exothermic reaction during polymerization on the stem cells could be controlled by trapping cells inside agarose gel particles. These agarose particles then were mixed with PEGDA-TMPTMP foam. Viability assay showed existing live cells during polymerization. The foam which was made with gas foaming method also showed interconnectivity and porous structure with pore size ranging from 500-600 $\mu$ m.

#### 5. Future Works

- Interconnectivity of scaffolds should be measured quantitatively.
- Additional experiments are also being performed to assess the differentiation potential of the gel encapsulated ASCs into osteoblasts

#### 6. Acknowledgments

The current work is funded by the NSF EPSCoR LA-SiGMA project under award #EPS-1003897.

#### 7. References

- [1] Meinel, Lorenz, et al. "Bone Tissue Engineering Using Human Mesenchymal Stem Cells: Effects Of Scaffold Material And Medium Flow." *Annals Of Biomedical Engineering* 32.1 (n.d.): 112-122. Biological Abstracts 1969 - Present. Web. 30 Apr. 2014
- [2] Lee, Hyeongjin, et al. "Physical And Bioactive Properties Of Multi-Layered PCL/Silica Composite Scaffolds For Bone Tissue Regeneration." *Chemical Engineering Journal* (2014): ScienceDirect. Web. 30 Apr. 2014.
- [3] Vilma Conceição, Costa, et al. "Preparation Of Hybrid Biomaterials For Bone Tissue Engineering." *Materials Research I* (2007): 21. Directory of Open Access Journals. Web. 30 Apr. 2014.
- [4] Martins, AM, et al. "Responsive And In Situ-Forming Chitosan Scaffolds For Bone Tissue Engineering Applications: An Overview Of The Last Decade." *Journal Of Materials Chemistry* 20.9 (2010): 1638-1645. Science Citation Index. Web. 30 Apr. 2014.
- [5] Rydholm, Amber E., Christopher N. Bowman, and Kristi S. Anseth. "Degradable Thiol-Acrylate Photopolymers: Polymerization And Degradation Behavior Of An In Situ Forming Biomaterial." *Biomaterials* 26.22 (n.d.): 4495-4506. Biological Abstracts 1969 - Present. Web. 30 Apr. 2014.

## Investigation of the Molecular Mechanism of Tin Sulfide (SnS<sub>2</sub>) as a Lithium Ion Battery Electrode Material

Kathleen E. Moyer,<sup>1\*</sup> Ayorinde Hassan,<sup>2</sup> Collin Wick,<sup>2</sup> and B. Ramu Ramachandran<sup>2</sup>

<sup>1</sup>Stevens Institute of Technology, Hoboken, NJ 07030

<sup>2</sup>Louisiana Tech University, Ruston, LA 71272

**Abstract:** We report the results of a first principles computational study of the first discharge curve for lithium sorption in nanoparticle and crystalline systems of (SnS<sub>2</sub>)<sub>n</sub>. These were found to have qualitative agreement with experimental discharge curves for SnS<sub>2</sub> nanosheets. The analysis of the computational results suggests that nanoparticle and crystalline systems behave in a similar manner at high Li content. Both conversion and alloying mechanisms were examined, and are shown to be thermodynamically feasible (i.e., yield positive voltages) leading to large capacities.

**Keywords:** Li-ion batteries, metal sulfides, anode materials, voltages

### 1. Introduction

Li alloy forming elements such as Sn, Sb, In & Al have attracted significant interest as prospective anode materials for lithium ion batteries (LIBs) due to fact that they have a larger theoretical capacity than graphite, the most popular commercial anode material at present.<sup>1</sup> Specifically, SnO<sub>2</sub> has been investigated as a potential anode material with very high capacities, but drastic volume change of up to 300% upon lithiation causes it to rapidly lose its structural integrity during cycling.<sup>2</sup> While SnO<sub>2</sub> has been studied extensively, SnS<sub>2</sub> has been examined to a much lesser extent. Details of the mechanisms by which SnS<sub>2</sub> functions is unclear, although a combination of conversion and alloying mechanisms have been proposed.<sup>3,4</sup> The conversion mechanism entails the formation of separate Sn metal phases and Li<sub>2</sub>S, while the alloying mechanism is the formation of Li<sub>x</sub>Sn alloys. A detailed understanding of the structural and electronic properties of these materials, and their sorption mechanism could offer strategies to mitigate the large volume change of Sn-based anode materials. We present a two-prong approach at understanding the lithiation of SnS<sub>2</sub> by looking at the sorption of lithium in both nanoparticles and bulk crystalline structure.

### 2. Computational methodologies

The structure, energetics, and electronic properties of the (SnS<sub>2</sub>)<sub>8</sub> nanoparticle system were determined using the PBE GGA functional<sup>5</sup> in conjunction with double numerical polarization (DNP) basis set, as implemented in the DMol3 program in the Materials Studio 6.0 suite. In addition to assessing the voltage profile, we examined the structural changes due to Li sorption by performing a bond analysis.

---

\* KEM was supported by the 2014 LA-SiGMA REU program.

Sorption in crystalline SnS<sub>2</sub> system was investigated using a “working cell” of stoichiometric (SnS<sub>2</sub>)<sub>8</sub> constructed from the optimized SnS<sub>2</sub> unit cell. Li atoms were added to the working cell in succession, and optimized by relaxing the ionic coordinates, cell shape, and volume of the structures with the conjugate gradient method. Periodic DFT calculations were carried out using the Vienna Ab initio Simulation Package (VASP)<sup>6</sup> using the PBE form of the GGA<sup>5</sup> with the projector augmented wave pseudopotential method.<sup>7,8</sup> The reference energy for a single Li atom was determined from the Li unit cell energy.

### 3. Results and Discussions

The various lithiated forms of nanoparticle Sn<sub>8</sub>O<sub>16</sub> structures are presented in Figure 1.

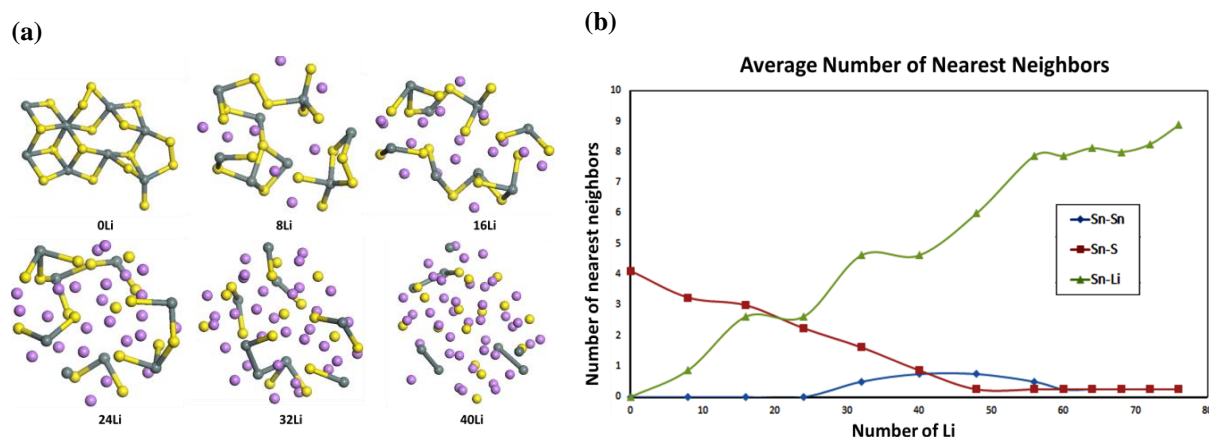


**Figure 1:** (a) Optimized structures of (SnS<sub>2</sub>)<sub>8</sub> nanoparticles with varying numbers of added lithiums. Sn atoms are greenish-gray, Sulfur yellow, and lithium atoms purple. (b) The average number of nearest neighbors of the indicated type for Sn atoms.

As clearly seen from Figure 1a, the addition of successive lithium atoms disrupts the bonding pattern between the Sn and S atoms in the nanoparticle. This behavior is confirmed by the bond analysis shown in Figure 1b, showing the number of sulfur neighbors of Sn atoms decreases as Li content increases. Additionally, the average number of Li atoms in the vicinity of Sn steadily increases. Analysis of the bond lengths and network of the atoms in the nanoparticle reveals that as more Li are added, the average Sn-Sn and Sn-S bond distances increase while Li-Sn distance decreases. These observations show that even at moderate Li concentrations, Li can be found near Sn atoms, indicating a degree of alloying.

The optimized structures of the bulk SnS<sub>2</sub> systems investigated are shown in Figure 2a, and the corresponding voltages and capacities as a function of the number of Li added are presented in Figure 2b. The voltages associated with the addition of lithium atoms were calculated according to the Nernst relationship for voltage calculation relative to a Li|Li<sup>+</sup> standard, but with the assumption that the free energy,  $\Delta G^\circ \approx \Delta E$ :<sup>9</sup>

$$\mathcal{E}(V) = \frac{[E^\circ_{(RuO_2)_n} + E^\circ_{Li} - E^\circ_{(RuO_2)_n Li}] Jmol^{-1}}{xF(Cmol^{-1})} \quad (1)$$

where  $E$ 's are the optimized energies,  $F$  is the Faraday constant,  $x$  is the number of moles of electrons involved.

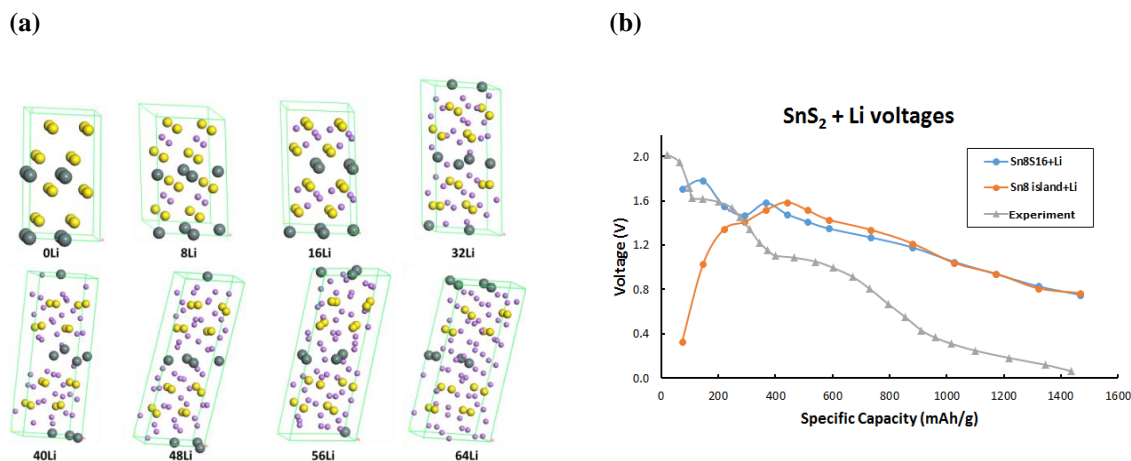


**Figure 2:** (a) Optimized structures of crystalline  $(\text{SnS}_2)_8$  with varying numbers of lithiums. (b) First discharge curves for crystalline  $\text{SnS}_2$  against  $\text{Li}|\text{Li}^+$ . The blue line represents voltages for the systems shown in Figure 2a. The orange line represents voltages calculated for a  $(\text{Sn})_8$  island in  $\text{Li}_2\text{S}$ , and the gray line is the experimental voltage from Ref [3]. Sn atoms are greenish-gray, Sulfur yellow, and lithium atoms purple.

Figure 2a suggests that the addition of Li up to a 1:1 Li:Sn ratio causes no noticeable distortion to the crystal structure, consistent with an intercalation mechanism. At moderate Li concentrations—between a 1:1 and ~3:1 Li:Sn ratio—the Li atoms reside between the S layers, indicating conversion to  $\text{Li}_2\text{S}$ . The Li was found to migrate into the sulfur layers during optimization even if they were placed in the Sn layer initially. At higher Li content—4:1 Li:Sn ratio and beyond—the added Li enter into the layer of Sn, and Sn-Li alloying becomes noticeable. This behavior is similar to that observed in the case of  $\text{SnS}_2$  nanoparticles. The voltages obtained from the crystalline material simulation (blue curve in Figure 2b) qualitatively agree with the experimentally observed voltages for the first discharge cycle of  $\text{SnS}_2$ -nanosheet, but overpredict the voltages for moderate to high capacities.<sup>3</sup>

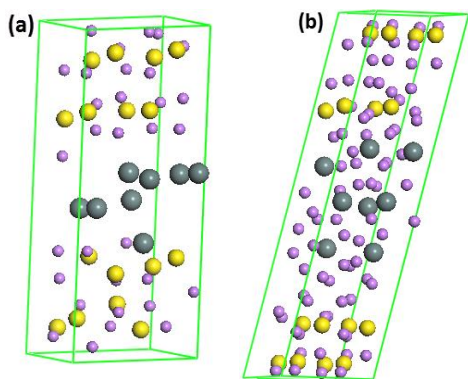


**Figure 3:** (a) The model  $\text{Sn}_8$  island surrounded by 32 Li and 16 S atoms. (b) The  $\text{Sn}_8$  island system with 80 total Li.

To examine the thermodynamics of full conversion leading to Sn islands in  $\text{Li}_2\text{S}$ , we modeled a  $\text{Sn}_8$  island in a  $\text{Li}_2\text{S}$  matrix by considering a working cell with the composition  $\text{Li}_{32}\text{Sn}_8\text{S}_{16}$ , as shown in Figure 3a. Starting from this structure, Li were removed sequentially to reach 0 Li, and added sequentially to reach 80 Li (Figure 3b). The resulting voltages are shown as the orange line in Figure 2b. Adding Li to the  $\text{Li}_{32}\text{Sn}_8\text{S}_{16}$  system results in Sn-Li alloying as the lithium atoms penetrate the  $\text{Sn}_8$  island instead of migrating to the sulfide layer. The quantitative similarity of the voltages from the two types of structures (blue and orange curves in Figure 2b) at high Li content supports the conclusion that alloying is

taking place in both cases. Interestingly, when Li is removed to reach Li:Sn ratios smaller than 4:1, the remaining lithium atoms rearrange and revert back to the S layer. The thermodynamics of Li removal, leading to the de-alloying of Sn at high Li content and the oxidation of Sn to SnS<sub>2</sub> at low Li content, are being investigated at present.

Three molecular mechanisms have been identified in the operation of metal oxide and sulfide electrode materials used as LIB anodes: intercalation into the crystal lattice, conversion leading to metal + lithium oxide or sulfide, and alloying of Li with the metal. In the case of RuO<sub>2</sub>, experimental evidence exists for full conversion leading to Ru islands in Li<sub>2</sub>O matrix (see paper by Hassan et al. in this volume). However, in sharp contrast to SnS<sub>2</sub>, the Ru islands remain tightly bound as Li content increases, leading to the deposition of the added Li in the interface between the Ru and the Li<sub>2</sub>O phases. In the case of SnS<sub>2</sub>, Li sorption follows the intercalation mechanism up to a 1:1 Li:Sn ratio, switches to conversion at moderate lithium content, and alloying takes over as the concentration of lithium increases. The voltages resulting from both the Sn<sub>8</sub>S<sub>16</sub> and the Sn<sub>8</sub> island systems converge to the same values at high Li content, showing that alloying is ultimately the mechanism of these materials at high lithium content regardless of intermediate phases.

The nanoparticle as well as the crystalline systems of SnS<sub>2</sub> show very similar behavior, including large volume changes with Li sorption. The nanoparticle Sn<sub>8</sub>S<sub>16</sub> system goes from 573 Å<sup>3</sup> at 0 Li to 1812 Å<sup>3</sup> at a 9:1 Li:Sn ratio, an expansion of 216%, while the crystalline Sn<sub>8</sub>S<sub>16</sub> system goes from 613 Å<sup>3</sup> at 0 Li to 1792 Å<sup>3</sup> at a 10:1 Li:Sn ratio, an expansion of 192%.

#### 4. Summary

We have studied the mechanism of Li sorption into both nanoparticle and bulk SnS<sub>2</sub> systems. Our methodology yields a qualitative agreement between experimental and theoretical discharge curves. Both nanoparticle and crystalline systems behave in similar ways at high Li content. This study shows that intercalation at low lithium content, conversion at moderate lithium levels, and alloying at high lithium concentration occurs during the sorption of Li in SnS<sub>2</sub> systems.

#### 5. Acknowledgments

This work is funded by the National Science Foundation under awards EPS-1003897 and EPS-1006891 with additional support from the Louisiana Board of Regents.

#### 6. References

- [1] Huggins, R. A. *Solid State Ionics* **1998**, 113–115, 57.
- [2] Larcher, D.; Beattie, S.; Morcrette, M.; Edstrom, K.; Jumas, J.-C.; Tarascon, J.-M. *Journal of Materials Chemistry* **2007**, 17, 3759.
- [3] Kim, T.-J.; Kim, C.; Son, D.; Choi, M.; Park, B. *J. Power Sources* **2007**, 167, 529.
- [4] Momma, T.; Shiraiishi, N.; Yoshizawa, A.; Osaka, T.; Gedanken, A.; Zhu, J.; Sominski, L. *J. Power Sources* **2001**, 97–98, 198.
- [5] Perdew, J. P.; Burke, K.; Ernzerhof, M. *Physical Review Letters* **1996**, 77, 3865.
- [6] Kresse, G.; Furthmüller, J. *Phys. Rev. B* **1996**, 54, 11169.
- [7] Blöchl, P. E. *Phys. Rev. B* **1994**, 50, 17953.
- [8] Kresse, G.; Joubert, D. *Phys. Rev. B* **1999**, 59, 1758.
- [9] Bard, A. J.; Faulkner, L. R. *Electrochemical Methods: Fundamentals and Applications.*; John Wiley & Sons: New York, 1980.

## Ionic liquids in the ordered mesoporous carbon CMK-5: Pore-pore correlation effects

Xiaoxia He,<sup>1</sup> Joshua Monk,<sup>2</sup> Ramesh Singh,<sup>3</sup> Lauren Lorio,<sup>4</sup> and Francisco R. Hung<sup>1,5</sup>

<sup>1</sup> Cain Department of Chemical Engineering, Louisiana State University, Baton Rouge, LA 70803

<sup>2</sup> Thermal Protection Materials Branch, NASA Ames Research Center, Moffett Field, CA 94035

<sup>3</sup> Department of Chemical and Biomolecular Engineering, University of Notre Dame, Notre Dame, IN 46556

<sup>4</sup> Baton Rouge Community College, Baton Rouge, LA 70806

<sup>5</sup> Center for Computation and Technology, Louisiana State University, Baton Rouge, LA 70803

**Abstract:** We performed classical molecular dynamics simulations of the ionic liquid (IL) [emim<sup>+</sup>][NTf<sub>2</sub><sup>-</sup>] confined in a model CMK-5 material, which consists of amorphous carbon nanopipes (ACNPs) arranged in a hexagonal array, and thus the ILs can adsorb inside and outside the ACNPs. We compare our findings against the behavior of the same ILs inside a model CMK-3 material (which is similar to CMK-5, but is formed by amorphous carbon nanorods). Our results indicate that the presence of IL adsorbed in the outer surface of an uncharged carbon nanopipe in CMK-5 can significantly affect the dynamics and the density of an IL adsorbed inside the carbon nanopipe, and vice versa. ILs adsorbed outside of the nanopipes in CMK-5 (i.e., with IL also adsorbed inside the nanopipes) have faster dynamics and remain closer to the carbon surfaces when compared to the same ILs adsorbed on CMK-3 materials. Overall, our results suggest the presence of pore-pore correlation effects between the IL inside and outside the ACNPs in CMK-5, which can impact the structure and dynamics of the confined ILs in these systems.

**Keywords:** ionic liquid; mesoporous carbon; molecular dynamics simulations

### 1. Introduction

Ionic liquids (ILs) are molten salts typically composed of bulky organic cations with smaller organic or inorganic anions, and usually are in liquid phase near room temperatures. ILs have attracted interest for applications as alternative electrolytes in electrochemical double layer capacitors (EDLCs)<sup>1, 2</sup> and dye-sensitized solar cells (DSSCs).<sup>3-5</sup> In EDLCs and DSSCs, the IL is in contact with a nanoporous electrode, and therefore a fundamental understanding of the properties of ILs inside nm-sized pores is crucial to rationally design EDLCs and DSSCs, and significantly advance those technologies. Molecular simulations are well positioned to make important contributions towards achieving a fundamental understanding of the interfacial properties of ILs near nanoporous electrodes. Previous simulation studies from our group<sup>6-10</sup> focused on understanding the structure and dynamics of ILs inside carbons with pores of different geometries. The main objective of this work is to study in detail the structural and dynamical properties of the IL 1-ethyl-3-methylimidazolium bis-(trifluoromethanesulfonyl) imide, [emim<sup>+</sup>][NTf<sub>2</sub><sup>-</sup>] confined inside an uncharged model of the ordered mesoporous carbon CMK-5. This material consists of hexagonally-packed nanopipes made of amorphous carbon. The amorphous carbon nanopipes (ACNPs) have uniform diameters and exhibit thin carbon walls with corrugations and curvature, and thus the nanopores in CMK-5 are interconnected in a regular way. We compare our results with those obtained for the same IL inside CMK-3 materials (which are made of amorphous carbon nanorods, ACNRs) of similar pore size. Our results suggest the presence of pore-pore correlation effects between the IL

inside and outside the ACNPs in CMK-5, which can impact the structure and dynamics of the confined ILs in these systems. The ordered mesoporous carbons CMK-3 and CMK-5 have been used in EDLCs in previous experimental studies<sup>11, 12</sup>. Furthermore, because of their uniform structure, these ordered mesoporous carbons are well suited for fundamental studies aimed at understanding the effects of variables such as pore size, pore geometry, surface roughness and pore interconnectivity on the properties of confined ILs.

### 2. Computational Details

Classical molecular dynamic (MD) simulations in the *NVT* ensemble were performed using the GROMACS MD package.<sup>13</sup> [emim<sup>+</sup>][NTf<sub>2</sub><sup>-</sup>] was initially placed in a lattice outside the CMK-3 and CMK-5 materials, and after energy-minimized using steepest descent schemes, we melted and annealed the IL to a temperature of 333 K. Afterwards, we allowed the IL to diffuse into the porous materials at the desired temperature. After the nanopore was totally filled with IL another 10 ns MD simulation run was performed to sample properties of interest. Periodic boundary conditions were applied in all directions. The carbons atoms in the both models were kept in fixed positions throughout our simulations. The rest of our simulation details are exactly the same as used in our previous studies.<sup>9, 10</sup> Representative snapshots of our simulations are depicted in Figure 1.

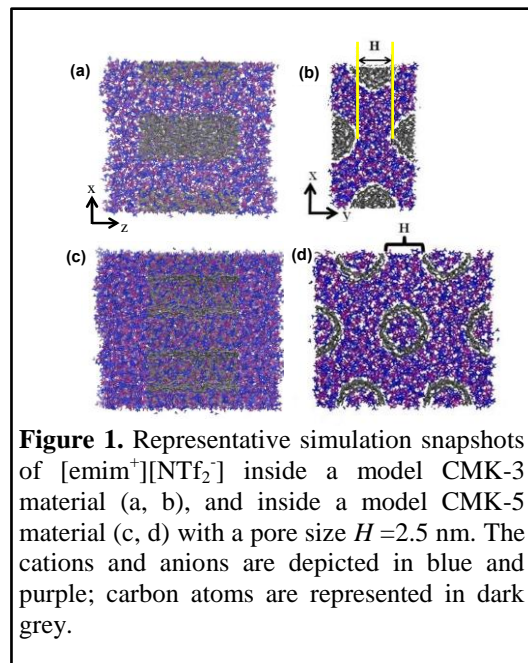


**Figure 1.** Representative simulation snapshots of [emim<sup>+</sup>][NTf<sub>2</sub><sup>-</sup>] inside a model CMK-3 material (a, b), and inside a model CMK-5 material (c, d) with a pore size  $H=2.5$  nm. The cations and anions are depicted in blue and purple; carbon atoms are represented in dark grey.

### 3. Results and Discussion

In Figure 2a and 2b we show density maps of [emim<sup>+</sup>] in the CMK-5 and CMK-3 model materials with  $H = 2.5$  nm, and in Figures 2c and 2d we show mass density profiles (in g/cm<sup>3</sup>) of [emim<sup>+</sup>] and [NTf<sub>2</sub><sup>-</sup>] in the same model materials (in CMK-5, the IL can be adsorbed inside and outside the ACNPs). Formation of distinct

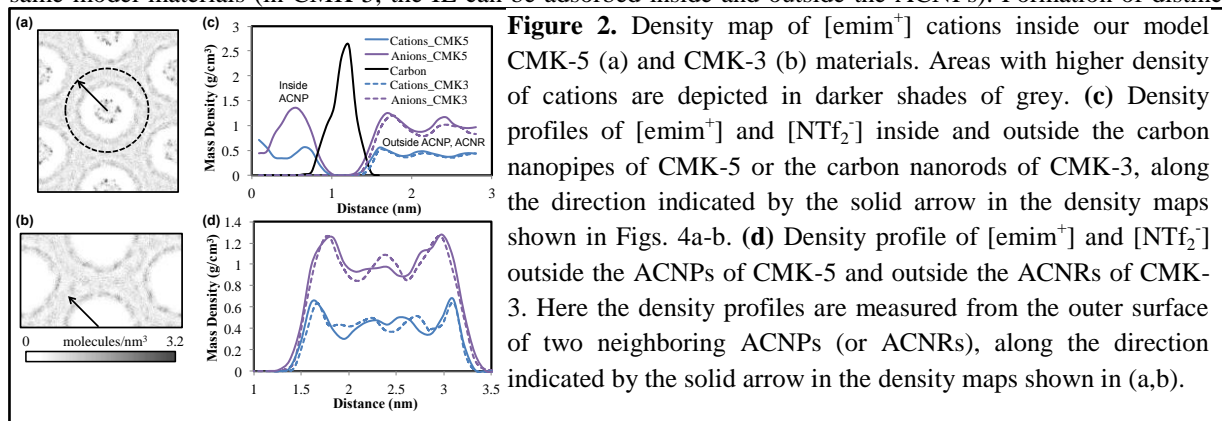


**Figure 2.** Density map of [emim<sup>+</sup>] cations inside our model CMK-5 (a) and CMK-3 (b) materials. Areas with higher density of cations are depicted in darker shades of grey. (c) Density profiles of [emim<sup>+</sup>] and [NTf<sub>2</sub><sup>-</sup>] inside and outside the carbon nanopipes of CMK-5 or the carbon nanorods of CMK-3, along the direction indicated by the solid arrow in the density maps shown in Figs. 4a-b. (d) Density profile of [emim<sup>+</sup>] and [NTf<sub>2</sub><sup>-</sup>] outside the ACNPs of CMK-5 and outside the ACNRs of CMK-3. Here the density profiles are measured from the outer surface of two neighboring ACNPs (or ACNRs), along the direction indicated by the solid arrow in the density maps shown in (a,b).

layers of cations and anions are noticeable in all these results. The ions near the carbon surface have higher density than the ions far away from the carbon surface. No significant differences are observed in the density profiles of the ions outside of the ACNPs in CMK-5 and outside of the ACNRs in CMK-3 (Fig. 2d). The number of layers observed in each of these systems naturally depends on the pore size  $H$  and on the size of the ions.

We further investigated the dynamics of  $[\text{emim}^+][\text{NTf}_2^-]$  inside our CMK-3 and CMK-5 model materials, by monitoring the axial component of the mean squared displacements (MSDs) of the ions as a function of time; these results are depicted in Figure 3. In these results we have split the ions into different layers based on their density profiles (Fig. 2), in order to study the local dynamical behaviors of the ions. As expected, all ions confined inside uncharged porous materials exhibit dynamics that are slower than those observed in a similar bulk system. The ions closer to the carbon surfaces in CMK-3 move slower than the ions that are further away from these surfaces. Similarly, the ions closer to the outer surface of the ACNPs of CMK-5 move slower than the ions that are further away from these surfaces. Interestingly, the results shown in Fig. 3 indicate that the ions in the surface layer and middle regions in CMK-5 exhibit slightly faster dynamics than their counterparts in the same layers/regions in CMK-3, keeping in mind that the pore size of CMK-5 and CMK-3 are the same. This observation might be due to several reasons. Small differences in the density of the IL outside the CMK-5 nanopipes and the CMK-3 nanorods might be a possibility; although the density profiles of the IL outside the CMK-5 nanopipes and the CMK-3 nanorods (Fig. 2) are very similar, the ions outside of the ACNPs in CMK-5 seem to be closer to the carbon surfaces than the ions in CMK-3. A second reason might be correlation effects between the IL that is inside the CMK-5 nanopipes and the IL that is adsorbed on the outer surface of the ACNPs. The presence of IL inside the ACNPs can accelerate the dynamics of the IL outside of the ACNPs in CMK-5, with respect to those observed for the same ILs in CMK-3 materials. The IL adsorbed outside of the ACNPs in CMK-5 experiences long-range electrostatic interactions

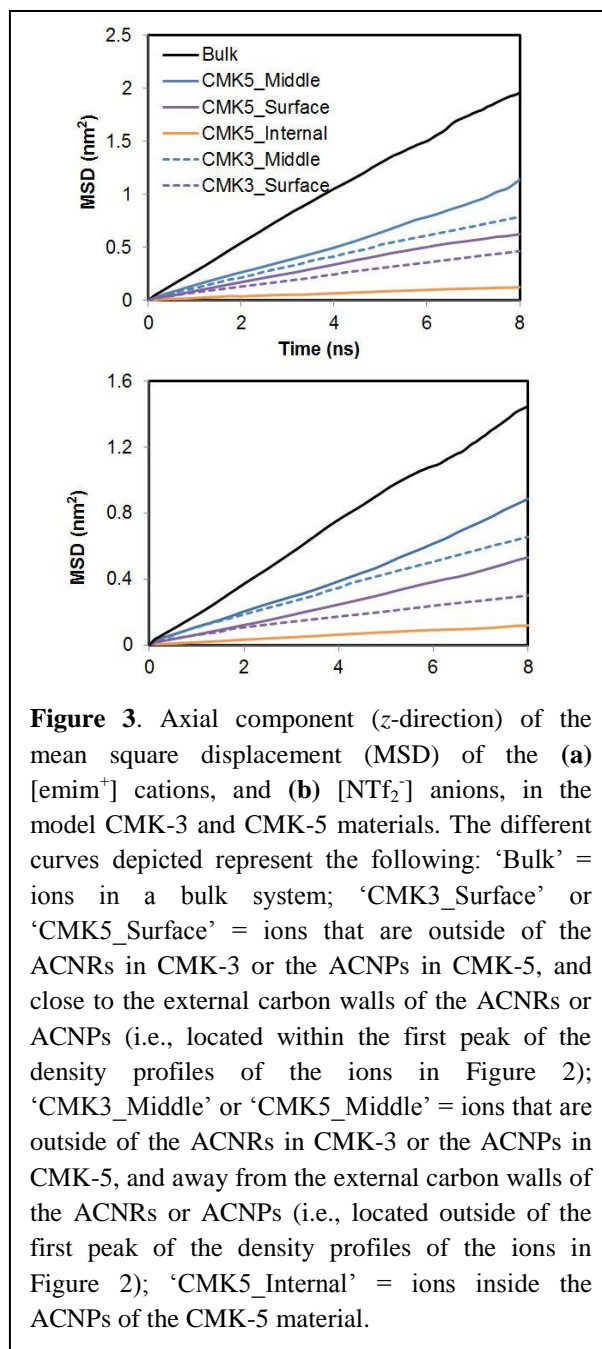


**Figure 3.** Axial component ( $z$ -direction) of the mean square displacement (MSD) of the (a)  $[\text{emim}^+]$  cations, and (b)  $[\text{NTf}_2^-]$  anions, in the model CMK-3 and CMK-5 materials. The different curves depicted represent the following: ‘Bulk’ = ions in a bulk system; ‘CMK3\_Surface’ or ‘CMK5\_Surface’ = ions that are outside of the ACNRs in CMK-3 or the ACNPs in CMK-5, and close to the external carbon walls of the ACNRs or ACNPs (i.e., located within the first peak of the density profiles of the ions in Figure 2); ‘CMK3\_Middle’ or ‘CMK5\_Middle’ = ions that are outside of the ACNRs in CMK-3 or the ACNPs in CMK-5, and away from the external carbon walls of the ACNRs or ACNPs (i.e., located outside of the first peak of the density profiles of the ions in Figure 2); ‘CMK5\_Internal’ = ions inside the ACNPs of the CMK-5 material.

with the ions inside the ACNPs, in addition to the interactions with the thin carbon walls of the ACNPs; in contrast, the IL adsorbed in CMK-3 materials only interacts with the carbon atoms of the ACNRs. The figure also indicates that the ions inside the ACNPs of CMK-5 have the slowest dynamics, mainly because of the small value of the average internal diameter of the ANCPs (~1.5 nm), which subject the ions to a very large degree of confinement.

#### 4. Concluding Remarks

Classical molecular dynamics (MD) simulations were conducted to study the structure and dynamics of the ionic liquid [emim<sup>+</sup>][NTf<sub>2</sub><sup>-</sup>] confined inside a model CMK-3 and CMK-5 material. Our results indicate that the presence of IL adsorbed in the outer surface of an uncharged carbon nanope can affect significantly the dynamics and the density of an IL adsorbed inside the carbon nanope, and vice versa. For both models, layering behavior was observed; the dynamics of the IL are dependent on their distance from the carbon surface. Our results show the molecules have faster dynamics when they are adsorbed outside of the ACNPs in CMK-5 than when they are in CMK-3 materials of the same pore size. This observation suggests that IL adsorbed inside of the ACNPs can affect the dynamics of the IL outside the ACNPs. Overall, our results suggest the presence of pore-pore correlation effects between the IL inside and outside the ACNPs in CMK-5. Interactions between molecules located in neighboring pores can act in a cooperative way and are known to induce important changes in the behavior of several nonpolar and polar fluids inside nanopores.<sup>14-16</sup> Pore-pore correlation effects might play an important role in determining the macroscopic properties of the electrical double layer; these effects deserve further investigation in follow-up studies.

#### Acknowledgements

This work was partially supported by the NSF (EPSCoR Cooperative Agreement EPS-1003897 and CAREER Award CBET-1253075), and by the Louisiana Board of Regents. High-performance computational resources were provided by HPC at LSU (<http://www.hpc.lsu.edu>) and LONI (<http://www.loni.org>).

#### References

- [1] M. Armand, F. Endres, D. R. MacFarlane, H. Ohno and B. Scrosati, *Nat. Mater.* **8** (8), 621-629 (2009).
- [2] C. Largeot, C. Portet, J. Chmiola, P. L. Taberna, Y. Gogotsi and P. Simon, *Journal of the American Chemical Society* **130** (9), 2730-2731 (2008).
- [3] A. Hagfeldt, G. Boschloo, L. Sun, L. Kloo and H. Pettersson, *Chemical Reviews* **110** (11), 6595-6663 (2010).
- [4] Y. Cao, J. Zhang, Y. Bai, R. Li, S. M. Zakeeruddin, M. Graetzel and P. Wang, *The Journal of Physical Chemistry C* **112** (35), 13775-13781 (2008).
- [5] P. V. Kamat, *Accounts Chem. Res.* **45** (11), 1906-1915 (2012).
- [6] R. Singh, J. Monk and F. R. Hung, *J. Phys. Chem. C* **114**, 15478-15485 (2010).
- [7] R. Singh, J. Monk and F. R. Hung, *J. Phys. Chem. C* **115** (33), 16544-16554 (2011).
- [8] J. Monk, R. Singh and F. R. Hung, *J. Phys. Chem. C* **115** (7), 3034-3042 (2011).
- [9] N. N. Rajput, J. Monk, R. Singh and F. R. Hung, *The Journal of Physical Chemistry C* **116** (8), 5169-5181 (2012).
- [10] N. N. Rajput, J. Monk and F. R. Hung, *J. Phys. Chem. C* **116** (27), 14504-14513 (2012).
- [11] S. H. Joo, S. J. Choi, I. Oh, J. Kwak, Z. Liu, O. Terasaki and R. Ryoo, *Nature* **412** (6843), 169-172 (2001).
- [12] A. B. Fuertes, F. Pico and J. M. Rojo, *J. Power Sources* **133** (2), 329-336 (2004).
- [13] B. Hess, C. Kutzner, D. van der Spoel and E. Lindahl, *Journal of Chemical Theory and Computation* **4**(3),435-447(2008).
- [14] B. K. Peterson, K. E. Gubbins, G. S. Heffelfinger, U. M. B. Marconi and F. Vanswol, *Journal of Chemical Physics* **88** (10), 6487-6500 (1988).
- [15] G. Menzl, J. Koefinger and C. Dellago, *Phys. Rev. Lett.* **109** (2), 020602 (2012).
- [16] R. Radhakrishnan and K. E. Gubbins, *Physical review letters* **79** (15), 2847 (1997).

## Lithiation mechanism of RuO<sub>2</sub>, and its potential use as Lithium-Ion Battery Anode Material

Ayorinde Hassan,<sup>1</sup> Ramu Ramachandran,<sup>1</sup> Collin Wick,<sup>1</sup> Anantharamulu Navulla<sup>2</sup> and Lamartine Meda<sup>2</sup>

<sup>1</sup>Louisiana Tech University, Ruston, LA 71270

<sup>2</sup>Xavier University of Louisiana, New Orleans, LA 7012

**Abstract:** First principles computational studies were used to understand the molecular mechanism of lithium sorption into crystalline bulk RuO<sub>2</sub>. The calculated discharge curves for lithium in RuO<sub>2</sub> lattice showed qualitative agreement with experimental results for RuO<sub>2</sub> nanoplates. Our molecular level analysis showed that an intercalation mechanism was exclusively operational until a 1:1 Li:Ru ratio, followed by a conversion mechanism into Ru metal and Li<sub>2</sub>O. Furthermore, in agreement with experiment, calculations also predict superstoichiometric capacity of RuO<sub>2</sub>, i.e. more than a 4:1 Li:Ru ratio, which can be largely explained by the nature of the material. Computations confirm that the extra capacity can be explained without invoking electrolyte or solvent electrolyte interface effects.

**Keywords:** Li-ion batteries, metal oxide, anode materials, voltages

### 1. Introduction

Lithium-ion batteries (LIBs) have attracted intense academic and industrial interest in recent years because they provide higher energy density compared to other types of secondary (rechargeable) batteries. There is intense interest to develop electrode materials that exceed the capacity of currently available LIBs, which exploit the intercalation mechanisms of cobalt oxide as cathode and graphite anodes. While this combination is clearly stable, operating exclusively by intercalation severely limits their capacity. Specifically, the currently used anode material, graphite, can only topotactically host up to 1 lithium per 6 carbon atoms,<sup>1,2</sup> which translates to a theoretical capacity of 372 mAh g<sup>-1</sup>. Transition metal oxides have been shown to accommodate a higher density of lithium atoms, and therefore provide much higher energy density.<sup>3</sup> RuO<sub>2</sub> has good thermal and chemical stability, and low resistivity,<sup>4-6</sup> and can therefore be a good potential candidate for a Li-ion electrode. A recent experimental work by Balaya et al.,<sup>7</sup> reported a high capacity of 1130 mAh g<sup>-1</sup> for RuO<sub>2</sub> nanoparticles as an anode material in the first discharge. However, a high degree of capacity loss was observed in subsequent charging/discharging cycles.

The Meda group recently fabricated crystalline RuO<sub>2</sub> nanoplates of varying thicknesses deposited on stainless steel using chemical vapor deposition, and found a similar high capacity, but improved cyclability over previous work. We have embarked on computational studies of these materials and their lithiation process to gain insight into the mechanisms at work in these electrodes.

## 2. Computational methodologies

All calculations reported were done using the Vienna Ab initio Simulation Package (VASP),<sup>8</sup> which is a plane wave Density Functional Theory (DFT) package widely used in computational materials science. The exchange-correlation energy was determined using the Perdew-Burke-Ernzerhof (PBE)<sup>9</sup> form of the generalized gradient approximation (GGA) in conjunction with the projector augmented wave (PAW) method.<sup>10,11</sup> The minimum ground state energies of structures considered were found by relaxing the ionic coordinates, cell shape, and volume of the structures with the conjugate gradient method. Unit cells of RuO<sub>2</sub> and metallic Li were optimized first with appropriate energy cut-offs and the first Brillouin zone sampling with appropriate Monkhorst-Pack<sup>12</sup> k-point meshes. A “working cell” of (RuO<sub>2</sub>)<sub>8</sub> was constructed from the optimized RuO<sub>2</sub> unit cell such that the (*a*,*b*) plane of the working cell coincided with the (110) crystal plane. To computationally study the experimentally observed result of conversion reactions in RuO<sub>2</sub>, we also constructed a cell containing an island of 8 ruthenium atoms surrounded by a sea of Li<sub>2</sub>O. The reference energy for a single Li atom was determined from the Li unit cell energy, in keeping with standard practice.

## 3. Results and Discussions

The RuO<sub>2</sub> working cell and its various lithiated forms with increasing numbers of intercalated lithium atoms were optimized, allowing the full relaxation of geometry, lattice volume, and shape. The optimized structures are presented in Figure 1, along with the associated voltage profile.

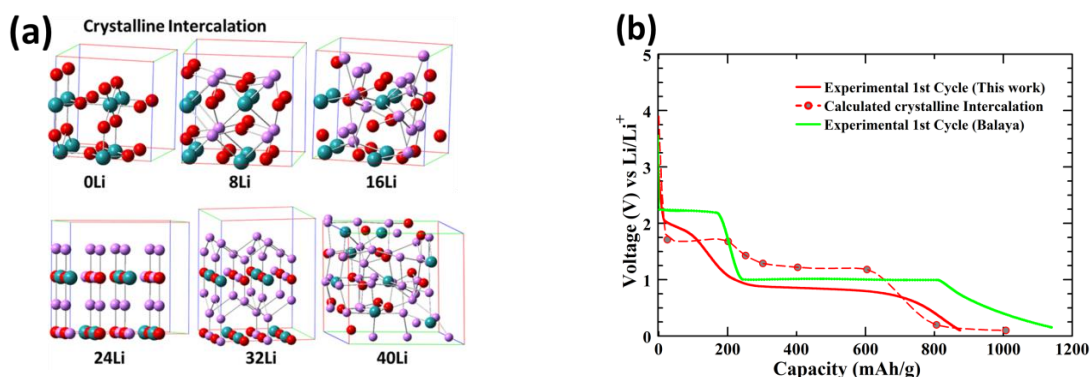


**Figure 1:** (a) Optimized structures of (RuO<sub>2</sub>)<sub>8</sub> with varying numbers of intercalated lithiums. Ru atoms are dark green (teal), oxygen red, and lithium atoms purple. (b) Experimental 1<sup>st</sup> discharge curve for 850 nm RuO<sub>2</sub> nanoplates (solid red line) from Meda et al. [to be published; this work], and the calculated voltage profile for the first discharge (this work). The curves are interpolations through the computed points which are shown as symbols. The experimental 1<sup>st</sup> discharge from Balaya et al. (solid green line; see ref.7).

It is evident from the top row of Figure 1 that the first 8 Li added (reaching Li:Ru ratio of 1:1) are intercalated into the RuO<sub>2</sub> lattice with minimal distortion to the crystal. Increasing the Li:Ru ratio to 2:1 causes significant distortion of the crystal structure. The working cell become severely disordered when Li content reaches 5:1 Li:Ru ratio (40Li), and the corresponding voltage drops to about 0.1 V. Removing lithium from this highly disordered state *does not result in the crystal regaining its original rutile structure* in our calculations.

The voltages associated with the addition of lithium atoms were calculated according to the Nernst relationship for voltage calculation relative to a  $\text{Li}|\text{Li}^+$  standard, but with the assumption that the free energy,  $\Delta G^\circ \approx \Delta E$ .<sup>13</sup>

$$\mathcal{E}(V) = \frac{[E^\circ_{(\text{RuO}_2)_n} + E^\circ_{\text{Li}} - E^\circ_{(\text{RuO}_2)_n\text{Li}}] \text{Jmol}^{-1}}{xF(\text{Cmol}^{-1})} \quad (1)$$

where  $E$ 's are the optimized energies,  $F$  is the Faraday constant,  $x$  is the number of moles of electrons involved.

The voltage and capacity of the metal oxide as a function of the number of Li added is presented in Figure 1b. Note that the “reactant”  $(\text{RuO}_2)_8$  for the first discharge is the rutile structure on the top row left of Figure 1a while for subsequent discharges, it is a more disordered  $\text{RuO}_2$  phase, which resulted from the sequential removal of 40 Li atoms from the bottom right structure shown in Figure 1a. The experimental and calculated discharge curves are qualitatively similar, and there is almost quantitative agreement between the voltages. The first discharge curve shows multiple voltage plateaus that are also similar to those published by Balaya et al.<sup>7</sup>

The first plateau in the first discharge curve near 2.0 V is interpreted as intercalation of Li into the original rutile lattice. The constant voltage (plateau) as increasing amounts of Li are added up to 8Li shows that the incoming Li are occupying energetically equivalent and favorable sites. The drop in voltage beyond this point is indicative that intercalation of additional Li is less favorable. The voltage plateau at ~1.0 V has been a subject of much debate. It has been suggested to be due to an intermediate  $\text{Li}_x\text{RuO}_2$  phase ( $x=1.2$ ) and conversion of  $\text{RuO}_2$  into  $\text{Ru}^0$  in a matrix of  $\text{Li}_2\text{O}$ .<sup>14-16</sup> Experimental evidence for the latter was recently obtained through high-resolution TEM images,<sup>17</sup> as seen in Figure 2a. Figure 2b shows a periodically replicated image of the  $\text{Ru}_8$  island system mentioned above, which was used to study the thermodynamics of the conversion reaction, leading to the voltage profile shown in Figure 2c.

Judging from Figure 2c, beyond the 1:1 ratio, conversion is thermodynamically more favorable than intercalation. It should be pointed out that around 12Li for our working cell, these two mechanisms have about the same thermodynamic favorability. In fact, earlier experiments have observed Ru,  $\text{RuO}_2$ , and  $\text{Li}_2\text{O}$  around this point.<sup>16</sup>

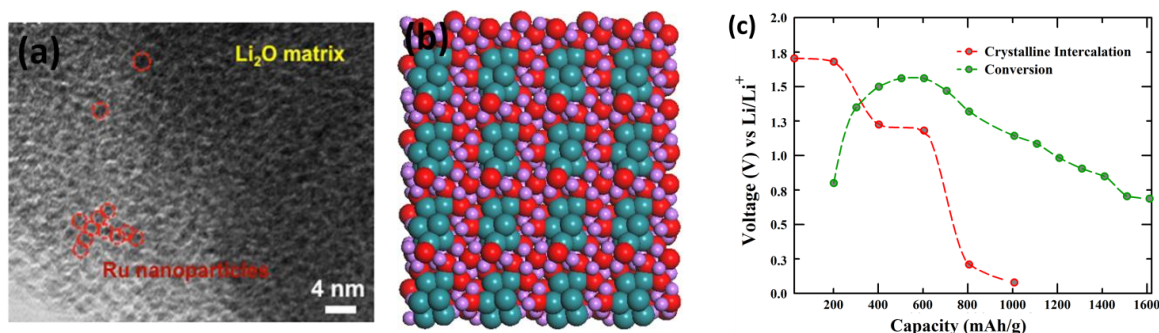


**Figure 2:** (a) HRTEM image of Ru nanoparticles and  $\text{Li}_2\text{O}$  [from ref.17], (b) 3D image of optimized structures of Ru island in  $\text{Li}_2\text{O}$ . Ru atoms are dark green (teal), oxygen red, and lithium atoms purple, (c) Calculated voltage profile for the intercalation of Li into  $\text{RuO}_2$ , and conversion reaction of Ru nanoparticles in  $\text{Li}_2\text{O}$  matrix.

Based on Li NMR experiments, “interfacial storage” has been offered as a possible mechanism to account for the ‘super-stoichiometric’ capacity of RuO<sub>2</sub> beyond a 4:1 Li:Ru ratio.<sup>14,15</sup> However, these experiments have not been able to shed light on the precise nature of the interface, although the most likely candidate was suspected to be the solvent-electrolyte interface.<sup>18</sup> Our calculations suggest that Li storage in the interface between the Ru islands and the Li<sub>2</sub>O matrix is likely to play a significant role in this extra capacity. Even at approximately 10:1 Li:Ru ratio, the calculated voltage is about 0.80 V, suggesting that accommodation of even more Li may be thermodynamically favorable. Due to the fact that there is no electrolyte present in this work, our calculations also find that the extra capacity can be explained without invoking the solvent electrolyte interface formation.

#### 4. Summary

This work presents results of experimentally motivated computational investigations on the molecular mechanism of Li sorption into RuO<sub>2</sub> when the latter is used as a lithium ion battery anode material. Our methodology has yielded semi-quantitative agreement between the experimental and theoretical first discharge curves, and permitted a detailed investigation of the mechanisms operational in this electrode material. This study shows that extra capacity of RuO<sub>2</sub> material can be attributed to conversion followed by interfacial storage within the electrode material itself. Thus, the extra capacity can be explained without considering the effect of the electrolyte.

#### 5. Acknowledgments

This work is funded by the National Science Foundation under awards EPS-1003897 and EPS-1006891 with additional support from the Louisiana Board of Regents.

#### 6. References

- [1] Armand, M.; Tarascon, J. M. *Nature* **2008**, *451*, 652.
- [2] Wu, Y. P.; Rahm, E.; Holze, R. *J. Power Sources* **2003**, *114*, 228.
- [3] Poizot, P.; Laruelle, S.; Grugeon, S.; Dupont, L.; Tarascon, J. M. *Nature* **2000**, *407*, 496.
- [4] Zheng, J. P.; Cygan, P. J.; Jow, T. R. *J. Electrochem. Soc.* **1995**, *142*, 2699.
- [5] Krusin-Elbaum, L.; Wittmer, M.; Yee, D. S. *Appl. Phys. Lett.* **1987**, *50*, 1879.
- [6] Soudan, P.; Gaudet, J.; Guay, D.; Bélanger, D.; Schulz, R. *Chem.Mater.* **2002**, *14*, 1210.
- [7] Balaya, P.; Li, H.; Kienle, L.; Maier, J. *Adv. Funct. Mater.* **2003**, *13*, 621.
- [8] Kresse, G.; Furthmüller, J. *Phys. Rev. B* **1996**, *54*, 11169.
- [9] Perdew, J. P.; Burke, K.; Ernzerhof, M. *Physical Review Letters* **1996**, *77*, 3865.
- [10] Blöchl, P. E. *Phys. Rev. B* **1994**, *50*, 17953.
- [11] Kresse, G.; Joubert, D. *Phys. Rev. B* **1999**, *59*, 1758.
- [12] Monkhorst, H. J.; Pack, J. D. *Phys. Rev. B* **1976**, *13*, 5188.
- [13] Bard, A. J.; Faulkner, L. R. *Electrochemical Methods: Fundamentals and Applications.*; John Wiley & Sons: New York, 1980.
- [14] Jamnik, J.; Maier, J. *Phys. Chem. Chem. Phys.* **2003**, *5*, 5215.
- [15] Bekaert, E.; Balaya, P.; Murugavel, S.; Maier, J.; Ménétrier, M. *Chem. Mater.* **2009**, *21*, 856.
- [16] Delmer, O.; Balaya, P.; Kienle, L.; Maier, J. *Adv. Mater.* **2008**, *20*, 501.
- [17] Gregorczyk, K. E.; Liu, Y.; Sullivan, J. P.; Rubloff, G. W. *ACS Nano* **2013**, *7*, 6354.
- [18] Laruelle, S.; Grugeon, S.; Poizot, P.; Dollé, M.; Dupont, L.; Tarascon, J.-M. *J. Electrochem. Soc.* **2002**, *149*, A627.

## Magnetic Structure of Metamagnetic Fe<sub>3</sub>Ga<sub>4</sub>

Yan Wu<sup>1</sup>, Huibo Cao<sup>2</sup>, A. Karki<sup>1</sup>, J. C. Prestigiacomo<sup>1</sup>, B. Fulfer<sup>3</sup>, R. Jin<sup>1</sup>, Julia Chan<sup>4</sup> and J. F. DiTusa<sup>1</sup>

<sup>1</sup>Department of Physics and Astronomy, Louisiana State University, Baton Rouge, LA 70803

<sup>2</sup>Quantum Condensed Matter Division, Oak Ridge National Laboratory, Oak Ridge, TN 37831

<sup>3</sup>Department of Chemistry, Louisiana State University, Baton Rouge, LA 70803

<sup>4</sup>Department of Chemistry, The University of Texas at Dallas, Richardson, TX 75080

**Abstract:** The metallic magnet Fe<sub>3</sub>Ga<sub>4</sub> displays several magnetic transitions below 700 K including a transition from the ferromagnetic (FM) ground state to an undetermined antiferromagnetic-like (AFM) state at 68 K. In addition, the metamagnetic transition, a transition from the AFM to FM state with the application of magnetic field, is unusual in that the critical field increases with temperature. In order to determine the structure of the AFM state and to explore this unusual transition we have performed extensive single crystal neutron diffraction investigations. We have confirmed a FM ordering both below 68 K and between 370 and 420 K as well as discovering that the AFM state is incommensurate, having a spin-density wave-like structure with a wavevector of  $0.27c^*$ . Our refinement of the diffraction data indicates a small non-coplanar moment which we believe to be the cause of our previously discovered topological Hall Effect.

**Keywords:** neutron diffraction, order parameter, reflection plane, in-equivalent

### 1. Introduction

As a metallic material with base-centered monoclinic crystal structure ( $C12/m1$ ), Fe<sub>3</sub>Ga<sub>4</sub> has attracted attention because of its interesting magnetic and charge transport properties<sup>1-6</sup>. The 4 in-equivalent Fe sites in this low symmetry crystal structure provide multiple magnetic moments and a variety of nearest neighbor distances along with the more itinerant electrons that result in a close competition between two magnetic states. The result is a series of complex magnetic transitions that occur over a wide temperature range<sup>1-5, 7, 8</sup>. This rich magnetic behavior has previously only been investigated in polycrystalline samples<sup>1, 4, 8</sup> which established the framework of the magnetic phase diagram<sup>9</sup>. However, many questions about the nature of the magnetic states and the competitions between them that result in such a complex magnetic phase diagram remain unresolved. Previous attempts to determine the magnetic order in this compound via polycrystalline neutron diffraction measurements<sup>3</sup> were inconclusive.

To explore the magnetic states of this system and to establish the relationships between the various magnetic states accessed by varying temperature, field, and pressure, we have carried out extensive neutron diffraction measurements on large single crystal of Fe<sub>3</sub>Ga<sub>4</sub> grown via optical furnace techniques. These measurements have allowed us to confirm a FM ordering both below 68 K and between 370 and 420 K and to establish the magnetic structure of the intermediate phase that lies between the regions of FM ordering. Our measurements show that this phase consists of an incommensurate spin-density wave- (SDW) like structure with a wavevector of  $q=0.27 c^*$  and having a small non-coplanar magnetic moment.

## 2. Experimental Details

Single crystals of  $\text{Fe}_3\text{Ga}_4$  samples as large as 80 mg were grown successfully with high purity (0.99999) Fe powders and (0.99999) gallium pieces employing optical furnace techniques. The resulting crystals were sealed in quartz tubes under vacuum and annealed at 550 °C for 48 hours to remove any residual stress. The quality and structure of the crystals was confirmed with single crystalline X-ray diffraction and magnetic measurements carried out in a SQUID magnetometer revealed behavior indistinguishable from previously grown vapor transport crystals.

The neutron diffraction investigation was performed using the 4-circle diffractometer at HB-3A of Oak Ridge National Laboratory. Data was collected using a neutron wavelength of  $1.536 \text{ \AA}$  over a temperature range from 4.5 to 450 K. A large region of reciprocal space was scanned in both the FM (at 5 K) and AFM (at 100 K) states allowing a full refinement of the data to determine the magnetic structures. In addition, we established the magnetic phase diagram by scanning the temperature dependence of the  $\langle 111 \rangle$  and  $\langle 201 \rangle$  Bragg peaks over the entire temperature range. The magnetic structure of the AFM state was determined to be incommensurate and its temperature dependence was measured by closely following the  $\langle 2,0,0.7 \rangle$  reflection as a function of temperature at zero and in a 0.5 T magnetic field. Determination of both the nuclear and magnetic structures was performed using the FULLPROF program suite<sup>10</sup>.

## 3. Results and Analysis

In Fig. 1 the magnetic susceptibility,  $\chi$ , measured in a field of 1 kOe is displayed along with the scattering intensity from the  $\langle 111 \rangle$  and  $\langle 201 \rangle$  Magnetic Bragg reflections after subtraction of a background contribution from the nuclear peak. From Fig.1, it is clear that the low temperature state is FM and that there is a first order transition to a AFM-like state at 68 K. In addition, our neutron diffraction data confirm that there is also a region of FM ordering between 370 and 420 K. At temperatures between 68 and 370 K we have discovered sharp reflections at  $\langle h,k,0.29 \rangle$  and the symmetry related  $\langle h,k,0.71 \rangle$  positions indicating an incommensurate AFM state exists at temperatures between these FM regions. In Fig. 2 we demonstrate the temperature dependent scattering at the  $\langle 2,0,1 \rangle$  and  $\langle 2,0,0.71 \rangle$  positions indicating the order parameters for both phases at  $H=0$  and  $H=0.5$  T. The data in field are consistent with our magnetization data which show a metamagnetic transition at a critical magnetic field which increases with temperature. Thus, with a field of 0.5 T the transition to the AFM state is driven up to 120 K.

A scan of the magnetic reflection along the  $\langle 2,0,L \rangle$  direction is shown in Fig. 3 over the temperature range from 5 to 450 K. At the top of

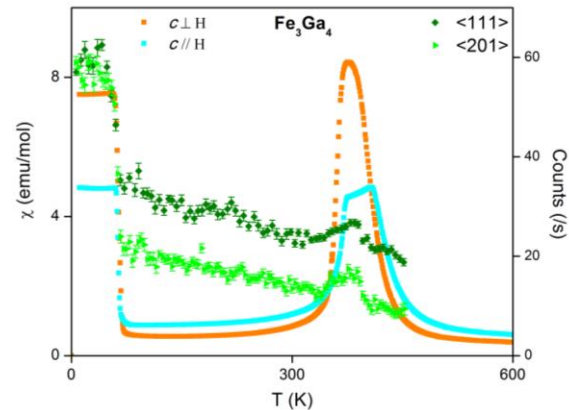


Fig.1: Magnetic susceptibility and temperature dependent scattering. Magnetic susceptibility,  $\chi$  (left axis) taken in a field of 1 kOe for two different crystal orientations. Scattering intensity at the  $\langle 111 \rangle$  and  $\langle 201 \rangle$  Bragg positions demonstrating FM ordering in two temperature regimes.

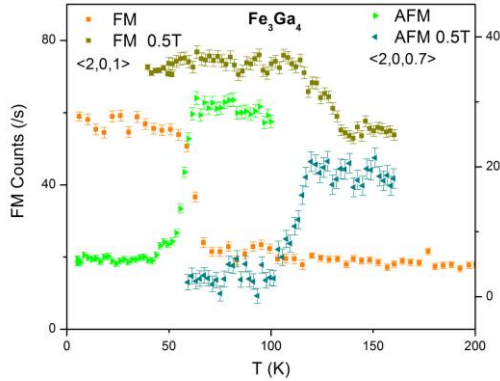


Fig. 2: FM and AFM order parameter. Scattering intensity at the  $\langle 2,0,1 \rangle$  Bragg position (left axis) demonstrating the FM order parameter. Scattering intensity from the  $\langle 2,0,0.7 \rangle$  reciprocal lattice point as a function of temperature (right axis) demonstrating the AFM order parameter.

Using a large number of measured reflections, the magnetic structure in both the FM and AFM states was fully refined. The results of this procedure are shown in Fig. 4 for the models which best fit our data. In FM state the four inequivalent Fe-sites contributes a moment along the c-axis of the  $\text{Fe}_3\text{Ga}_4$  monoclinic structure. We find magnetic moments of 1.754(2), 1.315(2), 1.136(2) and 1.477(1) for Fe1 through Fe4 all of which correlate well to previous Mössbauer measurements in polycrystalline samples<sup>8</sup>. The best fit structure in the AFM phase consists of  $q$  of (0 0 0.27) with the Fe sites split into 7 inequivalent sites. This state resembles that of a SDW type structure. In this calculation the AFM wavevector,  $q$  was set to  $0.25c^*$ , a nearby commensurate position in order to simplify the calculation. In addition, we find that two of the Fe-sites contribute moments along the  $b$ -axis providing a non-coplanar magnetic moment. We believe that this small out of plane moment is responsible for the topological contribution to the Hall Effect that we have previously measured.

#### 4. Conclusion

We have carried out an extensive neutron diffraction investigation of  $\text{Fe}_3\text{Ga}_4$  solving, for the first time, the magnetic order in the intermediate, AFM state. The ground state is confirmed as a robust FM state with magnetic

the frame the scattering at the  $\langle 201 \rangle$  Bragg peak is displayed in order to demonstrate temperature evolution of the FM state. We observe that the FM ordering is gradually diminished as the system enters the AFM state near 68 K. The region of FM behavior between 370 and 420 K is indicated by a slight increase in intensity. The light blue area in the vicinity of the  $\langle 2,0,0.7 \rangle$  plane is the scattering observed in the AFM state. As one can see in the inset where the scale is magnified to demonstrate the temperature- and wavevector-dependent scattering, the characteristic wavevector has a slight temperature dependence showing a tendency to shift toward larger  $L$  at both low and high temperatures. Thus the AFM state appears to unwind showing a longer wavelength as this state becomes unstable with either warming or cooling.

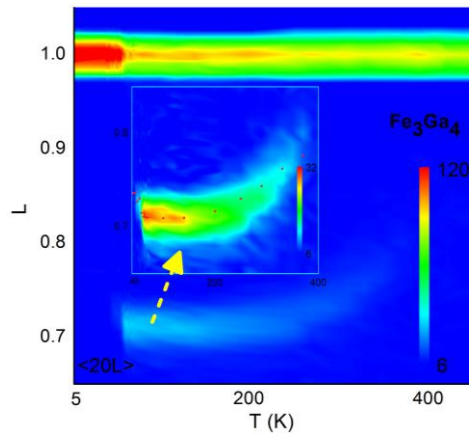


Fig.3: Neutron scattering intensity along the  $\langle 2,0,L \rangle$  direction as a function of temperature for  $\text{Fe}_3\text{Ga}_4$ . Inset: magnification of the scattering in the AFM state (new scale  $40\text{K} < T < 400\text{K}$ ) displaying the scattering intensity and the temperature dependence of the ordering wavevector. Data points indicate position of the peak intensity at each temperature measured.

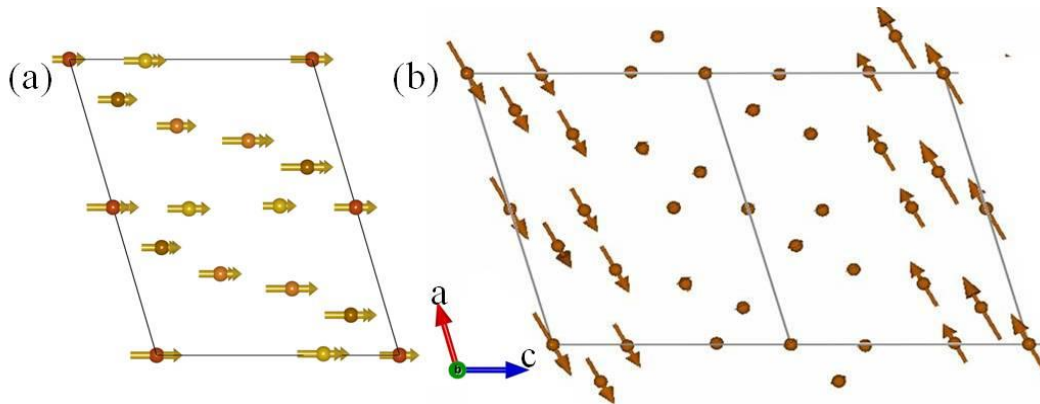


Fig.4: Magnetic Structure. (a) Magnetic structure of Fe<sub>3</sub>Ga<sub>4</sub> determined at 5 K (FM) as determined from a full refinement of the neutron scattering data. (b) Magnetic structure at 100 K simplified to a commensurate wavevector ( $q=0.25 c^*$ ) to simplify the calculation and the figure.

moments oriented along the crystallographic  $c$ -axis. Ferromagnetism is also confirmed for temperatures between 370 and 420 K. A broad search for magnetic scattering in the intermediate temperature range revealed an incommensurate AFM state resembling a SDW phase. Thus, we have successfully determined the magnetic structures of this interesting compound and confirmed the tendency to stabilize the FM state to higher temperatures in moderate magnetic fields.

## 5. Acknowledgments

The current work is funded by the NSF EPSCoR LA-SiGMA project under award #EPS-1003897 and the NSF under DMR1206763.

## 6. References

- [1] H. J. Al-Kanani and J. G. Booth, *Physica B: Condensed Matter* **211**, 90 (1995).
- [2] H. J. Al-Kanani and J. G. Booth, *Physica B: Condensed Matter* **246–247**, 537 (1998).
- [3] H. G. M. Duijn, E. Brück, K. H. J. Buschow, F. R. de Boer, and R. Coehoorn, *Physica B: Condensed Matter* **245**, 195 (1998).
- [4] J. A. Hutchings, M. F. Thomas, H. J. Al-Kanani, and J. G. Booth, *Journal of Physics: Condensed Matter* **10**, 6135 (1998).
- [5] M. Isoda, *Solid State Communications* **65**, 689 (1988).
- [6] A. T. M. K. Jamil, H. Noguchi, K. Shiratori, T. Kondo, and H. Munekata, *J Supercond* **18**, 321 (2005).
- [7] H. G. M. Duijn, *Magnetotransport and Magnetocaloric Effects in Intermetallic Compounds* (Universiteit van Amsterdam [Host], 2000).
- [8] N. Kawamiya and K. Adachi, *Journal of the Physical Society of Japan* **55**, 634 (1986).
- [9] M. Isoda, *Journal of the Physical Society of Japan* **53**, 3587 (1984).
- [10] J. Rodríguez-Carvajal, *Physica B: Condensed Matter* **192**, 55 (1993).

## Metal Organic Frameworks as Vehicles for Drug Delivery

Kiara Taylor-Edinbyrd, Tanping Li, Revati Kumar

Department of Chemistry, Louisiana State University, Baton Rouge, LA 70816, United States

**Abstract:** Metal organic frameworks (MOFs) are highly porous, crystalline nanomaterials composed of metal centers and connected by organic linkers and are capable of gas storage, separation, catalysis and adsorption. These robust nanomaterials can be synthesized in an array of combinations, which makes them highly tunable and thus desirable. While the widespread use of MOFs is due to their role in environmental research, MOFs have also gained traction for their potential roles as drug delivery vehicles. The use of MOFs as a catalyst in the release of chemically stored nitric oxide in *s*-nitrosothiols (RSNO's), where the R-group can be a methyl, cysteine or glutathione, has been shown experimentally; however the mechanism in the complex MOF environment remains elusive. In order to investigate this phenomenon computationally, a combination of gas phase *ab initio* studies and condensed phase classical molecular dynamics simulations is utilized to first study the solvation environment of this system with an ultimate goal of building a reactive model in an attempt to explore the mechanism of this reaction.

**Keywords:** Metal organic frameworks (MOFs), *s*-nitrosothiols (RSNOs), nitric oxide (NO)

### 1. Introduction

Metal organic frameworks have a wide range of applicability from catalysis to drug delivery, gas adsorption and storage.<sup>1</sup> MOFs are self-assembling, three-dimensional materials with high porosity allowing for an increased surface area that can be utilized for gas adsorption, proven to be superior to other contenders. The ability of MOFs to be post-synthetically modified and their various linker/metal combinations make them an ideal candidate to act as catalytic centers.

Nitric oxide (NO), is a gaseous free radical that has several biomedical applications including that of neurotransmission, vasodilation and anti-thrombosis, all of extreme biological significance.<sup>2,3</sup> Biocompatible materials capable of transporting NO in appreciable amounts are of interest and materials ranging from hydrogels, nanoparticles, liposomes and recently MOFs have been investigated for their potential ability to act as drug delivery systems. Due to the shortcomings of many previously studied delivery systems, a reliable and feasible exogenous drug delivery system has remained problematic. In order to surpass this dilemma, a biocompatible, controlled release mechanism with membrane permeability must be fabricated. Recent experimental observations by Harding et al. suggest that copper based MOFs (Figure 1) are not only able to store, convert and deliver NO, but that this process occurs in a sustained and controlled manner necessary for drug delivery systems.<sup>4</sup> Despite these observations, the mechanism of chemical

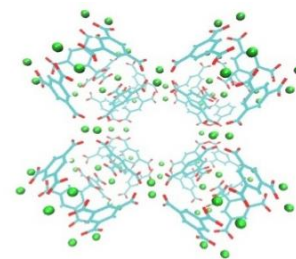


Figure 1: HKUST1-MOF

conversion and storage of NO within the MOF environment has yet to be resolved. While this mechanism wasn't fully determined, it has been suggested that the copper must be in the +1 oxidation state to be catalytically active to produce considerable amounts of NO. One of the focal points of my research is to utilize computational investigations to identify the mechanism in which this occurs within the MOF environment. Through a combination of *ab initio* (electronic structure) calculations and molecular dynamics (MD) simulations, MOFs will be probed for their ability to release chemically stored nitric oxide where release rates have been determined but elucidation into the mechanism remains elusive. The overarching goal of this project is to understand the mechanism of nitric oxide release in the MOF with the goal of optimizing the MOF system for optimal release rates.

In the experiment performed by Harding et al. it was determined that the decomposition reaction responsible for converting RSNO into RS-SR & NO occurred at a timescale of minutes when allowed to occur in a free copper solution (absence of the MOF).<sup>4</sup> What is noteworthy is the observation that the timescale extends tremendously once the RSNO is placed in the MOF environment. It is at this point that the reaction rate is decreased and occurs in a controlled and sustained manner (ideal for biomedical application) over a period of 10 hours. This is a tremendous increase in time for these reactions and we have set out to determine what phenomenon (or barrier) occurs in the MOF environment that is absent in the free copper solution to account for this occurrence. The focus of this paper is the development of a force-field, based on *ab initio* calculations, to accurately model and study the solvation environment around the copper ions in the complex MOF environment.

## 2. Methodology

Electronic Structure calculations: With the use of density functional theory (DFT)<sup>5</sup>, M06 functional<sup>6</sup> and the Gaussian09 software package, *ab initio* calculations are carried out to study simple clusters of copper and the RSNO species in an effort to obtain local minima and to scan the potential energies in the vicinity of these minima. The calculations are later used for the parameterization of the Cu<sup>+</sup>-SNO interaction and ultimately optimize the force field used for our system. Lastly, charges of RSNO (CH<sub>3</sub>SNO, CysNO & gluNO) and the MOF were obtained through the use of Charges from Electrostatic Potentials using a Grid (CHELPG) method.<sup>7</sup>

MD Simulations: Upon completion of electronic structure calculations, the next phase in this project was to carryout molecular dynamics simulations (MD) of RSNO in both the free copper solution and MOF environment (copper bound) using our newly developed force-field. Enhanced sampling methods in the form of umbrella sampling (US) permits the sampling of configurations along a range of distances (reaction coordinate) to generate free energy diagrams by the implementation of a harmonic bias potential. These simulations were carried out using the GROMACS package.<sup>8</sup>

## 3. Results

Through electronic structure calculations we were able to observe an elongation of the S-N bond when compared to the pre-optimized configuration of RSNO in the presence of copper. In addition to this elongation, a simultaneous decrease in bond length was observed between the N=O double bond. These optimizations were performed with copper approximately 3 Å away from the sulfur, whereas the post-

optimization distance was decreased to approximately 2.3 Å. This indicates that the elongation (S-N) is due to a decrease in bond character and the decrease in bond length (N=O) is due to an increase in bond strength. The US-MD simulations were used to obtain the free energy profiles along the reaction coordinate (Cu---S distance in our case). The small barrier observed in free copper is potentially due to the first solvation shell of ethanol packed densely around the copper. The barrier is observed for free copper-CH<sub>3</sub>SNO (top left) as well as CysNO (top right) at approximately 4 Å & depicted in the PMFs below (Figure 2). The local minima for each case is observed at a Cu-S distance of approximately 2.1 Å, this value lies within the normal range of Cu-S average bond distances. The free energy observed in MOF- CH<sub>3</sub>SNO (bottom left) illustrates a small barrier like that observed in free copper; however there is a large barrier observed when for the MOF-CysNO (bottom right) PMF when compared to MOF- CH<sub>3</sub>SNO.

Although the free copper simulations are simplified versions of the system, they are important markers for comparison to the MOF system. Several calculations can be compared for both environments, specifically the coordination number to study the solvation shell located around the copper. This gives insight into the ability or lack thereof for the RSNO to approach the copper (free or bound) and ultimately decompose into RSNO & NO.

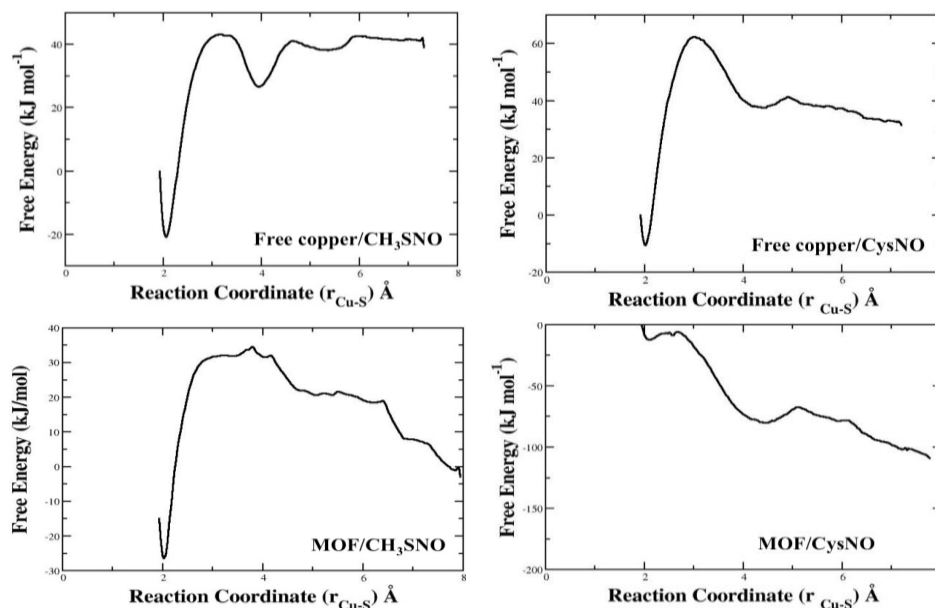


**Figure 2:** Top left- free copper/CH<sub>3</sub>SNO PMF, Top right- free copper/CysNO PMF, Bottom left- MOF- CH<sub>3</sub>SNO PMF, Bottom right- MOF-CysNO PMF

Furthermore, scrutiny of the CysNO (top & bottom right) free energy profiles show a dramatic difference as a

#### 4. Conclusion

The results obtained indicate that there is no significant difference in the Cu—S free energy profiles of CH<sub>3</sub>SNO (top & bottom left) in both the free Cu case and in the MOF; however the small barriers that are observed at approximately 4 Å are likely due to the need for CH<sub>3</sub>SNO to push through the first solvation shell located around copper.

very large barrier is observed in the case of CysNO within the complex MOF environment as compared to the free Cu case. It can be concluded that this barrier is a result of this larger molecule having less space to diffuse through the MOF as this resulting steric hindrance is not observed in the much smaller CH<sub>3</sub>SNO case. In addition to the structure of the complex MOF, it is also suggested that a change in the R-group (methyl, cysteine, glutathione) or organic linker size should affect diffusion through the MOF and ultimately the rate of reaction for this decomposition reaction. In order to further test this hypothesis, a larger molecule, s-nitrosoglutathione (GSNO) will also be investigated within free copper and MOF environments. This molecule is significantly larger than that of CysNO and therefore expected to yield a larger barrier and thus longer reaction time needed to overcome this barrier.

## 5. Acknowledgments

The current work is funded by the NSF EPSCoR LA-SiGMA project under award #EPS-1003897 and a Louisiana Board of Regents (BOR RCS grant # LEQSF(2014-17)-RD-A-02). Kiara Taylor acknowledges the NSF LSU Bridge to Doctorate Graduate Fellowship (NSF grant #1026662).

## 6. References

- [1] Furukawa, H.; Cordova, K. E.; O’Keeffe, M.; Yaghi, O. M. The Chemistry and Applications of Metal-Organic Frameworks. *Science* **2013**, *341*.
- [2] Dishy V, S. G., Harris PA, Kandcer M, Zhan F, Wood AJ, Stein CM. The effect of sildenafil on nitric oxide-mediated vasodilation in healthy men. *Clinical Pharmacology and Therapeutics* **2001**, *70*, 270-279.
- [3] Amedea B. Seabra, P. D. M., Larissa B. de Paula,; Durán, N. New Strategy for Controlled Release of Nitric Oxide. *Journal of Nano Research* **2012**, *20*, 61-67.
- [4] Harding, J. L.; Reynolds, M. M. Metal Organic Frameworks as Nitric Oxide Catalysts. *Journal of the American Chemical Society* **2012**, *134*, 3330-3333.
- [5] Calais, J.-L. Density-functional theory of atoms and molecules. R.G. Parr and W. Yang, Oxford University Press, New York, Oxford, 1989. IX + 333 pp. Price £45.00. *International Journal of Quantum Chemistry* **1993**, *47*, 101-101.
- [6] Yan Zhao, D. G. T. The M06 suite of density functionals for main group thermochemistry, thermochemical kinetics, noncovalent interactions, excited states, and transition elements: two new functionals and systematic testing of four M06-class functionals and 12 other functionals. *Theor. Chem. Account* **2007**, *120*, 215-241.
- [7] Breneman, C. M.; Wiberg, K. B. Determining atom-centered monopoles from molecular electrostatic potentials. The need for high sampling density in formamide conformational analysis. *Journal of Computational Chemistry* **1990**, *11*, 361-373.
- [8] Van Der Spoel, D.; Lindahl, E.; Hess, B.; Groenhof, G.; Mark, A. E.; Berendsen, H. J. C. GROMACS: Fast, flexible, and free. *Journal of Computational Chemistry* **2005**, *26*, 1701-1718.

## Micellization of cationic linear peptide analogs studied using molecular dynamics simulations

Brian Novak, Dorel Moldovan

Department of Mechanical and Industrial Engineering, Louisiana State University, Baton Rouge  
Center for Computation and Technology, Louisiana State University, Baton Rouge

**Abstract:** The self-assembly of cationic linear peptide analogs (LPAs) with the formula Lys-NH(CH<sub>2</sub>)<sub>n</sub>CO-Arg-NH(CH<sub>2</sub>)<sub>n</sub>CO-Arg with n varying from 4 to 13 has been studied using molecular dynamics simulations. These LPAs were designed to deliver an anionic phosphopeptide into cells, and it was shown experimentally that LPAs with n = 11 were much more effective than n = 4 or 7 at penetrating cell membranes and disrupting liposomes. Self-assembly of n = 11 LPAs in solution was also observed, and may be related to their activity. Our results show that stable LPAs micelles formed in aqueous solution for n > 7 and LPAs in those micelles had increased β-sheet type structure consistent with experimental results.

**Keywords:** MD simulation, peptide analog, self-assembly, cylindrical micelle

### 1. Introduction

Cationic linear peptide analogs (LPAs) with the structure shown in Fig. 1 were first designed and synthesized in 2007.[1] They consist of a lysine and two arginines separated by amino acid analogs containing linear hydrocarbon segments of length n. They were designed bind to and transport a phosphotyrosine peptide, GpYEEI, across cell membranes. Leakage due to LPAs with n = 4, 7, and 11 interacting with zwitterionic dipalmitoylphosphatidylcholine (DPPC)[2], anionic dipalmitoylphosphatidylglycerol (DPPG) + DPPC[2], and anionic dipalmitoylphosphatidylserine (DPPS) + DPPC[3] vesicles and uptake of tagged LPAs into cells has been studied experimentally. It was found that only the n = 11 LPAs which have the highest hydrophobic content showed significant activity. It was also found that LPAs with n=11 (LPA-C<sub>11</sub>) formed aggregates in solution at concentrations greater than 10-30 μM.[1] LPAs are amphiphilic with the pattern hydrophilic-hydrophobic-hydrophilic-hydrophobic-hydrophilic. This is not the hydrophobic-hydrophilic pattern found in many surfactants, but the flexibility of the hydrocarbon chains can allow for arrangements of the molecules into structures with hydrophobic cores and hydrophilic surfaces. Circular dichroism showed that the LPA-C<sub>11</sub> had a partial β-sheet type structure,[1,3] which is likely associated with its aggregation. We have simulated LPAs in solution to study their self-assembly

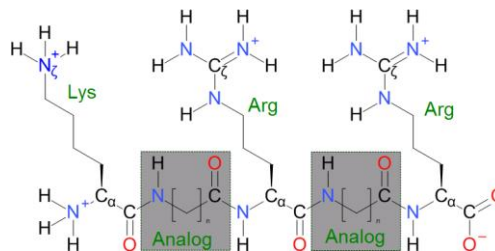


**Figure 1: LPA chemical structure.** Lys indicates a lysine group and Arg indicates an arginine residue. The amino acid analog residues are shown in gray boxes. The [ ]<sub>n</sub> notation indicates a linear hydrocarbon segment with n carbon atoms.

behavior and the structure of the assemblies which could be related to the ability or inability of LPAs with different  $n$  to cross lipid bilayers and therefore to potentially deliver drugs into cells.

## 2. Methods

The MD simulations were performed using the GROMACS[4] software and the GROMOS 54a7 united atom force field.[5] The parameters for the amino acid parts of the LPAs are known. The parameters for lipid tails were used for the LPA hydrocarbon segments, and the parameters for the connection between the amino acid parts and the hydrocarbon segments was based on molecules with similar chemical groups found on the Automated Topology Builder (ATB) site (<http://compbio.chemistry.uq.edu.au/atb/>). For the micellization simulations, 31 LPAs were placed at random starting positions in aqueous solution using the packmol program[6]. For LPA-C<sub>11</sub>, a 186 LPA system was also simulated. In the 31 LPA simulations, there were 16,000 water molecules and counterions (124 chloride ions and 31 sodium ions) for each charged LPA group (N-terminus, lysine side chain, two arginine side chains, and C-terminus). The 186 LPA system contained 6 times the number of all species. The LPA concentration was slightly less than 0.1 M.

## 3. Results

The determination of whether two LPA molecules belonged to the same cluster or micelle was made using the following criterion. Only the backbone carbon atoms of the LPAs were considered for clustering. The backbone was defined as the C<sub>α</sub> and carbonyl carbons of the amino acid residue backbones plus the carbon atoms in the amino acid analog residues. See Fig. 1. Any backbone atom within 0.45 nm of any other backbone atom was taken to be part of the same cluster. With this cut off distance, all backbone atoms in each LPA were guaranteed to be in the same cluster. Use of this criterion minimized the instances of two distinct clusters in temporary close proximity being counted as one cluster since the hydrophobic carbon atoms were not likely to be near the surface of the cluster.

For  $n = 4$ , no significant clustering was observed; the average number of clusters was about the same as the number in random starting configurations. In the case of  $n = 5$  to 7, only small clusters or unstable clusters were observed. For  $n > 7$ , a stable set of clusters was observed after an equilibration period. Figure 2 is a plot of mean

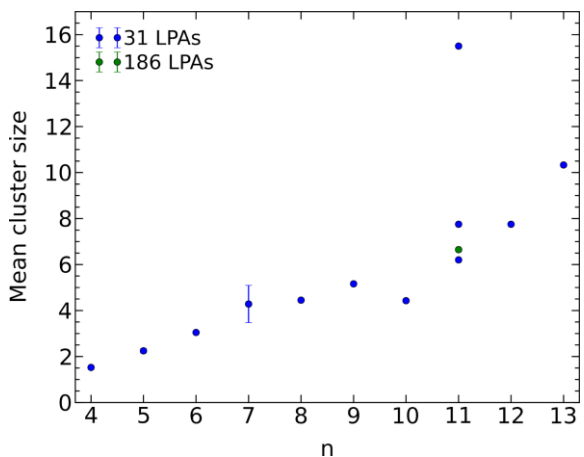


Figure 2: Mean cluster size versus number of carbons in the hydrocarbon segments ( $n$ ). Stable clusters are seen for  $n > 7$ . Error bars extend to one standard error from the mean.

clusters size versus  $n$  after equilibration. Error bars are smaller than the symbol size except in the case of  $n = 7$  where larger clusters (compared to  $n < 7$ ) tended to form but then break apart.

The micelles appear to be cylindrical if large enough. This is based on calculation of the average radii of gyration ( $r_1$ ,  $r_2$ ,  $r_3$ ) around the principal axes as a function of size as well as visualization. The results are shown in Fig. 3. For sizes from about 4 to 8, the micelles are relative spherical since all of the radii are similar. For larger sizes, two of the radii keep increasing with size while the smallest one stops increasing as much. This is typical of cylindrical growth and snapshots show elongated micelles for sizes of 14 and 26 molecules.

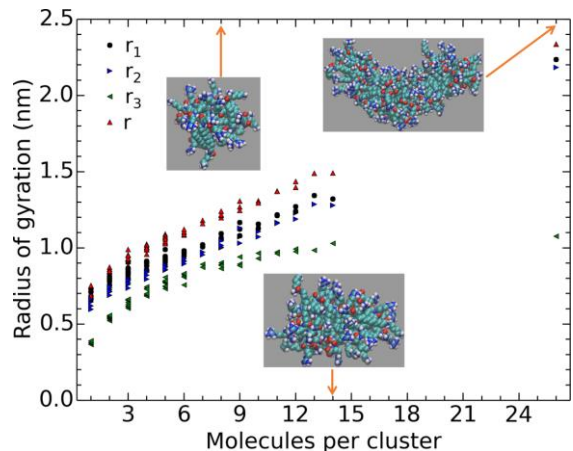


Figure 3: Average radii of gyration around the principal axes ( $r_1$ ,  $r_2$ ,  $r_3$ ) and radius of gyration ( $r$ ) as a function of cluster size. Points are shown for each simulation (each  $n$ ). Insets are snapshots of clusters of sizes 8, 14, & 26 with their longest principal axes aligned with the horizontal.

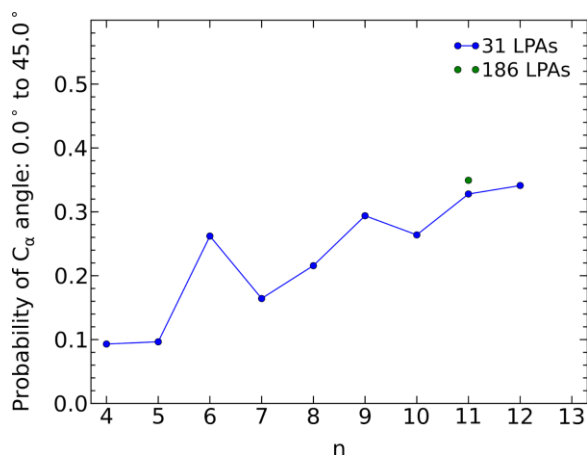


Figure 5: Probability of the angle between the  $C_\alpha$  atoms of the amino acid residues being less than or equal to  $45^\circ$  as a function of  $n$ .

being less than  $45^\circ$  was used. It increases with increasing  $n$  as shown in Fig. 5. A  $\gamma$ -turn is defined by the backbone atoms of three adjacent residues, and is associated with hydrogen bonding between the backbones of residues  $i$  and  $i+2$  which is between the two amino acid analogs in the case of LPAs (Fig 4.). The number of these hydrogen bonds was nearly twice as high for  $n = 8$  to 11 where stable micelles were observed than for  $n = 4$  to 7 where no stable micelles were observed. The number increased by another 1.5 to 2

The structure of the LPAs within the micelles was examined to determine if they had a  $\beta$ -sheet type structure as observed in experiments.[1,3] In simulations,  $\beta$ -turns are typically defined based on the backbone atoms of four adjacent amino acids. In the LPAs, there are only three adjacent residues with amino acid backbones; the two amino acid analogs and the middle arginine. Therefore, a  $\beta$ -turn cannot be defined in the usual way. Instead the probability of the angle between the  $C_\alpha$  atoms of the amino acid residues (Fig. 4)

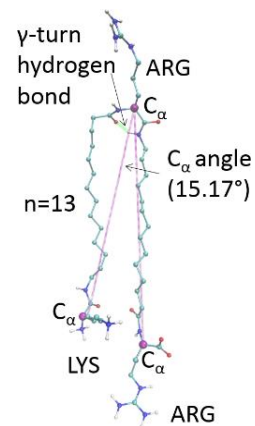


Figure 4: Definition of angle between  $C_\alpha$  atoms and hydrogen bond for a  $\gamma$ -turn.

times for  $n = 11$  and  $12$ . The formation of stable micelles appears to be correlated with  $\beta$ -sheet structure as previously suggested based on the experiments.

#### **4. Conclusions**

Molecular dynamics simulations of the self-assembly of cationic linear peptide analogs showed that stable micelles formed when the number of carbon atoms in the linear hydrocarbon segments ( $n$ ) was greater than 7. Cluster sizes were typically less than 15 LPA molecules with one outlier with 26 molecules. Clusters with  $n = 4$  to 8 were roughly spherical, but a further increase in size led to cylindrical shapes. Increased  $\beta$ -sheet type structure as seen in experiments for  $n = 11$  was observed for the same  $n$  for which stable micelles were seen;  $n > 7$ . Comparison with the structures of single LPAs in solution would be required to determine if this type of structure is adopted during micelle formation or if micelle formation is a result of this type structure.

#### **5. Acknowledgments**

The current work is funded by the NSF EPSCoR LA-SiGMA project under award #EPS-1003897. Computational resources were provided by Louisiana Optical Network Initiative (LONI) and HPC@LSU.

#### **6. References**

- [1] G. F. Ye *et al.*, *Journal of Medicinal Chemistry* **50**, 3604 (2007).
- [2] G. F. Ye *et al.*, *Colloids and Surfaces B-Biointerfaces* **76**, 76 (2010).
- [1] A. Gupta *et al.*, *Eur. Biophys. J.* **40**, 727 (2011).
- [4] B. Hess *et al.*, *J. Chem. Theory Comput.* **4**, 435 (2008).
- [1] N. Schmid *et al.*, *Eur. Biophys. J.* **40**, 843 (2011).
- [6] L. Martinez *et al.*, *J. Comput. Chem.* **30**, 2157 (2009).

## **Molecular Dynamics Simulation Study of the Transport of DNA Mononucleotides Through Nanoslits Driven by Electric Fields**

Kai Xia<sup>1</sup>, Brian Novak<sup>1</sup>, Dimitris Nikitopoulos<sup>1</sup>, Steven Soper<sup>2</sup> and Dorel Moldovan<sup>1</sup>

<sup>1</sup>Department of Mechanical Engineering, Louisiana State University, Baton Rouge, LA 70803

<sup>2</sup>Department of Biomedical Engineering and Department of Chemistry, University of North Carolina, Chapel Hill, NC 27599

**Abstract:** Transport of DNA mononucleotides through nanochannels might be used to distinguish them by comparing their flight times over a fixed distance. Using nonequilibrium molecular dynamics (MD) simulations we investigate the dynamics of DNA mononucleotides moving through hydrophobic nanoslits driven by electric fields. Our simulations show that during the translocation process all four nucleotides adsorb and desorb from the slit-walls multiple times. The mechanism of absorption/ desorption events was studied by monitoring the angle of the nucleotide bases with the walls. Various nucleotide properties such as their velocity depend on whether or not the nucleotide is adsorbed on the walls and on the strength of the electric field. The distance to fully distinguish the four dNMPs is estimated.

**Keywords:** Molecular dynamics, DNA sequencing, nanoslit, sodium-nucleotide association

### **1. Introduction**

Interesting new nanotechnologies are being developed for sequencing hetero-polymers such as DNA. This paper addresses an approach to DNA sequencing which combines sequential DNA disassembly and subsequent transport of mononucleotides through a nanochannel sensor. The four kinds of mononucleotides that result from DNA disassembly can be distinguished by measuring their flight time during their translocation through a nanochannel of a given length. The basic idea is that every kind of mononucleotide has a specific flight time which depends on its molecular identity and on the specificity of interaction with the channel walls. The advantage of the proposed sequencing methodology is that in practice only the presence of the mononucleotides rather than their identity needs to be detected. The realization of this device for directly reading structural information from DNA requires a fundamental understanding of the transport dynamics of mononucleotides through nanochannels and the characteristics of the interaction between mononucleotides and nanochannel walls.

### **2. Simulation Method**

To help understand the dynamics of mononucleotide travelling through a nanochannel, equilibrium and non-equilibrium molecular dynamics simulation were performed with LAMMPS [1] software package. The

CHARMM27 force field [2] was used to describe the interactions of the mononucleotides. The interaction of water molecules is described by CHARMM TIP3P model. The simulation system consists of a single mononucleotide (dAMP, dCMP, dGMP or dTMP) in water-NaCl solution of 89 mM concentration located between two slabs composed of Lennard-Jones atoms distributed randomly in the slabs and tethered to their original positions. The 1.2 nm thick slit walls are placed 3 nm away from each other. Only the wall atoms were thermostatted at 300K using the Berendsen thermostat method [3]. The flow in the slit was generated by applying an external electric field. The electrostatic interactions were evaluated by using the 3-dimensional particle-particle particle-mesh (PPPM) method [4] corrected for slab geometry. The box length in the non-periodic direction was taken to be three times the simulation box length in the direction along which the electric field was applied. The simulation system is shown in Fig. 1. Several different electric fields (0.6, 0.3, 0.1 and 0.0144V/nm) are applied.

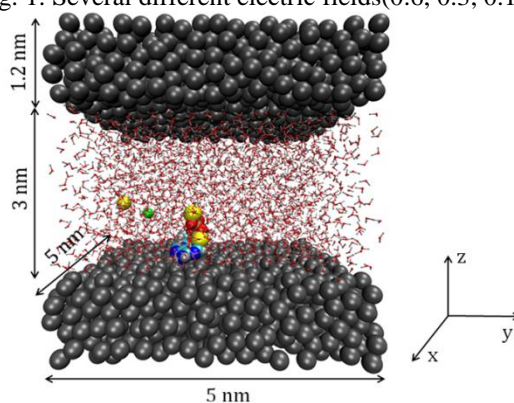


Fig. 1. The simulation system consisting of a mononucleotide, sodium chloride, water and walls. The walls are composed of tethered Lennard-Jones atoms thermostatted at 300K. The green sphere represents a chloride ion, yellow represents sodium ions, red represents non-water oxygen atoms, blue represents nitrogen atoms and water molecules are the smaller background molecules (red and white). Periodic boundary conditions were applied in x and y directions

### 3. Results and Discussions

The simulations show that the phosphate group of the mononucleotides on which the net charge is  $-2e$  ( $e$  = electronic charge) can be associated with sodium ions due to the electrostatic interaction. This association significantly influences the traveling velocity of mononucleotides. The mononucleotides are driven by electric field and the driving force is proportional to the net charge on it. Therefore, the more sodium ions that are associated with a mononucleotide, the lower the net charge the complex has and the slower its motion. Fig. 2 shows the association number and the position of dTMP in the direction of the electric field versus time. This show that indeed the mononucleotide moves slower when the association number is 1 than when no sodium ion is associated. As illustrated in Fig. 2, in the 40 ns to 50 ns interval, the average association number is equal to 2 and accordingly the mononucleotide hardly moves forward.

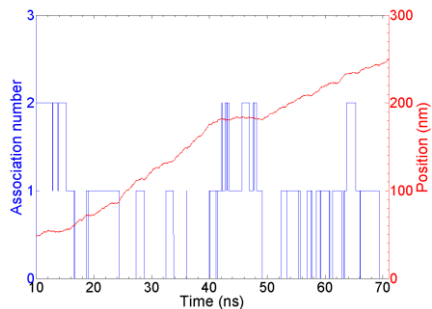


Fig. 2. Time dependence of the association number and the coordinate along the direction of the applied electric field ( $x$ ) for a dTMP molecule moving in the slit. When one or two sodium ions are associated with the ionic phosphate group, the velocity of the nucleotide decreases significantly.

In both no-flow (equilibrium) and flow simulations the nucleotides are adsorbed and desorbed from the wall multiple times. In the adsorbed state the hydrophobic base part of the nucleotides tends to sit on the surface while the hydrophilic phosphate group points away from the surface. All four nucleotides once they are adsorbed on the wall they stay on wall for a while. Fig. 3 shows the  $z$  position of dTMP versus time. This clearly shows that the dTMP is adsorbed and desorbed from the wall several times during the 60ns interval.

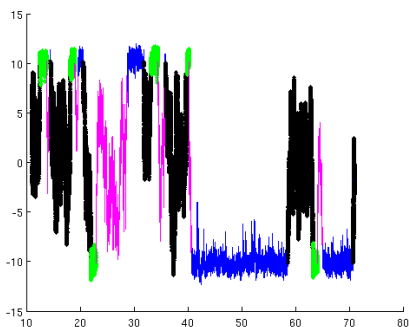


Fig. 3. A 60 ns trajectory segment of a dTMP depicting the time dependence of the  $z$ -coordinate of the mononucleotide center of mass. The green and blue lines represent adsorption periods, black and pink lines represent desorption periods.

Table 1 shows the required distances to separate the six different dNMP pairs for  $E = 0.1$  V/nm. The maximum of these values is the necessary distance to fully distinguish the four dNMPs which is the dAMP-dGMP distance of  $757.29 \mu\text{m}$  corresponding to  $N = 1514580$  segments of length  $0.5$  nm.

	dAMP	dCMP	dGMP	dTMP
dAMP	$\infty$	4.92	<b>757.2</b>	46.39
dCMP	4.92	$\infty$	3.62	13.55
dGMP	<b>757.2</b>	3.62	$\infty$	22.95
dTMP	46.39	13.55	22.95	$\infty$

Table 1: Required distances ( $\mu\text{m}$ ) to separate the time of flight distributions of the dNMP pair types to three standard deviations from the means of the distributions.

#### 4. Conclusion

Using MD simulations we investigated the translocation of DNA nucleotides through 3 nm wide slits in the presence of an electric field. Our simulations indicate that during the translocation process the phosphate group of the nucleotide bases may associate with one or two neutralizing sodium ions. This association process has a strong impact on the nucleotide motion in the nanoslit. When one or two sodium ions associate with the ionic phosphate group of the nucleotide, the velocity of the nucleotide decreases significantly in both adsorbed and desorbed states. The distance to fully distinguish the four dNMPs is estimated based on the current simulation results.

#### 5. Acknowledgments

Work supported in part by NSF-EPSCoR Grant # EPS-1003897. Computer resources were provided by LONI and HPC @ LSU.

#### 6. References

- [1] S. Plimpton, *J. Comput. Phys.* 117, 1, 1995.
- [2] N. Foloppe, and A. D. MacKerell, *J. Comput. Chem.* 21, 86, 2000.
- [3] H. J. C. Berendsen et al., *J. Chem. Phys.* 81, 3684 (1984).
- [4] R. W. Hockney and J. W. Eastwood, "Computer Simulation Using Particles" ,Adam Hilger, 1989.

## Monte Carlo study of a Spin Glass model with Correlated Disorder

K.-M. Tam<sup>1,2</sup>, J. Willard<sup>3</sup>, J. Moreno<sup>1,2</sup>, and M. Jarrell<sup>1,2</sup>

<sup>1</sup> Department of Physics & Astronomy, Louisiana State University, Baton Rouge, Louisiana 70803, USA

<sup>2</sup> Center for Computation & Technology, Louisiana State University, Baton Rouge, Louisiana 70803, USA

<sup>3</sup> Department of Physics & Astronomy, Macalester College, Saint Paul, Minnesota, 55105, USA

**Abstract:** We employ modern spin glass simulation techniques to study a spin glass model with correlated disorder. We focus particularly on the recently proposed spin glass susceptibilities ratio for detecting the spin glass transition. We find that both the correlation length and the susceptibilities ratio for different system sizes show crossing behavior. Importantly, the crossing point tends to be at a higher temperature for the susceptibilities ratio.

**Keywords:** spin glass, frustration, randomness, Monte Carlo

### 1. Introduction

Almost all materials exhibit spontaneous symmetry breaking at sufficiently low temperature. In magnetic systems the spin rotational symmetry is broken to form magnetic ordering. The discovery of metallic alloys which fail to form conventional magnetic order has been a puzzle for the last few decades. Unfortunately, analytical calculations cannot provide an unbiased answer to this problem. On the other hand, numerical Monte Carlo simulations require long equilibration time. With extensive numerical simulations efforts, some of the idealized models have been studied in detail. The general consensus is that for models with uncorrelated disorder there is a finite spin glass critical temperature in three dimensions. However, in real materials, the disorder is usually somewhat correlated. In this work, we employ modern spin glass simulation techniques to study a spin glass model with correlated disorder. We find that the critical temperature is enhanced due to the correlations. We also analyze the recently proposed spin glass susceptibilities ratio, we find that the critical temperature obtained from the susceptibilities ration may be slightly overestimated compared to that obtained from the correlation length.

### 2. Spin Glass materials

The phase diagram of a spin glass material— $\text{LHo}_x\text{Y}_{1-x}\text{F}$  is shown in Fig. 1a. The non-magnetic Ytterbium ions can be substituted by the magnetic Holmium ions which are coupled by long range dipolar interactions. The system forms ferromagnetic ordering in a wide range of concentration of Holmium ions, the critical temperature falls off linearly with the concentration as predicted by the mean field theory. However, when the concentration drops to around 15%, the systems cannot support ferromagnetic order anymore, instead spin glass behaviors have been observed [1,2,3].  $\text{LHo}_x\text{Y}_{1-x}\text{F}$  is a typical example of spin glass material, in which the frustration from the long range coupling (note that the sign of the dipolar coupling depend on the angle between the two spins) combined with the randomness (random dilution) form a spin glass phase at low concentration of the magnetic ions.

Fig. 1a)

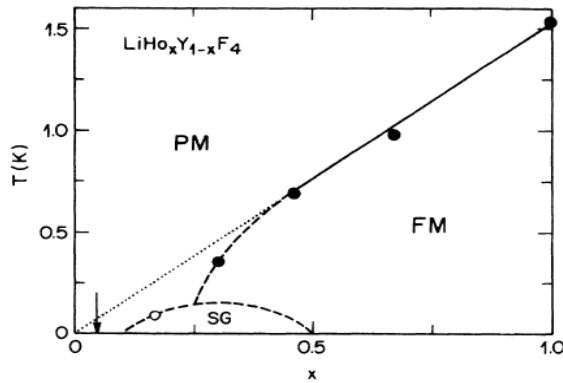


Fig. 1b)

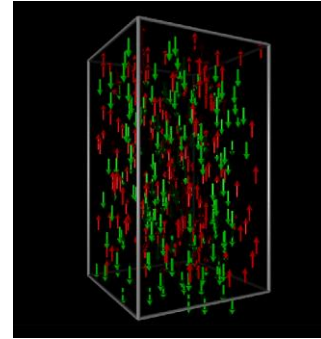


Fig. 1 a) Phase diagram of  $\text{LiHo}_x\text{Y}_{1-x}\text{F}_4$  obtained from experiments [1]. The magnetic Holmium ions are coupled with each other by the long range dipolar interaction. At high concentration of magnetic Holmium ions the systems form ferromagnetic (FM) ordering, at low concentration, the FM is unstable towards spin glass (SG) ordering. The frustration and randomness are introduced by the random dilution of Holmium ions. Fig. 1 b) Snapshot of spin configuration in the spin glass phase [2], it lacks a preferential direction or periodic structure as it is the case of magnetic ordering.

### 3. Nature of Spin Glass Phase

The existence of a spin glass phase in three dimensions is confirmed by numerical simulations, including some models with rather realistic couplings such as the dipolar spin glass model mentioned above. However, the nature of the spin glass phase is far from being fully understood. There are two main competing theories, the replica symmetry breaking scenario [4] and the scaling or droplet scenario [5]. The replica symmetry breaking scenario is developed from the mean-field model. The physical idea is that the number of states with similar free energy (different by  $N^{-1/2}$ ) could be very large or even infinite for system in the thermodynamic limit. See Fig. 2a for a schematic diagram of spin configurations with nearly degenerate free energies. While the global properties such as energy for these states are similar, their local properties could be vastly different. A useful quantity to characterize this property is the overlap between two states. The overlap function will have a non-trivial structure different from the ferromagnetic phase, in which there are only two delta functions because of the two-fold degenerate ground states. An important consequence of the replica symmetry breaking scenario is the existence of a finite critical external field for the spin glass phase. On the contrary, the droplet scenario does not have massively degenerate states separated by barriers, and the spin glass phase is unstable with respect to a magnetic field. However, to demonstrate the existence of a spin glass phase in an external field encounter various difficulties, a prominent one is the choice of a dimensionless quantity which exhibits scaling behavior around a putative critical point. Recently, the spin glass susceptibilities ratio has been proposed [6], in this work we will study this quantity for a spin glass model with correlated disorder and compare it with the data for the correlation length.

**4. A Spin Glass model with correlated disorder**

The Hamiltonian which describes the energy of the system can be written as

$$H = \sum_{i,j} J_{ij} S_i S_j$$

. For the canonical spin glass model, the Edwards-Anderson model with bimodal distribution, the coupling  $J$  is randomly chosen to be +1 or -1 and each of the random variable is independent. The spins are Ising with two states +1 or -1. Now, we assign two random numbers with bimodal distribution at each site,  $\alpha_i$  and  $\gamma_i$ , and set the coupling between site  $i$  and  $j$  as  $J_{ij} = \alpha_i \gamma_j + \gamma_j \alpha_i$ . This model was proposed by van Hemmen and can be solved exactly in the infinite dimension limit [7]. For three dimensions, it has been showed that the overlap function does not have a many-valued structure [8]. This suggests that the spin glass phase is “trivial” without replica symmetry breaking and the equilibrium could be easier to attain. Thus this model is a good testbed for detecting the spin glass transition by using the susceptibilities ratio.

Fig. 2a)

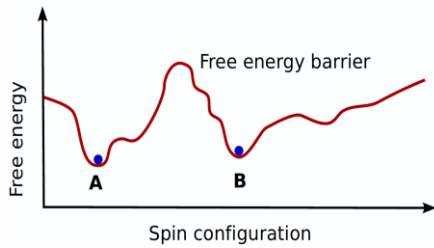


Fig. 2b)

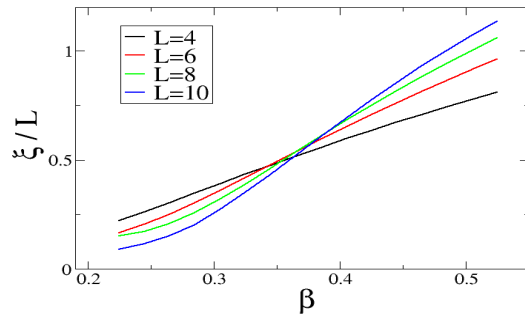


Fig. 2c)

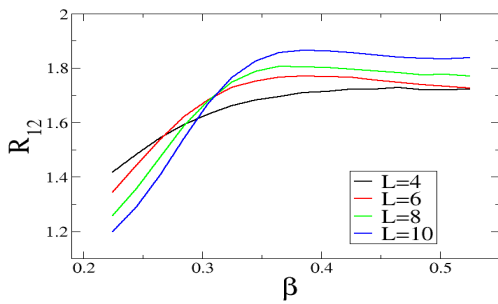


Fig. 2d)

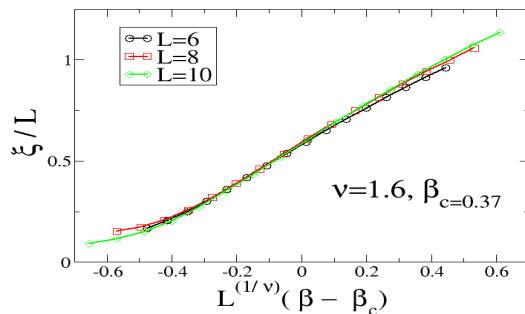


Fig. 2a) The schematic diagram of a rugged free energy landscape with nearly degenerate local minima. Fig. 2b) Correlation lengths for different system sizes cross at around  $\beta=0.37$ . This indicates a finite spin glass critical temperature. Fig. 2c) The susceptibility ratios for  $L=6, 8,$  and  $10$  cross at around  $\beta=3.1$ . This also indicates a finite spin glass critical temperature. However, the correction for the scaling may be large and it

needs further study. Fig. 2d) The correlation lengths for  $L=6, 8,$  and  $10$  scales around the spin glass critical temperature. The critical exponent for the correlation length is about  $1.6$ , which is smaller than that of the Edwards- Anderson model which is about  $2.4$ .

We studied this model using a parallel tempering Monte Carlo simulation. First we define the spin glass susceptibility  $\chi(k) = 1/N \sum_{i,j} \langle s_i s_j \rangle^2 \exp(ik \cdot (r_i - r_j))$ , where  $\langle \dots \rangle$  denotes thermal average and  $[\dots]$  denotes realization average. We define the correlation length based on the Ornstein-Zernike formula  $\xi/L = 1/(2\sin(2\pi/L)) \sqrt{\chi(k_0)/\chi(k_1) - 1}$ , where  $k_0 = (0,0,0)$  and  $k_1 = (2\pi/L, 0, 0)$ . The ratio of susceptibilities at two non-zero momenta has been proposed as a new parameter for detecting the spin glass transition. It is defined as  $R_{12} = \chi(k_1)/\chi(k_2)$ , where  $k_2 = (2\pi/L, 2\pi/L, 0)$ . We show the correlation lengths in fig 2b, they show crossing for  $L=6,8,10$ . In fig 2d, we show the scaling analysis for the correlation length exponent, we find that it is about  $1.6$  which is smaller than that of the Edwards-Anderson model which is about  $2.4$ [9]. In fig 2c, we show the susceptibilities ratios, crossing behavior is also observed for  $L=6,8,10$ , but the crossing point is at a higher temperature than that from the correlation lengths.

## 5. Conclusion

We used the parallel tempering Monte Carlo to study the three-dimensional van Hemmen spin glass model with correlated disorder. We found that the recently proposed susceptibilities ratio tends to overestimate the putative critical temperature.

## 6. Acknowledgments

The current work is funded by the NSF EPSCoR LA-SiGMA project under award #EPS-1003897.

## 7. Reference

- [1] D. H. Reich, B. Ellman, J. Yang, T. F. Rosenbaum, G. Aeppli, and D. P. Belanger, Phys. Rev. B 42, 4631 (1990).
- [2] K.-M. Tam and M. J. P. Gingras, Phys. Rev. Lett. 103, 087202 (2009).
- [3] J. C. Andresen, H. G. Katzgraber, V. Oganessian, M. Schechter, arxiv1407.4782.
- [4] M. Mezard, G. Parisi and M. A. Virasoro, Spin Glass Theory and Beyond (World Scientific, Singapore, 1987).
- [5] D. S. Fisher and D. A. Huse, Phys. Rev. Lett. 56, 1601 (1986).
- [6] Janus Collaboration: R. A. Baños, et al., Proc. Natl. Acad. Sci. USA 109, 6452 (2012).
- [7.] J. L. van Hemmen, Phys. Rev. Lett. 49, 409 (1982).
- [8]M. Katoot, U. Hansmann, and T. Celik, Computer Simulation Studies in Condensed-Matter Physics VI Springer Proceedings in Physics Volume 76, 152 (1993).
- [9] H. G. Katzgraber, M. Koerner, A. P. Young, Phys. Rev. B 73, 224432 (2006).

## Multi-scale theory in the molecular simulation of electrolyte solutions

Wei Zhang, Xinli You, Lawrence R. Pratt<sup>1</sup>

<sup>1</sup>Department of Chemical & Biomolecular Engineering, Tulane University

**Abstract:** The McMillan-Mayer (MM) theory for electrolyte solutions [1-3], which integrates-out the solvent from the statistical mechanics, is strongly established and difficult, both conceptually and practically. Therefore the preponderance of molecular simulation simply ignores the molecular-scale statistical mechanical theory of electrolyte solutions. Nevertheless, that basic theory should be helpful in treating the multiple length-scales that are unavoidable for these chemically complex materials. We reanalyze this situation by showing how modern quasi-chemical theory (QCT) can be brought bear on the short length-scales that are the serious problem for applications of MM theory.

**Keywords:** McMillan-Mayer theory, quasi-chemical theory, statistical thermodynamics, electrolyte solutions

### 1. Introduction

*Ab initio* molecular dynamics (AIMD) is required for simulation problems of chemical interest. But the computational difficulty of AIMD calculations is  $10^3 - 10^6$  larger than for simulations that only require pre-established inter-atomic force fields. Thus AIMD calculations are typically not practical for the forefront problems addressed by classic simulation calculations. Some sort of multi-scale theory seems required to address this difficulty.

One picture for multi-scale theory is to assume that small time and length scale tools are available, then to develop the statistical mechanical procedures to extend those tools to long time and length scales. To address AIMD we suggest an alternative multi-scale strategy: assume that classic simulation calculations will address long time and length scales, then develop the statistical mechanical results to proceed accurately to short time and length scales.

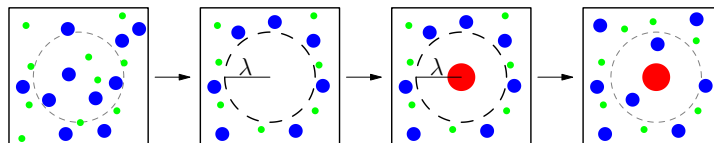


**Figure 1: Evaluation of the excess chemical potential of a distinguished ion (red disk), patterned according to QCT. The blue and green disks are other ions in the system, and the solvent is in the background. The stepwise contributions are “packing,” “outer shell,” and “chemical” contributions, from left to right.**

Some necessary statistical mechanical results – here the McMillan-Mayer theorem – are old and have fallen into obscurity [4-5]. Another essential feature here – quasi-chemical theory – has old roots but new realizations in the

context of the theory of liquids. This present work develops and tests these statistical mechanical results for the multi-scale purposes suggested here.

## 2. Methods

This study organizes McMillan-Mayer theory [1], the potential distribution approach [6], and quasi-chemical theory [7] to provide theory for the thermodynamic effects associated with long-length scales. The theory treats composition fluctuations which would be accessed by larger-scale calculations, and also longer-ranged interactions that are of special interest for electrolyte solutions. [8] The quasi-chemical organization breaks-up governing free energies into physically distinct contributions: packing, outer-shell, and chemical contributions. Here we study specifically the outer-shell contributions that express electrolyte screening. For that purpose we adopt a primitive model suggested by observation of ion-pairing in tetra-ethylammonium tetra-fluoroborate dissolved in propylene carbonate. We estimate a non-electrostatic contribution directly by trial insertions, then electrostatic contribution on the basis of distributions. Gaussian statistical models are shown to be effective physical models for outer-shell contributions, and they are conclusive for the free energies within the quasi-chemical formulation. In addition, for comparison, Bennett method and Hypernetted-chain (HNC) theory are implemented in such systems with different box size. The details of simulations are shown as Table 1:

$C$ (mol/dm <sup>3</sup> )	$L$ (nm)	$N$ (ion-pairs)	$\kappa^{-1}$ (nm)	$\beta q^2 \kappa / 2\epsilon$
0.01	32.15	200	2.67	0.17
0.05	18.80	200	1.19	0.39
0.1	14.92	200	0.84	0.55
0.2	11.84	200	0.60	0.77
0.4	9.4	200	0.42	1.11
0.5	9.4	250	0.37	1.26
0.6	9.4	300	0.34	1.37
0.8	9.4	400	0.30	1.55
1.0	9.4	500	0.27	1.72
2.0	7.5	500	0.19	2.44

**Table 1: Specifications for Monte Carlo simulation of a primitive model with dielectric constant, ion charges and sizes corresponding to the atomically detailed [TEA][BF<sub>4</sub>]/PC case. Specifically the model dielectric constant is  $\epsilon = 60$ , and  $d_{++} = 0.6668$  nm,  $d_{--} = 0.6543$  nm,  $d_{+-} = 0.45$  nm are distances of closest approach for the hard spherical ions. These calculations utilized the Towhee package adapted to the present system, conventional cubical periodic boundary conditions at  $T = 300$ K, and the indicated concentrations  $C$ . Each calculation was extended to 106 cycles after aging, each cycle comprising 2n ion-pairs attempted moves. 10,000 configurations are saved and used for the following analyses.**

For HNC theory, same concentrations as simulations are studied and the HNC equation can be solved in a simple chain recursion way [9],

$$g_{\text{HNC}} = e^{-\beta u^*} e^{C_1} e^{\tau_{\text{HNC}}} \quad (1)$$

where  $u^*$  is short range interaction between two ions,  $C_1$  can be determined as  $-e_a e_b \beta e^{-\kappa r} / \epsilon r$ , and  $\tau_{\text{HNC}}$  can be evaluated through the recursion process [9]. Since  $h_{\text{HNC}} = g_{\text{HNC}} - 1$  that has been evaluated, the excess chemical potential for the HNC methods can also be determined.

### 3. Results

The selective radial distribution function results are shown as Figure 2. It shows that the radial distribution function of simulations and HNC calculations agree with each other.

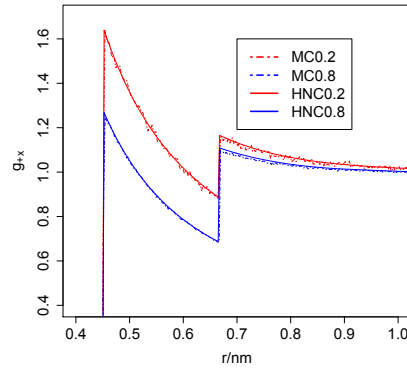


Figure 2: Radial distribution function obtained with Monte Carlo simulations and HNC calculations.  $g_{+x}$  means the radial distribution function of positive ion to any other ions.

The comparisons of Gaussian method, Bennett method and HNC method are shown in Figure 3.

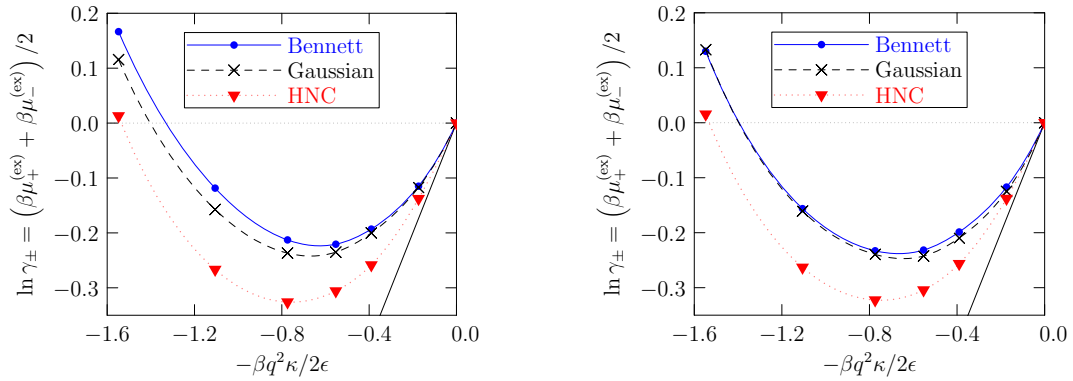


Figure 3: Mean activity coefficients obtained with the gaussian approximation, the Bennett evaluation, and HNC theory without QCT conditioning (left figure) and with QCT conditioning (right figure). The mean

activity coefficients (Left figure) obtained with the gaussian approximation, the Bennett evaluation and HNC theory are qualitatively similar but quantitatively different from each other. Through QCT conditioning (right figure), the mean activity coefficients evaluated by the Bennett method and the gaussian approximation now accurately agree, while HNC is still disagree with these. This suggests that both Gaussian and Bennett are physically reliable with this conditioning, but HNC has some deviations from the simulation results.

#### 4. Conclusions

This theory develops a mechanism for addressing effects associated with longer spatial scales, involving also characteristically longer time scales. The theory treats composition fluctuations which would be accessed by larger-scale calculations, and also longer-ranged interactions and correlations that are of special interest for electrolyte solutions. With the present data-set the gaussian physical approximation obtains more accurate mean activity coefficients than does the Bennett direct evaluation of that free energy. Also, as a method with clear physical assumptions, Gaussian models show better results provided that the variances of the binding energies are well evaluated. System size effects are tested to be small in such results.

#### 5. Acknowledgements

The current work is funded by the NSF EPSCoR LA-SiGMA project under award #EPS-1003897.

#### 6. References

- [1] W. G. McMillan Jr and J. E. Mayer, *J. Chem. Phys.* **13**, 276 (1945).
- [2] T. L. Hill, *STATISTICAL THERMODYNAMICS* (Addison- Wesley, Reading, MA USA, 1960) Chap. SS19.1.
- [3] H. L. Friedman and W. D. T. Dale, in *STATISTICAL MECHANICS PART A: EQUILIBRIUM TECHNIQUES*, edited by B. J. Berne (Plenum, New York, 1977) pp. 85–136.
- [4] P. G. Kusalik and G. N. Patey, *J. Chem. Phys.* **89**, 7478 (1988).
- [5] C. P. Ursenbach, D. Wei, and G. N. Patey, *J. Chem. Phys.* **94**, 6782 (1991).
- [6] T. L. Beck, M. E. Paulaitis, and L. R. Pratt, *THE POTENTIAL DISTRIBUTION THEOREM AND MODELS OF MOLECULAR SOLUTIONS*, (Cambridge University Press, Cambridge, 2006).
- [7] D. Asthagiri, P. D. Dixit, S. Merchant, M. E. Paulaitis, L. R. Pratt, S. B. Rempe, and S. Varma, *Chem. Phys. Letts.* **485**, 1 (2010).
- [8] W. Zhang, X. You and L. R. Pratt, *J. Phys. Chem. B*, **118**, 28, pp. 7730-7738 (2014).
- [9] W. D. T. Dale and H. L. Friedman, *J. Chem. Phys.* **68**, 8 (1978).

## **OPTIMIZING GROWTH CONDITIONS OF ZINC SACRIFICIAL LAYER FOR MICRO-ORIGAMI TECHNOLOGY**

**Rahmatollah Eskandari<sup>1</sup>, Brandon Buchannan<sup>2</sup>, Leszek Malkinski<sup>1</sup>**

<sup>1</sup>Advanced Materials Research Institute, University of New Orleans, LA 70148

<sup>2</sup>Allegheny College, Department of Physics, Meadville, PA 16335

**Abstract:** Micro-origami technology is suitable for fabrication of complex three-dimensional architectures from flat film patterns. For instance multiwall microtubes of magnetic and piezoelectric materials can be made by self-rolling of rectangular bilayers with interfacial stresses between the two layers which cause bending and eventually rolling of the rectangles. In order to be released from the substrate the film patterns must be grown on top of a sacrificial underlayer which can be removed without affecting the patterns. Zinc is a new candidate for the sacrificial layer because it can be removed in vacuum by sublimation at temperature lower than 200°C. The growth of Zn films on sapphire substrate with Ru and Ti buffer layers was studied to optimize technological conditions for smooth thin films. The films were deposited using magnetron sputtering and electron beam evaporation. Their microstructure was studied using RHEED, Auger spectroscopy and scanning electron microscopy. The best Zn films were grown by e-beam evaporation on Ti at room temperature and at low deposition rates.

**Keywords:** Thin films, Multifunctional materials, Micro-origami

### **1. Introduction**

Complex 3-dimensional structures of multifunctional materials can be fabricated by the means of micro-origami techniques. This technology relies on bending, folding, twisting or rolling flat thin film patterns to form free-standing functional structures. Although different mechanisms, such as residual stresses in the films or surface tension of liquid droplets can be used to achieve deformation of the film pattern, the films which undergo deformations must be released from the substrate. This can be achieved by wet or dry etching or by dissolving a sacrificial layer on top of which the patterns are grown. The process of removal of the sacrificial layer must be extremely selective, so it does not affect the film patterns or the substrate. For example, selectivity of chemical etching as high as 1:10,000 was required (e.g., Prinz et al. [1]) to fabricate multiwall nanotubes from GaAs/InGaAs semiconductor films using AlAs as a sacrificial layer. Finding a new sacrificial layer is especially challenging in the case of heteroepitaxial structures, because in addition to high selectivity of removal of the sacrificial layer, both the sacrificial layer and the films grown on top of it must match the crystallographic structure of the substrate. Previously, we used sacrificial layer of Cu and wet chemical etching with Cu-etchant to fabricate polycrystalline microtubes of magnetic/non-magnetic bilayers and microtubes of magneto-electric composites [2-4]. We have recently proposed to use zinc as a sacrificial layer because it can be selectively removed by sublimation in vacuum at relatively low temperatures ranging from 160°C to 200°C, depending on the vacuum pressure [5]. Zn also matches the lattice constant of several hexagonal elements, such as Ru, Ti and Co.

## 2. Materials and Methods

While a vast literature exists on fabrication methods of ZnO, which has potential for applications in solar cells, little information can be found about the growth of metallic Zn films. Therefore, we explored both deposition methods: magnetron sputtering and electron beam evaporation (or their combination) available in the Thin Film Technology Lab of the Advanced Materials Research Institute in UNO. Three-chamber physical deposition system ORION-8 from AJA International Co. is equipped with the in-vacuum analysis tools such as thin film growth sensors, Reflection High Energy Diffraction (RHEED) from Staib Co. and Auger spectrometer (from OCI), which were used to determine, the thickness, crystallinity and composition of deposited films. The microstructure of the films was additionally investigated using electron microscopy tools: scanning electron microscopy and Electron Dispersive X-ray Spectroscopy (EDS). Both Auger spectroscopy and EDS were used to verify that the Zn film was sublimated by increasing the temperature of the sample holder to 200°C at the vacuum pressure of about  $10^{-7}$  Torr.

Sapphire ( $\text{Al}_2\text{O}_3$ ) pieces with (0001) orientation were selected as the substrates for all depositions. Prior to deposition, they were cleaned in acetone for 10 minutes, in distilled water for 10 min and rinsed with isopropyl alcohol and dried under nitrogen flow. Since it is known that many metals do not grow epitaxially on oxides at room temperature, and the temperature limit for Zn is limited by the sublimation temperature, the growth of Zn was also studied on Ru and Ti buffer layers. Ru films were deposited by sputtering on sapphire substrate at 600°C, following the procedure developed by Sutter et al. [6]. Electron-beam evaporation was used to deposit Ti films [7] on the sapphire substrate at 200°C at deposition rate of 0.2 angstrom/s. Samples were coated with 5 nm Pt film prior to observation with SEM.

## 3. Results and Discussion

Deposition of Zn in different conditions resulted in markedly different morphologies of the film (see Fig.1)

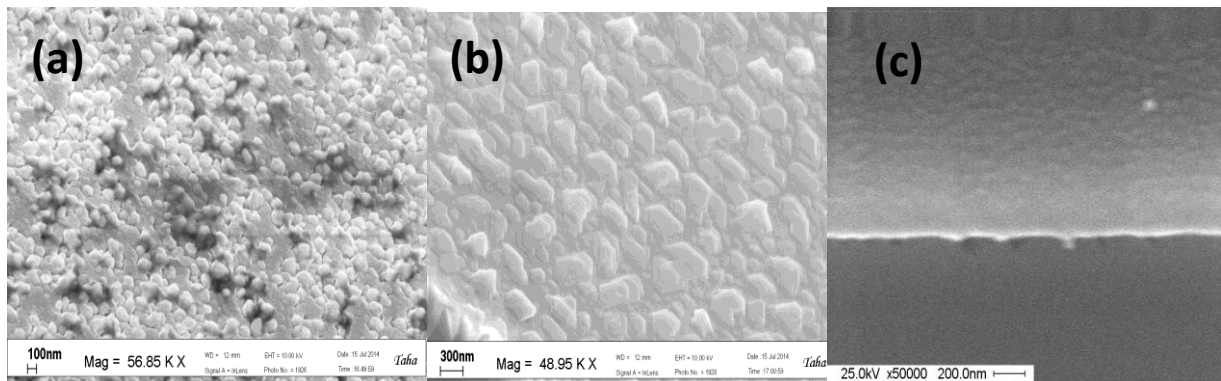


Fig.1. SEM images of Zn films evaporated on Ru at room temperature (a) and at 100°C (b), and on Ti at room temperature.

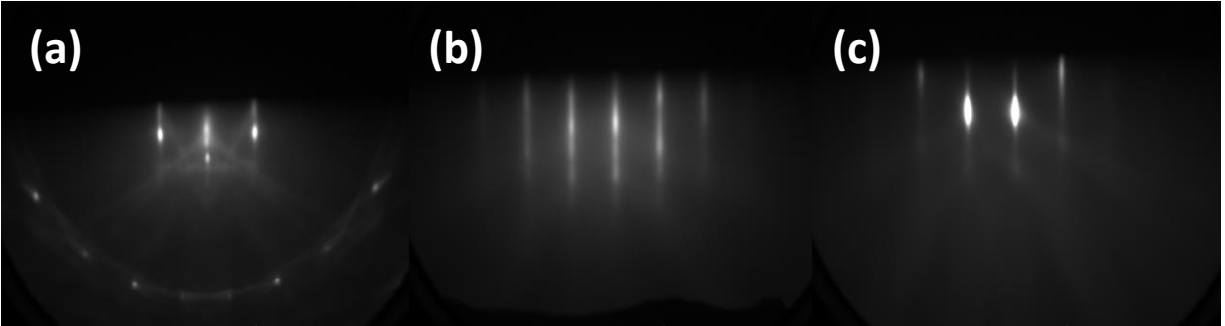


Fig. 2. RHEED images of: (a) sapphire substrate, (b) 100 nm film of Ti deposited by e-beam evaporation at 200°C and (c) 100 nm film of Zn evaporated on top of Ti at room temperature.

Deposition of Zn by the means of sputtering or evaporation directly on sapphire substrate always resulted in island growth and formation of large well separated grains. The films with this kind of morphology cannot serve as sacrificial layers. Better results were achieved using electron-beam evaporation on top of Ru buffer layer. Depositions were made at room temperature, 50°C and at 100°C using small deposition rate of 0.2 angstrom/s and moderate rate of 1 angstrom/s. The increasing substrate temperature promoted growth of larger crystals with better crystallinity. A comparison between morphologies of films deposited at room temperature and at 100°C is presented in Fig. 1. Higher deposition rates gave rise to reduced grain size of the polycrystalline films. Relatively smooth polycrystalline films with fine grain size were evaporated at higher rates and at room temperature. They can be used as sacrificial layers for polycrystalline films.

The most promising results were achieved for deposition of Zn on Ti buffer layer. Morphology of the film deposited on Ti is presented in Fig.1 (c) and no granular structure has been observed in this case. Electron diffraction patterns measured with RHEED at 20 keV represent: (a) substrate, (b) film of Ti and (c) Zn film on top of Ti.

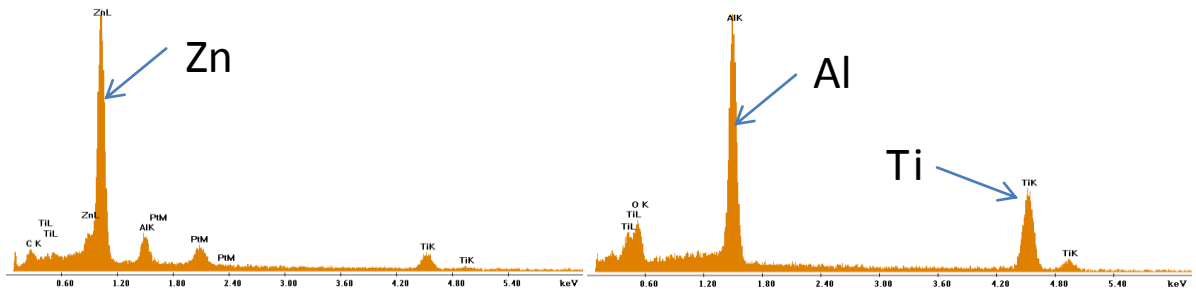


Fig. 3. EDS graphs for the Zn film (left) prior to sublimation and after sublimation (right graph)

Although additional TEM studies of the film would give more details about the microstructure, the image in Fig 2c provides evidence for sufficient crystallinity of the Zn film to serve as a template for growing heteroepitaxial films. Figure 3 shows EDS spectra of the film surface prior to and after sublimation of Zn. No Zn peak was observed after sublimation took place. Similar results were received from the Auger spectroscopy.

#### 4. Conclusions

Because of lack of literature data on the growth of single crystalline Zn films, we carried out pioneering studies to establish the best growth conditions. Zn film is envisioned as an excellent candidate for the sacrificial layer for micro-origami patterns, because it can be selectively removed by sublimation in vacuum at relatively low temperatures. Because the films grown by sputtering and e-beam evaporation directly on sapphire substrate were polycrystalline and rough, Ru and Ti buffer layers were deposited on sapphire. Although, both Ru and Ti films were good quality single crystals, as evidenced by RHEED patterns, smoother films were found to grow at room temperature by e-beam evaporation on Ti buffer layer. Further refinements of deposition conditions on single crystal Ti film, which include adjustment of the substrate temperature and deposition rate, will enable further improvement of the Zn film quality. Zn films were successfully sublimated in vacuum chamber by increasing the substrate temperature to 200°C. Patterns of multilayered films of Co, Ti, Ru or C with hexagonal lattice constant and matching lattice constants will be deposited on Zn and subsequently rereleased by sublimation of the sacrificial layer to form micro-origami patterns.

#### 5. Acknowledgments

The current work is funded by the NSF EPSCoR LA-SiGMA project under award #EPS-1003897.

#### 6. References

- [1] Prinz VY, Seleznev VA, Gutakovskiy AK, Chehovskiy AV, Preobrazhenskii VV, Putyaot MA, Gavrilova TA (2000), "Free-standing and overgrown InGaAs/GaAs nanotubes, nanohelices and their arrays," *Physica E* vol. 6, pp. 828-831
- [2] S. Min, J.H. Lim, J. Gaffney, K. Kintle, J. B. Wiley, L. Malkinski, "Fabrication of scrolled magnetic thin film patterns", *J. Appl. Phys.*, **111**, 07E518 (pp.1-3) (2012)
- [3] S.-G. Min., J. Gaffney, R. Eskandari, J. Tripathy, J.-H. Lim, J. B. Wiley and L. Malkinski, "Novel approach to control diameter of self-rolled magnetic microtubes by anodizing Ti layer" *Magnetics Letters*, **3**, 4000304, pp.1-4 (2012)
- [4] L. Malkinski, "Magnetics with a twist", *Magnetics Technology International magazine*, pp 8-14, 2013
- [5] T. Yamaguti and Y. Watanabe, Sublimation of cleaved surfaces of zinc and galena single crystals, *Thin Solid Films* **147**, 57-64 (1987)
- [6] P. W. Sutter, P. M. Albrecht and E.A. Sutter, Graphene Growth on Epitaxial Ru thin films on sapphire, *Appl/Phys. Lett.* **97**, 213101 pp.1-3 (2010)
- [7] S. Rao Peddada, I. M. Robertson, and H.K. Binbaum, Growth of Ti thin films on sapphire substrate, *J. Materials Research* **12** (7) pp. 1856-65 (1997)

## **Parallelizing Protein Docking Code to Accelerate Drug Discovery**

**Brad Burkman<sup>1</sup>, Michal Brylinski<sup>2,3</sup>, Wei Feinstein<sup>2,3</sup>**

<sup>1</sup>Department of Mathematics, Louisiana School for Math, Science, and the Arts

<sup>2</sup>Center for Computation and Technology, Louisiana State University

<sup>3</sup>Department of Biology, Louisiana State University

**Abstract:** The majority of drugs work by binding to specific regions of pharmacologically relevant proteins (enzymes, receptors, regulatory proteins, etc.) to attenuate or even impair their molecular functions. Because protein-protein interaction sites are attractive targets for therapeutics, the accurate modeling of protein assemblies at the atomic level is critical in modern computer-aided drug discovery.

This work took an academic version of ZDOCK, one of the most widely used protein docking algorithms, and attempted to speed up the code through parallelization on multiple CPU cores, as well as using MIC and GPU accelerators. In anticipation of LSU's new SuperMIC cluster becoming operational, this study used the Stampede cluster, an XSEDE resource at the Texas Advanced Computing Center.

Thus far, a ten-fold speedup has been achieved using just the sixteen cores on the CPU and a four-fold speedup by offloading Fast Fourier Transforms to the GPU. Work with the MIC continues. By combining and refining these techniques, hope for a twenty-fold speedup in this key step in drug discovery is reasonable.

**Keywords:** Parallel Computing, Computational Biology, Protein Docking, GPU, MIC

### **1. Introduction**

This project sought to accelerate one step in the process of drug discovery by cutting the time required to execute a widely used protein docking algorithm, ZDOCK.

The process of drug discovery often starts with a target protein (human enzyme, receptor, regulatory protein), many (perhaps thousands of) drug candidates, and often other proteins whose interaction with the drug would cause side effects. With thousands of proteins and thousands of drug candidates (“ligands”), millions of interactions must be considered to determine which drug candidates (if any) are most likely to have the desired effect on the target protein without having undesired effects on other proteins.

Testing these millions of interactions experimentally is not feasible. Using insights from molecular dynamics, software like ZDOCK can score and rank the likelihood that a drug candidate (ligand) will dock with a particular

protein. Using the results from scoring (some subset of) the millions of interactions, biologists hope to identify the best candidates for experimental testing.

The design and usage of ZDOCK requires expertise in four areas. First, the decision of which proteins and ligands to consider require understanding in medicine, pharmacology, and biology. Next, the protein structure and molecular dynamics expertise come from chemistry and physics. Third, at the heart of the scoring mechanism are Fast Fourier Transforms (FFT), an unusual application of well-established mathematics. Finally, the computation of those FFT's, either in serial or in parallel, across different types of hardware, is a computer science problem.

This summer project, part of the Research Experiences for Teachers program attached to the LA-SiGMA REU Site, focused on the last area, making the code run faster. Given any ligand and protein, can we get the same results faster?

## **2. Hardware Options**

In anticipation of the SuperMIC cluster coming online, this project used the Stampede cluster at the Texas Advanced Computing Center (TACC). Both clusters have Intel multi-core central processing units (CPU), Intel Many-Integrated Core coprocessors (MIC), and NVIDIA general-purpose graphics processing units (GPU). Each CPU has several fast and powerful cores, each MIC has smaller cores (but more of them), and each GPU has thousands of tiny cores.

## **3. Serial Code Profile**

At the heart of the code is a loop of thousands of independent processes, each requiring several Fast Fourier Transforms.

Section of Code	Runtime (Seconds)	Runtime (Proportion)
Before loop	1.94	0.57 %
Loop	340.38	<b>99.32 %</b>
After loop	0.39	0.11 %

Code with this type of profile are so susceptible to parallelization that they are called “embarrassingly parallelizable” on the CPU or across nodes.

#### **4. Parallelizing for one CPU**

The ZDOCK code with which the project began ran in serial, only using one CPU core. Stampede nodes have sixteen-core CPU's, and SuperMIC will have twenty-core CPU's. The first step in parallelizing the big loop was to determine which data needed to be private to each thread, and which data could be shared (public). Putting an OpenMP pragma around the reorganized loop gave about ten times speedup.

#### **5. Parallelizing for one GPU**

The GPU parallelization took a different model. Rather than run several FFT's simultaneously, the GPU can do each FFT calculation, one at a time but faster, because optimized cuFFT libraries automatically parallelize the computation of the FFT on the GPU. The cuFFT library requires different data organization, so most of the code had to be revised. Currently, the code uses one CPU core to organize the data for each FFT, send the data to the device, calculate the FFT on the device, and copy the data back to the CPU to calculate scoring. Future plans include calculating the scoring on the device, and utilizing the other cores of the CPU.

The results from the current code for the GPU are the same (allowing for double/float rounding) up until an inverse FFT. The XSEDE Extended Collaborative Support Services group is helping diagnose the source of the discrepancies.

#### **6. Parallelizing on one MIC**

The MIC offers great potential for accelerating science, but the hardware technology is new and the software to utilize it effectively, including FFT libraries, has not fully developed. Passing data for FFT calculation to the MIC is possible but not as straightforward as for the GPU, because the fftw structs have to be flattened and reconstructed by hand. Doing FFT on the MIC is possible, but not the low-hanging fruit that the GPU parallelization was.

#### **7. Parallelization Results**

Parallelizing on the sixteen cores of the CPU achieved about ten-fold speedup. Calculating the FFT's on the GPU made the serial code run about four times faster. Combining these two techniques may achieve twenty-fold speedup.

Protein Size	Serial Code (Seconds)	Parallel on CPU (Seconds)	Speedup on CPU	Parallel on GPU (Seconds)	Speedup on GPU
Small	319	33	<b>9.5 x</b>	110	<b>2.9 x</b>
Medium	1410	112	<b>12.5 x</b>	342	<b>4.1 x</b>
Large	14000	1230	<b>11.4 x</b>	2800	<b>5.0 x</b>

## 8. Future Work

Future work should use the CPU and GPU effectively together (hoping for 20x speedup), determine whether the MIC is a useful tool for this project, and expand to multiple nodes using MPI. Once the CPU/GPU version is debugged and tested, user-friendly documentation should be written and the code released to the community.

## 9. Acknowledgments

This material is based upon work in the LA-SiGMA Research Experiences for Teachers program, supported by the National Science Foundation under the NSF EPSCoR Cooperative Agreement No. EPS-1003897 with additional support from the Louisiana Board of Regents.

This work used the computing resources of the Extreme Science and Engineering Discovery Environment (XSEDE), which is supported by National Science Foundation grant number OCI-1053575.

## Periodic Anderson model with electron phonon interaction and its antiferromagnetic susceptibility

Enzhi Li<sup>1</sup>, Peng Zhang<sup>2</sup>

Ka-Ming Tam<sup>1,3</sup>, Shuxiang Yang<sup>1,3</sup>, Juana Moreno<sup>1,3</sup>, Mark Jarrell<sup>1,3</sup>

<sup>1</sup>Department of Physics and Astronomy, Louisiana State University

<sup>2</sup>Carnegie Institute of Washington

<sup>3</sup>Center for Computation and Technology, Louisiana State University

**Abstract:** The periodic Anderson model (PAM) has been used to study the heavy-fermion behavior of transition metals. Recently, PAM with electron-phonon interaction was introduced to explain the volume collapse of Cerium under high pressure. It has been shown that PAM with electron-phonon interactions gives rise to two phases, local moment and Kondo singlet, which are separated by a first order phase transition line that terminates at a second order phase transition point. However, the local moment phase is beset by the residual entropy problem at low temperature, and thus an ordering at low temperature is expected. In this work, we show the evidence for a phase transition that renders the local moment antiferromagnetically ordered at low temperature.

**Keywords:** Period Anderson Model, heavy fermions

### 1. Introduction

Various scenarios have been proposed to explain the experimental observation of the volume collapse of Cerium [1], among which the Mott transition and Kondo volume collapse are the two leading theories. The Kondo volume collapse scenario can be studied via the microscopic periodic Anderson model (PAM). The PAM has been extensively used for studying heavy-fermion behavior of transition metals [2, 3]. The dynamical mean field approximation (DMFT) [4, 5, 6, 7], which is exact in infinite dimension, was widely used to tackle this problem. Recent experiments of the volume collapse of Cerium suggested that the electron-phonon coupling contributes a substantial amount of entropy to the first order transition [8]. This triggered our interest in studying the effect of electron-phonon coupling in the PAM. Some interesting results have emerged in recent publications [9]. According to Ref [9], two phases, local moment and Kondo singlet may emerge due to the electron-phonon interaction in the PAM, and a second order phase transition point was approximately located. However, we know that the local moment phase could not possibly persist at extremely low temperature, and thus at low temperatures, an ordered phase, which is believed to be antiferromagnetic in nature, is expected. In this proceedings, we study the nature of the anticipated ordered phase by studying the behavior of the antiferromagnetic susceptibility for different model parameters.

### 2. Model Hamiltonian

In the Anderson model, there are two kinds of electrons,  $c$  electrons, and  $f$  electrons. The  $c$  electrons may hop from one site to its nearest neighbor site, while  $f$  electrons can only move in form of hybridization with  $c$  electrons. The periodic Anderson model with electron-phonon interaction can be described by this Hamiltonian:

$$\hat{\mathcal{H}} = \hat{\mathcal{H}}_0 + \hat{\mathcal{H}}_{int}$$

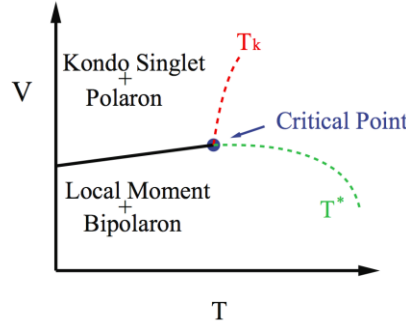
$$\hat{\mathcal{H}}_0 = -t \sum_{\langle i,j \rangle, \sigma} (c_{i,\sigma}^\dagger c_{j,\sigma} + c_{j,\sigma}^\dagger c_{i,\sigma}) + \epsilon_f \sum_{i,\sigma} f_{i,\sigma}^\dagger f_{i,\sigma} + V \sum_{i,\sigma} (c_{i,\sigma}^\dagger f_{i,\sigma} + f_{i,\sigma}^\dagger c_{i,\sigma}) + \sum_i \left( \frac{P_i^2}{2m} + \frac{1}{2} k X_i^2 \right)$$

$$\hat{\mathcal{H}}_{int} = U \sum_i n_{i,\uparrow}^f n_{i,\downarrow}^f + g \sum_{i,\sigma} n_{i,\sigma}^c X_i$$

Here, in the Hamiltonian,  $t$  is the energy it takes for one electron to hop to its nearest neighbor site,  $c_{i,\sigma}^\dagger$  ( $c_{i,\sigma}$ ) creates (annihilates) a  $c$  electron with spin  $\sigma$  one site  $i$ . The same rules apply to  $f_{i,\sigma}^\dagger$  and  $f_{i,\sigma}$ , except that they create and annihilate  $f$  electrons, respectively.  $\epsilon_f$  is the energy of  $f$  electron on one site,  $V$  is the hybridization strength between  $c$  electrons and  $f$  electrons,  $P_i$  is the momentum for on phonon, and  $X_i$  is the displacement of a phonon.  $U$  is the interaction strength between two  $f$  electrons on the same site, and  $g$  measures the interaction strength between one phonon and a  $c$  electron. We have made the assumption that only  $c$  electrons can couple to phonons, and thus there is only one electron-phonon interaction term in the interaction Hamiltonian. Under the DMFT approximation, this periodic Anderson model was mapped to a single impurity Anderson model, and the continuous time quantum Monte Carlo method [10] was used to solve this impurity problem.

### 3. Bethe-Salpeter equation and susceptibilities

It has been established in Ref [9] that there are two phases for PAM, the local moment phase, and Kondo singlet phase. The phase diagram from Ref [9] is shown below ( $V$  is the hybridization strength between  $c$  and  $f$  electrons,  $T$  is the temperature):



According to this phase diagram, the two phases are separated by a first order phase transition line that terminates at a critical point. The critical point is approximately pinpointed at  $V_c = 0.96, T_c = \frac{1}{60}$ . We believe that the local moment phase could not persist at low temperature, and there should be a phase transition from disordered local moment phase to an ordered phase, which is believed to be antiferromagnetic in nature. To study this disorder to order phase transition, antiferromagnetic susceptibilities were calculated. Under the DMFT approximation, antiferromagnetic susceptibility should behave as this:

$$\chi_{antiferro} \propto \frac{1}{T - T_c}$$

Here,  $T_c$  is the antiferromagnetic transition temperature that may depend on the value of hybridization value  $V$ , and the electron-phonon interaction strength. To calculate the antiferromagnetic susceptibility, we need to calculate the two particle Green's function with the help of Bethe-Salpeter (BS) equation[3].

Bethe-Salpeter equation relates the bare susceptibility with the fully interacting susceptibility, and can be written as:

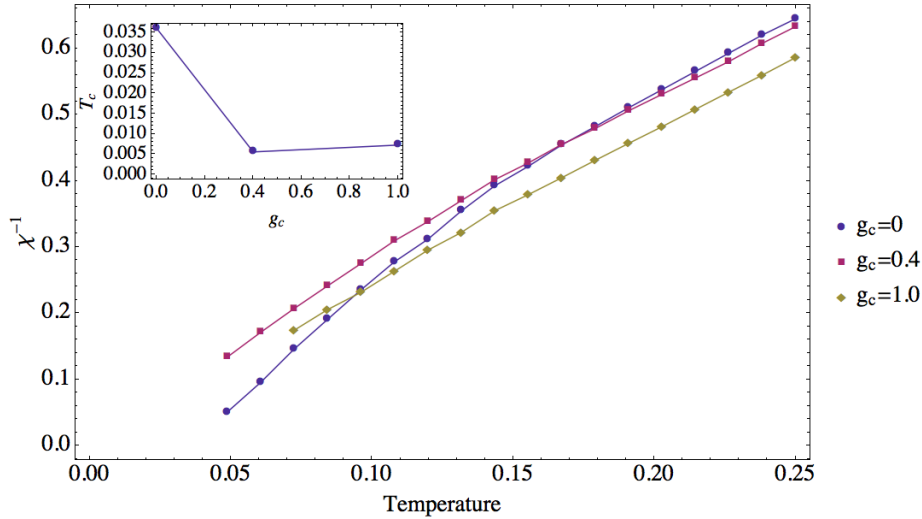
$$\chi_z^{\gamma\delta\alpha\beta}(i\omega_n, i\omega_{n'}) = \delta_{nn'} \chi_0^{\gamma\delta\alpha\beta}(i\omega_n) + \chi_0^{ab\alpha\beta}(i\omega_n) \Gamma_{cd,z}^{ab}(i\omega_n, i\omega_{n'}) \chi_z^{\gamma\delta dc}(i\omega_{n'}, i\omega_n)$$

Here, in this equation,  $\chi_z$  is the fully interacting susceptibility,  $\chi_0$  is the bare susceptibility, and  $\Gamma_z$  is the vertex function that is assumed to be independent of momentum under DMFT approximation. The above equation is an iterative equation, and can be solved as [5, 7]

$$\chi_{\mathbf{q}}^{-1} = \chi_{loc}^{-1} + [\chi_{\mathbf{q}}^0]^{-1} - [\chi_{loc}^0]^{-1}$$

We can find the value of  $\chi_{loc}$  using Monte Carlo impurity solver, and once we know the value of  $\chi_{\mathbf{q}}^0$  which is the bare lattice susceptibility, we can calculate out the fully interacting lattice susceptibility.

Since we are trying to find the phase transition from local moment to antiferromagnetic state, we should set our hybridization value below  $V_c \approx 0.96$ . The figure below plots the inverse of antiferromagnetic susceptibility versus temperature when  $V = 0.6$ ,  $U = 4$ , with electron-phonon interaction strength  $g_c$  as a tuning parameter.



As can be seen from the above picture, the antiferromagnetic transition temperature, which is identified as the extrapolated point where  $\chi^{-1}$  vanishes, is positive, indicating the existence of a phase transition. The inset of the figure plots the extrapolated transition temperature as a function of electron-phonon interaction strength. The trend is clear from the inset that as electron-phonon interaction strength increases, the antiferromagnetic transition temperature decreases. The physical reason for this is that antiferromagnetic correlation between local moments is mediated by Ruderman-Kittel-Kasuya-Yosida (RKKY) interaction[2, 11, 12], which may be reduced by the mass renormalization of  $c$  electrons due to their coupling to phonons. However, it has not escaped our attention that

when  $g_c$  increases from 0.4 to 1.0, the curve for transition temperature is almost flat. In this region, maybe some other mechanisms are playing their role.

#### 4. Conclusion

We have shown that there is a phase transition from local moment phase to antiferromagnetic phase for certain range of parameters. The transition temperature is not a constant; rather, they change when the electron phonon interaction strength is modified. The trend is that as electron-phonon interaction strength increases, the transition temperature tends to decrease.

#### 5. Acknowledgments

The current work is funded by the NSF EPSCoR LA-SiGMA project under award #EPS-1003897.

#### 6. References

- [1] Lawson, A. W., and Ting-Yuan Tang. "Concerning the high pressure allotropic modification of cerium." *Physical Review* 76.2 (1949): 301.
- [2] Jarrell, M., Hossein Akhlaghpour, and Th Pruschke. "Periodic Anderson model in infinite dimensions." *Physical Review Letters* 70.11 (1993): 1670.
- [3] Jarrell, M. "Symmetric periodic Anderson model in infinite dimensions." *Physical Review B* 51.12 (1995): 7429.
- [4] Müller-Hartmann, E. "The Hubbard model at high dimensions: some exact results and weak coupling theory." *Zeitschrift für Physik B Condensed Matter* 76.2 (1989): 211-217.
- [5] Jarrell, M. "Hubbard model in infinite dimensions: A quantum Monte Carlo study." *Physical review letters* 69.1 (1992): 168.
- [6] Freericks, J. K., M. Jarrell, and D. J. Scalapino. "Holstein model in infinite dimensions." *Physical Review B* 48.9 (1993): 6302.
- [7] Georges, Antoine, et al. "Dynamical mean-field theory of strongly correlated fermion systems and the limit of infinite dimensions." *Reviews of Modern Physics* 68.1 (1996): 13.
- [8] I.-K. Jeong, T. W. Darling, M. J. Graf, Th. Proffen, R. H. Heffner, Yongjae Lee, T. Vogt, and J. D. Jorgensen "Role of the Lattice in the  $\gamma \rightarrow \alpha$  Phase Transition of Ce: A High-Pressure Neutron and X-Ray Diffraction Study" *Physical Review Letters*. 92, 105702 (2004).
- [9] Zhang, Peng, et al. "Periodic Anderson model with electron-phonon correlated conduction band." *Physical Review B* 87.12 (2013): 121102.
- [10] Assaad, F. F., and T. C. Lang. "Diagrammatic determinantal quantum Monte Carlo methods: Projective schemes and applications to the Hubbard-Holstein model." *Physical Review B* 76.3 (2007): 035116.
- [11] Ruderman, Melvin A., and Charles Kittel. "Indirect exchange coupling of nuclear magnetic moments by conduction electrons." *Physical Review* 96.1 (1954): 99.
- [12] Van Vleck, J. H. "Note on the Interactions between the Spins of Magnetic Ions or Nuclei in Metals." *Reviews of Modern Physics* 34.4 (1962): 681.

## Quantum chemistry studies of $\text{Zn}^{2+}$ and $\text{Mg}^{2+}$ ions in aqueous environments

Lisa Hartman,<sup>1</sup> Marielle Soniat,<sup>2</sup> and Steven W. Rick<sup>2</sup>

<sup>1</sup>Benjamin Franklin High School

<sup>2</sup>Department of Chemistry, University of New Orleans

**Abstract:** Charge transfer is an important contribution to the interaction between ions and water. Using quantum methods, such as DFT (TPSS, PBE), HF, and MP2 in various combinations, the optimal distances between the metal ions  $\text{Mg}^{2+}$  and  $\text{Zn}^{2+}$  and water molecule(s) are determined. By altering the distances between the metal ion and the water molecules, the charge and charge transfer per water molecules are examined. Data from different charge partitioning methods, including electrostatic potential (ESP) fitting and atoms in molecules or Bader partitioning, are compared. The charge transfer amounts are included in a simple expression as part of a molecular mechanics force field which includes charge transfer interactions. Overall, the results indicate significant amounts of charge transfer between water and the divalent ions. This amounts to about 0.03 of an electron per water molecule, or 0.18  $e$  to the full six-member solvation shell for  $\text{Mg}^{2+}$ .

**Keywords:** charge transfer, molecular dynamics, zinc, magnesium, atoms in molecules

### 1. Introduction

It has been found that in aqueous solutions of ions, the charge of the metal ion results in a non-integer quantity due to the transfer of charge to the ion from the surrounding water molecules.<sup>1</sup> The purpose of the project was to develop a charge transfer model for aqueous solutions of  $\text{Zn}^{2+}$  and  $\text{Mg}^{2+}$ . Quantum mechanical calculations were performed using the Hartree-Fock and Density Functional Theory methods to determine the charges of the ions after charge transfer. Various structures were studied, including dimers, trimers, six-water clusters and also water clusters which included up to eighteen waters found in the first and second shells of the structure. Understanding how charge is transferred in such multi-body aqueous systems involving  $\text{Zn}^{2+}$  and  $\text{Mg}^{2+}$  ions will enhance the study of biological functions, such as those revolving around maintaining homeostasis of the human body.

### 2. Methods

The approach to studying charge transfer involved using the results of quantum mechanical calculations (using the Gaussian software<sup>2</sup>) to parameterize potentials for molecular dynamic simulations. Quantum calculations were

performed for various  $\text{Zn}^{2+}$  and  $\text{Mg}^{2+}$  structures with water. The geometries of ion-water dimers were optimized using density functional theory. Hartree-Fock, Moller-Plesset perturbation theory (MP2), and density functional theory methods were used to study the amount of charge transferred. The basis set for water and magnesium is aug-cc-pvTz. For zinc, an ECP (effective core potential) is used. In the zinc-water dimers, no significant difference in charge transfer is found between the cc-pvDz basis set and the MDF10 ECP. Data obtained from these calculations included total energy and charge of the metal ion obtained using an ESP (electrostatic potential) fit for the structures. These charges were then compared to charges determined by AIM<sup>3,4</sup> (atoms in molecules).

For  $\text{Mg}^{2+}$ , parameters were optimized using the SOP (simplex optimization program) method. The SOP uses a merit function which is minimized so that the differences between the target and calculated properties of the various structures of the magnesium ion are as small as possible. Having good parameters allows for accurate calculation of  $\text{Mg}^{2+}$  and  $\text{Zn}^{2+}$  properties from molecular dynamics simulations.

**Table I:** Target Properties for ion-water interactions. These properties are an aggregate of high-level quantum mechanical data and experiment.

Ion	Dimer Properties		Aqueous Properties					
	$E_{\text{min}}$ kcal/mol	$r(\text{M-O})$ Å	$g(r)_{\text{M-O}}$ 1 <sup>st</sup> max	$r_{\text{mzx}}$ Å	$g(r)_{\text{M-O}}$ 1 <sup>st</sup> min	$r_{\text{min}}$ Å	$2^{\text{nd}} r_{\text{max}}$ Å	$n_{\text{coord}}$
$\text{Mg}^{2+}$	-99.0	1.86	17	2.08	0	3.08	4.3	6.0
$\text{Zn}^{2+}$	-78.8	1.94	16	2.04	0	2.91	4.4	6.0

### 3. Results and Discussion

The  $\text{Zn}^{2+}$ -water distances are shorter than the  $\text{Mg}^{2+}$  water distances. The water geometry is more distorted from the geometry of an isolated water molecule when in complex with zinc. Charge transfer (CT) is greater from water to zinc than from water to magnesium. As the distance between the ion and water is increased, CT decreases exponentially. The ion-water distances are the same when the ions are surrounded by six waters. The amount of CT per water decreases when more water molecules are coordinated to the ion. The charge of each ion in aqueous solution is expected to be similar to its charge when coordinated by six waters (the same as both ions' aqueous coordination number), namely  $q(\text{Zn}) = 1.57 e$  and  $q(\text{Mg}) = 1.81 e$ .

**Table II:** Magnesium QM CT Data

Structure	Optimization method	r (M-O) Å	Charge method	ESP+d q(M) e	AIM q(M) e	CT per water
Mg <sup>2+</sup> •(H <sub>2</sub> O)	TPSS	1.93	HF	1.9401	1.9333	0.0667
			MP2	1.9308	1.9256	0.0745
			TPSS	1.9079	1.9079	0.0921
Mg <sup>2+</sup> •(H <sub>2</sub> O) <sub>6</sub>	PBE	2.11	HF	2.0240	1.8374	0.0271
	HF	2.10	HF	2.4144	1.8354	0.0274
	TPSS	2.10	TPSS	2.1425	1.7888	0.0352
			HF	2.4275	1.8321	0.0279

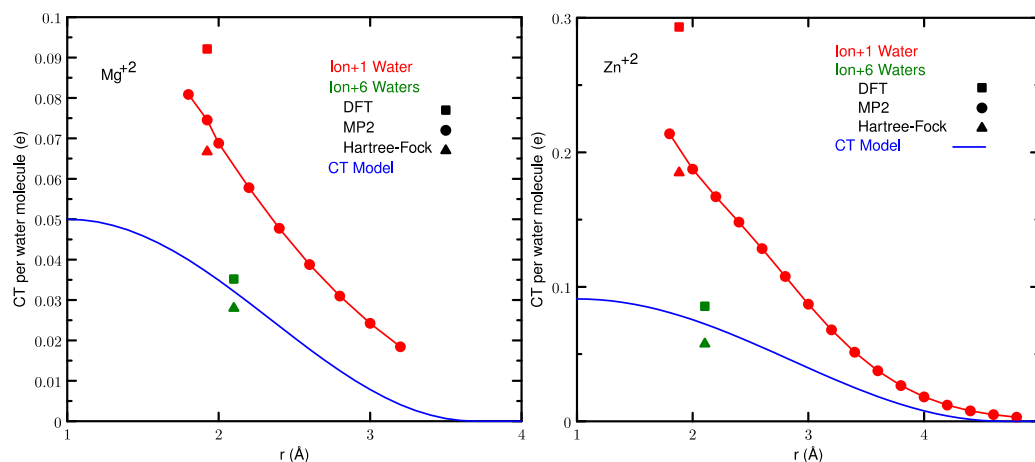
**Table III:** Zinc QM CT Data

Structure	Optimization method	r (M-O) Å	Charge method	ESP+d q(M) e	AIM q(M) e	CT per water
Zn <sup>2+</sup> •(H <sub>2</sub> O)	TPSS	1.87	HF	1.8798	1.8293	0.1707
			MP2	1.8449	1.7882	0.2118
			TPSS	1.7886	1.7357	0.2643
	TPSS-GD3BJ	1.88	TPSS	1.7505	1.7068	0.2932
			MP2	1.8198	1.7699	0.2301
			HF	1.8587	1.8151	0.1849
Zn <sup>2+</sup> •(H <sub>2</sub> O) <sub>6</sub>	TPSS	2.11	TPSS	2.1202	1.4868	0.0855
			HF	2.4032	1.6546	0.0576
	PBE	2.10	HF	2.3342	1.6586	0.0569

Ongoing research is focused on determining if the amount of CT between water molecules is altered by the presence of a divalent cation. Previous results show that monovalent cations and halide anions do not alter the CT between water molecules.<sup>1</sup> To investigate this, structures with 6+4, 6+8, and 6+12 coordination, where the first number indicates the waters directly coordinated to the ion and the second number shows the waters coordinated to the first solvation shell waters, were optimized. The charge of the waters in the second solvation shell is expected to be +0.04e, based on the hydrogen bond imbalance, if the ion does not affect the water-water CT. So far, the results are inconclusive, as they are highly dependent on basis set.

Parameters which fit the CT model to the quantum data have been found, and the fit is shown in Figure 1.

**Figure 1:** Charge transfer between water and  $Mg^{2+}$  (left) and  $Zn^{2+}$  (right) from AIM.



#### 4. Conclusion

Quantum mechanical calculations have been carried out on  $Zn^{2+}$ - and  $Mg^{2+}$ -water systems. The amounts of charge transfer (CT) have been calculated for these systems and will inform the parameterization of a molecular dynamics model which includes CT

#### 5. Acknowledgments

The current work is funded by the NSF EPSCoR LA-SiGMA project under award #EPS-1003897.

#### 6. References

- [1] Marielle Soniat and Steven W. Rick. *The Journal of Chemical Physics*. 137, 044511 (2012).
- [2] Gaussian 09, Revision D.01, M. J. Frisch, *et al.*, Gaussian, Inc., Wallingford CT, 2013.
- [3] R. F. W. Bader, *Atoms in Molecules- A Quantum Theory* (Oxford University Press, Oxford, 1990).
- [4] AIMAll (Version 13.05.06), Todd A. Keith, TK Gristmill Software, Overland Park KS, USA, 2013.

# QUANTUM COHERENT MANIPULATION OF TWO-LEVEL SYSTEMS IN SUPERCONDUCTING CIRCUITS

Alexander Burin<sup>1</sup>, Andrii Maksymov<sup>1</sup>, Kevin Osborn<sup>2</sup>

<sup>1</sup>Department of Chemistry, Tulane University, New Orleans, LA 70118, USA

<sup>2</sup>Laboratory for Physical Sciences, 8050 Greenmead Drive, College Park, MD 20740, USA

**Abstract:** The number one problem for any quantum computer designer is protecting qubit quantum state from decay, thus keeping information undamaged during calculations. Usually it is done by adding error correctors or shadow lattices. But what if we can make the environment of qubits, which usually serves as a source of decoherence, act in a useful way? We introduce an approach that allows one to minimize energy losses in qubits by manipulating surrounding two-level systems (TLSs) in a coherent way through simultaneous application of time-varying bias and continuous microwave fields. Deleterious effects of TLSs can be thus eliminated by the population inversion produced in a Landau-Zener passage of TLSs through resonance with the AC microwave field.

**Keywords:** two-level systems, population inversion, Landau-Zener passage

## 1. Introduction

Nanoscale two-level tunneling systems, also referred as two-level systems (TLSs), are found within various dielectrics used for circuits of superconducting qubits, including interlayer dielectrics, native oxides at surfaces and Josephson junction barriers. TLSs usually bring decoherence [1] in these circuits, but superconducting qubits can also experience a benefit from TLSs if manipulated coherently e.g. if their population (occupation) is controlled. The latter can be performed in a consequence of Landau-Zener crossings created by TLSs passing through resonance with the AC mode of a superconducting microwave resonator.

We investigate the control of TLSs using AC field and time-varying bias as [2,3] to get rid of their destructive influence on qubits instead of constructing protective shadow lattices as [4].

In the standard model of TLSs for amorphous insulators, double well energy potentials (figure 1) are used to describe spatial tunneling between two nanoscale atomic configurations. In this model the energy of the TLS,

$E = \sqrt{\Delta^2 + \Delta_0^2}$ , is a function of the asymmetry energy,  $\Delta$ , and the tunneling energy,  $\Delta_0$ . The application of time-varying bias affects the TLS asymmetry,  $\Delta$ , as experienced by the TLS dipole moment,  $\mathbf{p}$ , which makes TLSs with different asymmetry pass the resonance sequentially, thus avoiding saturation of TLSs with resonant asymmetry at large fields. The tunneling energy can be treated as a constant [5].

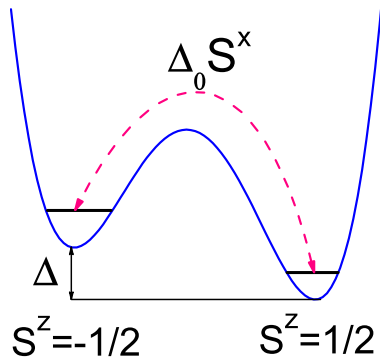


Fig 1. The potential of a tunneling two-level system in an amorphous solid.  $\Delta$  is the energy difference between the left and right well, with similar curvature near their minima. The energy states are coupled with tunneling amplitude  $\Delta_0$ .

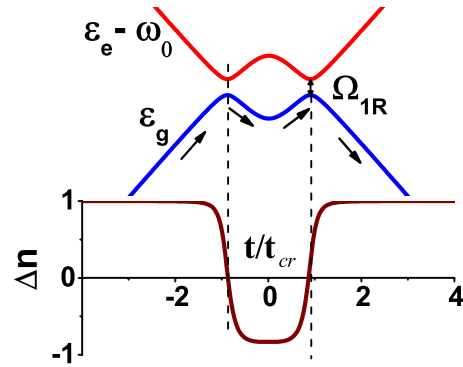


Fig 2. Two-level system population inversion due to the adiabatic passage through resonances. Curves on top show adiabatic quasi-energies of TLS ground and excited states. Bottom graph illustrates the population difference changing in time.

The TLS energy passage through resonance creates the Landau–Zener crossing shown in figure 2, where  $\Omega_{1R}$  is the TLS Rabi frequency and  $\varepsilon_{g,e}$  are quasi-energies of TLS ground and excited states. With only two single photon resonances considered, a slow sweep will invert the TLS population at the first crossing ( $t = t_- = -t_{cr}$ ), and in the absence of relaxation will return to the ground state population at the second crossing ( $t = t_+ = t_{cr}$ ).

This population inversion will form the gain for electromagnetic waves in the related frequency domain. In order to study the effect of population inversion we performed several numerical simulations.

## 2. Model and simulations

The simulations assume the low-temperature regime ( $T < 50\text{mK}$ ), such that the thermal energy is much smaller than the resonant TLS energy. At this temperature TLS dephasing is negligible, which is justified by dipolar echo measurements in BK7 glass [6].

The quantum TLS and its dipole moment  $\hat{\mathbf{p}} = 2\mathbf{p}S^z$  can be described using a pseudospin 1/2 operator, where two spin projections  $S^z = \pm 1/2$  correspond to the TLS localization within the left or the right wells, respectively. The Hamiltonian of a TLS interacting with external time-varying bias and microwave field can be expressed as

$$\hat{H} = \hbar(vt - 2\Omega_R \cos(\omega_0 t + \varphi))S^z + \Delta_0 S^x, \quad (1)$$

where  $\Delta = \hbar vt$  and  $\Delta_0$  are the TLS asymmetry and tunneling amplitude, respectively. Here  $v = \mathbf{p}\dot{\mathbf{F}}_{bias}/\hbar$  stays for TLS sweep rate, which is assumed to be constant [3]. TLS asymmetry passes through zero at time  $t = 0$ .

To investigate the single TLS population dynamics under the presence of AC field and time varying bias, we evaluated the TLS population difference considering the evolution of its density matrix. We chose the density matrix approach because relaxations can be conveniently introduced using this representation. The time evolution of Bloch's vector can be described by three differential equations of the form

$$\begin{aligned}\dot{\rho}_x &= -\frac{1}{2}k_1\rho_x + \left(\frac{E(t)}{\hbar} + 2\Omega_R \frac{vt}{E(t)} \cos(\omega_0 t)\right) \rho_y \\ \dot{\rho}_y &= -\frac{1}{2}k_1\rho_y - \left(\frac{E(t)}{\hbar} + 2\Omega_R \frac{vt}{E(t)} \cos(\omega_0 t)\right) \rho_x + 2\Omega_R \frac{\Delta_0}{E(t)} \cos(\omega_0 t) \rho_z \\ \dot{\rho}_z &= -2\Omega_R \frac{\Delta_0}{E(t)} \cos(\omega_0 t) \rho_y - k_1(\rho_z - 1),\end{aligned}\quad (2)$$

where  $k_l = T_l^{-1}$  is the TLS relaxation rate,  $E(t) = \sqrt{v^2 t^2 + \Delta_0^2}$  is the instantaneous adiabatic TLS energy in the absence of an AC field and  $\Omega_R = \mathbf{pF}_{AC}/\hbar$  is the TLS Rabi frequency. Here we ignored TLS dephasing and assumed the equilibrium population difference to be equal to unity within the low temperature limit under consideration,  $k_B T \ll \hbar \omega_0$ .

We focused on  $\Delta n = n_e - n_g$  ( $\rho_z$  in equation (2)) because this parameter describes the population inversion, which takes place at  $\rho_z < 0$ . We investigated TLS population inversion solving equation (2) numerically, choosing the initial time  $t_i$  at the three-photon resonance and the final time  $t_f = -t_i$ . From the Landau-Zener theory [7,8] follows the population inversion after each transition as  $\Delta n = 2e^{-\xi} - 1$  with the Landau-Zener parameter  $\xi = \frac{\pi \Omega_R^2}{2v}$  for the single photon resonance, which is considered for the small Rabi frequency limit  $\Omega_R \ll \omega_0$ .

The effective population difference has been calculated using Monte-Carlo averaging of individual TLS population differences over all the TLS tunneling energies and different TLS dipole orientations. The distribution of TLS tunneling energies is chosen according to the known distribution for amorphous solids [9-11]. The results of calculations show good agreement with Landau-Zener theory for intermediate sweep rates, but for slow passages transfer is weaker than predicted by theory because theory works only for weak TLS-field coupling.

### 3. Influence of relaxation

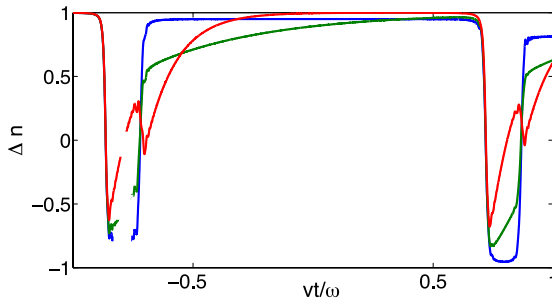


Fig 3. TLS population inversion in the presence of relaxation (factors of  $v/\omega_0$  are shown) for the two AC fields with  $\Delta\omega = 5\Omega_R$  and  $v=0.2\Omega_R^2$ .

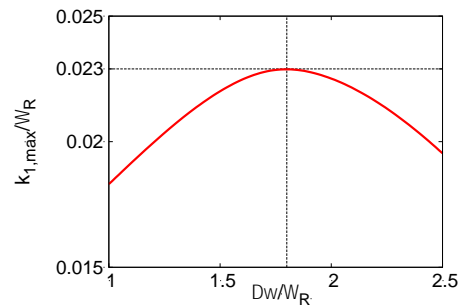


Fig 4. Maximum relaxation rate permitting population inversion as a function of the gain domain bandwidth.

The relaxation process returns TLSs with inverted population back to their ground states. Therefore the relaxation should be avoided during the population inversion domain passage time. This imposes restrictions for the relaxation rate  $k_I \ll \nu/\omega_0$ . If two monochromatic fields with close frequencies are applied then the population inversion occurs in the narrow domain between those two frequencies as shown in figure 3. Thus one may obtain much weaker constraints for the relaxation rate  $k_I \ll \nu/\Delta\omega$ .

Our theoretical expectations are quite consistent with the numerical calculations shown in figure 4. The maximum relaxation rate permitting the population inversion  $k_{I,max} \approx 0.023\Omega_R$  can be reached at the gain bandwidth  $\Delta\omega \approx 1.75\Omega_R$  and energy sweep rate  $\nu \approx 0.4\Omega_R^2$ . This is a much weaker constraint for the relaxation rate compared to the one tone scheme in the practically important case of  $\Omega_R \ll \omega_0$ .

#### 4. Conclusion

We investigated quantum TLS population inversion from adiabatic crossings with photon resonances induced by microwave and time-varying bias fields using density matrix formalism. It is shown that two AC fields setup with close frequencies is more effective to get population inversion in the presence of relaxations. Controlling the population inversion of TLS can reduce losses in nearby circuits. The results of measuring the dipole moment and relaxation rate in thin dielectrics [12] give optimistic prospects for devices with dielectric films.

#### 5. Acknowledgments

The current work is funded by the NSF EPSCoR LA-SiGMA project under award number #EPS-1003897.

#### 6. References

- [1] Martinis M J et al 2005 Phys. Rev. Lett. 95 210503
- [2] Khalil M S, Gladchenko S, Stoutimore M J A, Wellstood F C, Burin A L and Osborn K D 2014 Landau-Zener population control and dipole measurement of a two level system bath submitted to Phys. Rev. B arXiv:1312.4865 [cond-mat.mes-hall]
- [3] Burin A L, Khalil M S and Osborn K D 2013 Phys. Rev. Lett. 110 157002
- [4] Kapit E, Hafezi M and Simon H S 2014 Induced self-stabilization in fractional quantum Hall states of light arXiv:1402.6847v2 [cond-mat.mes-hall]
- [5] Hunklinger S and Raychaudhuri A K 1986 Progr. Low Temp. Phys. 9 265
- [6] Burin A L, Leveritt J M III, Ruyters G, Schötz C, Bazrafshan M, Faßln P, von Schickfus M, Fleischmann A and Enss C 2013 Europhys. Lett. 104 57006
- [7] Landau L 1932 Phys. Sov. Union 2 46
- [8] Zener C 1932 Proc. Roy. Soc. 137 696
- [9] Anderson PW, Halperin B I and Varma CM 1972 Phil. Mag. 25 1
- [10] Phillips W A 1972 Low J. Temp. Phys. 7 351
- [11] Hunklinger S and Raychaudhuri A K 1986 Progr. Low Temp. Phys. 9 265
- [12] Paik H and Osborn K D 2010 Appl. Phys. Lett. 96 072505

## Quantum Confinement Effect on Electron-phonon interaction in Atomically Thin Nb<sub>3</sub>SiTe<sub>6</sub>

J. Hu<sup>1</sup>, X. Liu<sup>1</sup>, C.L. Yue<sup>1</sup>, J.Y. Liu H.W. Zhu, J. Wei<sup>1</sup>, Z.Q. Mao<sup>1</sup>, L.Yu. Antipina<sup>2</sup>, Z.I. Popov<sup>2</sup>, P.B. Sorokin<sup>2</sup>, T.J. Liu<sup>3</sup>, P.W. Adams<sup>3</sup>, J. Heng<sup>4</sup>, D. Natelson<sup>4</sup>

<sup>1</sup>Department of physics and Engineering Physics, Tulane University, New Orleans, USA

<sup>2</sup>Technological Institute for Superhard and Novel Carbon Materials, Moscow, Russia

<sup>3</sup>Department of Physics and Astronomy, Louisiana State University, Baton Rouge, USA

<sup>4</sup>Department of Physics and Astronomy, Rice University, Houston, USA

**Abstract:** Fascinating properties of two dimensional (2D) materials such as graphene and MX<sub>2</sub> (M = Mo or W, X = S, Se) monolayers, highlight the potential that quantum confinement effect may lead to a wide spectrum of distinct properties. In this letter, we report unusual quantum transport properties probed in a new 2D ternary transition metal chalcogenide - Nb<sub>3</sub>SiTe<sub>6</sub> few-layer crystals. We show Nb<sub>3</sub>SiTe<sub>6</sub> can be thinned down to one-unit-cell using microexfoliation. When the thickness is reduced to a few unit-cells, we observed unexpected, enhanced weak-antilocalization effect. This result provides first magneto-transport evidence for the long-predicted phonon dimensionality effects on electronic properties - 2D quantum confinement effect leads acoustic phonon spectra to open a gap near zero momentum, thus resulting in weakened electron-phonon scattering.

**Keywords:** novel 2D material, weak-antilocalization, electron-phonon interaction

### 1. Introduction

The advances in microexfoliation technique [1, 2] have greatly enriched the family of 2D atomic layered crystals and significantly promoted the research on low dimensional physics, as exemplified by the discoveries of exotic quantum phenomena in graphene [3, 4] and MX<sub>2</sub> monolayers [5, 6]. Those developments have motivated us to extend the efforts to layered ternary materials. In this work, we report the observation of the long-predicted phonon dimensionality effect on electronic properties [7] in a new 2D system - Nb<sub>3</sub>SiTe<sub>6</sub> few-layer crystals.

### 2. Results and Discussions

Nb<sub>3</sub>SiTe<sub>6</sub> was discovered two decades ago but scarcely studied [8]. As shown in Fig. 1, the structure of Nb<sub>3</sub>SiTe<sub>6</sub> is similar to that of MX<sub>2</sub>: both are formed from the stacks of sandwich layers, with comparable van der Waals (vdW) gaps. We have grown Nb<sub>3</sub>SiTe<sub>6</sub> single crystals using the chemical vapor transport method; the lateral dimension of crystals can reach a few mm (Fig. 1c, inset). Sharp (0k0) X-ray diffraction peaks of these crystals (Fig. 1c) confirm the excellent crystallinity. Our resistivity measurements along in-plane ( $\rho_{||}$ ) and out-of-plane ( $\rho_{\perp}$ ) directions (Fig. 1d) indicate that Nb<sub>3</sub>SiTe<sub>6</sub> is a quasi-two-dimensional metal, with the anisotropic ratio  $\rho_{\perp}/\rho_{||}$  increasing from 9 at 300 K to 22.5 at 2 K (Fig. 1d, left inset).

Due to the sizable vdW gap, atomically thin Nb<sub>3</sub>SiTe<sub>6</sub> crystals can be obtained on Si/SiO<sub>2</sub> substrates using the microexfoliation technique as the case of graphene and MX<sub>2</sub> [1, 2]. The flake thickness was estimated according to the color contrast under an optical microscope and the precise thickness was then measured by an atomic force microscope (AFM). Thin layers of ~3-5 nm can be easily found. Flakes as thin as only one unit cell (bi-layer) are even accessible, as illustrated by the micrograph of a large (> 10  $\mu$ m) bi-layer thin flake (Fig. 2a and

2b). To the best of our knowledge, this is the first success in obtaining atomically thin layers of ternary transition metal chalcogenides.

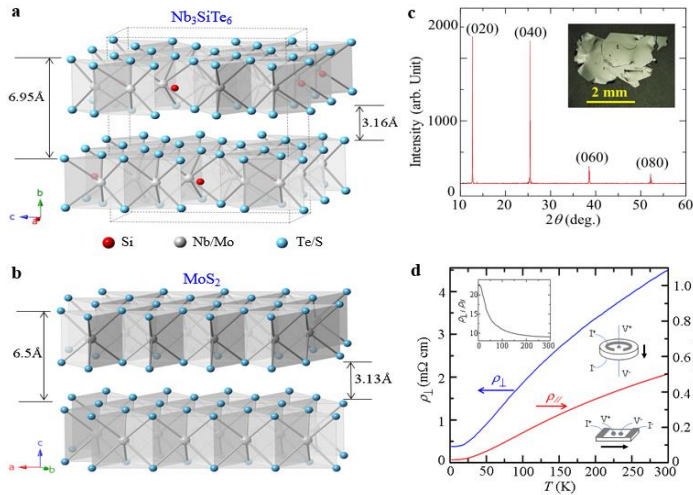


**Figure 1 | Structure and electronic properties of bulk  $\text{Nb}_3\text{SiTe}_6$ .** **a** and **b**, The crystal structures of (a)  $\text{Nb}_3\text{SiTe}_6$  and (b)  $\text{MoS}_2$ . **c**, Single crystal X-ray diffraction along the (0k0) plane for bulk crystal. Inset in **c**: an optical image of a bulk crystal. **d**, Temperature dependences of in-plane ( $\rho_{\parallel}$ ) and out of plane ( $\rho_{\perp}$ ) resistivity for bulk crystals. Left inset: anisotropic ratio ( $\rho_{\perp}/\rho_{\parallel}$ ) as a function of temperature. Right insets: Configurations for  $\rho_{\perp}$  (upper) and  $\rho_{\parallel}$  (lower) measurements.

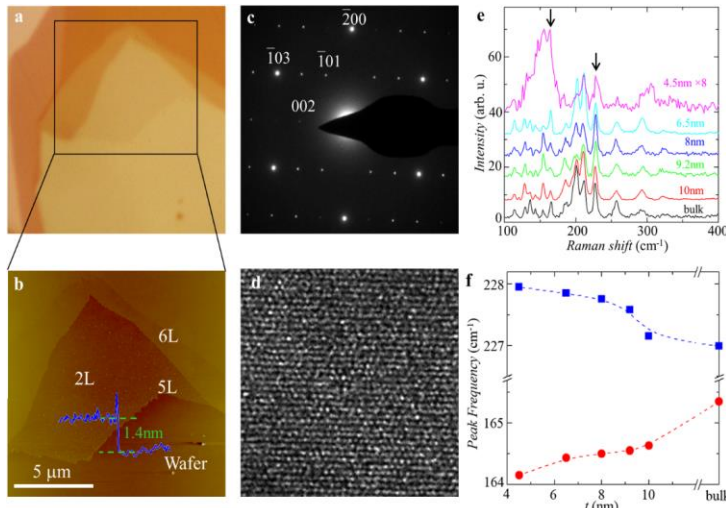


**Figure 2 | AFM, TEM and Raman observation of  $\text{Nb}_3\text{SiTe}_6$  atomically thin layers.** **a**, Optical image of a  $\text{Nb}_3\text{SiTe}_6$  thin flake. **b**, AFM image of a selected area from Image **a**; The inset shows the height of the bi-layer from the profile scan. **c**, [010] zone SAED pattern of a  $\text{Nb}_3\text{SiTe}_6$  thin flake. **d**, HRTEM image of the thin flake shown in **c**. **e**, Raman spectra of  $\text{Nb}_3\text{SiTe}_6$  crystals with various thickness. The arrows indicate the Raman peaks around  $165$  and  $227 \text{ cm}^{-1}$ , which show red- and blue-shift with the decrease of thickness as depicted in **f**.

We characterized  $\text{Nb}_3\text{SiTe}_6$  thin flakes through Raman and Transmission Electron Microscope (TEM) measurements. As compared to  $\text{MX}_2$  which displays only  $E_{2g}^1$  and  $A_{1g}$  phonon modes [9, 10],  $\text{Nb}_3\text{SiTe}_6$  exhibits more Raman modes (Fig. 2e) which may be attributed to its relatively complex lattice structure. We observed noticeable frequency shifts with the decrease of thickness for the  $165$  and  $227 \text{ cm}^{-1}$  modes (Fig. 2f), implying the variation of phonon spectra with the reducing dimensionality. The TEM observations indicate that  $\text{Nb}_3\text{SiTe}_6$  flakes are stable. As shown in Fig. 2c, the [010]-zone electron diffraction spots can be indexed according to the  $\text{Nb}_3\text{SiTe}_6$  structure, suggesting the excellent crystallinity. Moreover, the high-resolution TEM image also shows no visible amorphous structure (Fig. 2d).

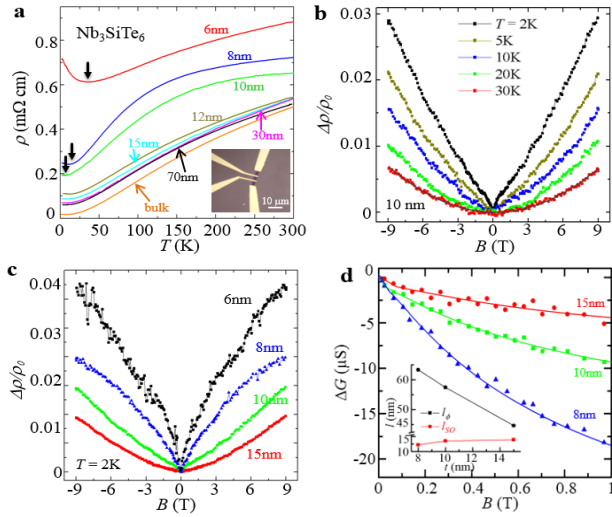


**Figure 3 | Transport properties of  $\text{Nb}_3\text{SiTe}_6$  nano-devices.** **a**, Temperature dependence of resistivity of various thicknesses flakes. The downward arrows mark the resistivity upturns. Inset: Optical image of a device. **b**, Normalized magnetoresistivity,  $\Delta\rho/\rho_0 = [\rho(B) - \rho(B=0)]/\rho(B=0)$ , for a 10 nm thick flake. A fitting to  $B^2$  is shown for  $T=30\text{K}$  data. **c**,  $\Delta\rho/\rho_0$  at  $T=2\text{K}$  of different thickness flakes. **d**, The fitting of magnetoconductance  $\Delta G(B)$  to 2D WAL model. The inset shows the coherence length  $l_\phi$  and spin relaxation length  $l_{SO}$  extracted from fitting.

The resistivity measurements show an increase of resistivity with the decrease of thickness (Fig. 3a). For relatively thick flakes the resistivity presents a temperature dependence similar to bulk. When the thickness is decreased below 12 nm, the resistivity displays remarkable changes: A greater  $d\rho/dT$  for  $T < 150\text{K}$  is seen for 10 and 8 nm, and diminishes in 6 nm flakes. At low temperatures, a resistivity upturn gradually develops and becomes more pronounced in thinner flakes. The enhanced  $d\rho/dT$  in 10 and 8 nm flakes suggests enhanced metallicity. Meanwhile, with decreasing thickness, electrons tend to be restricted to the 2D thin layers near substrate and become sensitive to interfacial scattering, this may account for low temperature upturns. Other mechanisms such as Kondo effects or weak localization (WL) are less likely, since Kondo effect generally arises at very low temperatures in dilute magnetic impurity systems and weak antilocalization (WAL) occurs in  $\text{Nb}_3\text{SiTe}_6$ .

As shown in Fig. 3b and 4d, the low temperature magnetoresistivity (MR) of the  $\text{Nb}_3\text{SiTe}_6$  flakes with the thickness less than 15 nm exhibits dips at zero field, which is a typical signature of WAL. Such MR dip broadens and finally disappears with increasing temperature owing to the enhanced inelastic scattering which breaks phase coherence, and a quadratic field dependence from a classical Lorentz effect appears (Fig. 3b). It is not surprising to observe WAL effect in  $\text{Nb}_3\text{SiTe}_6$  due to the strong SOC induced by heavy elements Nb and Te.

In general, WAL weakens with the decrease of thickness in thin film samples due to enhanced interfacial scattering. For instance, WAL is significantly suppressed in Bi thin films as the thickness is decreased below 18.5 nm [11]. However, we observed surprising enhancement of WAL in thinner  $\text{Nb}_3\text{SiTe}_6$  flakes. As shown in Fig. 3c, the MR dip becomes much sharper as the thickness is decreased. In contrast, the 15 nm flake does not show a clear dip in MR, suggesting the suppression of WAL in thicker samples. The suppression of WAL normally occurs as a result of strong dephasing process or weak SOC. In the case of ultra-thin samples on a substrate, the scattering from the interfacial roughness and impurities could be the possible dephasing process [11]. Given that the resistivity upturns at low temperature in thinner samples (Fig. 3a) suggesting interfacial scatterings, the enhancement of WAL in thin flake thickness is clearly opposite to the generally expected trend.

To gain more insights into this unusual enhancement of WAL in  $\text{Nb}_3\text{SiTe}_6$ , we fitted the MR data using the Hikami-Larkin-Nagaoka (HLN) model [12] and extracted the quantum coherence length  $l_\phi$  and spin relaxation length  $l_{SO}$ , which characterizes the strength of quantum coherence and SOC. As shown in Fig. 3d, the HLN model

fits well with our data. With the decrease of thickness,  $l_{SO}$  shows very weak thickness dependence, in sharp contrast with the 50% increase of  $l_\phi$  (Fig. 3d, inset). This indicates that the enhanced phase coherence is the major cause of the observed unusual WAL enhancement in Nb<sub>3</sub>SiTe<sub>6</sub> flakes.

Electron phase coherence is usually disturbed by energy transfer processes, e.g, inelastic scatterings [13]. Thus the  $l_\phi$  enhancement in our thinner samples implies the suppression of inelastic scatterings, consistent with the aforementioned enhanced metallicity in 10 and 8 nm flakes. Since Nb<sub>3</sub>SiTe<sub>6</sub> is non-magnetic, its transport mechanism should involve electron-phonon (e-p), electron-electron (e-e), electron-impurity and interfacial scatterings. With reducing dimensionality, the e-e and impurity scattering rate should increase due to modified screening of electrons [14], while the interfacial scattering should play a more significant role and suppress  $l_\phi$  as stated above. Therefore, the  $l_\phi$  increase in Nb<sub>3</sub>SiTe<sub>6</sub> thin flakes can only be attributed to suppressed e-p scattering.

Indeed, our Nb<sub>3</sub>SiTe<sub>6</sub> flakes are sufficiently thin to induce 2D quantum confinement on phonon spectra as suggested by Raman studies (Fig. 2c and 3d). Weakening of e-p scattering at low temperatures can be caused by the reduction of the phonon populations ( $\sim k_B T / \hbar \omega$ ): First, at low temperatures the optical phonons are expected to be forbidden owing to their high energy  $\hbar \omega$  and the e-p interaction is dominated by acoustic phonons whose energy reaches zero at zero momentum. Second, theoretical calculations have shown that the 2D confinement of acoustic phonons significantly modifies phonon spectra [7]: The presence of substrate imposes a rigid boundary condition for lattice vibrations, causing a gap at zero momentum in acoustic phonon spectrum [7]. Therefore, like optical phonons, the finite energy of acoustic phonons causes strong reduction of phonon populations at low temperatures, leading to significant suppression of e-p interaction which causes enhanced quantum coherence.

### 3. Conclusion

To summarize, we have obtained a new atomic thin ternary chalcogenide Nb<sub>3</sub>SiTe<sub>6</sub> with the thinnest thickness reaching only one unit cell. Through simple electronic transport measurements, we found clear evidence for the long-predicted suppression of e-p interactions caused by reducing phonon dimensionality.

### 4. Acknowledgments

The current work is funded by the NSF EPSCoR LA-SiGMA project under award #EPS-1003897.

### 5. References

- [1] K. S. Novoselov, et al., *Science* **306**, 666 (2004).
- [2] K. S. Novoselov, et al., *Proc. Natl. Acad. Sci. USA* **102**, 10451 (2005).
- [3] A. H. Castro Neto, et al., *Rev. Mod. Phys.* **81**, 109 (2009).
- [4] A. K. Geim and K. S. Novoselov, *Nat Mater* **6**, 183 (2007).
- [5] Q. H. Wang, et al., *Nat. Nano.* **7**, 699 (2012).
- [6] S. Z. Butler, et al., *ACS Nano* **7**, 2898 (2013).
- [7] B. A. Glavin, et al., *Phys. Rev. B* **65**, 205315 (2002).
- [8] J. Li, et al., *J. Alloy. Comp.* **184**, 257-263 (1992).
- [9] C. Lee, et al., *ACS Nano* **4**, 2695-2700 (2010).
- [10] P. Tonndorf, et al., *Opt. Express* **21**, 4908 (2013).
- [11] S. Sangiao, et al., *Europhys. Lett.* **95**, 37002 (2011).
- [12] A. K. Geim, *Science* **324**, 1530 (2009).
- [13] J. J. Lin and J. P. Bird, *J. Phys.: Condens. Matter* **14**, R501 (2002).
- [14] B. L. Altshuler, et al., *Phys. Rev. Lett* **44**, 1288 (1980).

## Redeveloping and Optimizing the Interactive Chromatin Modeling Web Server Kernel

Gyanadeep Kankanala<sup>1</sup>, Inderbin Sondh<sup>2</sup>, Thomas C Bishop<sup>3</sup>

<sup>1</sup>Department of Electrical Engineering, Louisiana Tech University

<sup>2</sup> Department of Bioengineering, University of Pittsburgh Swanson School of Engineering

<sup>3</sup>Department of Physics and Chemistry, Louisiana Tech University

**Abstract:** The Interactive Chromatin Modeling Web Server [ICM] is a tool for modeling DNA and chromatin interactively. The outputs include three-dimensional models of both free DNA and folded chromatin as well as a nucleosome energy level diagram. The ICM kernel includes routines that assign known DNA parameters to each base step of the sequence. That parameter(a.par file) is subsequently translated into cartesian coordinates (a .XYZ file) that can be rendered graphically by molecular modeling software such as VMD or Jmol. The algorithm used to convert parameter data to coordinate data is presented by El Hassan(1). The aim of the project is to redevelop the current FORTRAN ICM code using C++ with the expectation that the new program will efficiently process DNA sequences up to millions of base pairs long and introduce increased functionality as compared to the FORTRAN code.

**Keywords:** Molecular modeling, Base pairs.

### 1. Introduction

#### A. Parameter File

A DNA strand is made up of a long chain of four different bases: Adenine, Thymine, Cytosine, and Guanine(A, T, C, G). Familiar B-form DNA exists in a double helix configuration, each base being paired with its corresponding partner (A to G and C to T). Moving along a strand of DNA will give its sequence (e.g. GATCCG). Each step such as G-A, A-T, and so on (referring to the example sequence just mentioned) constitutes a base-step. Each of the 16 possible base-steps has a unique set of six helical parameters. Shift, Slide, and Rise dictate movement (Angstroms) in the X, Y, and Z directions, respectively, while Tilt, Roll, and Twist indicate rotation (degrees) about the respective axes. When a DNA sequence is entered into ICM, a parameter file is the first file produced.

Table 1. Parameter File

```

9850 base_pairs
0 ***local base-pair & step parameters***

```

	Shear	Stretch	Stagger	Buckle	Prop-Tw	Opening	Shift	Slide	Rise	Tilt	Roll	Twist
A-T	0	0	0	0	0	0	0	0	0	0	0	0
G-C	0.03	-0.02	-0.02	-1.43	-7.76	0.21	0.1	-0.25	3.22	-0.58	3.16	28.49
G-C	0.03	-0.02	-0.02	-1.44	-7.76	0.21	-0.15	-0.28	3.34	-0.16	5.68	29.57
G-C	0.03	-0.02	-0.02	-1.44	-7.76	0.21	-0.15	-0.28	3.34	-0.16	5.68	29.57
G-C	0.03	-0.02	-0.02	-1.44	-7.76	0.21	-0.15	-0.28	3.34	-0.16	5.68	29.57
G-C	0.03	-0.02	-0.02	-1.44	-7.76	0.21	-0.15	-0.28	3.34	-0.16	5.68	29.57
G-C	0.03	-0.02	-0.02	-1.44	-7.76	0.21	-0.15	-0.28	3.34	-0.16	5.68	29.57

Part of an example parameter file. Only the last six parameters (Shift, Slide, Rise, Tilt, Roll, Twist) are used in our calculations. Note that Twist and Rise are always much larger in magnitude than the other parameters, giving DNA its signature double helix shape.

## B. Coordinate Files

The .par file is converted to an .xyz file using El Hassan's algorithm. A file in .xyz format can be directly fed into VMD, Jmol or similar software to produce a three dimensional rendering. The graphics can be modified to provide clarity and ease of viewing.

Table 2. XYZ File

COMMENT	TcB	par2xyz		
CA	0	0	0	
H1	1	0	0	
H2	0	1	0	
H3	0	0	1	
CA	0.20316	0.30208	3.10882	
H1	1.07516	0.76669	2.95469	
H2	-0.26086	1.18691	3.15081	
H3	0.35905	0.33699	4.09598	
CA	0.68503	0.44353	6.25969	
H1	1.17272	1.30483	6.11718	
H2	-0.16804	0.94839	6.39157	
H3	0.87056	0.50079	7.24066	

Part of an example .xyz file.

In our model, DNA is displayed as a yellow bead, with each bead representing 5 base pairs. To accurately study flexibility of DNA, one must consider the helical parameters as well as the effects of temperature. Our C++ program represents thermal fluctuations by introducing a random Gaussian variation (centered around the standard parameter value) for each parameter. The standard deviation of the distribution is specified in the original ICM paper by Bishop(2) and is appropriately scaled by the temperature given on the ICM input page. A temperature of zero introduces no variation from the ideal conformation of each base pair step.

## 2. Method

Application of El Hassan's Algorithm.

The process to convert a .par file to a .xyz file involves rotating (denoted by Rx, Ry and Rz) and translating the coordinate axes of each base pair by the specified Tilt, Roll, Twist (rotations) and Shift, Slide, Rise (translations).

$$\mathbf{R}_x(\theta) = \begin{pmatrix} 1.00 & 0.00 & 0.00 \\ 0.00 & \cos(\theta) & -\sin(\theta) \\ 0.00 & \sin(\theta) & \cos(\theta) \end{pmatrix}$$

$$\mathbf{R}_y(\theta) = \begin{pmatrix} \cos(\theta) & 0.00 & \sin(\theta) \\ 0.00 & 1.00 & 0.00 \\ -\sin(\theta) & 0.00 & \cos(\theta) \end{pmatrix}$$

$$\mathbf{R}_z(\theta) = \begin{pmatrix} \cos(\theta) & -\sin(\theta) & 0.00 \\ \sin(\theta) & \cos(\theta) & 0.00 \\ 0.00 & 0.00 & 1.00 \end{pmatrix}$$

The beginning rotation matrices are defined using standard direction sines and cosines.

$$\mathbf{T}_{i+1} = \left[ \mathbf{R}_z\left(\frac{\Omega}{2} - \phi\right) \mathbf{R}_y(\Gamma) \mathbf{R}_z\left(\frac{\Omega}{2} + \phi\right) \right] \mathbf{T}_i \quad (9)$$

$$\mathbf{T}_{mst} = \left[ \mathbf{R}_z\left(\frac{\Omega}{2} - \phi\right) \mathbf{R}_y\left(\frac{\Gamma}{2}\right) \mathbf{R}_z(\phi) \right] \mathbf{T}_i \quad (10)$$

$$\mathbf{r}_{i+1}^o = \mathbf{r}_i^o + D_x \mathbf{x}_{mst} + D_y \mathbf{y}_{mst} + D_z \mathbf{z}_{mst} \quad (11)$$

Equation (10) provides a 3x3 matrix containing the mid-step triad  $\mathbf{T}_{mst}$  located between the two base pairs  $i$  and  $i+1$ . The columns of this matrix are multiplied by Shift, Slide, and Rise ( $D_x$ ,  $D_y$ , and  $D_z$  respectively) as in Equation (11) and added to  $CA_i$  to obtain the coordinates of  $CA_{i+1}$ . Adding the values of  $CA_{i+1}$  to the corresponding columns of  $\mathbf{T}_{i+1}$  from Equation (9) gives coordinates for the axis directors labeled H1, H2, and H3 in Table 2.

### 3. Results

#### A. Rendering of XYZ Files

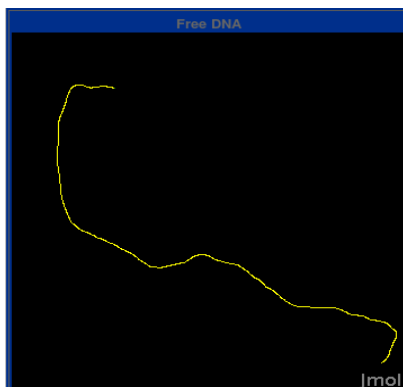


Fig. 1. Jmol was used to produce these graphic models. This specific sequence was ~9850 base pairs long. ICM must be efficient enough to process sequences millions of base pairs long, interactively.

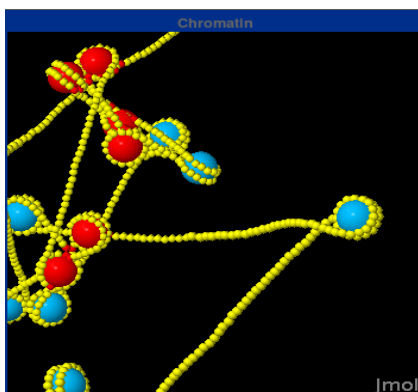


Fig. 2. Histones are displayed in blue. A red histone indicates close contact and thus steric hindrance and/or an unstable energy conformation.

**B. Running Time Data**

Using UNIX's time utility, we collected running times of our C++ parameter-to-xyz conversion when processing sequences up to 1,000,000 base pairs long. Values are tabulated in Table 3.

Table 3

Running Time Comparison of New and Old Code					
# of Base Pairs	C++		FORTRAN		
	Running Time (s)	CPU Usage (%)	Running Time (s)	CPU Usage (%)	
1000000	68.3	74.5	25.69	100	
100000	7.3	74.8	2.54	99.6	
10000	0.83	66.2	0.25	100	
1000	0.09	55.5	0.03	66.6	
100	0.02	50	0.003	0	
10	0	0	0	0	

**4. Discussion**

Currently there are some file I/O inefficiencies that cause an unnecessarily long running time, longer than the current ICM code in FORTRAN. This is not acceptable, as the goal is to make a more efficient program. Fixing these inefficiencies along with other program organization issues is predicted to reduce the running time to be at least as fast as the FORTRAN code. Also, the current C++ ICM code only supports 'Free DNA' modeling, the chromatin and nucleosome code is still under testing and development.

**5. Discussion/Conclusion**

There is strong evidence that once the C++ code is better organized and I/O problems are fixed, the program running time will be cut-down significantly. One current plan is to introduce a new data structure that encapsulates all the data normally in a .par file. This would involve a multidimensional array containing base-pairs along with their twelve corresponding helical parameters. Having such a structure will prevent having to access the .par file so many times. It was also discovered that the running time of the program scales linearly with the size of the sequence file, e.g. a 10000 base pair file takes 3 seconds, a 100000 one would take 30 seconds. Algorithmic developments are being considered as a means of eliminating linear dependence.

**6. Acknowledgment**

This material is based upon work supported by the National Science Foundation under the NSF EPSCoR Cooperative Agreement No. EPS-1003897 with additional support from the Louisiana Board of Regents.

**7. References**

[1] M.A. El Hassan and C.R. Calladine, "The Assessment of the Geometry of Dinucleotide Steps in Double-Helical DNA; a New Local Calculation Scheme," J. Mol. Biol. (1995) 251, 648-664, June. 1995.

[2] T.C. Bishop and R.C. Stolz, "ICM Web: the interactive chromatin modeling web server," W254-W261 Nucleic Acid Research, Web Server issue, DOI: 10.1093/nar/gkq/496 June. 2010, vol.38.

## Sign-Learning Kink-Based Path Integral Calculations of Molecules H<sub>2</sub>O, N<sub>2</sub>, and F<sub>2</sub>

Josef Baylis<sup>1</sup>, Xiaoyao Ma<sup>2</sup>, Frank Löffler<sup>3</sup>  
Randall Hall<sup>1</sup>, Karol Kowalski<sup>4</sup>, Mark Jarrell<sup>2,3</sup>, Juana Moreno<sup>2,3</sup>

<sup>1</sup>Department of Natural Sciences and Mathematics, Dominican University of California, San Rafael, CA 94901

<sup>2</sup>Department of Physics and Astronomy, Louisiana State University, Baton Rouge, LA 70803

<sup>3</sup>Center for Computation & Technology, Louisiana State University, Baton Rouge, LA 70803, USA

<sup>4</sup>William R. Wiley Environmental Molecular Sciences Laboratory, Battelle, Pacific Northwest National Laboratory, Richland, Washington 99352, USA

**Abstract:** The sign-learning kink-based path integral formalism is used to calculate the ground state energies of the molecules H<sub>2</sub>O, N<sub>2</sub> and F<sub>2</sub> and a variety of geometries. The method uses a learning algorithm to overcome the notorious sign problem in fermionic systems. The learning process uses a Monte Carlo scheme to identify states that contribute significantly to the canonical partition function and then includes them in the correlated wavefunctions to calculate the canonical averages. The calculations use the STO-3G basis set and obtain both precision and accuracy. A comparison with the popular CCSD method for including correlation demonstrates the sign-learning kink method is overall more accurate than the CCSD method.

**Keywords:** Path Integral Formalism, Monte-Carlo

### 1. Introduction

Studies of correlated electronic systems pose challenges for computational methods. The Feynman's path integral (PI) formulation of quantum mechanics is such a method and is the focus of this work, as its features include exact inclusion of correlation and the calculation of the partition function. For details about this so-called Sign-Learning Kink-Based Path Integral Formalism, see (1). In this exploratory work, we compare the results of a computer implementation of the Sign-Learning Kink-based integral formalism to published results. Path integral approaches often use a complete set of states which offers a route to an "exact" determination of the partition function for a many-body system (2-19). These approaches have been frustrated by the sign of the fermion density matrix, which can lead to computational difficulties in obtaining precise results. Thus, before the path integral method can be applied to the study of correlated electronic systems, it is necessary to develop ways to avoid the sign problem.

It is well known that finite basis sets are capable of producing accurate results for many systems (20). The Sign-Learning Kink (SiLK) Formalism uses finite basis sets and the discretized version of the PI expression for Q, the canonical partition function, to develop a "kink" expansion (21,22). In the discretized version of Q, paths are divided into small imaginary time segments. When using finite basis sets a path will spend some imaginary time in one (many-electron) state, have a transition to another state during one imaginary time segment, spend some

imaginary time in the second state, have a transition, etc. The transitions between states are called 'kinks' (22). A path can therefore be classified by the number of kinks and states involved.

## **2. SiLK Formalism**

The SiLK formalism is described in detail in (1). We will not review these details here, but only very briefly summarize the main idea. The formalism assumes a usually finite set of orthonormal, N-particle states. The partition function can be written in terms of these states. The problem that arises numerically in a Monte-Carlo simulation is that the sign of each of the summands is not determined; in particular, it can be negative. This means that the estimator for Q can change sign, leading to large statistical errors. Using the SiLK formalism described in detail in (1), this sum is recast into a sum ordered by the number of so-called "kinks", i.e., as a sum of all  $\{\alpha_i\}$  with  $j_k$  equal (no kinks), one  $j_k$  different (2 kinks), two  $j_k$  different (3 kinks), etc. This has the advantage that in the limit of no kinks the sign can be shown to be positive. In particular, the contributions from both zero kinks ( $Q_0$ ) and two kinks ( $Q_2$ ) are by construction positive. In practice this means that for a system with no or only few kinks the sign-problem is either eliminated, or at least greatly reduced.

In addition, the method was made adaptive in the following manner. An initial set of N-electron states was chosen by diagonalizing the single particle Hamiltonian. During the course of the Monte Carlo calculation, we kept track of the N-electron states that appeared at each step. For a certain number of steps initially, we periodically performed diagonalizations using only these states. Thus, a subset of the total number of N-electron states were diagonalized. After each diagonalization, all the Hamiltonian matrix elements were updated. Therefore, after a number of diagonalizations, we arrived at states which were linear combinations of the original set of N-electron states. During subsequent Monte Carlo steps, we expected the adapted states to produce fewer kinks and to reduce the sign problem.

## **3. SiLK Implementation**

Initial states are taken as input from the NwChem (23) package, using the coupled-cluster-singles-doubles (CCSD) approximation, in form of a matrix, the Hamiltonian. This matrix is of the size of the number of states in the system, squared. A straight-forward way to solve the problem would be direct diagonalization. For the cases discussed here this is possible, and is in fact used to validate our results. In general however, the large size of this matrix prevents a practical direct diagonalization. After the initial setup of the Hamiltonian we follow the formalism described in Sec. 2, including adapting the current basis set to the appearing states.

## **4. Results**

We applied our SiLK formalism to three particular systems. These have been chosen to be small enough to allow for exact diagonalization, and use the STO3G basis set (24,25). More complex scenarios will be part of future work. We compare against results from exact diagonalization, and to CCSD energies. In order to confirm that our method also works for non-equilibrium geometries we vary geometric parameters for each studied molecule.

Water is the smallest of the studied molecules (in terms of number of states), but it also is the only one allowing for two geometric degrees of freedom. Because of this, we were able to perform simulations for a wide range of both angle and distance. The comparison between our results using SiLK, direct diagonalization, and CCSD are shown in Fig. 1. It is evident that SiLK is able to produce results with a much smaller error than the ones obtained

by CCSD (which is mainly due to the more severe approximations made by CCSD). Moreover, we show that the results using SiLK are consistent with the results obtained using exact diagonalization.

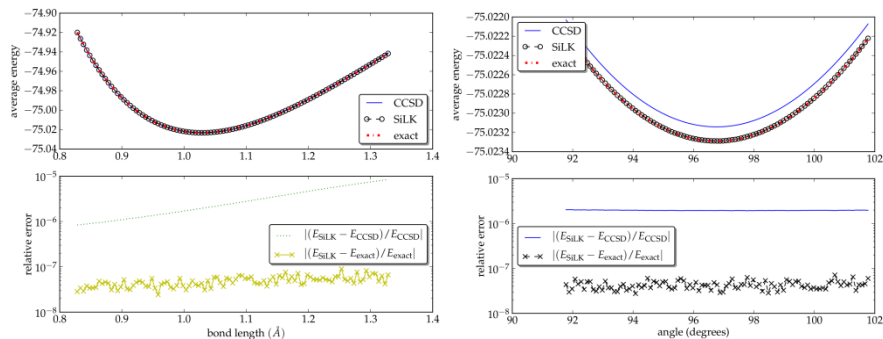


Fig. 1: Shown is the average binding energy of an H<sub>2</sub>O molecule through the geometric energy minimum, depending on the H-O molecular distance (left), and the H-O-H angle (right).

For both molecular fluoride and nitrogen the number of states involved is larger than for water. However only one geometric degree of freedom exists here. For both molecules we performed calculations for a range of distances and compare against results from direct diagonalization and CCSD, as shown in Fig. 2. For F<sub>2</sub>, both CCSD and SiLK are able to achieve a very low relative error. In contrast, a clear discrepancy to the exact result can be seen in the case of N<sub>2</sub> for CCSD, while the error of SiLK is at least two orders of magnitude smaller for all distances. This is expected, as the CCSD approximation is not a particularly well suited approximation for the N<sub>2</sub> molecule.

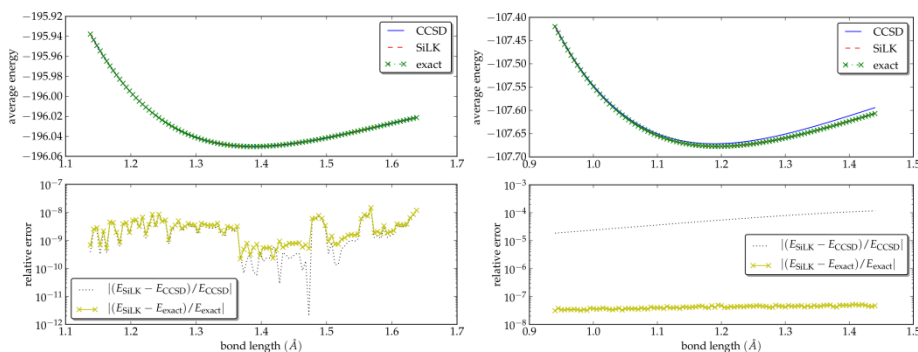


Fig 2: Shown is the average binding energy of an F<sub>2</sub> molecule (left), and an N<sub>2</sub> molecule (right), depending on the molecular distance

## 5. Conclusions

The SiLK formalism has been shown to be successful in overcoming the sign problem inherent in standard path integral approaches, for the case of H<sub>2</sub>O, F<sub>2</sub>, and N<sub>2</sub> in the STO3G basis set. While these systems are small, in fact

small enough to allow for direct diagonalization, allowing for a direct comparison and error analysis, there is no reason why this method should not work for larger systems too. Several questions however are left to investigate. It remains to be seen how the method scales with the number of basis functions when this grows too large for an exact diagonalization. As system size increases, memory management becomes an issue when the whole Hamiltonian cannot be stored in a naive way, but either needs to be compressed (e.g., as sparse matrix), or be calculated, at least in part, on-the-fly. Future work will focus on these particular issues, aiming at much larger basis sets.

## 6. Acknowledgments

This work was supported by the National Science Foundation (NSF) under the EPSCoR LA-SiGMA Cooperative Agreement No. EPS-1003897 with additional support from the Louisiana Board of Regents. Randall Hall is supported by the Lillian L.Y. Wang Yin, Ph.D. Endowed Professorship of Chemistry at Dominican University of California. Portions of this research were conducted with HPC resources provided by the Louisiana State University (allocation hpc\_critical).

## 7. References

1. **Mak, CH, Egger, R and Weber-Gottschick, H.** 1998, Phys Rev Lett, Vol. 81, pp. 4533-4536.
2. **Mak, CH and Egger, R.** 1999, J Chem Phys, Vol. 110, pp. 12-14.
3. **Hall, Randall W.** 2002, Journal of Chemical Physics, Vol. 116 (1), pp. 1--7.
4. **R, Egger, Muhlbacher, L and CH, Mak.** 2000 : s.n., Phys Rev E, Vol. 61, pp. 5961-5966.
5. **Miura, S and Okazaki, S.** 2000, J Chem Phys, Vol. 112, pp. 10116-10124.
6. **Militzer, B, Magro, W and DCeperley.** 1999, Contributions to plasma physics, Vol. 39, pp. 151-154.
7. **Newman, WH and Kuki, A.** 1992, J Chem Phys, Vol. 96, pp. 1409-1417.
8. **Hall, RW.** 1991, J Chem Phys, Vol. 94, pp. 1312-1316.
9. **Hall, RW and Prince, MR.** 1991, J Chem Phys, Vol. 95, pp. 5999-6004.
10. **Ceperley, DM.** 1992, Phys Rev Lett, Vol. 69, pp. 331-334.
11. **Roy, P, Jang, S and Voth, GA.** 1999, J Chem Phys, Vol. 111, pp. 5303-5305.
12. **Roy, P and Voth, GA.** 1999, J Chem Phys, Vol. 110, pp. 3647-3652.
13. **B Militzer, W Magro, and D Ceperley.** 1999, Contrib Plasma Phys, Vol. 89, pp. 151-154.
14. **Ceperley, DM.** 1996, In: Monte Carlo and molecular dynamics of condensed matter systems.
15. **Feynman, Richard P. and Hibbs, A.R.** s.l. : McGraw-Hill, 1965.
16. **Rom, N, et al.** 1998, J. Chem. Phys, Vol. 109, pp. 8241-8248.
17. **Rom, N, Charutz, D M and Neuhauser, D.** 1997, Chem. Phys. Lett, Vol. 270, pp. 382-386.
18. **Asai, Y.** 2000, Phys. Rev. B, Vol. 62, pp. 10674-10679.
19. **Baer, R, Head-Gordon, M and Neuhauser, D.** 1998, J. Chem. Phys, Vol. 109, pp. 6219-6226.
20. **Hehre, WJ, et al.** s.l. : Wiley, 1986.
21. **Schotte, KD and Schotte, V.** 1971, Phys Rev B, Vol. 4, p. 2228.
22. **Chiles, RA, et al.** 1986, J Chem Phys, Vol. 81, p. 2039.
23. **Valiev, M., et al.** 2010, Computer Physics Communications, Vol. 181(9), pp. 1477-1489.
24. **Hehre, W. J., Stewart, R. F. and Pople, and J. A.** 1969, Journal of Chemical Physics, Vol. 51(6), pp. 2657-2664.
25. **Collins, J. B., et al.** 1976, The Journal of Chemical Physics, Vol. 64, pp. 5142-5151.

## Simulation of the Controlled Release of Molecules from Halloysite Nanotubes

Divya Elumalai<sup>1</sup>, Marybeth McCoy<sup>2</sup>, Yuri Lvov<sup>1</sup>, Joshua Tully<sup>1</sup>, Pedro Derosa<sup>1,3</sup>

<sup>1</sup>Institute for Micromanufacturing, Louisiana Tech University

<sup>2</sup>Ouachita Parish School Board

<sup>3</sup>Department of Mathematics and Physics, Grambling State University

**Abstract:** Encapsulation and the controlled release of active agents like drugs, nutrients, cosmetics and protective agents in efficient delivery vehicles, like nanotubes, have been studied for some time now. However it is difficult to predict the diffusion and flow in these systems in the nano regime using established techniques, like molecular dynamics, where the computational times become exorbitant. Here, we describe how the release profiles predicted by our 3D time quantified Monte Carlo model of diffusion through and from nanotubes, scale with respect to: the number of particles diffusing out of the nanotube and the radius of nanotube under constant volume number density conditions. This project was part of the research activity of one of the RET (Research Experience for Teachers) high school teachers.

**Keywords:** Diffusion, Nanotubes, Sustained Release, Scaling, Time Quantified Monte Carlo.

### 1. Introduction

Nanotechnology gave scientists a number of materials and objects that enable experimental realization of concepts that they previously considered to be the exclusive domain of thought experiments. No other nano materials have proven more valuable in this regard than nanotubes. Nanotubes have become promising materials for nanofluidics and membrane technology, opening perspectives to applications involving controlled release. The adaptation of Halloysite microtubules for controlled release was the result of the work of Burke and Singh [2]. Price *et al.*[3]<sup>47</sup> reported the entrapment of oxytetracycline HCl in copper coated micro cylinders utilized in antifouling coatings for delivery of hydrophilic and hydrophobic active agents, they also reported the use of microcylinders for the delivery of proteins and growth factors [4]. For many applications, microcylinders made from either lipids or carbon nanotubes or other inorganic nanotubes are cost prohibitive. Halloysite nanotubes (HNT) were found to be a viable alternative. The use of Halloysite offers significant advantages over other nanotubes. HNT are found in nature and do not require tedious or hazardous production, they are biocompatible and less cytotoxic than carbon nanotubes, they are inexpensive compared to other nanotubes, particularly carbon nanotubes, and the loading procedure is simple. HNTs have unique electronic properties (like polarizability, dielectric and the presence of opposite charges on the inner most and outermost surfaces), mechanical, and structural properties and are chemically stable, which make them ideal material for nano carriers [5]. HNTs

are 0.5 -1  $\mu\text{m}$  long hollow aluminum-silicate cylinders that have outer diameters between 50-100 nm with an average inner lumen of 15nm [6]. In each HNT, the external surface is composed of siloxane (Si-O-Si) groups, whereas the internal surface consists of gibbsite-like arrays of aluminol (Al-OH) groups [6]. In the last few years, several controlled-release systems using HNTs have been developed [7, 8]. HNTs can be functionalized with different functional groups thereby changing properties like surface charge density and tube lumen. In order to design optimal functional controlled delivery mechanisms in nano fluidic devices using nanotubes, a much more detailed understanding of the diffusion of charged nano particles/ions (NPs) through nanotubes is required. The past decade represented a period of concerted experimental and theoretical research efforts to elucidate several of the hitherto incompletely understood aspects. The need to accurately control release rates and be able to consistently predict controlled delivery/release characteristics such as release times, motivates this research. To achieve optimal release profiles for a given set of initial conditions, (like initial molecular concentration, pH and temperature of surrounding media) only a few simulations parameters need to be tested; the results obtained from simulations can then be utilized to help guide experiments. The aim of the project is to study the effect of the number of particles and the length of the tube, on the release profile. From this study optimal system size for simulation can be determined allowing for an efficient tradeoff between accuracy and simulation time.

## 2. Methodology

We describe how the release profiles, predicted by our 3D time quantified Monte Carlo model (that efficiently simulates NP diffusion in long, defect free nanotubes) scale with respect to: the number of particles diffusing out of the nanotube for two different NT radii, the length of the NT is adjusted to ensure the concentration of particles is the same in all the simulations. The model studies the diffusion out of the ends of the nanotubes. The NPs and the HNT are assumed to be immersed in a medium of constant dielectric. The hydrodynamic radius, is the effective radius of a hydrated molecule in solution and in this work is the radii assigned to the NPs. The NPs are considered to be spherical in shape and are initially distributed throughout the nanotube such that 60% of the particles are near the tube openings while the rest are uniformly distributed throughout the nanotube. NP motion is simulated based on a concentration dependent random walk to sample the configuration space subject to collisions and interactions between the NPs and between the NPs and the nanotube walls. Particles are moved one at a time in an arbitrary direction. There is an upper limit on the maximum length the NPs can move. The change in energy of the system due to the move is calculated to determine if the move is energetically viable at a given temperature. The overall energy of the system is calculated with contributions from particle-wall and particle-particle interactions (equation 1).

$$U(r) = \begin{cases} U_{VDW} + U_{CB} + U_{wall} & r < \lambda_d \\ U_{CB} + U_{wall} & r > \lambda_d \end{cases} \quad (1)$$

Here  $\lambda_d$  is the Debye length. The wall-particle interactions  $U_{wall}$  are modeled by summing up the contributions from dipole-charge interactions, shielded Coulombic interactions, and Van Der Waals interactions. NP-NP

interactions are modeled primarily by taking into consideration the screened electrostatic potential for a spherical charged particle of radius  $R$  immersed in an electrolyte ( $U_{CB}$ ), and the NP-NP Van Der Waals contributions ( $U_{VDW}$ ). Our Monte Carlo simulations have time implicit in them. The mean free path of the molecules is taken to be the maximum hop distance (the mean free path is predicted by the Chapman-Enskog equation for free molecular gas flow). The velocity of the particles during hops combines the contributions of the thermal drift velocity due to the internal energy of the system of NPs in the nanotube. Elapsed time per time step is then calculated by dividing the total mean displacement of all particles in that time step by our derived velocity.

### 3. Results and Discussion

Figure 1a) shows the release profiles for 10, 20, 50, and 100 Dexamethasone particles from Halloysite nanotubes of radius 10 nm at pH 7.4, the dissolution volume is assumed to be at least 3-10 times the saturation solubility of the NPs. This means that the NPs inside the nanotube are not affected by the NPs released into the medium. Nanotube length is adjusted to ensure the nanoparticle concentration is the same in all cases. Figure 1b) shows the release profiles for 10, 20, 50, and 100, 500, and 700 Dexamethasone particles from Halloysite nanotubes of radius 5 nm at pH 7.4. In both cases the release profiles are compared to expected release profiles obtained from running simulations with 1000 particles (with 60% particles near the tube openings). In all the cases studied the interaction between the molecules and the nanotube walls is attractive.

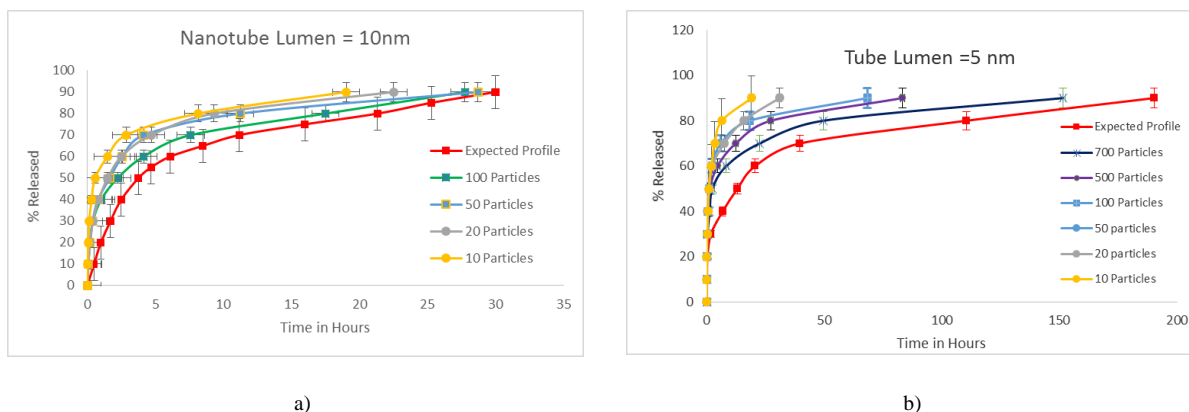


Figure.1.a) Release profiles for Dexamethasone at pH. 7.4 from Halloysite nanotube of lumen 10nm and b) Release profiles for Dexamethasone at pH. 7.4 from Halloysite nanotube of lumen 5 nm.

The out diffusion of the molecules is faster in the case of nanotubes with larger diameters (10 nm case studied here), because the molecules attracted to the walls shield the molecules near the center of the nanotube from experiencing an attraction to the charged inner wall of the nanotubes. In the smaller 5 nm nanotubes fewer molecules are able to cross a given cross-sectional area of the nanotube at once. Scaling the number of particles

and length of the nanotubes is in our simulations viable, for the 10nm NT, the results show less sensitivity to the number of particle such that 100 particles are enough to reproduce the much larger simulation (1000 Particle case) within the statistical error. On the other hand in the case of 5 nm tubes the convergence is much slower, 700 particles are still statistically different from the 1000 particles' case. More radii should be tested before this trend can be confirmed. In both the 5 nm and the 10 nm case the rate of release of NPs from the HNT slows down as we increase the number of NPs. This can be attributed to the fact that the NT is larger and the NPs have to travel farther to diffuse out of the nanotubes. The contribution to the internal energy of the tube due to the longer tube clearly over shadows the increase in the inter particle interaction due to increase in the number of NPs.

#### **4. Conclusion**

Diffusion in the cases studied occurs in two distinct phases with an initial burst phase, followed by a longer slower saturation phase [8]. Faster release of dexamethasone occurs from nanotubes of larger radii (10 nm). The release profiles do not scale well with respect to the number of particles (and length of nanotube) for nanotubes of smaller radii. For nanotubes of larger radii (10 nm case here) the system with 100 NPs shows promising results with release profiles very similar to the expected release profile.

#### **5. Acknowledgments**

The current work is funded by the NSF EPSCoR LA-SiGMA project under award #EPS-1003897.

#### **6. References**

- [1] Knudsen M., *Ann Phys*, 1909, 28, p.75–130
- [2] T. G. Burke, *et al.*, *Annals of the New York Academy of Sciences*, 1987, 507, p. 330-333.
- [3] R. Price and M. Patchan, *J Microencapsul*, 1991, . 8, p. 301-6.
- [4] R. R.Price, *et al.*, *11th International Symposia on Microencapsulation*, Bangkok, Thailand, 1998.
- [5] V. Vergaro, *et al.*, *Biomacromolecules*, 2010, . 11, p. 820-826.
- [6] B. K. G. Theng, *et al.*, *Clays and Clay Minerals*, 1982, 30, p. 143-149.
- [7] Forsgren, J., & Jämstorp, E., *Journal of Pharmaceutical Sciences*, 2010. **99**(1): p. 219–227.
- [8] Abdullayev, E. and Y. Lvov, *Journal of Materials Chemistry*, 2010. **20**(32): p. 6681-6687.
- [9] Derosa, P., *et.al.*, 2 nd Annual Proceedings of the Louisiana EPSCoR RII LA-SiGMA 2012 Symposium, 2012.

## Simulations of ions in non-aqueous solvents

Andy Vuong<sup>1</sup>, Steve Wagstaff,<sup>2</sup> Steven W Rick<sup>3</sup>

<sup>1</sup>Wake Forest University

<sup>2</sup>Missouri University of Science and Technology

<sup>3</sup>Department of Chemistry, University of New Orleans

**Abstract:** Molecular mechanics models in computational chemistry are used to understand the dynamics behind interactions at the molecular level. Ethylene carbonate is one of the most common solvents used for the production of batteries in cars, phones, and laptops. Using the commonly used models GAFF and OPLS, the dynamics of the ions fluorine, chlorine, bromine, iodine, and potassium in ethylene carbonate are studied to better understand the efficacy of the materials used in battery production. Using known calculated quantum theory values for the dimer energy and geometry between an ion and a single molecule of ethylene carbonate, it was found that both the GAFF and OPLS models were accurate in reproducing solvent-ion interactions. In addition, for the GAFF model, free energy calculations were performed to further validate the model with experimental data. For each of these calculations, the optimal values for sigma and epsilon stayed consistent with trends following the size of the ions. These models with their optimized input values can more accurately simulate the interactions between ethylene carbonate and the given ions, thus leading to better results.

**Keywords:** Ionic solutions, molecular dynamics, potential models

### 1. Introduction

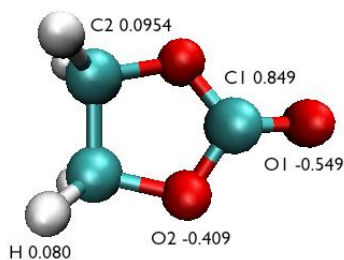


**Figure 1.** Ethylene carbonate showing atom labels and charges.

Ethylene carbonate (EC, see Figure 1) is a polar, aprotic solvent and a good solvent for ions. These properties make it a good solvent for lithium batteries.<sup>1,2</sup> Molecular level computer simulations are a useful tool for understanding these materials. These methods require a potential energy function, or force field, which is Ethylene carbonate (EC, see Figure 1) is a polar, aprotic solvent and a good solvent for ions. These properties make it a good solvent for lithium batteries.<sup>1,2</sup> Molecular level computer simulations are a useful tool for understanding these materials. These methods require a potential energy function, or force field, which is characterized by a set of parameters. Optimally, parameters developed for one system with a particular composition, temperature and pressure could be transferred to another. There has been significant effort in developing potentials for aqueous systems, in which the parameters are optimized to reproduce experimental values for thermodynamic, structural and transport properties. In using these parameters for non-aqueous systems some parameters may require adjustment

to achieve an accurate model. Here we present calculations of the free energy of solvation for a series of monatomic, monovalent ions (four halide anions and the potassium cation) in EC, for which there is directly comparable experimental data.<sup>2</sup> Quantum chemical calculations for the EC-dimer energy and distance provide additional data for parameterization.

## 2. Methods

The interactions between the particles are taken to be a combination of Lennard-Jones and Coulombic terms so that the interaction between two (non-bonded) atoms  $i$  and  $j$  is given by

$$E_{ij}(r_{ij}) = 4\epsilon_{ij} \left[ \left( \frac{\sigma_{ij}}{r_{ij}} \right)^{12} - \left( \frac{\sigma_{ij}}{r_{ij}} \right)^6 \right] + \frac{q_i q_j}{r_{ij}}$$

where  $r_{ij}$  is the distance between the atoms,  $q_i$  is the charge of atom  $i$ , and  $\epsilon_{ij}$  and  $\sigma_{ij}$  are the Lennard-Jones parameters for  $i$  and  $j$ . This level of molecular interactions, including as it does excluded volume (the  $r^{-12}$  term), dispersion ( $r^{-6}$ ) and Coulombic interactions ( $r^{-1}$ ), can be thought of as a minimal description and is commonly used in molecular simulations. More complicated potentials can include polarizability and charge transfer, among other terms. The Lennard-Jones parameters for atoms of different types are determined from combining rules, in this study, the Lorentz-Berthelot rules are used,  $\sigma_{ij} = \frac{1}{2}(\sigma_i + \sigma_j)$  and  $\epsilon_{ij} = \sqrt{\epsilon_i \epsilon_j}$ . For each atom type, this gives three parameters ( $\epsilon_i$ ,  $\sigma_i$  and  $q_i$ ). For monatomic ions, the charge can be thought of as a given, although other approaches treat a particle's charge as variable,<sup>3-5</sup> giving two adjustable parameters.

The GROMACS<sup>6</sup> (GRoningen Machine for Chemical Substances) molecular dynamics software package was used to run the simulations. The simulations were run with periodic boundary conditions at constant temperature and pressure. GAFF<sup>7</sup> and OPLS<sup>8</sup> models were used with a single ion and 1000 EC molecules. Dimer energies and geometries were calculated by energy minimization. Thermodynamic integration was used to calculate free energy changes for each ion. Surface potential corrections to the single ion free energies are made.<sup>9</sup>

**Table 1.** Calculated free energies for free energy optimized Lennard-Jones parameters using the GAFF model for EC compared to experiment.

ion	optimized parameters			experiment
	$\epsilon$ (kcal/mol)	$\sigma$ (Å)	$\Delta G$ (kcal/mol)	$\Delta G$ (kcal/mol)
F <sup>-</sup>	0.1038	2.47	-84.9	-84.61
Cl <sup>-</sup>	0.1276	3.55	-68.9	-68.60
Br <sup>-</sup>	0.1516	3.90	-64.7	-64.77
I <sup>-</sup>	0.1576	3.75	-66.6	-66.68
K <sup>+</sup>	0.0598	2.69	-88.5	-88.67

## 3. Results

Initial estimates for the values for the Lennard-Jones parameters were generated to reproduce the quantum dimer energy and separation taken from MP2 calculations. The values of the Lennard-Jones parameters optimized to reproduce the experimental free energy data of Peruzzi, *et al*<sup>2</sup> are given in Table 1. Those calculations used the GAFF model for EC.

Using these values, the dimer energies and structures were calculated. The dimer properties are shown in Table 2. Parameters for the ions  $\text{Li}^+$  and  $\text{Na}^+$ , for which there is not the free energy data are shown as well. For comparison, the dimer properties were also calculated using the OPLS model for EC. The results are slightly different between the models not only because the EC parameters (charges and Lennard-Jones parameters) are different but also the combining rules are different. OPLS uses the geometric mean for both  $\epsilon_{ij}$  and  $\sigma_{ij}$ .

**Table 2.** Dimer properties using the optimized ion parameters and GAFF and OPLS models for EC compared to MP2 results.

Ion	$\epsilon(\text{kcal/mol})$	$\sigma(\text{\AA})$	GAFF		OPLS		MP2	
			$r_{\text{min}}$	$E_{\text{min}}(\text{kcal/mol})$	$r_{\text{min}}(\text{\AA})$	$E_{\text{min}}(\text{kcal/mol})$	$r_{\text{min}}(\text{\AA})$	$E_{\text{min}}(\text{kcal/mol})$
$\text{F}^-$	0.1038	2.15	5.845	-28.17	5.708	-28.09	5.7946	-33.58
$\text{Cl}^-$	0.1276	3.15	6.422	-21.47	6.318	-20.68	6.3942	-23.68
$\text{Br}^-$	0.1516	3.55	6.624	-19.72	6.515	-19.00	6.5246	-21.65
$\text{I}^-$	0.1576	3.80	6.557	-20.37	6.442	-19.61	---	---
$\text{Li}^+$	0.145	1.35	1.678	-45.27	1.556	-45.25	1.767	-51.66
$\text{Na}^+$	0.190	1.925	1.953	-36.44	1.917	-33.53	2.140	-37.49
$\text{K}^+$	0.250	2.60	2.280	-28.17	2.300	-25.91	2.51	-28.26

The distance given in Table 2 represents the distance from the O1 oxygen (see Figure 1) and the ions. Representative structures for both the anions and cations are shown in Figure 2. The EC molecule has a big dipole (6.21 Debye for the GAFF model and 5.48 Debye for the OPLS model). The cations associate with the positive end of the dipole, near the O1 oxygen, and the anions with the negative end, on the other side of the EC molecule.

#### 4. Conclusion

With modifications to the Lennard-Jones parameters, models for ions can be made which give good agreement with *ab initio* calculations for the EC-ion dimer as well as experimental data for the solvation free energy. The potential can then be used to understand the structure and dynamics of ions in ethylene carbonate.

#### 5. Acknowledgments

The current work is funded by the NSF EPSCoR LA-SiGMA project under award #EPS-1003897. Useful conversations and electronic structure data from Tom Beck and Ayse Arslanargin are gratefully acknowledged.

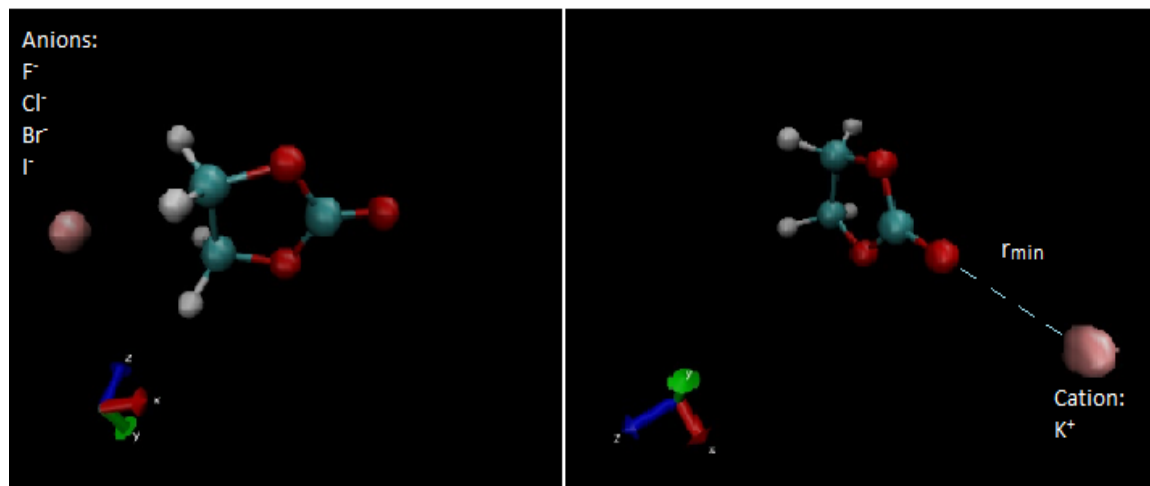


**Figure 2.** Geometries for the representing the minimum energy dimer for anions (left) and cations (right) with ethylene carbonate.

## 6. References

- [1] J. Jones, M. Anouti, M. Caillon-Caravanier, P. Williams, & D. Lemordant. Lithium fluoride dissolution equilibria in cyclic alkylcarbonated and water *J. Mol. Liq.* **153**, 146–152 (2010).
- [2] N. Peruzzi, B.W. Ninham, P. Lo Nostro, & P. Baglioni, Hofmeister Phenomena in Nonaqueous Media: The Solubility of Electrolytes in Ethylene Carbonate. *J Phys Chem B* **116**, 14398–14405 (2012).
- [3] T.G.A. Youngs & C. Hardacre, Application of static charge transfer within an ionic-liquid force field and its effect on structure and dynamics. *ChemPhysChem* **9**, 1548–1558 (2008).
- [4] I. Leontyev & A. Stuchebrukhov, Accounting for electronic polarization in non-polarizable force fields. *Phys Chem Chem Phys* **13**, 2613 (2011).
- [5] M. Soniat & S.W. Rick, The effects of charge transfer on the aqueous solvation of ions. *J Chem Phys* **137**, 044511 (2012).
- [6] B. Hess, C. Kutzner, D. Van Der Spoel, & E. Lindahl, GROMACS 4: Algorithms for highly efficient, load-balanced, and scalable molecular simulation. *J. Chem. Theory Comput.* **7**, 306 (2008).
- [7] J. Wang, W. Wang, P.A. Kollman, & D.A. Case, Automatic atom type and bond type perception in molecular mechanical calculations. *J. Molec. Graphics and Design* **25**, 247260 (2006).
- [8] C. Coleman, P.J. van Maaren, M. Hong, J.S. Hub, L.T. Costa, L.T., & D. van der Spoel, Force Field Benchmark of Organic Liquids: Density, Enthalpy of Vaporization, Heat Capacities, Surface Tension, Isothermal Compressibility, Volumetric Expansion Coefficient, and Dielectric Constant, *J. Chem. Theor. Comput.* **8**, 61-74 (2012)
- [9] Beck, T. L. Hydration Free Energies by Energetic Partitioning of the Potential Distribution Theorem. *J. Stat. Phys.* **145**, 335–354 (2011).

## Study of CO Adsorption and Dissociation on Metal clusters using DFT

Suraj Gyawali<sup>1</sup>, Dr. Daniela S. Mainardi<sup>2</sup>

<sup>1</sup>Institute for Micro-Manufacturing, Louisiana Tech University

<sup>2</sup>Chemical Engineering, Louisiana Tech University

**Abstract:** Results from density functional theory calculations indicate that the CO molecule adsorbs strongly on the Cobalt based bimetallic system than pure Cobalt and Iron cluster. We show the energy cost to dissociate CO molecule on the surface of the catalysts varies as the composition of the nano-cluster is manipulated. Thus, more detailed kinetic studies, taking into account the effect of CO coverage and varying the core-shell composition, are likely to reduce the energy costs.

**Keywords:** density functional theory, transition state theory, catalysts, Fischer-Tropsch, CO adsorption energy, CO dissociation

### 1. Introduction

Due to the limitation of easily accessible fossil fuels, there has been a stimulation to many researchers for the search of alternative energy sources [1]. The role of Natural Gas, Coal, and Biomass as a feedstock for the synthesis of chemicals and fuels has continued to grow. Natural gas, Coal, and Biomass can be utilized to produce synthesis gas which can be later used to synthesize higher aliphatic hydrocarbons too [2]. One way of converting synthesis gas to fuels is via Fischer Tropsch synthesis. Synthesis gas comprises of CO and H<sub>2</sub> molecules in a certain ratio. CO and H<sub>2</sub> binds on the surface of the catalysts at first as an initial step in heterogeneous catalytic reaction process. Then CO dissociates on the surface of the catalysts for further polymerization to form hydrocarbons on the surface of the catalyst. The catalysts mainly used in the F-T synthesis are transition metals like copper and iron [2].

CO activation is considered to be a preliminary step in Fischer Tropsch reaction which is technologically important to understand the reactivity of transition metals that are responsible to form hydrocarbons [3]. Studies based on CO activation has also concluded that F-T reaction can be categorized as a structure sensitive reaction [4]. This has led many researchers to study Fischer Tropsch reaction on different type of catalytic surfaces like stepped and corrugated surfaces [5]. There are many theoretical and experimental studies being done in order to find out the active sites and reaction pathway on the surface of the catalysts for the FT reaction. This will help us to find appropriate shaped catalysts which will be suitable for F-T synthesis [5].

### 2. Methodology

Fischer Tropsch Synthesis process initiates with the adsorption of carbon monoxide on the surface of the catalyst. Therefore it is important to study the adsorption of CO on various surface sites of the catalysts [5]. All the studies in this paper have been performed using Density Functional Theory [6].

The cluster models of catalysts, the reactants and the products species were created using Materials Studio Visualizer. Cluster models of Cobalt, Iron, and Bimetallic cluster of Cobalt and Iron with the radius of 3.5 Å are created. The cobalt cluster contains 14 atoms while the iron clusters contains 15 atoms. This paper includes also two bimetal clusters. The first one is cobalt-iron bimetal with 10 cobalt atoms as shell and 4 iron atoms as core which is represented as Co<sub>10</sub>Fe<sub>4</sub>, and the second one is iron-cobalt cluster with 10 iron atoms as shell and 4 cobalt atoms as core which is represented as Fe<sub>10</sub>Co<sub>4</sub> which are represented in fig 1 respectively.

All the geometry optimization and binding energy calculations are performed with DMol3. Density Functional theory is used to optimize the clusters with the gradient corrected exchange-correlation functional according to revised Perdew, Barke and Ernzerhof (rPBE) [6] and double numerical basis set in a p-polarization function (DNP). CO dissociation on the surface of the catalysts were studied using transition state calculations. TS calculations are performed by using synchronous methods which utilizes the optimized reactant and products since the transition state is unknown [7]. DMOL3 utilizes two synchronous trait methods to determine the transition state: Linear Synchronous Transit (LST) and Quadratic Synchronous Transits (QST) to identify the transition state of a reaction. The reaction barrier is calculated after this iterative process is continued until the convergence is reached. All the calculations for the cluster models are done by analyzing vibrational frequencies to ensure if a stationary point is a minimum state with no negative frequencies or transition state with only one negative frequency.

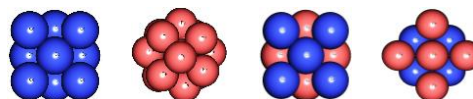


Figure 1 Cobalt and Iron based nano-clusters

### 3. Results

#### 3.1 CO Adsorption on Metal Clusters

The different surface sites include top, bridge, and hollow sites on 3-d transition metal nano-cluster which is represented in the figure 2:-

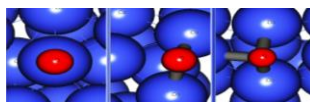


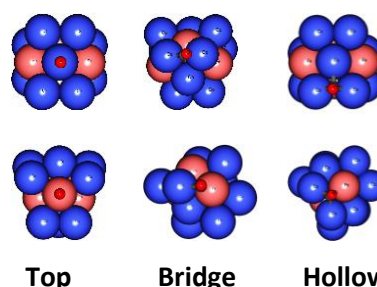
Figure 2 Top, Bridge and Hollow Sites respectively on Cobalt Cluster.

The adsorption of CO is studied on four different types of catalyst that are pure cobalt cluster, pure iron cluster, cobalt based bimetal cluster (cobalt as shell and iron as core), and iron based bimetal cluster (iron as shell and cobalt as core) as shown in the figure 2.

The CO adsorption energy values on the different catalysts are calculated using equation 1.

$$BE = E_{system} - (E_{cluster} + E_{CO}) \dots \dots \dots 1$$

The calculated chemisorption energy for the pure cobalt cluster are given as -1.73, -1.64, and -1.36 eV for the top, bridge, and hollow sites respectively. Hence, CO binds more strongly on the top site of the pure cobalt cluster. Similarly, the binding energy of CO on iron cluster is computed which are -2, -1.81, and -1.65 eV for the top, bridge, and hollow sites respectively. Since the lowest binding energy is -2 eV, it suggests that CO binds stronger on the top site of the iron cluster. There are more reaction sites for the bimetallic catalysts than the pure catalysts. All the possible reaction sites for the bimetallic sites are shown in figure 3. The calculated chemisorption energies for the bimetallic cluster  $\text{Co}_{10}\text{Fe}_4$  and  $\text{Fe}_{10}\text{Co}_4$  are also given in the table



Catalysts	BE (eV)	Catalysts	BE (eV)
$\text{Co}_{10}\text{Fe}_4$ (Co Top)	-3.74	$\text{Fe}_{10}\text{Co}_4$ (Fe Top)	-4.38
$\text{Co}_{10}\text{Fe}_4$ (Co-Co-Co Hollow)	-3.80	$\text{Fe}_{10}\text{Co}_4$ (Fe-Fe Bridge)	-4.35
$\text{Co}_{10}\text{Fe}_4$ (Co-Co-Co Hollow)	-3.81	$\text{Fe}_{10}\text{Co}_4$ (Fe-Fe-Fe Hollow)	-3.91
$\text{Co}_{10}\text{Fe}_4$ (Fe Top)	-3.94	$\text{Fe}_{10}\text{Co}_4$ (Co Top)	-4.75
$\text{Co}_{10}\text{Fe}_4$ (Fe-Co Bridge)	-3.15	$\text{Fe}_{10}\text{Co}_4$ (Fe-Co Bridge)	-4.65
$\text{Co}_{10}\text{Fe}_4$ (Fe-Co-Co Hollow)	-3.75	$\text{Fe}_{10}\text{Co}_4$ (Fe-Fe-Co Hollow)	-5.17

From the table, we can see that the calculated active sites for two bimetallic system. The first system is  $\text{Co}_{10}\text{Fe}_4$  where Cobalt atoms are the shell and Iron are the core atoms. The most preferred sites in the nano-cluster is the adsorption of CO on the top position of the iron atom with the binding energy -3.94 eV. The second most preferred sites is the hollow position where CO binds with three Cobalt atoms with the binding energy of -3.81 eV. The binding of CO with bridge position of two Cobalt atoms changed to hollow position of three Cobalt atoms after the geometry optimization with the binding energy of -3.80 eV. Similarly, the binding energy of CO

Figure 3 All possible active sites on bimetallic catalyst  $\text{Co}_{10}\text{Fe}_4$

Table 1 Calculation of binding energy on bimetallic cluster.

molecules on  $\text{Fe}_{10}\text{Co}_4$  is minimum for the hollow position with two Iron atoms and a Cobalt atom with the binding energy of -5.17 eV. The second most preferred active site for CO molecule is on the top of the Cobalt atom with the binding energy of -4.75 eV.

### 3.2 Dissociation of CO molecules on the surface of the cluster

After finding the most stable reaction sites on the surface of the nano-cluster, dissociation of CO on their surface were studied using dmol3 transition state calculation. The most preferred reaction sites (with minimum binding energy) are responsible for the low CO dissociation energy, and this includes CO top on Cobalt cluster, CO top on iron cluster, CO top on iron atom of  $\text{Co}_{10}\text{Fe}_4$  cluster and Co hollow on three cobalt atoms on  $\text{Co}_{10}\text{Fe}_4$  cluster, CO hollow on iron-iron-cobalt atoms of  $\text{Fe}_{10}\text{Co}_4$ , and CO top on cobalt atom of  $\text{Fe}_{10}\text{Co}_4$  cluster.

According to the transition state calculation using dmol3 which utilizes LST/QST tool, the energy cost to dissociate CO molecule on the surface of cobalt cluster is 2.21 eV which is quite lower than the energy cost to dissociate CO molecule on iron cluster which is 3.20 eV. The energy cost to dissociate CO molecule binding in hollow configuration with three cobalt atoms on  $\text{Co}_{10}\text{Fe}_4$  is 2.67 eV while the energy cost to dissociate CO molecule binding on top of iron atom is 2.71 eV. The energy cost to dissociate CO molecule binding in hollow configuration with two cobalt atoms and an iron atom on  $\text{Fe}_{10}\text{Co}_4$  is 3.02 eV while to CO molecule binding on top of cobalt atom is 2.78 eV.

#### 4. Conclusion

In bimetallic nano-cluster the binding of CO molecule was observed to be most stable and stronger than pure Cobalt cluster and Iron cluster. This suggests that the probability of formation of long chain hydrocarbon is possible in bimetallic nano-cluster. While on the other hand, dissociation of CO molecule also plays an important role for the selection of the catalysts, because it is the first step in the reaction mechanism of Fischer Tropsch synthesis. Dissociation of CO molecule should not be high because it should not be the rate limiting step for the reaction to proceed on. Dissociation of CO molecule is least in Cobalt cluster with 2.21 eV. We can also see that, iron atoms as shell has lower CO binding energy and higher CO dissociation energy than iron atoms as core. This is suggesting that adding iron atoms in cobalt, we can increase the CO binding energy, but at the same time we are also increasing the CO dissociation energy.

#### 5. Acknowledgments

The current work is funded by the NSF EPSCoR LA-SiGMA project under award #EPS-1003897.

#### 6. References

- [1] Breejen, J. d., Radstake, P. B., Bezemer, G. L., Bitter, J. H., Froseth, V., Holmen, A., & Jong, K. d. (2009). On the Origin of the COBalt Particle Size Effects in Fischer-Tropsch Catalysis. *American Chemical Society*, 7197-7203.
- [2] Filot, I. A., Shetty, S. G., Hensen, E. J., & Santen, R. A. (2011). Size and Topological Effects of Rhodium Surfaces, Clusters, and Nanoparticles on the Dissociation of CO. *The Journal of Physical Chemistry*, 14204-14212.
- [3] Kim, H. Y., Han, S. S., Ryu, H. J., & Lee, H. M. (2010). Balance in Adsorption Energy of Reactants Steers CO Oxidation Mechanism of  $\text{Ag}_{13}$  and  $\text{Ag}_{12}\text{Pd}_1$  Nano-particles: Association Mechanism versus Carbonate-Mediated Mechanism. *Journal of Physical Chemistry*, 3156-3160.
- [4] Liu, Z. P., & Hu, P. (2003). General Rules for Predicting Where a Catalytic Reaction Should Occur on Metal Surfaces: A Density Functional Theory Study of C-H and C-O Bond Breaking/Making on Flat, Stepped, and Kinked Metal Surfaces. *American Chemical Society*, 1958-1967.
- [5] Olusola, J. O., Choudhary, B., Mesubi, M. A., & Maity, S. (2012). Reflections on the Chemistry of the Fischer Tropsch synthesis. *The Royal Society of Chemistry*, 7347-7366.
- [6] Shetty, S., Jansen, A. P., & Santen, R. A. (2009). Direct versus Hydrogen-Assisted CO Dissociation. *American Chemical Society*, 12874-12875.
- [7] Tian, F. Y., Shen, J., & Wang, Y. X. (2010). Density Functional Study of CO Adsorbed on  $\text{MnN}$  (N=2-8) Clusters. *Journal of Physical Chemistry*, 1616-1620.

# Study of the Three-Dimensional Edwards-Anderson Model in an External Field with a Multi-spin Coding Parallel Tempering Monte Carlo Simulation

Sheng Feng<sup>1,2</sup>, Ye Fang<sup>2,3</sup>, Ka-Ming Tam<sup>1,2</sup>  
Juana Moreno<sup>1,2</sup>, J. Ramanujam<sup>2,3</sup>, Mark Jarrell<sup>1,2</sup>

<sup>1</sup>Department of Physics and Astronomy, Louisiana State University

<sup>2</sup>Center for Computation and Technology, Louisiana State University

<sup>3</sup>ECE Division, School of Electrical Engineering and Computer Science, Louisiana State University

**Abstract:** We implement the Monte Carlo method for the Edwards-Anderson model in the Graphics Processing Units architecture. The multi-spin coding method is used to accommodate memory size requirements and the parallel-tempering method is used to accelerate the thermalization of the Monte Carlo simulation. We confirm previous findings that conventional indicators for the spin glass transition, including the Binder ratio and the correlation length do not show any indication of a transition for rather low temperatures. However, the ratio of spin glass susceptibilities do show crossing behavior, albeit a systematic analysis is beyond the reach of the present data.

**Keywords:** Spin Glass, Ising Model, Parallel Tempering, GPU, CUDA, Multi-spin Coding

## 1. Introduction

Although magnetism is a well-studied topic in the field of condensed matter physics, the effects of frustration and randomness in magnetic systems remain in the forefront of research.<sup>1</sup> In particular, the unusual behaviors of disordered materials due to glassy magnetic systems are still being intensively studied. Unlike a ferromagnet, in which the spin rotational symmetry is broken, a spin glass manifests itself in the lack of ergodicity, i.e., the symmetry is broken in time. Therefore, a truly equilibrium phase is not attainable in the thermodynamic limit. Some of the experimental features, including their frequency-dependent susceptibilities and the discrepancy between zero-field and field cooling measurements, suggest that spin glasses have very slow dynamics.

It is believed that randomness and frustration are crucial in most of the spin glass systems. In real materials, the dilution introduces randomness; and directional or distance-dependent coupling, such as dipolar coupling in insulating systems and the Ruderman-Kittel-Kasuya-Yoshida coupling<sup>2,3,4</sup> in metallic systems, introduces frustration. A simple theoretical model that captures the consequences of disorder is an Ising model with quenched random disorder couplings. This model was first proposed by Edwards and Anderson.<sup>5</sup> The mean field solution of the Edwards-Anderson model for infinite dimensions was first attempted by Sherrington and Kirkpatrick.<sup>6</sup> However, the mean field solution was found to be unstable below the Almeida-Thouless line.<sup>7</sup> The difficulty of obtaining a stable solution was solved by Parisi with his replica symmetry breaking ansatz.<sup>8,9</sup>

Although the mean field solution has been proven to be the correct description of the spin glass phase<sup>10,11</sup> for the Sherrington-Kirkpatrick model, the spin glass physics for finite dimensions, which presumably is more relevant to experiments, is still not fully understood. Indeed, it had been debated for a long time whether the spin glass phase at finite temperature exists in three dimensions.

The Edwards-Anderson model may be deceptively simple. Since it is a classical spin model one may think that its numerical study can be simply carried out by Monte Carlo methods. A defining signature of spin glass systems is their long relaxation time. In addition, it has been proved that finding the ground state of the three dimensional Edwards-Anderson model is an NP-complete problem.<sup>12</sup> For sufficiently low temperature, the system becomes very sluggish and equilibration is prohibitively difficult to obtain even for modest systems sizes. Unfortunately, unlike the unfrustrated systems, an efficient cluster Monte Carlo algorithm is not available.

The breakthrough in the numerical study of spin glass systems came along with the introduction of the parallel tempering method, which allows the study of larger system sizes at lower temperatures than the simple single spin flip Monte Carlo method.<sup>13,14,15,16</sup> Combined with the use of the correlation length instead of ratio of cumulants for finite size scaling, it is now widely believed that the thermodynamic finite temperature spin glass phase does exist in the Edwards-Anderson model for three dimensions.<sup>17</sup>

A prominent problem is what is the nature of the spin glass phase below the upper critical dimension. In particular if the spin glass can still be described by the replica symmetry-breaking scenario, there should be an Almeida-Thouless line below the upper critical dimension. One of the possible tests on whether the Almeida-Thouless line exists is to determine whether a spin glass phase exists under an external magnetic field. Recent studies on this problem do not come to a universal consensus. The analysis based on correlation length suggests the absence of the spin glass phase.<sup>18</sup> On the other hand, a recent study in four-dimensional lattices shows that by using the ratio of susceptibilities for the finite size scaling analysis, a spin glass phase can be revealed.<sup>19</sup>

Given the on-going controversy on the nature of the spin glass phase below the upper critical dimension, it is desirable to implement an efficient parallel-tempering (PT) Monte Carlo algorithm that utilizes the architecture of graphics processing units (GPU). In this work we will show that using the multi-spin coding method, the Monte Carlo algorithm can be implemented efficiently in the GPU.<sup>20,21</sup> The code provides substantial speed up compared to other GPU implementations, and approaches close to fifty percent of the speed achieved on special-purpose field programmable gate array (FPGA) architectures.<sup>22</sup>

## 2. Algorithm

We use the Monte Carlo Metropolis update to do single spin flips in a three-dimensional cubic lattice. There are  $L$  sites on each dimension, and therefore  $L^3$  sites in total. On each site, there is a spin pointing up or down, represented by +1 or -1, and the spins interact with each other following the Hamiltonian:  $H = \sum_{\langle i,j \rangle} J_{ij} S_i S_j + \sum_i h S_i$ , where  $\langle i,j \rangle$  stands for nearest neighbors, and  $J_{ij}$  is a random interaction between the them. To optimize performance, we adopt the multi-spin technique by coding the spins as bits in integers, so that we can use bit operations to manipulate multiple spins in parallel.<sup>23</sup>

For the model we are interested in, the energy landscape is rugged and complicated. It is difficult for the system, especially at very low temperatures, to get through the energy barriers and explore the phase space efficiently. In order to ease this problem, we use the parallel tempering or replica exchange method. For each of the disorder realizations,  $N_B$  different replicas are simulated at the same time, with temperatures ranging from above to below the critical temperature. During the simulation, we propose to exchange the configuration of two replicas, and accept the change with probability  $P = e^{-\Delta E \Delta \beta}$ . In this way, the spin configuration of systems with different temperatures will be swapped frequently throughout the simulation.

### 3. Results

We perform Monte Carlo simulations of the three-dimensional Edwards-Anderson model in a finite external field. We focus on the equilibrium quantities of this notoriously difficult system. By taking advantage of the new commodity multi-threaded graphic computing units architecture we drastically reduce the computation time. The results for the Binder ratio and correlation length show no signal of intersection, thus they point to the absence of spin glass transition according to conventional wisdom. On the other hand, the ratio of susceptibilities  $R_{12}$  does show crossing behavior for relatively small system sizes ( $L = 6$  and  $8$ ). With the present system sizes and the statistical error bar, a rigorous data analysis does not seem to deliver unbiased information.

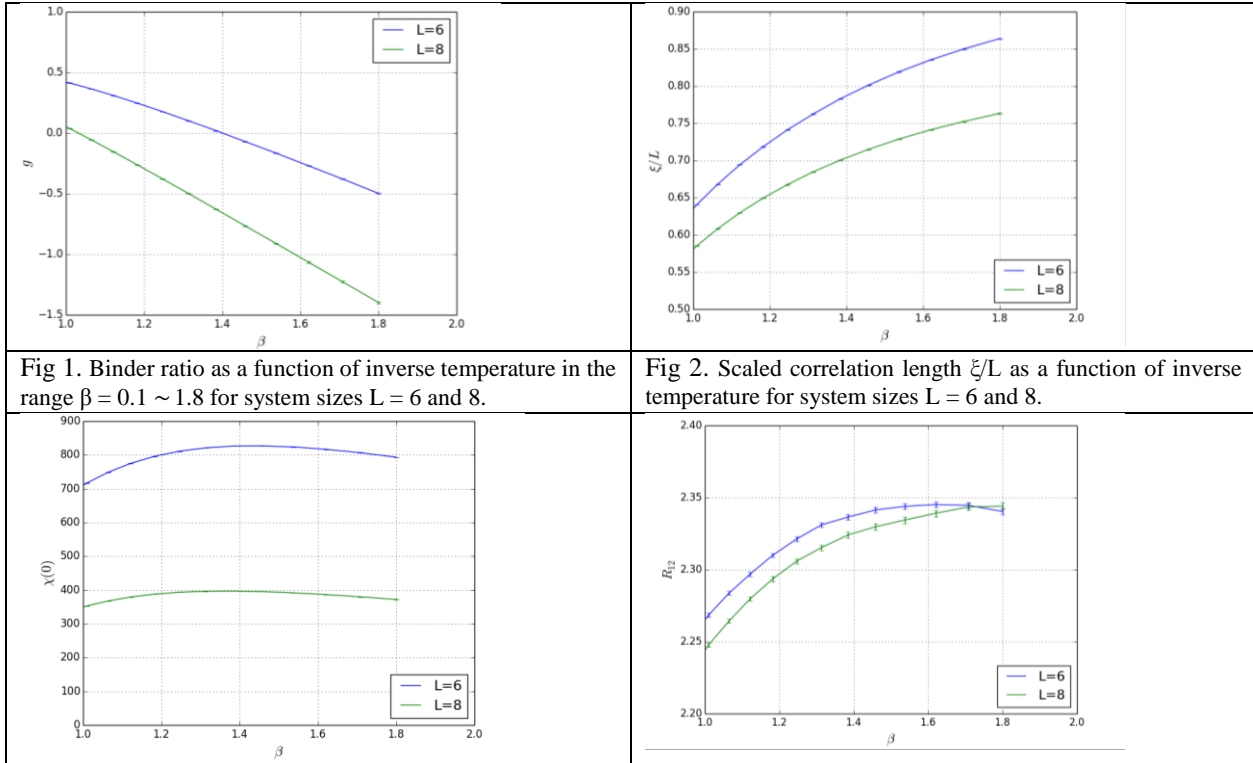


Fig 1. Binder ratio as a function of inverse temperature in the range  $\beta = 0.1 \sim 1.8$  for system sizes  $L = 6$  and  $8$ .

Fig 2. Scaled correlation length  $\xi/L$  as a function of inverse temperature for system sizes  $L = 6$  and  $8$ .

<p>Fig 3. Spin glass susceptibility at zero momentum, <math>\chi(0)</math>, as a function of inverse temperature for system sizes <math>L = 6</math> and <math>8</math>.</p>	<p>Fig 4. <math>R_{12}</math> as a function of inverse temperature for different system sizes. An intersection can be seen at around <math>T \approx 0.6</math>. We use the jackknife method to estimate the error bar from sample-to-sample variation.</p>
--	---

#### 4. Acknowledgments

The current work is funded by the NSF EPSCoR LA-SiGMA project under award #EPS-1003897. Portions of this research were conducted with high performance computational resources provided by Louisiana State University (<http://www.hpc.lsu.edu>). We thank Helmut Katzgraber and Karen Tomko for useful conversations.

#### 5. References

- [1] K. Binder and A. P. Young, *Rev. Mod. Phys.* **58**, 801 (1996).
- [2] M. A. Ruderman and C. Kittel, *Phys. Rev.* **96**, 99 (1954).
- [3] T. Kasuya, *Prog. Theor. Phys.* **16**, 45 (1956).
- [4] K. Yosida, *Phys. Rev.* **106**, 893 (1957).
- [5] S. F. Edwards and P. W. Anderson, *J. Phy. F: Met. Phys.* **5**, 965 (1975).
- [6] D. Sherrington and S. Kirkpatrick, *Phys. Rev. Lett.* **35**, 1792 (1975).
- [7] J. R. L. de Almeida and D. J. Thouless, *J. Phys. C:* **11**, 983 (1978).
- [8] G. Parisi, *J. Phys. A: Math. Gen.* **13**, 1101 (1980).
- [9] M. Mezard, G. Parisi, and M. A. Virasoro, “Spin glass theory and beyond”, Singapore: World Scientific.
- [10] M. Talagrand, *Ann. Probab.* **28**, 1018 (2000).
- [11] F. Guerra and F. L. Toninelli, *Commun. Math. Phys.* **230**, 71 (2002).
- [12] F. Barahona, *J. Phys. A* **15** (1982) 3241.
- [13] R. H. Swendsen and J.-S. Wang, *Phys. Rev. Lett.* **57**, 2607 (1986).
- [14] C. J. Geyer, *Computing Science and Statistics: Proceedings of the 23rd Symposium of the Interface*, 156 (1991).
- [15] E. Marinari and G. Parisi, *Europhys. Lett.* **19**, 451 (1992).
- [16] K. Hukushima and K. Nemoto, *J. Phys. Soc. Jpn.* **65**, 1604 (1996).
- [17] H. G. Ballesteros, A. Cruz, L. A. Fernández, et al., *Phys. Rev. B* **62**, 14237 (2000).
- [18] A. P. Young and H. G. Katzgraber, *Phys. Rev. Lett.* **93**, 207203 (2004).
- [19] Janus Collaboration: R. A. Baños, A. Cruz, L.A. Fernandez, et al., *Proc. Natl. Acad. Sci. USA*, **109**, 6452 (2012).
- [20] M. Creutz, L. Jacobs, and C. Rebbi., *Phys. Rev. Lett.* **42**, 1390 (1979).
- [21] C. Rebbi and R. H. Swendsen, *Phys. Rev. B* **21**, 4094 (1980).
- [22] Janus Collaboration: F. Belletti, I. Campos, A. Cruz, et al. *Computing in Science & Engineering* **8**, 41 (2006).
- [23] Y. Fang, S. Feng, K.-M. Tam, Z. Yun, J. Moreno, J. Ramanujam and M. Jarrell, *Computer Physics Communications*, **185** 2467 (2014).

## **Synthesis and Characterization of Dendronized Polymers based on Poly(Ethylene Glycol)**

**Brittany K. Myers<sup>1</sup>, Scott M. Grayson<sup>1</sup>**

<sup>1</sup> Department of Chemistry, Tulane University, New Orleans, LA 70118

**Abstract:** The ability to encapsulate guest molecules has garnered a lot of attention for conventional micelles. Yet, small molecule amphiphiles are known to yield micelles with limited stability and even amphiphilic linear polymers are susceptible to disaggregation at low concentrations. For this reason, branched, covalently-bound amphiphilic units are attractive because the resulting molecules are robust when conventional micelles would disaggregate and exhibit no critical micelle concentration. MALDI-ToF MS was used to characterize well-defined hybrids consisting of linear poly(ethylene glycol) and dendritic polyesters because this technique provides tremendously detailed data to confirm the high structural purity of the dendronized PEG analogs. Characterization via MALDI-ToF MS at each step of the synthesis ensured that each step of the dendronization procedure was carried to completion. This is in contrast to methods such as NMR and GPC which, though useful for rudimentary product characterization, could not verify the overall structural purity. Because polymer purity is paramount for in vivo biomedical applications, MALDI-ToF MS represents a valuable technique for the detailed monitoring of these dendronization reactions and characterization of their products.

**Keywords:** Poly(ethylene) glycol, PEG, Dendrimer, Micelle, MALDI-ToF MS

### **1. Introduction**

Conventional micelles have received considerable attention because of their ability to encapsulate guest molecules. They are generally physical aggregates of amphiphilic block copolymers only stable in selective solvents and conditions. While self-assembly can yield well-defined aggregates, they disaggregate at low concentrations.<sup>1</sup> For this reason, amphiphilic units which are covalently bound together to prevent disaggregation are attractive. As a result, these “unimolecular micelles” are hardy under conditions in which conventional micelles would disaggregate and exhibit no critical micelle concentration (CMC).

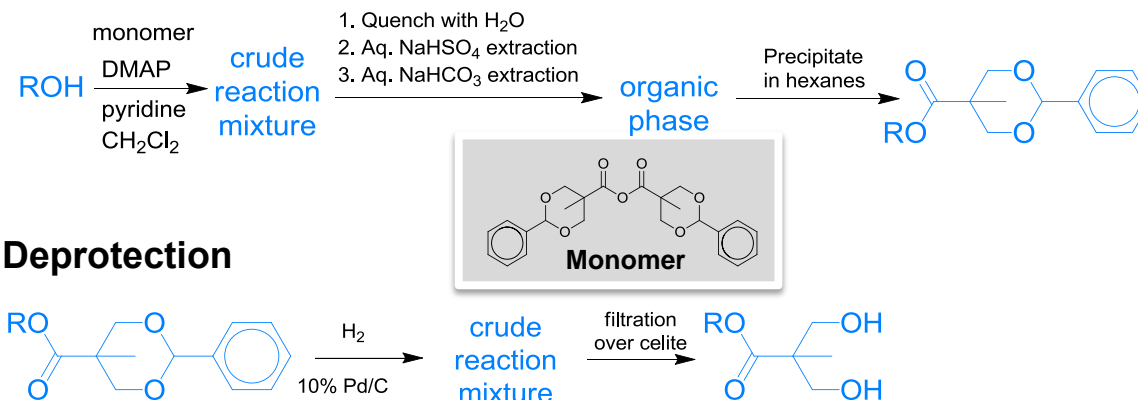
The first unimolecular micelles were prepared from dendritic polymers. Dendrimers are highly branched macromolecules that are an ideal scaffold for preparing unimolecular micelles because their number of peripheral end-groups increases exponentially with each generation and can easily be functionalized with groups of contrasting polarity. Per the De Gennes limit, the outside of the dendrimer becomes densely packed while shielding the interior void spaces from the environment. These void spaces can then be used to house guests of an appropriate size (usually a few angstroms). The “generation” of the dendrimer, the number and properties of its peripheral groups, and the properties of its scaffolding<sup>2</sup> can ultimately affect solubility<sup>3</sup>, viscosity<sup>4</sup>, and various other characteristics.<sup>5</sup> These unique properties make dendrimers strong candidates for guest molecule encapsulation and various other supramolecular functions attributed to conventional micelles.

As stated previously, the De Gennes limit ultimately dictates the amount of void space within a dendrimer. This could pose a problem if the guest molecules are particularly large or require substantial loading efficiencies. One way to construct a more modular unimolecular micelle with larger void spaces is to incorporate linear polymer components between dendritic branching units. For example, this can be done by dendronizing a star core, such as linear polyethylene glycol (PEG) grown from a poly-ol initiators.

## 2. Synthesis

The benzylidene-protected bis-(hydroxymethyl)propionic anhydride was synthesized using a previously reported technique. While such dendronized PEGs have been reported in the past, their detailed analysis by MALDI-ToF MS and GPC have not been reported.<sup>6</sup> Two different low PDI linear PEGs were used to create the dendritic-linear hybrids: a monomethyl ether PEG alcohol (5000 Da) and a linear PEG diol (4700 Da). These average molecular weights were determined via MALDI-ToF MS and agreed closely with manufacturer's specifications. These hybrids were then synthesized by subjecting each of the core molecules (Fig. 1) to repetitions of an acid anhydride esterification "dendron growth" reaction and a palladium-catalyzed hydrogenolysis "deprotection" reaction (Scheme 1). The linear-dendritic hybrids were synthesized up to the third generation.

### Coupling



Scheme 1: General dendronization scheme showing both coupling and deprotection.

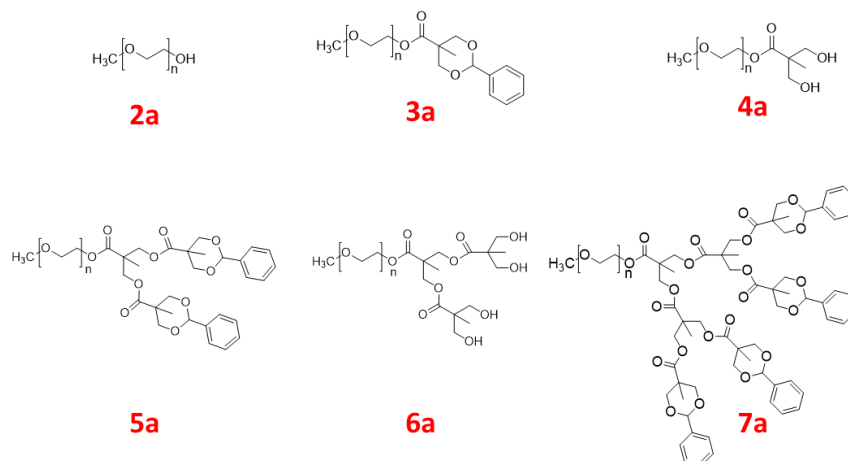


Figure 1: Monomethyl ether PEG alcohol (2a) and its dendronized derivatives (3a-7a).

### 3. Characterization

#### 3.1 MALDI-ToF MS Characterization

Matrix-assisted laser desorption/ionization time-of-flight mass spectrometry (MALDI-ToF MS) shows the expected mass gains and losses associated with each dendronization and deprotection of the monomethyl ether PEG alcohol ending with the third generation (Figure 2). A polymer with 109 repeat units is

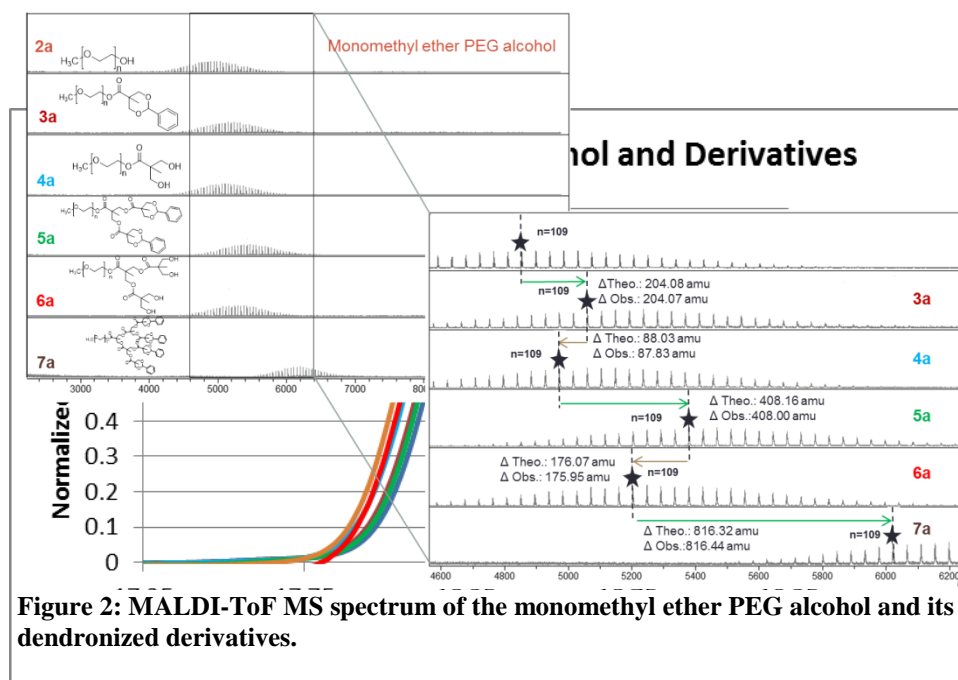


Figure 2: MALDI-ToF MS spectrum of the monomethyl ether PEG alcohol and its dendronized derivatives.

Figure 2: Gel permeation chromatograms of the monomethyl ether PEG alcohol and its derivatives through the third generation.

used to highlight this aspect of the characterization process.

### **3.2 Gel Permeation Chromatography Characterization**

Gel permeation chromatography (GPC) is used as a complementary technique to MALDI-ToF MS which, due to its high mass accuracy, is much more conclusive. This because, when using GPC, it is difficult to know that the molecules are fully coupled and deprotected throughout the dendronization process due to the very subtle changes in retention time for each derivative. It can be noted, though, that as the generation increases, we see a trend of shifting toward shorter retention times (Figure 3).

### **4. Conclusion**

Dendronized derivatives of monomethyl ether PEG alcohol were successfully synthesized and characterized. The process of dendronization ultimately increased the functionality four-fold, thus creating more points at which the derivatives could be further functionalized in the future.

### **5. Acknowledgments**

The current work is funded by the NSF EPSCoR LA-SiGMA project under award #EPS-1003897.

### **6. References**

- [1] Shi, Wenzhang. et al. *J. Phys. Chem. B*, 2006, 110, 2638-2642.
- [2] Percec, V. et al. *Science*, 2010, 328, 1009-1014.
- [3] Frechet, J. M. J. et al. *Polymer*, 1994, 35, 4489-4495.
- [4] Mourey, T. H. et al. *Macromolecules*. 1992, 25, 2401-2406.
- [5] Ornelas, C. et al. *Chem. Rev.* 2010, 110, 1857-1959.
- [6] H. Ihre, O.L. Padilla de Jesus, J.M.J. Frechet, *J. Am. Chem. Soc.*, 2001, 123, 5908–5917.

## Synthesis of Novel Amphiphilic Capping Ligands as an Organic Coating for Nanoparticulate Iron Oxide Imaging and Delivery Agents

Denis Nilov<sup>1</sup>, Pavel Kucheryavy<sup>1</sup>, Rajesh Komati<sup>1</sup>, Carl Mitchell<sup>1</sup>, Anastasia LeBeaud<sup>1</sup>, Alex Burin<sup>2</sup>, Vladimir Kolesnichenko<sup>1</sup> and Galina Goloverda<sup>1</sup>

<sup>1</sup> Department of Chemistry, Xavier University

<sup>2</sup> Department of Chemistry, Tulane University

### Abstract:

In the course of development of novel capping ligands with variable steric factor, which will be used as an organic coating for metal oxide nanoparticles, a base-catalyzed nucleophilic oxirane ring-opening addition reaction between dimethyl 5-hydroxyisophthalate and allyl glycidyl ether was studied. The allyl-terminated 1-1, 1-2 and 1-3 adducts and dihydroxylated derivative of the 1-1 adduct, 5-diglyceryoxy isophthalic acid, were synthesized. The latter binds to the surface of 5 nm  $\gamma$ -Fe<sub>2</sub>O<sub>3</sub> nanoparticles in reaction with their surfactant-free diethylene glycol colloids. Further improvement of the binding strength is attempted by introducing the phenolic OH-group between the carboxyls in isophthalate moiety.

**Keywords:** capping ligand, epoxide ring-opening addition, solvent-free synthesis, metal oxide nanoparticles

### 1. Introduction

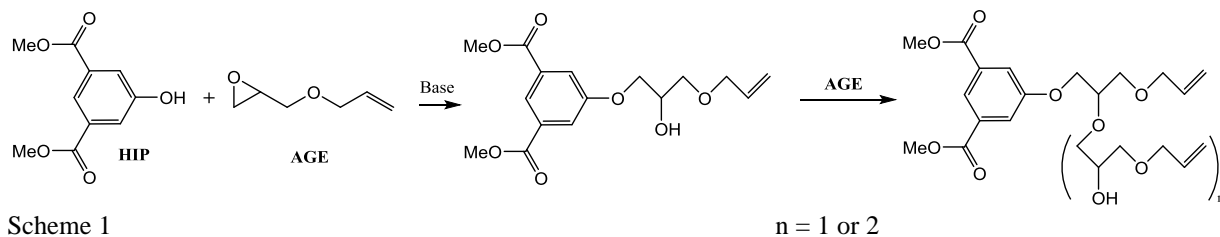
Development and study of magnetic nanoparticles for biological and clinical applications remains a field of intensive investigation for the last two decades.<sup>1-13</sup> It involves a multidisciplinary endeavor and is one of the most challenging research areas in chemistry and materials science. Application of magnetic nanoparticles has been already explored in a wide variety of non-invasive medical treatment and diagnostic procedures, such as cancer therapy for inoperable tumors, gene therapy, blood detoxication, radiation treatment, magnetic resonance imaging (MRI).<sup>3-11</sup> The performance of these particles as, for example, drug delivery, MRI, hyperthermia or cell tracking agents, depends on their magnetic susceptibility, however, their ability to form stable aqueous colloids, the mobility, and diffusion properties in biological media, largely rely on organic coating. Functional nanoparticles used in clinical research these days are usually coated with hydrophilic biocompatible polymers such as dextrans or poly(ethylene glycol)s. Excessively large macromolecules of these polymers make the nanocomposite unwieldy, and thus limit its mobility and penetration properties. Due to large diamagnetic component, polymers suppress the desired response to an external magnetic field. In addition, they restrict water exchange between superparamagnetic core and biological fluids, which is highly desired for the MRI contrast agent applications.

To address some downfalls associated with polymers, in this work we attempted to develop a non-polymeric organic coating of an adjustable size. The future capping ligand would contain two distinct structural parts: the coordinating head and a bulky substituent with reactive functional group on its end. Coordinating head should be able to act as a polydentate bridging ligand due to several donor atoms in it, which are adequately spaced from one another. Benzenecarboxylic acids offer multiple degrees of freedom, and isophthalic acid was our choice because of its geometry which seemed to be most appealing for the purpose. Selection of the substituent was more challenging as it should have a variable length and solvent affinity properties, and it should be

functionalizable at its end. The easiest way to address the size is performing an oligomerization reaction under controlled conditions, and we selected an oxirane ring-opening addition reaction which offers not only an easy control of the condensation, but also amphiphilic properties to the product. Readily available 5-hydroxyisophthalic acid and allyl glycidyl ether were used as an initiator and a monomer respectively, leading to the targeted capping ligand. The chain length was adjusted by changing the stoichiometric ratio of the nucleophile to oxirane monomer. Its oxygen-rich substituent would provide hydrophilic properties, while allyloxy pendant would offer some freedom for boosting the hydrophobic properties or for conjugating the capping ligand to a biomolecule.

## 2. Results and Discussion

**Synthesis of substituted isophthalates.** A reaction between dimethyl 5-hydroxyisophthalate (HIP) and AGE was studied in solvent-free systems, at different temperatures and at a presence of a base catalyst. It was found that the reaction of HIP with 1.0-1.1 molar equivalents of AGE and 0.01 eq. of base catalyst can be driven to completion at 103-105°C in about 24 hours, and it produces a corresponding ether-ester product HIP-AGE 1-1 E (1) in > 90% isolated yield (Scheme 1). The identity of this compound was confirmed by <sup>1</sup>H, <sup>13</sup>C and 2D NMR and ESI-MS.



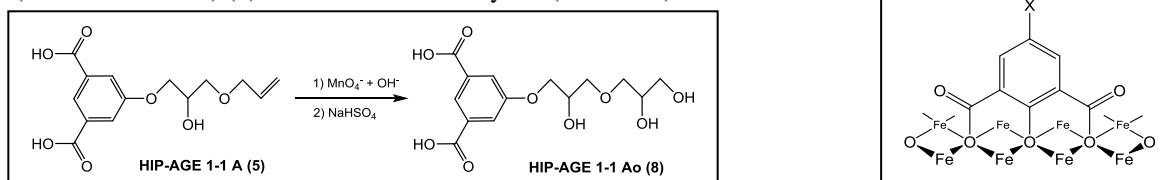
Scheme 1

In order to synthesize 1-2 E and 1-3 E homologs, we studied a reaction of crude (still base-activated) 1-1 ester (1), with an additional equivalent of AGE under the same conditions as in Scheme 1. After the workup, the reaction product was analyzed by GC-MS, and the ratio of (1), (2) and HIP-AGE 1-3 E (3) adducts was found to be 1 : 2.3 : 1.2, respectively. The mixtures were separated by a preparative chromatography and the identity of the compounds was confirmed by <sup>1</sup>H, <sup>13</sup>C and 2D NMR and ESI-MS.

Based on proton and C-13 NMR spectra, this reaction is highly regioselective, and HIP attacks the AGE oxirane ring at the less substituted side, which is typical for a base-promoted ring opening. Proton NMR spectra show a splitting pattern which is typical for diastereotopic protons. For adducts with more than one molecule of AGE, carbon spectra reveal duplicated peaks, which is typical for diastereomeric product formation.

The ester product (1) was hydrolyzed by heating in ethanol solution with NaOH producing disodium salt of HIP-AGE 1-1 A acid (4), which was subsequently converted into a corresponding acid (5) by acidification of its aqueous solution, followed by water evaporation and extraction with MTBE. The acid was achieved in 70-75 % isolated yield and recrystallized from water, producing white needles (hydrate), m.p. 162-165 °C. The HIP-AGE 1-2 A (6) and HIP-AGE 1-3 A (7) were obtained from the corresponding esters in a similar way. The identity of these compounds was confirmed by <sup>1</sup>H, <sup>13</sup>C and 2D NMR and ESI-MS.

Oxidation of the terminal double bond into a corresponding 1,2-diol was done with cold basic permanganate taken in stoichiometric amount (alkene to KMnO<sub>4</sub> = 3:2), afforded 5-diglyceroxy isophthalic acid (HIP-AGE 1-1 Ao) (8) with 55.7 % isolated yield (Scheme 2).



### Scheme 2

As it was evidenced by NMR and ESI mass-spectra, oxidation of the allyl double bond appeared to be highly selective, as the vicinal diol forms under the reaction conditions as a primary product.

### Scheme 3

**Organic-inorganic nanoparticulate adducts.** The ability of the synthesized isophthalate-based capping ligands to bind to metal oxide nanoparticles was tested by reacting 5-diglyceroxy isophthalic acid (8) with 5 nm  $\gamma$ -Fe<sub>2</sub>O<sub>3</sub> nanoparticles colloid in surfactant-free diethylene glycol solution, prepared as we reported earlier.<sup>14</sup> The reaction stoichiometry was calculated based on an assumption that each molecule of ligand will bind to two metal atoms on the nanoparticle's surface. The added amount of capping ligand was based on the known nanoparticles' concentration and their size. In order to calculate the number of metal atoms on each nanoparticle surface, the following formula was used:  $F = 4/n^{1/3}$  where  $F$  = fraction of atoms,  $n$  = total number of atoms per particle. The total number of atoms per particle was, in turn, calculated from the particle diameter, its volume, its mass (density = 4.87 g/cm<sup>3</sup>), number of mols and formula units per particle.<sup>15</sup>

The room-temperature reaction between capping ligand and  $\gamma$ -Fe<sub>2</sub>O<sub>3</sub> in diethylene glycol which was monitored by the Dynamic Light Scattering (DLS), showed no change in hydrodynamic particle size (7.5 nm), which evidenced colloid stability. For further characterization, the reaction product was isolated in a pure form by coagulating its colloid with ethyl acetate, separating the precipitate using permanent magnet, washing with isopropanol and drying in vacuum. The IR spectrum of the powdery sample showed features of the coordinated capping ligand. The obtained organic/inorganic adduct tested negative for water solubility or otherwise reactivity at room temperature. This is a typical behavior for the nanoscale powders after they were freed from the surfactant and solvent. In order to further confirm the identity of this product, we performed its high-temperature hydrolysis, followed by separation of the organic and inorganic component on an NMR sample scale. A sample of the adduct was heated with 1 mL of D<sub>2</sub>O at 100°C for ~30 min, and then precipitated iron oxide was separated by magnet. The remaining colorless solution was filtered through a 100 nm microfilter. <sup>1</sup>H NMR spectrum of this solution showed presence of the free ligand, which evidenced the hydrolysis and de-ligation reaction of the  $\gamma$ -Fe<sub>2</sub>O<sub>3</sub>-ligand adduct.

**Synthesis of substituted 2-hydroxyisophthalates.** It is our hypothesis that introducing a phenolic OH-group between the carboxyls of isophthalate moiety can improve binding ability of the capping ligand to the surface of metal oxide nanoparticles (Scheme 3). Several strategies for the synthesis of such a ligand are currently in progress and will be reported after the next term. Colloid and surface chemistry studies are underway.

### **3. Conclusions**

In a search for novel non-polymeric capping ligands for metal oxide nanoparticles, three 5-substituted derivatives of isophthalic acid with ethylene oxide chain substituents were synthesized by reacting dimethyl 5-hydroxyisophthalate (HIP) with allyl glycidyl ether (AGE) in the presence of a base catalyst. The main step, an anionic epoxide ring-opening reaction, was performed using a solvent-free reaction technique, and products with 1, 2 and 3 molecules of AGE attached to HIP via its formerly phenolic oxygen, were isolated and characterized.

An allyl group of the 1-1 adduct was converted into a 1,2-diol by aqueous oxidation, and resulting product (5-diglyceroxy isophthalic acid) was tested as a capping ligand and found to bind to the surface of 5 nm  $\gamma$ -Fe<sub>2</sub>O<sub>3</sub> nanoparticles. The ligand-capped nanoparticles form stable colloid in diethylene glycol. The organic/inorganic adduct isolated in a pure powdery form, appears to be stable to hydrolysis at ambient temperatures, but undergoes de-ligation in boiling water. Aiming the development of novel capping ligands with further improved binding capacity, new synthesis, surface and colloidal chemistry studies based on 2-hydroxyisophthalate derivatives, have been initiated.

#### 4. Acknowledgments

Research reported in this publication was supported by the National Institutes of Health grants SC3GM088042 and 8G12MD007595-05, and by the Louisiana Cancer Research Consortium. This research was also supported by the National Science Foundation LA-SIGMA EPS-1003897 and PREM DMR-0934111 grants.

#### 5. References

- [1] Reddy, L. H.; Arias, Jose L.; Nicolas, J.; Couvreur, P. *Chem. Rev.* **2012**, *112*(11), 5818.
- [2] Bychkova, A. V.; Sorokina, O. N.; Rosenfeld, M. A.; Kovarski, A. L. *Russian Chemical Reviews* **2012**, *81*(11), 1026.
- [3] Knezevic, N. Z.; Ruiz-Hernandez, E.; Hennink, W. E.; Vallet-Regi, M. *RSC Advances* **2013**, *3*(25), 9584.
- [4] A.E. Merbach and E. Toth (Eds), *The Chemistry of Contrast Agents in Medical Magnetic Resonance Imaging*. Chichester, *Wiley & Sons LTD*, 2001.
- [5] Challa Kumar (Ed), *Biofunctionalization of Nanomaterials*, Wiley-VCH Verlag GmbH & Co KGaA, Weinheim, 2005.
- [6] V. Nikiforov and E. Filinova. "Biomedical Applications of Magnetic Nanoparticles", in: *Magnetic Nanoparticles*, p. 393-444. Edited by S. Gubin, 2009, Wiley-VCH Verlag GmbH & Co KGaA, Weinheim.
- [7] J. Kreuter, in: J. Kreuter (Ed), *Colloidal Drug Delivery Systems*, Marcel Dekker, New York, 1994.
- [8] Portet, D.; Denizot, B.; Rump, E.; Lejeune, J.; Jallet, P. Nonpolymeric Coatings of Iron Oxide Colloids for Biological Use as Magnetic Resonance Imaging Contrast Agents. *Journal of Colloid and Interface Science* (2001), *238*(1), 37-42.
- [9] A.S. Lubbe, C. Bergemann, *Clinical Applications of Magnetic Carriers*, U. Hafeli, W. Schutt, J. Teller, M. Zborowski (Eds), Plenum: New York, 1996, pp. 457-480.
- [10] W. Andra, H. Novak (Eds). *Magnetism in Medicine. A Handbook*, Wiley-VCH Verlag, Berlin, 1998.
- [11] Xu, Chenjie; Sun, Shouheng, Monodisperse magnetic nanoparticles for biomedical applications, *Polymer International* (2007), *56* (7), 821-826.
- [12] Yan, Kai; Li, Penghui; Zhu, Haie; Zhou, Yingjie; Ding, Jingde; Shen, Jie; Li, Zheng; Xu, Zushun; Chu, Paul K. *RSC Advances* **2013**, *3*(27), 10598.
- [13] Rosi, N. L.; Mirkin C. A. *Chem. Rev.* (2005), *105*, 1547-1582.
- [14] Kucheryavy, P.; He, J.; John, V.T.; Maharjan, P.; Spinu, L.; Goloverda, G.Z.; Kolesnichenko, V.L. *Langmuir*, **2013**, *29*, 710
- [15] Goloverda, G.Z.; Jackson, B.; Kidd, C.; Kolesnichenko, V.L. *J. Magn. Magn. Mater.* **2009**, *321*, 1372.

## **The role of defects in the metal-nonmetal transition in SrVO<sub>3</sub> thin films**

**Gaomin Wang and Jiandi Zhang,**

Department of Physics and Astronomy, Louisiana State University

**Abstract:** Metal-insulator transition (MIT), or more generally, metal-nonmetal transition has always been an intriguing topic in condensed matter physics. Being one of the major driving mechanisms of metal-nonmetal transition, the role of defects or disorder induced mainly by the oxygen vacancies is what we are studying in the ultrathin films of metallic oxide SrVO<sub>3</sub>. So far, we have experimentally achieved successful growth of the SrVO<sub>3</sub> thin film in layer-by-layer fashion on the SrTiO<sub>3</sub> (001) substrate, as a necessary preliminary step. It is found that the surface of the films has C(2x2) structure based on our images of low energy electron diffraction. Further investigation of the system, including both experimental and theoretical effort, remains to be done in the near future.

**Keywords:** Metal-insulator transition, disorder, oxygen vacancy, surface characterization

### **1. Introduction**

Metal-insulator transitions (MIT) have been one of the most fundamental phenomena in condensed matter physics [1]. From solid state physics, we know that resistivity only comes from the scattering of electrons from defects in the crystal. The existence of the defects, or disorder, introduces an additional random potential to the periodic potential and causes the Bloch waves to lose coherency on a scale of the electron mean free path. Anderson localization theory states that when the amount of impurities becomes so large that the random potential can no longer be treated as perturbative, the electrons may become completely localized, driving the system into insulating phase, which experimentally corresponds to infinite resistivity as the temperature approaches zero. When the disorder is not strong enough, the electronic states will be a mixture of extended states and localized states, resulting in a nonmetal phase instead of completely insulating and a stop of the resistivity curve at finite value as the temperature reaches zero.

Apart from the effect of disorder, there are also several other driving forces of MIT. Dimensionality effect is one of these important mechanisms. As the system goes from bulk to thin film, a potential well is gradually formed along the changed dimension, and therefore causes the localization of electrons when the thickness is reduced to a critical value. When the dimension of the system is far from the critical thickness, the effect of disorder is usually overshadowed; as the system approaches the critical thickness, disorder effect becomes strong enough to alone drive the system into MIT.

We aim to work with perovskite transition metal oxide (TMO) systems. The narrow 3d band in TMOs often leads to electron correlations which give rise to a variety of interesting phenomena, such as MIT, high temperature superconductivity [2], and colossal magnetoresistance [3]. The simple structure of the perovskites--usually cubic--makes it an ideal candidate for study and applications. Disorder can be introduced into this system by either

chemical doping of A-site atoms, or the relatively control of the oxygen vacancies. The former one causes lattice distortion and sometimes changes the valence of the transition metal and induces charge disordering. The latter can be achieved experimentally by fabricating thin film in a layer-by-layer fashion under different oxygen partial pressure and subsequent annealing.

We choose SrVO<sub>3</sub> as the system for this study due to its simple structure and the absence of magnetic ordering or doping-induced disorder in the bulk form, which makes it feasible for theoretical understanding without the involvement from spin degree of freedom. The main cause of the disorder effect is oxygen vacancy existing in the system. Bulk SrVO<sub>3</sub> crystal is a paramagnetic metal across all temperature range. Angle-resolved photoelectron spectroscopy (ARPES) study reported that MIT occurs at a critical thickness of 2-3 ML (defined as one unit cell thickness) for SrVO<sub>3</sub> thin films grown on Nb-doped SrTiO<sub>3</sub> (001) substrate, while as above the critical thickness, quantum well state are formed showing typical metallic character under spatial confinement due to the finite film thickness [4, 5]. The spectral weight on the energy density curves near the Fermi edge decreases as the film thick is reduced and approaches the critical thickness. A pseudogap comes into shape and eventually evolves into a band gap if the system goes to insulator. A direct visualization of the shape of the band structure can be obtained from the dispersion image [4]. However, what drives the film into nonmetallic behavior is still unclear. One probable origin is the oxygen vacancies which cause the disorder effect as we mentioned above.

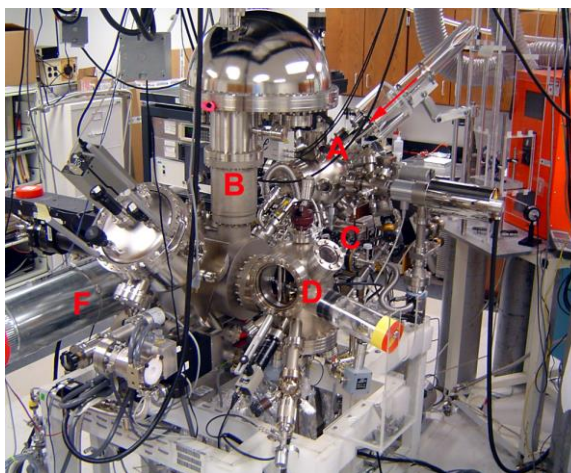


**Fig. 1** An view of the PI's integrated UHV material fabrication and characterization system: (A) *In-situ* LMBE; (B) Small-spot monochromated ARXPS/ARPES; (C) Crystal cleaving setup; (D) STM/AFM; (E) Mini-thermal MBE; and (F) LEED setup.

With our integrated material growth and *in-situ* characterization facility, we are able to grow crystalline SrVO<sub>3</sub> thin films on SrTiO<sub>3</sub> (001) and study *in-situ* on the lattice structure, chemical composition, and electronic properties. Figure 1 shows our experimental setup for the study, including laser-MBE for film growth, low energy electron diffraction for surface structure, scanning tunneling microscopy (STM) for local structural and electronic property, X-ray photoelectron spectroscopy (XPS) for chemical composition, and ARPES for valence electron band structure. The experimental results will be used for theoretical modeling on the issues of Anderson-type localization in reduced dimensionality.

## 2. Growth and characterization of ultrathin SrVO<sub>3</sub>

With a Sr<sub>2</sub>V<sub>2</sub>O<sub>7</sub> target, we have successfully achieved layer-by-layer growth of SrVO<sub>3</sub> thin film on Nb-doped SrTiO<sub>3</sub> (100) substrate, which is a semi-conducting perovskite with cubic structure and a lattice constant of 0.3905 nm. By HF-etching and subsequent annealing in oxygen at 900 °C, we are able to obtain a good flat TiO<sub>2</sub>-terminated surface on the substrate with clear step edges. We have found the optimized growth condition for the

SrVO<sub>3</sub> films as follows: substrate temperature of 450 °C, pressure of 1x10<sup>-7</sup> Torr, laser pulse rate of 1Hz and laser energy of 2.5 J/cm<sup>2</sup>. Figure 2a shows an image of the Reflection High Energy Electron Diffraction (RHEED) pattern during the growth,

indicating the ordered structure of the film. The layer-by-layer growth is evident from the intensity oscillation (see Fig. 2b) of a RHEED diffraction spot vs. deposition time. Figure 2b presents the intensity of the spot during the growth of a 30 monolayer (ML) SrVO<sub>3</sub> sample grown under the conditions stated above.

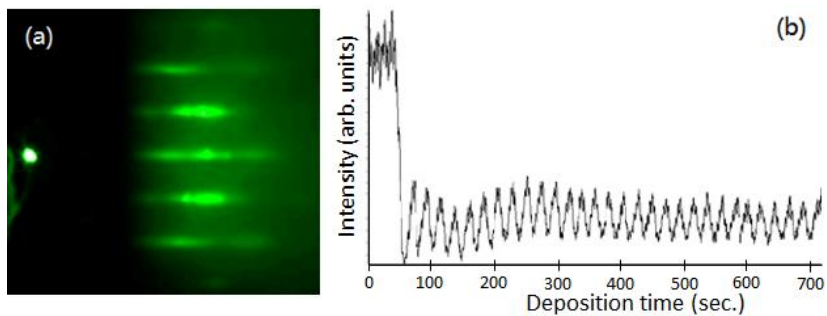


**Fig 2** (a) RHEED diffraction pattern of 30 ML SrVO<sub>3</sub> film and (b) Intensity oscillations of a RHEED diffraction spot during the growth of the SrVO<sub>3</sub> film.

A study of SrVO<sub>3</sub> film by Low energy electron diffraction (LEED) is shown in Fig. 3. It is observed that the film always displays a c(2x2) pattern despite of the growth condition we use. Post-annealing to a certain temperature enhance the quality of the pattern, indicating the enhancement of the film crystallinity. We further investigated the surface morphology of a 30 ML SrVO<sub>3</sub> film by Scanning Tunneling Microscopy (STM), shown in Figure 4.

The morphology images indicate the good quality of the film with the step height between different terraces matches single unit cell height. Some interesting features were observed from the film after post-annealing, which seem like atomic

rows with the size of each “atom” about twice the lattice constant along each side. The origin of these atomic rows still remains to be investigated. Some hypothesis includes strontium segregation on the surface similar to La<sub>2/3</sub>Sr<sub>1/3</sub>MnO<sub>3</sub> [6], and surface reconstruction [7]. But here the situation can be different since here there is no A-site substitution in contrast to La<sub>0.7</sub>Sr<sub>0.3</sub>MnO<sub>3</sub>.

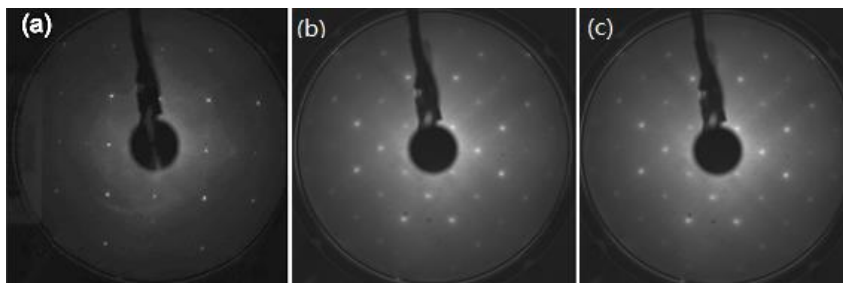


**Fig. 3** LEED images of (a) SrTiO<sub>3</sub> (001) substrate, (b) 10 ML SrVO<sub>3</sub> thin film grown at 490 °C without post-annealing and (c) the same film post-annealed at 730 °C under a vacuum condition of 10<sup>-10</sup> Torr.

### 3. Conclusion

We have successfully grown and characterized SrVO<sub>3</sub> thin film on Nb-doped SrTiO<sub>3</sub> (001) substrate. We found that the film is grown in layer-by-layer fashion with the crystal structure as that of the substrate. While the surface of the films exhibit a c(2×2) reconstruction. We hope to gain more insight of the mechanism behind the metal-nonmetal transition observed in this system through further investigation.

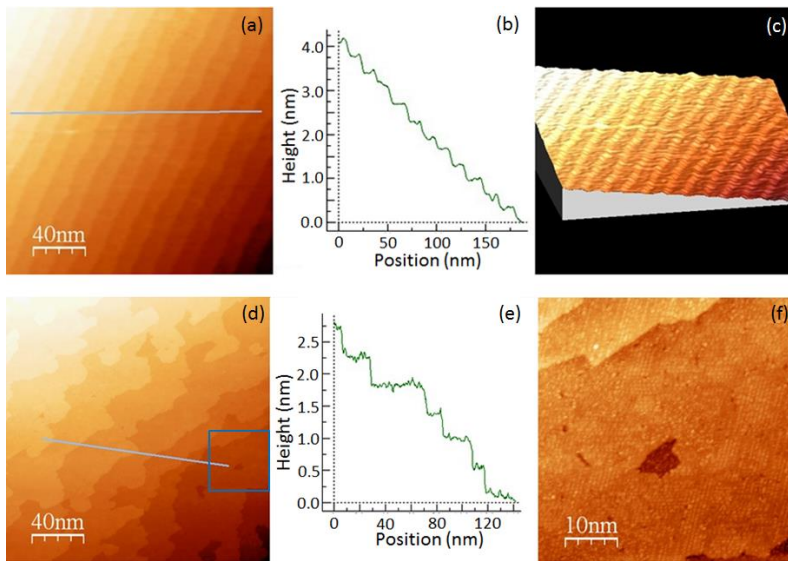


**Fig. 4** (a-c) STM morphology, line profile and 3D image of a 30 ML as-grown SrVO<sub>3</sub> film on Nb-doped SrTiO<sub>3</sub> (001) imaged at room temperature; (d-e) STM morphology and line profile of the same film after post-annealing at 650 °C in vacuum for an hour; (f) The zoom-in image of the area boxed in (d).

### 4. Acknowledgments

The current work is funded by the NSF EPSCoR LA-SiGMA project under award #EPS-1003897.

### 5. References

- [1] M. Imada, A. Fujimori, Y. Tokura, *Rev. Mod. Phys.*, 70 (1998) 1039-1263.
- [2] J. Orenstein and A. J. Millis, *Science* 288, 468 (2000).
- [3] *Colossal Magnetoresistive Oxides*, edited by Y. Tokura (Gordon and Breach, London, 2000).
- [4] K. Yoshimatsu, T. Okabe, H. Kumigashira, S. Okamoto, S. Aizaki, A. Fujimori, and M. Oshima, *Phys. Rev. Letts*, 104 (2010) 147601.
- [5] K. Yoshimatsu et al. *Science* 333, 319 (2011)
- [6] R. Bertacco, J. P. Contour, A. Barthélemy, and J. Olivier, *Surf. Sci.*, 511 (2002) 366.
- [7] K. Fuchigami, Z. Gai, T. Z. Ward, L. F. Yin, P. C. Snijders, E. W. Plummer, and J. Shen, *Phys. Rev. Letts*, 102 (2009) 066104.

## Toward Online Comparative Genomics of Mononucleosomes

Venkat Perreddy<sup>1</sup>, Parthasarathi Mahadasyam<sup>1</sup>, Mohammad Sufian Badar<sup>2</sup> and Thomas C. Bishop<sup>3</sup>

<sup>1</sup>Dept. Of Computer Science, Louisiana Tech University

<sup>2</sup>Dept. Of Biomedical Engineering, Louisiana Tech University

<sup>3</sup>Depts. Of Chemistry & Physics, Louisiana Tech University

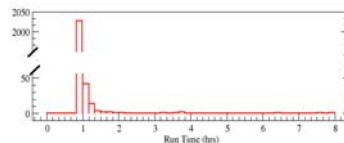
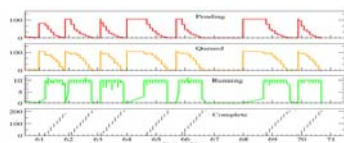
**Abstract:** The largest supercomputers contain 1,000,000+ processors and advanced co-processors which enable molecular dynamic simulation of large ensembles of biomolecular systems. Here, we report on a workflow for High Throughput Computing(HTC) – High Performance Computing(HPC), simulations and tools for sharing data with colleagues and world. The workflow will compare a set of 2100 simulations run on Lonestar (Texas Advanced Computing Center) using BigJob [1] with a set of 900 simulations run on Kraken (Oak Ridge National Lab) using standard queuing options. The simulations are of nucleosomes. So called “sin” mutants lead to nucleosomal destabilisation, altered nucleosome structure-function and inactivation of SWI/SNF complex [4]. Here we investigate six sin mutations which occur near the nucleosome dyad. It is also important to share the research data with collaborators. For this purpose, we used iBIOMES [2], a freely available tool which automatically parse and publish the molecular dynamics and quantum mechanics data in a user friendly web format. The Lite version of iBIOMES allows researchers to quickly track and share their MD or QM computations without any special tools or programs. The integrated Rule Oriented Data System, iRODS [3] version provides additional features and capabilities, including simulation queries based on metadata and seamless integration of local and remote data servers. Here we demonstrate the features of iBIOMES Lite [5] and full iBIOMES with iRODS implementation.

**Keywords:** HPC, HTC, Nucleosomes, iBIOMES, iRODS

### 1. WorkFlow

#### Running on Lonestar using BigJobs:

The total workload on Lonestar consists of 2100 individual MD simulation tasks of 1ns duration. There are 15 chromosomes, each chromosome consists of 21 replicas and each replica is simulated for 20 ns using 1 ns simulation tasks. Each task requires 240 cpu and 1 hr of run time. BigJob requests 2400 core for a 24 hour period and automatically manages 10 simultaneous 240 core simulation tasks.

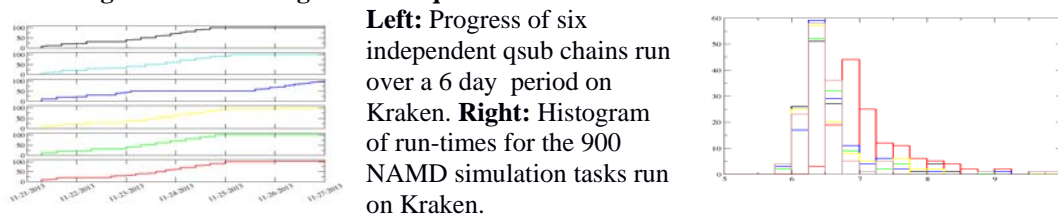


**Left:** Progress of seven BigJob runs over a 10 day period on Lonestar. **Right:** Histogram of run-times for the 2100 NAMD simulation tasks run on Lonestar.

The above plots characterize the throughput of 2100 tasks over a 10 day period managed by BigJob [1]. Any failed tasks are automatically added to the next BigJob, thus BigJob requires little user intervention for proper execution. System errors due to hardware malfunctions or time-outs rather than simulation errors were the cause of failed jobs. All task restarts completed successfully.

The above histogram of run-times for all 2100 NAMD simulations indicates the shortest run-time was 54 minutes with a mean run time of 57 minutes and 2027 tasks (97%) completing in under 1 hour. The shortest run-time was 54 minutes. System size ranged from 158,015 to 158,191 atoms.

**Running on Kraken using standard qsub:**



The above plots characterize the throughput of 900 tasks over a 6 day period using simple qsub chains. Each qsub chain relies on dependency rules to execute the simulations tasks in proper order. Each chain runs 10 independent replicas simultaneously. Using qsub requires active user management. We initiated all six job chains simultaneously, leaving the queuing system to manage the overall throughput. The above histogram of run-times for all 900 NAMD simulations indicates a range of run times from 5.9 to 10.3 hours with an overall mean of 6.7 hours. About 80% of the 900 jobs completed with a wall clock time of under 7 hours. The systems varied in size from 387,061 to 387,089 atoms. Run time differences mostly are attributed to FFT configuration of the PME calculations.

**Results:**

We have demonstrated that BigJob and standard qsub features can be employed to efficiently manage high throughput-high performance MD simulations. BigJob provides simulation and data management capabilities, i.e. true pilot-job implementation, that cannot be achieved with qsub scripting. BigJob provides a set-it and forget-it simulation management solution that enables the domain scientist to focus on results rather than computing.

**2. Biology**

**Nucleosome Structure and Tail Modifications**

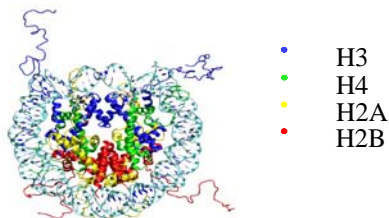


**Fig. 1. Nucleosome with different histones**

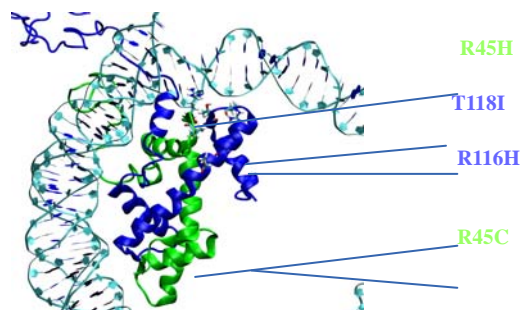


**Fig. 2. Nucleosome with sin mutants**

A canonical nucleosome contains two copies of four different histones: H3, H4, H2A, and H2B. Each histone has unstructured tail domains that extend out from the nucleosome core [6]. Chemical modification of the the histone tails at specific locations provides a reversible mechanism for regulating various genomic mechanisms [7]. Different patterns of chemical modification are associated with different mechanisms.

### Simulation Study

For this simulation study we chose to study six mutants, which alter in nucleosome mobility and positioning. Each mutant was subjected to 170 ns of all atom molecular dynamics simulation with explicit solvent. Each trajectory required over 200,000 hours of compute time and generated nearly 1TB of data.

**Table**

Mutant	Disk (G)	Time (ns)	CPU (su)
Wild type	863	170	213,428
E105K	866	170	233,732
R116H	864	170	211,716
T118I	876	170	213,537
R45H	892	170	212,412
V43I	768	170	210,870
	~5 TB	1020	3.5 Msu

### Simulation time details of different sin mutants.

Results:

Conformational sampling of the six different sin mutant simulations as observed during 170ns of molecular dynamics simulation. Each snapshot contains 34 superimposed conformational snapshots taken at a 0.5ns interval from each simulation. As indicated the histone tails sweep out different regions of space during the 170ns trajectories (figure not shown). Differences may be due to limited sampling, longer simulations are required to establish equilibrium of the tails. However, DNA helical parameter analysis indicates that 170ns is sufficient for the DNA structure (data not shown) to converge at some locations in the nucleosome while other locations show significant variation. These locations do not coincide with sites where the histone core has been mutated, but rather to locations where the DNA interactions with the unstructured tails.

### 3. Data Sharing

There is an increasing pressure on scientists to manage big data, this includes curating, archiving and sharing data with experts and non-experts alike. This requires tools that allow easy access to data by. iRODS stores and organizes large amount of distributed data on heterogeneous systems and data is registered or accessed through Micro-Services. We are developing such iRODS based micro-services to manage our simulation and analysis tasks. iCommands are used as the interface for user to communicate with the server.

### iBIOMES

iBIOMES allows us to both organize and share the 4TB of dewatered simulation and analysis data that we have accumulated. iBIOMES automatically categorizes results and extracts relevant information so that non-experts in molecular modeling can quickly navigate our data. iBIOMES is extensible allowing us to add plots, movies, and

other analysis in a consistent presentation format as they are generated. The rules in iRODS also allow us to monitor data integrity and implement archive policies.

**Summary of All Nucleosome Simulated to Date :** Our simulations are grouped into four studies. Each study utilized a different number of replicas and total simulation time. All of these studies are now available via <http://lasigma.latech.edu/~ibiomes>.

**Table 2.**

Study	Replicas	CPUs	Simulated time (ns)
ACGT	16	64	256
NFR	105	240	2100
YEAST	336	240	6720
SIN-MUTANTS	6	240	1020

**Study of different trajectories published in iBIOMES-Lite**

**4. Acknowledgments**

This work supported by Louisiana Alliance for Simulation Guides Materials Applications (LASIGMA) NSF award number #EPS-1003897. Chromatin model development supported by Louisiana Biomedical Research Network (LBRN) NIH award number #P20GM103424. We acknowledge with gratitude to Julien C. Thibault, NLP Research Engineer at Nuance Communications and an important member in developing iBIOMES as a Research Assistant in University of Utah under the guidance of Professor Thomas E. Cheatham. We acknowledge the works of Shantanu Jha, Assistant Professor, Rutgers University, Piscataway, NJ, USA. We sincerely thank our offshore team Viji Mahadevan, Suma Mohan, Bioinformatics Division, SASTRA University, India.

**5. References**

- [1]. Jack Smith, Melissa Romanus, James Solow, Pradeep Kumar Mantha, Yaakoub El Khamra, Thomas C. Bishop and Shantanu Jha. Scalable Online Comparative Genomics of Mononucleosomes: A BigJob, : 23:1-23:8,(2013).
- [2]. Julien C. Thibault ; Julio C. Facelli and Thomas E. Cheatham; iBIOMES: Managing and Sharing Biomolecular Simulation Data in a Distributed Environment., J. Chem. Inf. Model, 53 (3), pp 726–736, (2013).
- [3]. Reagan Moore and Arcot Rajasekar: IRODS: Integrated Rule-Oriented Data System. White Paper: IRODS: Integrated Rule-Oriented Data System (2008).
- [4]. Michael Bruno, Andrew Flaus, Chris Stockdale, Chantal Rencurel, Helder Ferreira, Tom Owen-Hughes, Histone H2A/H2B Dimer Exchange by ATP-Dependent Chromatin Remodeling Activities, Molecular Cell, Vol. 12, 1599–1606, December, (2003).
- [5]. Julien C. Thibault ;Thomas E. Cheatham and Julio C. Facelli; iBIOMES Lite: Summarizing Biomolecular Simulation Data in Limited Settings; J. Chem. Inf. Model, 54 (6), pp 1810–1819, (2014).
- [6]. A. P. Wolffe & J. J. Hayes - Chromatin disruption and modification. - Nucleic Acid Research, 27, 711-720 (1999).
- [7]. IBMS Bonekey (2010)7, 314â€³24 doi:10.1138/20100464 Published online September (2010).

## Typical Medium Dynamical Cluster Approximation study of disordered superconductors

E. Siddiqui<sup>1,2</sup>, C. E. Ekuma<sup>1,2</sup>, H. Terletska<sup>1,2</sup>, N. S. Vidyadhiraja<sup>1,3</sup>, J. Moreno<sup>1,2</sup>, M. Jarrell<sup>1,2</sup>

<sup>1</sup>Department of Physics & Astronomy, Louisiana State University

<sup>2</sup>Center for Computation & Technology, Louisiana State University

<sup>3</sup>Theoretical Sciences Unit, Jawaharlal Nehru Centre for Advanced Scientific Research

**Abstract:** We propose to study a disordered superconductor using the typical medium dynamic cluster approximation. The results obtained from previous studies using the coherent potential approximation do not include non-local effects and are unable to capture the Anderson localization. Therefore, we employ the typical medium dynamical cluster approximation to see these effects and hence the nature of the states in the superconductor - insulator transition.

### 1. Introduction

In the 1950s P.W Anderson asked the following question: “What happens if an electron is placed in a random potential?” Decades of research have demonstrated that one obtains localized wave functions if the disorder is strong enough or the system is  $< 3$ -dimensions. This localization is as a result of the destructive interference of randomly scattered waves. This phenomenon is known as Anderson Localization [1]. In order to understand this phenomenon, physicists have developed new techniques. One of the most common mean field approaches to study disordered system is the coherent potential approximation (CPA) [2,3]. In the CPA, a single impurity is embedded in an effective medium and the average density of states is calculated self-consistently. However, at the Anderson localization transition, the average density of states is not critical. Therefore, we are unable to capture the metal-insulator transition within the coherent potential approximation and its cluster extensions including the dynamical cluster approximations [4]. In order to incorporate the backscattering effects, a cluster extension of the CPA known as the dynamical cluster approximation (DCA) was developed by Jarrell and co-workers [4,5]. However, the DCA is also unable to capture the Anderson localization transition. In effort to develop an effective mean field for the Anderson localization, Dobrosavljević and co-workers [6-8] developed the typical medium theory (TMT) using the geometrical averaging. They demonstrated that indeed, the typical density of states is critical at the Anderson transition. However, the TMT is unable to give quantitative predictions in three dimensions (3D). The critical disorder strength calculated within the TMT is 1.65 instead of 2.1 [10,11]. Also the critical exponent of the order parameter is 1.0 instead of the recently reported value of 1.67 [12,13]. The typical medium theory also fails to describe the re-entrant behavior of the mobility edge [14,15]. All these can be attributed to its local approximation, since it neglects the coherent backscattering effects [16].

Recently, our group extended the local typical medium theory to a cluster typical medium theory for one and two dimensions [17]. In the cluster typical medium theory, the cluster density of states is replaced by  $\exp(\langle \ln(\rho^c(K, \omega)) \rangle)$ . In 3D there is a mixing of localized and extended states below the critical disorder  $W_c$ . Therefore the energy scales are different. Hence, self-averaging destroys the localization transitions as the cluster size is increased. In order to overcome this problem, our group further proposed and developed the typical medium dynamical cluster approximation (TMDCA) to study Anderson localization in 3D [18]. In simple terms,

the local part of the typical density of states is separated and explicitly treated with a geometrical average over disorder configurations. This method is the first self-consistent effective medium theory which captures the Anderson localization transition in 3D [18]. The calculated critical disorder strength  $W_c$  within the TMDCA is  $W_c^{\text{TMDCA}} = 2.10 \pm 0.01$  which is in good agreement with large scale simulations. In addition the TMDCA captures correctly the re-entrant behavior of the mobility edge trajectories as the cluster size is systematically increased. The TMDCA just as in the dynamical cluster approximation is computationally cheap as it requires the diagonalization of only small clusters [18]. Presently we are trying to produce results for the disordered superconductor using the dynamical cluster approximation with the long-term aim of extending it to the typical environment.

## 2. DCA self-consistency loop for superconductivity

We are solving the attractive Hubbard model with disorder. The cluster problem is set up by defining the cluster-excluded Green's function denoted in Nambu-spinor notation. For the first iteration it is set equal to the Bardeen, Cooper, Schrieffer(BCS) Green's function,

$$\begin{aligned} \underline{\mathcal{G}}(K, \omega) &= (\underline{I}\omega - \bar{\epsilon}_K \tau_3 + \phi \tau_+ + \phi^* \tau_-)^{-1} \\ &= \begin{pmatrix} \omega - \bar{\epsilon}_K & 2\phi \\ 2\phi^* & \omega + \bar{\epsilon}_K \end{pmatrix}^{-1} \end{aligned} \quad (1)$$

The coarse-grained bare dispersion is given as

$$\bar{\epsilon}_K = \frac{N_c}{N} \sum_{\tilde{k}} \epsilon(K + \tilde{k}) \quad (2)$$

where  $\underline{I}$  represents the identity matrix and the Pauli matrices are given as,

$$\tau_3 = \begin{pmatrix} 1 & 0 \\ 0 & -1 \end{pmatrix}, \tau_+ = \begin{pmatrix} 0 & 2 \\ 0 & 0 \end{pmatrix}, \tau_- = \begin{pmatrix} 0 & 0 \\ 2 & 0 \end{pmatrix}$$

$\phi$  is the pairing parameter consistent with the BCS order parameter.

Since the cluster problem is solved in real-space we Fourier transform  $\underline{\mathcal{G}}(K, \omega)$  to real space  $\underline{\mathcal{G}}_i$  and introduce diagonal disorder. The initial cluster Green's function is given as  $\underline{\mathcal{G}}_{co} = (\underline{\mathcal{G}}^{-1} - V \tau_3)^{-1}$  for each randomly chosen disorder. Here  $V$  represents randomly distributed disorder according to a probability distribution. Next we calculate the occupancy  $n_i$  and the pairing parameter  $\phi_i$  self consistently. In the equations below  $i$  represents site index.

$$n_i = \int_{-\infty}^{\infty} d\omega \frac{-2}{\pi} \text{Im} G_{co,i}^{11}(\omega) \quad (3.1)$$

$$\phi_i = \int_{-\infty}^{\infty} d\omega \frac{-1}{\pi} \text{Im} G_{co,i}^{12}(\omega) \quad (3.2)$$

After  $n_i$ , and  $\phi_i$  converge we obtain the normal and anomalous parts of the self-energy matrix ( $\Sigma$ ) as  $-\text{Un}_i$  and  $-U\phi_i$  respectively and the final cluster Green's function as  $\underline{G}_c^{-1} = \underline{G}^{-1} - V\tau_3 - \underline{\Sigma}$ . The disorder average is then carried out yielding  $\underline{G}_{c,avg} = \langle (\underline{G}^{-1} - V\tau_3 - \underline{\Sigma})^{-1} \rangle$ .

Next, we do a Fourier transform of  $G_{c,avg}$  to K-space and carry out coarse-graining.

$$\bar{G}(K, \omega) = \frac{N_c}{N} \sum_{\tilde{k}} \frac{1}{(G_{c,avg}^{-1}(K, \omega) + \Gamma_{old}(K, \omega) - \epsilon(K + \tilde{k})\tau_3 + \bar{\epsilon}(K)\tau_3)} \quad (4)$$

For the first iteration,  $\Gamma_{old}$  is taken to be zero.

We obtain the new hybridization matrix as

$$\Gamma_{new}(K, \omega) = \Gamma_{old}(K, \omega) + \xi[(G_c(K, \omega))^{-1} - (\bar{G}(K, \omega))^{-1}] \quad (5)$$

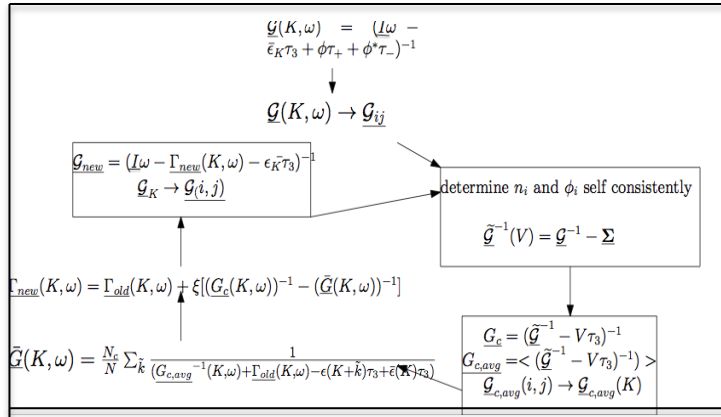
Here,  $\Gamma_{old}$  and  $\Gamma_{new}$  are the old and new hybridization matrices.

At the end of each iteration, we obtain a new cluster-excluded Green's function.

$$\underline{G}_{new}(K, \omega) = (\omega I - \Gamma_{new}(K, \omega) - \bar{\epsilon}_K \tau_3)^{-1} \quad (6)$$

The above procedure is repeated until the hybridization converges or  $\bar{G}(K, \omega) = \underline{G}_c(K, \omega)$ .

Figure 1: Flow chart for DCA self-consistency



### 3. Conclusions

In this project we want to study the disordered superconductor using Typical Medium Dynamical Cluster Approximation. We will first benchmark our results by studying the system using the Dynamical Cluster Approximation. To study the effects of localization we will use Typical Medium Dynamical Cluster Approximation.

### 4. Acknowledgments

The work is funded by the NSF EPSCoR LA-SiGMA project under award #EPS-1003897.

### 5. References

- [1] P.W. Anderson, Phys. Rev. **109**, 1492-1505 (1958).
- [2] P. Soven, Phys. Rev. **156**, 809-813 (1967).
- [3] B. Velický, S. Kirkpatrick, and H. Ehrenreich, Phys. Rev. **175**, 747–766 (1968); S. Kirkpatrick, B. Velický and H. Ehrenreich, Phys. Rev. B **1** 3250–3263 (1970).
- [4] M. H. Hettler *et al.*, Phys. Rev. B **61**, 12739 (2000).
- [5] M. Jarrell and H. R. Krishnamurthy, Phys. Rev. B **63**, 125102 (2001);
- [6] M. Jarrell *et al.*, Phys. Rev. B **64**, 195130 (2001).
- [7] M. Janssen, Phys. Rep. **295**, 1–91 (1998).
- [8] K. Byczuk, W. Hofstetter, and D. Vollhardt, Int. J. Mod. Phys. B **24**, 1727 (2010).
- [9] E. Crow and K. Shimizu, eds., Log-Normal Distribution–Theory and Applications, (Marcel Dekker , NY, 1988).
- [10] V. Dobrosavljević, A. A. Pastor, and B. K. Nikolić, Eur. Phys. Lett. **62**, 76 (2003).
- [11] K. Slevin and T. Ohtsuki, Phys. Rev. Lett. **82**, 382–385, (1999).
- [12] K. Slevin and T. Ohtsuki, Phys. Rev. B **63**, 045108 (2001); *ibid*: arXiv:1307.4483; *ibid*: Phys. Rev. Lett. **78**, 4083 (1997).
- [13] A. Rodriguez *et al.*, Phys. Rev. B **84**, 134209 (2011).
- [14] A. Rodriguez *et al.*, Phys. Rev. Lett. **105**, 046403 (2010); *ibid*: Phys. Rev. Lett. **102**, 106406 (2009); *ibid*: Phys. Rev. B. **78**, 195107 (2008).
- [15] B. Bulka, B. Kramer, and A. MacKinnon, Z. Phys. B **60**, 13–17 (1985); *ibid*: Z. Phys. B **66**, 21–30 (1987); B. Kramer and A. MacKinnon, Rep. Prog. Phys. **56**, 1469 (1993).
- [16] G. Schubert, A. Weibe, G. Wellin, and H. Fehske, HPC in Sci. & Eng., Garching 2004, (Springer, 2005).
- [17] C. E. Ekuma *et al* *J. Phys.: Condens. Matter* **26** 274209 (2014)
- [18] C. E. Ekuma, *et al.* Phys. Rev. B **89**, 081107(R) (2014) .

## Ultraviolet Radiation effects on the electrical resistivity of some La(Ca/Sr)MnO materials

William Raziano\*, Jermain Franklin#, Larry Henry, PhD&

\*REU student SUBR, BRCC, Baton Rouge, LA

#REU student SUBR, LSU, Baton Rouge, LA

&Mentor SUBR, Baton Rouge, LA

**Abstract:** The study investigated the effects of ultraviolet (UV) radiation<sup>3,9,10</sup> exposure on the electrical properties of some La(Ca/Sr)MnO (perovskite crystal structure<sup>10</sup>) compounds. The hypothesis was that if the UV radiation impacted the material then there should be an effect seen in the electrical resistance when the sample is exposed to the radiation. The project involved measuring the electrical resistance of the La(Ca/Sr)MnO samples under normal (i.e., no UV exposure) conditions, and then again while under exposure to UV radiation, while looking for any changes in the electrical properties of the samples.

**Keywords:** Ultraviolet Radiation, UV radiation, UVR, LaMnO, La(Sr/Ca)MnO, perovskite structure

### 1. Introduction:

The reemergence of interest in materials exhibiting the perovskite<sup>11</sup> crystal structure, such as Lanthanum Manganite based compounds, is rapidly becoming widespread<sup>4</sup>. Applications in photovoltaics and fuel cell technology demonstrate that the use of these materials has great potential importance to industrial use.

*Hypothesis: The irradiation of the La(Ca/Sr)MnO materials with UV light will cause a net movement of charge carriers, due to the photoelectric effect, at least on the surface. Moreover, this will affect the electromagnetic properties of the material and be manifested in a measureable way, specifically the resistance (resistivity) of the material.*

There are numerous indications that UV radiation can impact the structure of many substances and compounds at the atomic level<sup>12,13</sup>. The exposure of LaMnO based materials to UV radiation may produce some unexpected outcomes on its physical properties. Many research groups report experimentation involving both thin/thick films and bulk material for this type of experiment<sup>5,6,14,15</sup>. The research project at hand, depending on the outcome, could also suggest the possible future applications of this material, or even impact the material synthesis technique.

### 2. Experimental:

The use of UV radiation in this experiment justified the need for a/some UV radiation source(s), so two lamps of differing composition and energy output were used. The radiation sources were commercially obtained: One compact fluorescent “black light” as a source of UV-a and UV-b radiation, and one shrouded sanitizing lamp as a source of UV-c light. Initially, there was thought of using a microprocessor in the calibration and data collection process. Filtration mediums were employed to isolate certain wavelengths of UV light in order to test the apparent threshold of photoelectric reactivity<sup>13</sup>.

The LaMnO materials that were used in the experiment were synthesized by a solid state reaction process by the co-investigator. Details about the synthesis process are described elsewhere<sup>1</sup>. The calibration process to determine the relative intensity<sup>8</sup> of the light source required that the UV light source be placed at a measured distance from the photodiode array. In order to collect the data, the output of the photodiode array was connected to the microprocessor.

The experimentation process involved using the LaMnO based samples that the co-investigator synthesized as the materials on which to experiment. The LaMnO samples and the UV light source were placed inside a container to eliminate the effects of outside light sources. A four-probe resistance measurement method was employed to measure electrical resistance. In this method, a known electrical current (100mA) was applied to opposite ends of the sample and the voltage was measured between two points along the length of the sample. The following diagrams (fig. 1a & 1b) display the experimental setups:

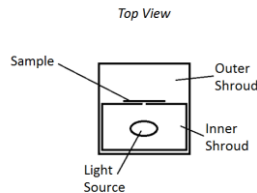


**Figure 1a.**

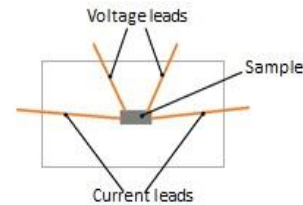


**Figure 1b.**

An additional step was taken to ensure that the UVR only illuminates the sample, and not the copper wire leads attached to the probes or the contacts at the sample. This involved making a cover with an aperture slit, and necessitated the consideration of diffraction<sup>7</sup> of electromagnetic radiation through the slit. Upon completion of this step, we found that the cover and aperture could be placed directly on the sample, which would effectively diminish the diffraction of electromagnetic radiation effect to a negligible factor. The dimensions of the materials used for experimentation were measured several times, and an average of those measurements established<sup>1</sup> in order to calculate electrical resistivity.

### 3. Data Analysis/Results:

The use of the microprocessor and amplifier boards proved to be unsuitable for use in the experiment, mostly due to excess electrical noise generated in the electronic circuitry. However, it was found that the photodiodes' output voltage could be effectively measured using a voltmeter of high sensitivity (Keithley Model 182 Digital Voltmeter). This method did not give the actual frequency or wavelength of the output of the UV lamps. However, this did not negate application of the intensity formula to determine the ideal distance of relative intensities of UVR emitted from the lamps.

Initially it was assumed that the two lamps produced UV radiation in different parts of the UV range. One lamp was a compact fluorescent "black light" lamp, so the assumption was that the light emitted was mainly in the UV-a range with some UV-b. The other lamp was a shrouded sanitizing lamp, and was believed to emit light mainly in the UV-c light range. However, our measurements disproved these assumptions, and there was almost no difference between the frequencies of the radiation produced by each of them. Using optical filters (some commercially obtained, and some homemade ones using sunscreen lotions sandwiched between glass slides), we determined that the actual composition wavelengths of the lamps could not be isolated enough to change the resultant composition wavelengths obtained by using the methods we employed. This was a minor stumbling block for the research, but points to the need for other possible methods and equipment for isolation of resultant wavelength compositions. Utilization of a clear vacuum chamber filled with ozone gas would effectively filter out all UV-c radiation, and most UV-b radiation. The use of pure forms of more energetic UV radiation (i.e., the UV-c range and beyond) would require other equipment, but may yield more concrete results.

After calibration of the light sources, and upon determining the ideal distance to place the samples from the light source (the optimum distance was determined to be 10cm from the center of the lamp) for irradiation. This was determined through the formula we used for intensity; as the distance from the lamp increases

beyond 0.1m (10cm), the denominator of the power to area ratio increases; thus, the intensity decreases. A four-probe resistance measurement method was employed to measure electrical resistance. In this method, a known electrical current (100mA) is applied to opposite ends of the sample and the voltage is measured between two points along the length of the sample.

As mentioned previously, several measurements of the dimensions of the samples were made in order to determine averages of their lengths and cross-sectional areas<sup>1</sup>. These averages along with the experimentally determined electrical resistance from the four probe measurements were used to obtain estimates of the electrical resistivities of the samples.

The electrical resistivity determination was made during two sets of conditions: (a) while the samples were illuminated by UV light, and (b) while no illumination of UV light took place. Our results indicated that there were no differences in the electrical resistivity of the samples with UV irradiation or without UV irradiation. Any changes, if they occurred at all, were too miniscule to determine with any degree of certainty.

The two samples used for this experiment had different chemical compositions, based on the ratios of doping chemicals Calcium and Strontium. This minor change in the chemical composition yielded some interesting findings in the stoichiometry of the materials<sup>1</sup>. The chemical compositions of the LaMnO samples, based on the dopants Calcium and Strontium, was completed and outlined in this table (table 1):

Base Chemical Equation ↓	Dopant Variance (x value) →	x = 0.3 (Sample Number 270614A)	x = 0.4 (Sample Number 010714A)
$La_{0.5}Ca_{0.5-x}Sr_xMnO_3$		$La_{0.5}Ca_{0.2}Sr_{0.3}MnO_3$	$La_{0.5}Ca_{0.1}Sr_{0.4}MnO_3$

Table 1.

The electrical resistance of the samples was measured before testing in order to calculate electrical resistivity, and to ascertain any property changes while they were exposed to the UVR. Using the four probe method, and changing the locations of the probes to find an average, the electrical resistance at room temperature for the samples was found. The following table (table 2) outlines the baseline measurements and calculations for the La(Ca/Sr)MnO samples:

Sample Number ↓	Properties Found →	h (height)	w (width)	l (length)	R (electrical resistance)	ρ (electrical resistivity)
270614A		2.11 mm	3.34 mm	4.425mm	$5.6375 \times 10^{-2} \Omega$	$8.978 \times 10^{-2} \Omega m$
010714A		1.788 mm	3.86 mm	4.89 mm	$7.8675 \times 10^{-3} \Omega$	$1.1101 \times 10^{-3} \Omega m$

Table 2.

When the samples (270614A and 010714A) were irradiated with the ultraviolet lamps, no discernable changes in electrical resistance were found. The samples were also tested for changes in voltage while an applied current was passed through them, and UVR was applied. It was found that there were no discernable changes in voltage of the samples as the ultraviolet light was introduced.

**4. Conclusion/Future direction:**

Based upon our hypothesis, we concluded that there were no discernable electrical property changes in the LaMnO samples using Ultraviolet Radiation in the UV-a, UV-b, and UV-c ranges as a catalyst at room temperature. However; this finding does raise additional questions about the sample materials. Based on previous findings<sup>2,5,6,10,15,16</sup>, and our electrical resistivity testing<sup>1</sup>, the material behaves in unpredictable ways at differing temperatures. It has been found that the conductivity of substances similar to the samples utilized in our experimentation will increase its temperature decreases<sup>2</sup>. The effects of doping the materials with Calcium

and Strontium does cause marked differences in atomic stoichiometry; therefore, variations in temperature should be introduced to samples of similar structure in the future. Given the perovskite<sup>12</sup> structure of the samples, and the fact that the electromagnetic properties of these materials can change greatly by applying heat or cold implies that further experimentation on them is warranted.

Another aspect of the experimentation that has not been mentioned is the fact that the materials utilized had very little surface area (approximately 2mm<sup>2</sup>) which was exposed to the UVR. The possibility does exist that the reduced surface area of the materials experimented on may have shown an effect so miniscule that it could not be measured using the devices we employed. Because the photoelectric effect occurs at the surface of a material, if the same amount of material was created exploiting the maximum surface area possible, then a determinate effect may occur in the presence of UVR using the same measuring equipment. The use of thin films of La(Ca/Sr)MnO materials may yet yield a measureable electrical property change when UVR is used as a catalyst, and this avenue of investigation should be taken in future experimentations.

The use of a spectrometer to ascertain the precise composition wavelengths of the light sources would give future investigators the measurements necessary to yield further information about our samples' behavior under UV radiation. This methodology may point to using more energetic forms of UV light (i.e., shorter wavelengths) to elicit a photoelectric effect; however, this methodology would require a suitable source of highly energetic UV light, and a clear vacuum chamber would be advantageous in order to isolate that light from any atmospheric occlusions that may occur. The use of said vacuum chamber may also be useful if filled with a filtering gas, such as ozone.

#### 5. Acknowledgments:

The current work is funded by the NSF EPSCoR LA-SiGMA project under award #EPS-1003897.

#### 6. References:

- [1] Franklin, Jermain. "The Synthesis of atomic spacing of  $\text{La}_{0.5}(\text{Ca}_{0.5-x}\text{Sr}_x)\text{MnO}_3$  for  $x=0.3$  and  $0.4$ , and the effect of UV radiation on the resistance of these materials". Proceedings of LA-SiGMA 2014 Symposium. 2014.
- [2] Gilabert et al. "Effects of illumination on the electrical properties of oxygen-deficient cuprates and manganites". (2000). Journal Title: Superconducting and related oxides, physics and nanoengineering IV, 331-7, 4058.
- [3] "ISO 21348 Definitions of Solar Irradiance Spectral Categories". Web. 2 July 2014.  
[http://www.spacewx.com/pdf/SET\\_21348\\_2004.pdf](http://www.spacewx.com/pdf/SET_21348_2004.pdf).
- [4] Jacoby, Mitch. "Tapping Solar Power with Perovskites". 24 February 2014. <http://cen.acs.org/articles/92/i8/Tapping-Solar-Power-Perovskites.html>. Web. 15 July 2014.
- [5] Mandal and Ghosh. "Transport, magnetic, and structural properties of  $\text{La}_{1-x}\text{M}_x\text{MnO}_3$  (M=Ba, Ca, Sr) for  $0 \leq x \leq 0.2$ ". Physical Review B 68, 014422. 21 July 2003.
- [6] Markovich et al. "Magnetotransport properties of ferromagnetic  $\text{LaMnO}_{3+\delta}$  nano-sized crystals". Journal of Magnetism and Magnetic Materials 322 (1311-1314). 16 April 2009. Web. 5 June 2014.
- [7] Norton, Andrew(2000). "Dynamic Fields and Waves". CRC Press (Vol. 6). p. 106. ISBN 978-0-7503-0719-2. Web. 9 July 2014.
- [8] Paschotta, Rüdiger. "Optical Intensity". Encyclopedia of Laser Physics and Technology. RP Photonics. Web. 2 July 2014.
- [9] Pyle et al. "Toward the Development of a Proposal to Study the Effects of UV Radiation on some La(Sr/Ca)MnO Compounds". Proceedings of Louisiana EPSCoR RII LA-SiGMA 2013 Symposium. 2013.
- [10] Reitz, John et al. (1992). Foundations of Electromagnetic Theory (4th ed.). Addison Wesley. ISBN 0-201-52624-7. Web. 3 July 2014.
- [11] S. Satpathy et al. (1996). "Electronic Structure of the Perovskite Oxides:  $\text{La}_{1-x}\text{Ca}_x\text{MnO}_3$ ". Physical Review Letters 76: 960. doi:10.1103/PhysRevLett.76.960. Web. 15 July 2014.
- [12] Schinke, Reinhard. Photodissociation Dynamics. Cambridge University Press. 1993. ISBN-10 978-0-521-38368-4. Web. 5 June 2014.
- [13] Serway, R. A. (1990). Physics for Scientists & Engineers (3rd ed.). Saunders. p. 1150. ISBN 0-03-030258-7. Web. 5 June 2014.
- [14] Snyder et al. "Intrinsic electrical transport and magnetic properties of  $\text{La}_{0.67}\text{Ca}_{0.33}\text{MnO}_3$  and  $\text{La}_{0.67}\text{Sr}_{0.33}\text{MnO}_3$  MOVCD thin films and bulk material". Physical Review B. Vol. 53, No. 21. 1 June 1996.
- [15] Thiele et al. "Influence of strain on the magnetism and the magnetoelectric effect in  $\text{La}_{0.7}\text{A}_{0.3}\text{MnO}_3/\text{PMN-PT}(001)$  (A=Ca/Sr)". Physical Review B 75, 054408. 12 February 2007.

## **Unifying Interactive Chromatin Model and Genome Browsing**

**Komala Priya Chitturi<sup>1</sup>, Thomas C. Bishop<sup>2</sup>**

<sup>1</sup>Graduate Student, Computer Science, Louisiana Tech University

<sup>2</sup>Associate Professor, Chemistry & Physics, Louisiana Tech University

**Abstract:** Our current Interactive Chromatin Modeling Web Server (ICM Web) is a tool that allows users to rapidly assess nucleosome stability and fold sequences of DNA into putative chromatin templates. ICM Web takes a sequence of A, T, G, C's as input and generates a nucleosome energy level diagram, coarse-grained representations of free DNA and of chromatin. We are in the process of updating Interactive Chromatin Modeling capabilities. We are testing Jsmol as our new 3D viewer, since Jsmol has improved security features and is compatible with most browsers and devices. And we are developing an interface that can be directly integrated into genome browsers for a more user friendly experience that also preserves data integration. In a separate effort we are developing a compute engine for energy optimization of the chromatin folds. This effort is not reported here as it is still being validated.

**Keywords:** ICM, Interactive Chromatin Modeling, Nucleosome

### **1. Introduction**

Our Interactive Chromatin Modeling web server can rapidly fold tens of thousands of base pairs into nucleosome arrays. There have been numerous changes in web technologies and available experimental data since this model was developed some five years ago. We are upgrading ICM capabilities to be compatible with the latest technologies by implementing Jsmol as our new 3D viewer and seek to allow direct integration of ICM into existing genome browser experience. Jsmol provides improved security and eliminates the necessity of Java which is not compatible with many current browsers and devices. Tight integration with a genome browser allows users to take advantage of abundant data resources available today as means of validating the models and exploring new hypotheses.

### **2. Current Implementation of Interactive Chromatin Model**

ICM usage requires the user to specify a sequence, thermal fluctuations, material properties, and nucleosome occupancy on the initial Input page, left image in Figure 1. A successful ICM run generates an output page, right image in Figure 1, that contains two 3D models and an energy level diagram. Each is explained in more detail below.

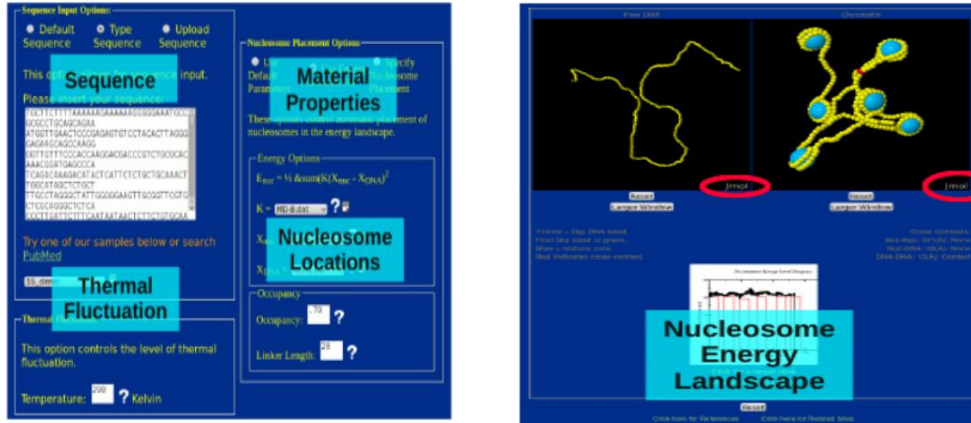


**Figure 1: Current ICM pages:** The current ICM web server consists of an input page (left) and an output page (right). The input page provides areas for specification of DNA sequence and material properties, thermal fluctuation and nucleosome locations. The output page includes two 3D models, one for free DNA and one for chromatin, and an energy level diagram for the nucleosomes. Further details are in the text.

## Inputs

**Sequence:** A sequence is provided by one of three options as a string of As', C's, G's or T's. The default sequence is the Mouse Mammary Tumor Virus promoter sequence, but users can type or cut-and-paste any sequence they want, select from a set of sample sequences, or upload a sequence from a fasta formatted file. The main drawback in the current process is that ICM does not preserve any linkage to the enormous amount of genomic data available through any modern genome browser.

**Thermal Fluctuation:** A temperature is specified in ICM as a means of determining the level of thermal fluctuations in the helical parameters for the regions of free DNA, i.e. the linker DNA. For any segment of DNA not in contact with histones the intrinsic conformation of the DNA is modified according to a random Gaussian distribution that matches the experimentally determined thermal fluctuation for the given base pair step. A temperature of 0 assigns each base pair step its ideal conformation in terms of the DNA helical parameters.

**Material Properties:** The material properties of DNA include specification of the intrinsic shape and flexibility of DNA denoted as  $X_0$  and  $K$  on the input page. The user must also specify the conformation of the nucleosome super helix by choosing from over 100 different possible predefined nucleosome folds. The super helix conformation is denoted  $X_{nuc}$  on the input page. These values determine an energy landscape as a function of base pair position, denoted  $s$ , using the expression  $E(s) = \frac{1}{2} \sum K_{s+i} (X_{nuc_i} - X_{0_{s+i}})^2$ , where the summation extends from  $i = 0$  to 147, i.e. the number of base pair in a nucleosome. Here  $K$ ,  $X_{nuc}$  and  $X_0$  are actually multidimensional arrays containing values associated with the six inter base pair helical parameters.

**Occupancy:** We define occupancy as the number and location of nucleosomes on a segment of DNA. ICM Web automatically places nucleosomes in the energy landscape based on occupancy criteria. The default is 70% of the maximum allowed number of nucleosomes be located on the given sequence of DNA. The locations are

determined as minima in the energy landscape,  $E(s)$ . This agrees well with experimental observations that approximately 70% of allowed position are occupied at any given instant of time under physiologic conditions.

### Outputs

A successful ICM run returns two 3D models and an energy level diagram,  $E(s)$ . Since nucleosome positions are calculated based only on nucleosome-DNA interactions, there is no *a priori* check to identify unfavorable steric interactions. For this reason, a distance calculation is conducted on the 3D nucleosome array to identify steric clashes. Any steric clashes are highlighted in red. An energy optimization routine is underdevelopment that will relax nonphysical steric clashes but retain the global fold corresponding to the indicated nucleosome positions. The two 3D models are displayed, as in Figure 1, using Jmol: an open-source Java viewer for chemical structures in 3D (<http://www.jmol.org/>). Jmol displays a yellow sphere for every 5 base pair of DNA in both the free DNA and chromatin models. For the chromatin model light blue spheres are also included. These represent the histone core regions.

### 3. Interactive Chromatin Model - with Jsmol

With our existing ICM, Free DNA and Chromatin models are displayed using Jmol that runs using Java applets. In general, to run ICM then the user is required to install Java on their system and go through the process of clicking security pop ups to allow the Jmol to actually run. Due to various security concerns, platforms such Android/IOS do not support Java which makes Jmol, and by extension, Interactive Chromatin Modeling impossible in these environments. To overcome these hurdles we have been testing Jsmol as a replacement for Jmol. Jsmol is supported by HTML5 which addresses the various Java issues we are facing. The Jsmol implementation of ICM provides an output page that is identical to the current ICM page based on Jmol. However it avoids all of the security and java install issues associated with Jmol. We are testing the Jsmol implementation to determine under what circumstances and on what devices truly interactive modeling can be achieved.

### 4. Integration with Genome Browser

Integrating Interactive Chromatin Modeling Web Server (ICM Web) with any of the existing genome browsers will preserve user access to vast stores of DNA sequence and related data along with all other functionality that are available in modern genome browsers. Such integration can even eliminate the need for nucleosome energy calculations and predictions since whole genome nucleosome positioning data is now available for a number of species. This allows ICM to be used as a tool for validation and/or verification of experimental data.

As an example a user can answer the simple question “Are experimentally determined nucleosome positions consistent with the known structure of nucleosome and sequence specific conformations of DNA?” We have used command line versions of the tools driving ICM to demonstrate that the answer to this question is a resounding no for nucleosome positions associated with promoter regions in the yeast genome. However our energy minimization routines under development suggest that there is sufficient conformational freedom to relax any of the steric clashed encountered to date without necessitating major conformational changes. Biologist will also rightly observe that there is more to the structure of chromatin than the core histones and DNA. What is

missing in the biologic literature is an appreciation for exactly how open and irregular these structures are and how misleading simple 1D foot print models of nucleosome positions can be. Clearly there is more to chromatin structure than merely the folding of DNA by core histones.



**Figure 2: Prototype ICM-GB Integration.** All of the functionality of the ICM input page can be accomplished by adding an interactive 1D nucleosome positioning track to an existing genome browser for placing. This track allows for adding, deleting, moving and selecting nucleosomes on a segment of DNA. ICM output can be returned to the browser as a new track. The 3D model will appear as before in a separate Jsmol/Jmol window.

## 5. Conclusions

The requirements for full integration of ICM with any genome browser are that the end product I) contain all of the functionality of an existing genome browser II) allow user to manipulate individual nucleosome (add, delete, select type and move) just by right clicking on any of the positioned nucleosomes in a linear model III) allow manipulation of groups and IV) automatically updated 3D models of free DNA and chromatin. Advanced options will allow for energy minimization of the resulting structures and selection of materials properties for the DNA and chromatin. Many observables can be readily injected into the browser experience as “user defined” tracks for DNA material properties, nucleosome energies, etc...

By integrating our existing Interactive Chromatin Modeling tools with an existing genome browser we expect to provide users with a completely different genomic analysis experience. No longer will genomes be considered simple linear sequences of DNA. Instead ICM-GB will provide users with the means for assessing the material properties (conformation and flexibility) of DNA and chromatin and a way to rapidly cross-validate structures with biophysical data. We fully expect that advancing our understanding of epigenetic mechanisms will require such tight coupling of traditional sequence based informatics approaches with physics based materials modeling and simulation approaches.

## 6. Acknowledgments

The current work is funded by the NSF EPSCoR CyberTools project under award #EPS-0701491.

## What is the valence of Mn in (Ga, Mn)N?

Ryky Nelson<sup>1</sup>, Tom Berlijn<sup>2</sup>, Wei Ku<sup>3</sup>, Juana Moreno<sup>1,4</sup>, Mark Jarrell<sup>1,4</sup>

<sup>1</sup>Department of Physics and Astronomy, Louisiana State University

<sup>2</sup>Center for Nanophase Materials Sciences and Computer Science and Mathematics Division,  
Oak Ridge National Laboratory, Oak Ridge, TN 37831-6494

<sup>3</sup>Condensed Matter Physics and Materials Science Department, Brookhaven National Laboratory

<sup>4</sup>Center for Computation and Technology, Louisiana State University

**Abstract:** Motivated by the potential high Curie temperature of (Ga, Mn)N, we investigate the controversial Mn-valence in this diluted magnetic semiconductor. From a first-principles Wannier-functions (WFs) analysis [1] of the high energy Hilbert space we find unambiguously the Mn charge state to be close to 2+ ( $d^5$ ), but in a mixed spin configuration with average magnetic moments of 4  $\mu$ B. By integrating out high-energy degrees of freedom differently, we further demonstrate the feasibility of both effective  $d^4$  and effective  $d^5$  descriptions. These two descriptions offer simple pictures for local and extended properties of the system, and highlight the dual nature of its doped holes. Our derivation highlights the general richness of low-energy sectors in interacting many-body systems and the generic need for multiple effective descriptions.

**Keywords:** Mn Valence state, Wannier functions, high-energy picture, low energy picture.

### 1. Introduction

Since the prediction by Dietl et al. [2] that (Ga, Mn)N could potentially become a dilute magnetic semiconductor (DMS) with a high Curie temperature ( $T_c$ ) many experimental and theoretical studies have been conducted to examine magnetism in (Ga, Mn)N. Instead of narrowing the search for high  $T_c$  DMSs down, more controversies arise from studying this material. One of those controversies is the issue of the Mn-valence state; i.e. whether it forms a  $d^4$  ( $Mn^{3+}$ ) or  $d^5$  ( $Mn^{2+}$ ) configuration. The Mn-valence state is one of the factors that determine the magnetic properties of (Ga, Mn)N.

The debate is mostly triggered by disagreement over experimental conclusions about the Mn-valence state in (Ga, Mn)N. Some experiments using X-rays absorption spectroscopy conclude that Mn-valence state is 3+ ( $d^4$ ) [3] [4], whereas others using the same technique conclude that Mn-valence state is 2+ ( $d^5$ ) [5] [6]. Studies using low-energy techniques, like optical absorption spectroscopy and electron paramagnetic resonance [7] [4] [8] [9], also arrive to different conclusions over the Mn-valence state.

As in experimental studies, disagreement over the Mn-valence state also exists in (Ga, Mn)N theoretical studies [2] [3] [4] [6] [10] [11]. One technique usually used in these studies is density functional theory (DFT). Although DFT is very useful, it cannot precisely determine the ionic structure

of Mn in (Ga, Mn)N because artificially chosen muffin-tins around Mn ions always miss the interstitial contributions.

## 2. Method

We start by performing first-principles DFT calculations in a zincblende supercell of 64 atoms ( $\text{Ga}_{31}\text{MnN}_{32}$ ) using Wien2k [12] implementation of the full-potential linearized augmented-plane-wave method. The LDA+U approximation is applied to Mn atoms with  $U = 4$  eV and  $J = 0.8$  eV. We then construct WFs [1] in three different ways to effectively integrate out various degrees of freedoms, to analyze the electronic structure at different energy scales and to illustrate the relevant physical effects.

## 3. Results and Discussion

Let us first see the high-energy properties by analyzing the resulting density of states using WFs of  $\text{N } sp^3$ ,  $\text{Ga } sp^3$ , and Mn-d symmetries. Fig. 1 (a) shows the total (black) and the partial Mn-d (orange and blue) densities of states (DOSs) obtained from the WFs-based downfolding method. As can be seen from the figure, (Ga, Mn)N forms a half-metallic system with partially occupied impurity bands in the gap of the majority channel. Mn-d orbitals spread from the valence bands to impurity bands and exist in both majority and minority channels. Fig. 1 (a), furthermore, shows partially filled impurity bands lying deep in the band gap similar to a previous DFT analysis [10]. Particularly, Fig. 1 (b) more clearly shows that  $\text{Mn-}t_{2g}$  are strongly hybridized with  $\text{N-}t_{2g}$  (originally from  $\text{N-}sp^3$  surrounding Mn). Integrating the DOS up to the Fermi energy, we found the Mn occupation to be 5.0, corresponding to

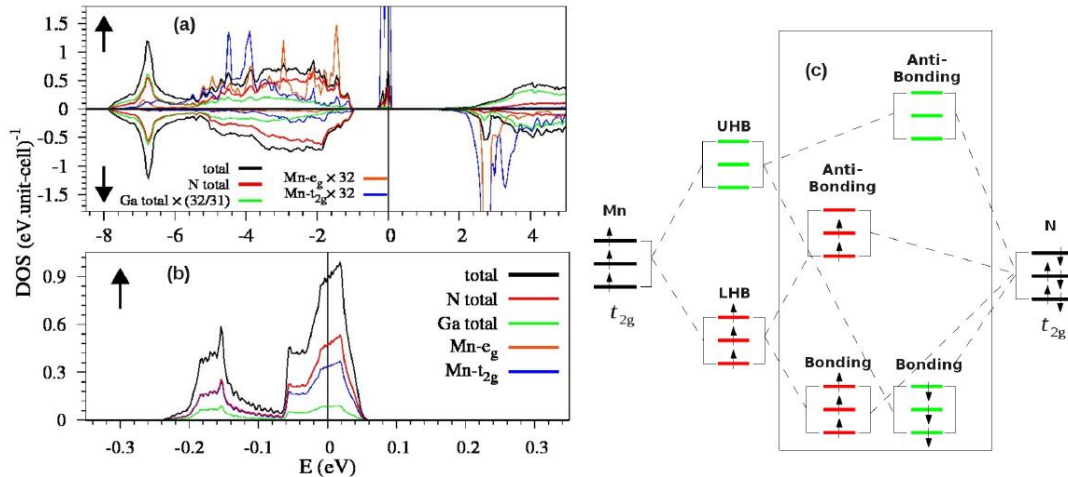


Figure 1. (a) The total and partial density of states (DOSs) of  $\text{Ga}_{31}\text{MnN}_{32}$ . (b) The same DOSs are zoomed on the impurity bands around the Fermi level ( $E_F = 0$ ). Black, red, green, brown, and blue lines denote total, N- $sp^3$ , Ga- $sp^3$ , Mn-e, and Mn- $t_2$  DOSs, respectively.

the charge of a  $\text{Mn}^{2+}$  ( $d^5$ ) ion. However, this seemingly clean  $\text{Mn}^{2+}$  charge distribution contributes to a total spin of only  $4 \mu_B$  (not  $5 \mu_B$ ). These results are precise because WFs analysis spans the entire Hilbert space and leaves no unaccountable charge.

Obviously due to the strong hybridization, the high-energy picture is completely inapplicable in the low energy sector. Instead, the physics should be described by effective Mn or N Wannier orbitals; i.e.  $d^4$  or  $d^5$  models.

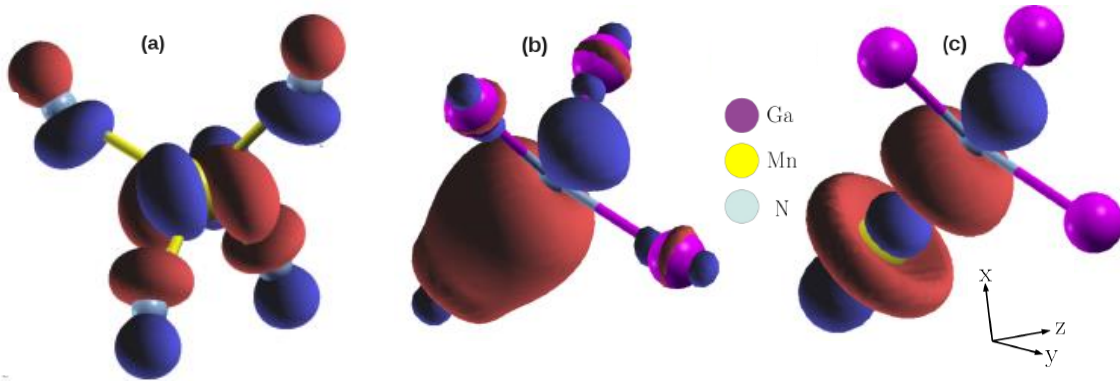


Figure 2. Isosurface plots of the low-energy (a)  $d^4$  and (b), (c)  $d^5$  Wannier orbitals at  $\rho = 0.07 \text{ bohr}^{-3/2}$ . (b) The effective  $d^5$  orbital around  $\text{NGa}_4$  and (c) around  $\text{MnNGa}_3$ .

In the effective  $d^4$  model the Wannier d-orbitals behaves like an atomic  $d^4$  configuration. One of Wannier d-orbitals (more precisely  $\text{Mn-}d_{yz}$ ) is shown in Fig. 2. (a). This orbital shows that the hole is centered at the Mn site and spreads around the 4 nearest-neighbors N to form the orbital tails. This model can describe the (Ga, Mn)N system at very low Mn concentrations where Mn atoms form localized magnetic moments, and it is appropriate for studying local phenomena like Jahn-Teller effects and paramagnetism of (Ga, Mn)N.

The other possible model can be constructed by integrating out the atomic  $d^4$  configuration from the DFT results to obtain an effective  $d^5$  state. The Hamiltonian of this model will look like the spin-Fermion Hamiltonian in which Mn acts like a classical local moment with  $S = \frac{5}{2}$  and the hole acts as an itinerant carrier wandering around in the N orbitals. Moreover, in the spin-Fermion model the local moment and the carrier interact only through a spin-spin interaction. Two of the N- $sp^3$  orbitals for the carrier are shown in Fig. 2. (b) & (c); Fig. 2 (b) shows the shape of a Wannier  $sp^3$  orbital around  $\text{NGa}_4$  and 2 (c) around  $\text{NGa}_3$ . This model is appropriate for studying magnetism mediated by carriers as well as magneto-transport.

#### 4. Summary

By investigating the current debate of the Mn valence in GaN, we advocate three general points in correlated materials: 1) Atomic or ionic valence is only meaningful for high-energy properties, but is not very relevant to the low-energy physical properties, 2) It is often possible to derive multiple effective pictures by integrating out the less relevant degrees of freedom, and 3) For challenging correlated systems, one thus should take advantage of such flexibility and employ the most convenient

picture for describing the physical properties of interest. Specifically, we found a total charge of 5.0e in Mn, but a non-atomic spin count of 4  $\mu$ B, illustrating the inadequacy of ionic valence in the atomic picture.

## 5. Acknowledgments

The current work is funded by the NSF EPSCoR LA-SiGMA project under award #EPS-1003897, and by the DOE BES CMCSN grant DE-AC02-98CH10886.

## 6. References

- [1] W. Ku, H. Rosner, W. E. Pickett and R. T. Scalettar, "Insulating Ferromagnetism in  $\text{La}_4\text{Ba}_2\text{Cu}_2\text{O}_{10}$ : An Ab Initio Wannier Function Analysis," *Phys. Rev. Lett.*, vol. 89, no. 16, p. 167204, 2002.
- [2] T. Dietl, H. Ohno and F. Matsukura, "Hole-mediated ferromagnetism in tetrahedrally coordinated semiconductors," *Phys. Rev. B*, vol. 63, no. 19, p. 195205, 2001.
- [3] A. Titov, X. Biquard, D. Halley, S. Kuroda, E. Bellet-Amalric, H. Mariette, J. Cibert, A. E. Merad, G. Merad, M. B. Kanoun, E. Kulatov and Y. A. and Uspenskii, "X-ray absorption near-edge structure and valence state of Mn in (Ga, Mn)N," *Phys. Rev. B*, vol. 72, no. 11, p. 115209, 2005.
- [4] W. Stefanowicz, D. Sztenkiel, B. Faina, A. Grois, M. Rovezzi, T. Devillers, F. d'Acapito, A. Navarro-Quezada, T. Li, R. Jakiela, M. Sawicki, T. Dietl and A. Bonanni, "Structural and paramagnetic properties of dilute  $\text{Ga}_{1-x}\text{Mn}_x\text{N}$ ," *Phys. Rev. B*, vol. 81, no. 23, p. 235210, 2010.
- [5] J. I. Hwang, Y. Ishida, M. Kobayashi, H. Hirata, K. Takubo, T. Mizokawa, A. Fujimori, J. Okamoto, K. Mamiya, Y. Saito, Y. Muramatsu, H. Ott, A. Tanaka, T. Kondo and H. Munekata, "High-energy spectroscopic study of the III-V nitride-based diluted magnetic semiconductor  $\text{Ga}_{1-x}\text{Mn}_x\text{N}$ ," *Phys. Rev. B*, vol. 72, no. 8, p. 085216, 2005.
- [6] O. Sancho-Juan, A. Cantarero, N. Garro, A. Cros, G. Martínez-Criado, M. Salomé, J. Susini, D. Olguín and S. Dhar, "X-ray absorption near-edge structure of GaN with high Mn concentration grown on SiC," *Journal of Physics: Condensed Matter*, vol. 21, p. 295801, 2009.
- [7] T. Graf, M. Gjukic, M. S. Brandt, M. Stutzmann and O. Ambacher, "The  $\text{Mn}^{3+/2+}$  acceptor level in group III nitrides," *Appl. Phys. Lett.*, vol. 81, p. 5159, 2002.
- [8] M. Zajac, J. Gosk, M. Kamińska, A. Twardowski, T. Szyszko and S. Podsiadło, "Paramagnetism and antiferromagnetic d-d coupling in GaMnN magnetic semiconductor," *Appl. Phys. Lett.*, vol. 79, p. 2432, 2001.
- [9] A. Wolos, M. Palczewska, M. Zajac, J. Gosk, M. Kaminska, A. Twardowski, M. Bockowski, I. Grzegory and S. Porowski, "Optical and magnetic properties of Mn in bulk GaN," *Phys. Rev. B*, vol. 69, no. 11, p. 115210, 2004.
- [10] E. Kulatov, H. Nakayama, H. Mariette, H. Ohta and Y. A. Uspenskii, "Electronic structure, magnetic ordering, and optical properties of GaN and GaAs doped with Mn," *Phys. Rev. B*, vol. 66, p. 045203, 2002.
- [11] T. C. Schulthess, W. M. Temmerman, Z. Szotek and A. Svan, "First-principles electronic structure of Mn-doped GaAs, GaP, and GaN semiconductors," *Journal of Physics: Condensed Matter*, vol. 19, p. 165207, 2007.
- [12] P. Blaha, K. Schwartz, G. K. H. Madsen, D. Kvasnicka and J. Luitz, *WIEN2K, an augmented plane wave and local orbitals program for calculating crystal properties*, Vienna, Austria: TU Wien, 2001.

## **Workflow Software for Keck & CAMD Tomography Systems**

**Jumao Yuan<sup>1</sup>, Braylon Cormier<sup>2</sup> and Leslie G. Butler<sup>1</sup>**

<sup>1</sup>Department of Chemistry, LSU

<sup>2</sup>Department of Mathematics, LSU

**Abstract:** Neutron & X-ray interferometry are now possible with microfabricated gratings. With W.M. Keck funding, we will build a laboratory X-ray tomography/interferometry system; related interferometers are being constructed at the LSU CAMD synchrotron and the UC Davis McClellan nuclear research center. The amount of data being processed requires new workflow software and new collaboration efforts. Highlighted here are initiatives with New York University on VisTrails and City University of New York on SNARK09. La-SIGMA has funded three visits; Keck funds an NYU subcontract; and two NSF proposals have been submitted. These collaborations have the potential for great progress in the research. VisTrails could become a standard for materials science tomography workflow. SNARK09 could provide the development framework for advanced interferometry data processing.

**Keywords:** Tomography, SNARK09, Vistrails, KiwiViewer, Keck, interferometry

### **1. Introduction**

Microfabricated gratings facilitate interferometry with incoherent sources. Each experiment yields three sets of images: absorption, differential phase contrast (DPC), and ultra-small angle scattering (dark field). For medical applications, DPC may offer a method of performing low-dose imaging; clinical trials for rheumatoid arthritis are underway [1].

The W.M. Keck Foundation project started 1/2014 and should yield its first images later this year. This instrument will have a stationary sample, like a medical CT, and is not found in most lab tomography systems due to rotation stage instabilities and electrical complexities. The interferometer will push grating fabrication to new limits, especially at higher X-ray energies. Applications are planned for (a) burning flame retardant/polymer samples; (b) testing the operation of lithium-ion polymer batteries; (c) imaging bioscaffolding in mice bone repair; and (d) 3D printing operations.

Advanced tomography reconstruction techniques are needed to reduce problems with phase wrapping, to mutually support reconstructions of the three image streams, and quantify the dark-field images. Solutions to the issue of phase wrapping are still currently being researched. The issue arises from the mathematical domain of trigonometric functions used in the data processing calculations. Workflow management software is required to simplify, enhance, and preserve provenance of the data processing.

## **2. SNARK09**

The problem of inverse radon reconstruction has appeared in a large number of scientific fields of research, including (but not limited to) computed tomography, electron microscopy, radiology, radio astronomy and holography. Many different methods have been suggested for its solution in the form of various reconstruction algorithms. SNARK09 is a software package designed for the reconstruction of 2D image from 1D projections. Its features include projection computation, digital difference analyzer (DDA), and over 30 reconstruction algorithms.

SNARK09 provides a system framework whereby the researcher may implement image reconstruction algorithms and evaluate their performance. SNARK09 is capable of treating projection geometries (both parallel and divergent) and is capable of creating test data to be tested by reconstruction algorithms. A number of the most commonly used reconstruction algorithms are incorporated into the software. SNARK09 is an updated version of SNARK05.

The following features are the primary improvements that are incorporated into the SNARK09 package:

1. Capability of generating mathematically generated phantoms that include various heterogeneities
2. Capability of adjusting polychromatic x-ray projection data with beam hardening corrections
3. Inclusion of the imagewise-region-of-interest figure of merit (FOM)
4. Handles up to ten algorithms created by the user, with at most five using blobs
5. The user can implement up to five user-defined FOMs. SNARK09 has been designed to be a highly adjustable program and is transportable to any system capable of running a standard Linux/Unix program [2].

## **3. VisTrails**

VisTrails is a new system combining features of workflow and visualization systems, including several packages, like VTK (Visualization Toolkit), matplotlib and ImageMagick. VisTrails also supports user-defined packages such as our Mathematica and Matlab codes written in Python scripts.

VisTrails is an open-sourced scientific workflow and provenance management software system that provides assistance for system simulations, data exploration, and data visualization. Whereas workflows have historically been used to automate repetitive tasks, for tasks that are exploratory in nature – things such as simulations, data analysis, visualization, etc. - very little of the process is repeated. These processes of exploration are under constant change. As an engineer or scientist creates and tests hypotheses about data under review, a series of different, although connected, workflows are created while a workflow is being adjusted in an interactive process. VisTrails was designed to manage these constantly changing workflows.

One of the key distinguishing features of VisTrails is its comprehensive provenance infrastructure that retains a detailed information history about the steps taken and data derived during the course of an exploratory task: VisTrails maintains a comprehensive provenance of the data outcomes from the workflows, of the workflows themselves that derive these products, and their executions. This information is persisted as XML files or in a relational database, and it allows users to maneuver through workflow versions in an intuitive fashion, to undo changes without losing any of the results, to visually compare different workflows and their results, and to examine the actions that led to a certain result [3].

#### **4. KiwiViewer**

KiwiViewer is a free, open-source visualization app for exploring scientific and medical datasets that runs on Android and iOS mobile devices with multi-touch interaction. KiwiViewer supports a variety of file formats, including obj, stl, ply, and vtk. Datasets may be loaded into KiwiViewer from the SD card, email attachments, or DropBox, or downloaded from a URL.

The development of KiwiViewer is supported by Kitware, Inc., the National Alliance for Medical Image Computing (NA-MIC), and Willow Garage. Kitware, whose team created and continues to extend the Visualization Toolkit (VTK), supports and consults the services for VTK, which is the primary format used in KiwiViewer. VTK supports a wide variety of visualization algorithms including: scalar, vector, tensor, texture, and volumetric methods. It also supports advanced modeling techniques such as: implicit modeling, polygon reduction, mesh smoothing, cutting, contouring, and Delaunay triangulation. VTK has an comprehensive information visualization structure, has a series of 3D interaction widgets, supports parallel processing, and integrates with various databases on GUI toolkits such as Qt and Tk. VTK is cross-platform and runs on Linux, Windows, Mac and Unix platforms [4].

#### **5. Future work**

**Instrumentation:** Soon, laboratory and synchrotron X-ray instruments will be operational. A DoD DURIP proposal for neutron interferometry is under review.

**Commercial:** An established Karlsruhe company, Microworks, will continue to collaborate with a newly formed LSU CAMD company. If clinical interferometry applications develop, market for microfabricated gratings may be \$5M/yr.

**MuhRec:** MuhRec, developed at the Paul Scherrer Institute, will continue to be used as a quick-check supplement to SNARK09 in our reconstructions. [5]

**SNARK09:** We will continue collaborating with CUNY colleagues to create improved reconstructions with SNARK. We hope to develop an NSF proposal to improve interferometry reconstructions.

ASTRA Tomography Toolbox: In collaboration with Vision Lab at the Department of Physics at the University of Antwerp, we will continue to explore reconstruction algorithms and options with the ASTRA Tomography Toolbox. [6]

VisTrails: We will continue to seek NSF funding for a NYU/LSU joint project.

KiwiViewer: We are developing an app to visualize objects in 3D. We are collaborating with members of the Department of Mechanical and Industrial Engineering. Using KiwiViewer, we propose an "educational triangle" of "Measure", "Draw", and "Print". "Measure" includes calipers, tomography, and AutoDesk's 123D Catch.

## **6. Acknowledgments**

The current work is funded by the NSF EPSCoR LA-SiGMA project under award #EPS-1003897, a Louisiana Board of Regents Industrial Ties Research Subprogram (ITRS) grant with an Albemarle cost match, NSF "GOALI: Dynamic Tomography and Materials Simulations for Polymer Blends", NSF (DMR-0923440) MRI: Acquisition of a Multipole Wiggler for the LSU Synchrotron", and NSF (CNS-1126739) MRI: Development of Melete". We thank the W.M. Keck Foundation, "Development of a Laboratory X-ray Tomography System with Stationary Sample and Phase Contrast Imaging".

## **7. References**

- [1] Tanaka, J.; Nagashima, M. etc., Cadaveric and in vivo human joint imaging based on differential phase contrast by X-ray Talbot-Lau interferometry. *Zeitschrift für Medizinische Physik* 2013, 23 (3), 222-227.
- [2] References must be sequential
- [3] VisTrails: <http://vistrails.org>
- [4] KiwiViewer: <http://www.kiwiviewer.org>
- [5] MuhRec: <http://www.psi.ch/niag/muhrec>
- [6] ASTRA Toolbox: [www.visionlab.ua.ac.be/software](http://www.visionlab.ua.ac.be/software)

2014 LA-SIGMA Poster Session		
Poster No.	Title	Author(s)
1	A Need for NOx exhaust sensor: Computational study of gaseous reaction over Au/YSZ substrate	S. Killa and D. Mainardi
2	Ab Initio Computation of Electronic and Transport Properties of w-AlN.	I. Nwigboji, Y. Malosvosky, J. Ejembi and D. Bagayoko
3	Ab-initio DFT Prediction of Electronic Properties and Effective Masses of Li2S	Y. Malozovsky, E.C. Ekuma and D. Bagayoko
4	Achieving High Efficiency in Serial and at Extreme Scale	Md Hasan, M. Sujon, and C. Whaley
5	Aligned Carbon Nanotube Forest as Supercapacitor Electrodes	M. Oguntoye, L. Pratt and N. Pesika
6	Aligning Metagenomic Short Read Sequences using GPGPUs and Expectation-Maximization Algorithm	M. Karnik, D. Anderson, P. Chowriappa and S. Dua
7	Anderson Localization in Systems with Off-Diagonal Disorder	H. Terletska, C.E. Ekuma, C. Moore, K.M. Tam, J. Moreno and M. Jarrell
8	Attosecond Transient Absorption with Time Dependent Hartree-Fock	A. Sissay and K. Lopata
9	Catalytic Reaction on FeN4/C Site of Nitrogen Functionalized Carbon Nanotubes as Cathode Catalyst for Hydrogen Fuel Cells	F. Gao, G. Zhao, Z. Wang, D. Bagayoko and D. Liu
10	Coarse-grained Biomolecule-Wall Interactions for Implementation into Multi-scale MD-Continuum Simulations	K. Hesary, B. Novak, D. Moldovan and D.E. Nikitopoulos
11	Computational Studies of Oxido-Reductases for Improved Biofuel Cell Design	E. Gomez, T. Tran, N. Tran and D. Chakravorty
12	Computational Study of the Self-Assembly of Surfactant Molecules	C. Whicker, S. Joseph, E. Gomez, S. Tumslime and D. Chakravorty
13	Crystallization and the Dimensionality Effect	T. Loeffler, A. Galatas and B. Chen
14	Design of Tailored Polymer via Molecular Dynamics Simulations	L. Liu, S. Parameswaren, A. Sharma, H. Ashbaugh, S. Rick and S. Grayson
15	Development of an Interactive Chromatin Model	J. Liman, T.C. Bishop, W. Johnston and D. Donze
16	Direct Dynamical Simulation of Filling of Carbon Nanotube Forests	X. You and L.R. Pratt
17	Dynamical Cluster Approximation Study of the Two-Dimensional Anderson-Hubbard Model	S. Yang, P. Haase, H. Terletska, T. Pruschke, J. Moreno and M. Jarrell
18	Effect of Nanoparticle Size, Shape and Orientation on Effective Dielectric Constant in Polymer-Nanocomposites	S. C. Sklare, S. Adireddy, V. Puli, J. Shipman and D. Chrisey
19	Electrical and Thermal Transport Properties of Superconducting Ca10Pt4As8((Fe1-xPtx)2As2)5 Single Crystals	A.B. Karki, J.Y. Pan, P. Watkins-Curry, G.T. McCandless, J.Y. Chan, E.W. Plummer and R. Jin
20	Energy Traps in Material Nucleation and the Dimensionality Effect	T. Loeffler
21	Equation of Motion Coupled Cluster Methods for Electron Attachment and Ionization Potential: Implementation and Applications	K. Bhaskaran-Nair, K. Kowalski, J. Moreno, M. Jarrell and W. Shelton
22	Exploiting Sparse Matrix Structure in a Monte-Carlo Arnoldi Iteration on Many-Core Architectures	R. Karimi and D. Koppelman
23	GeauxDock: A Novel Approach for Ligand Molecular Docking Using a Hybrid Force Field	Y. Ding, Y. Fang, W. Feinstein, D.M. Koppelman, J. Moreno, J. Ramanujam, M. Brylinski and M. Jarrell
24	Heterogeneous Computing Aided Material Science Research	Y. Fang, S. Feng, Y. Ding, K. M.Tam, W. Feinstein, Z. Yun, M. Brylinski, D. Koppelman, J. Moreno, M. Jarrell and J. Ramanujam
25	Homogeneous Nucleation of Crystals of Ionic Liquids from the Melt	Y. Shen, X. He, E. Santiso and F. Hung
26	In Situ Polymerization of Thiol-acrylate Nanocomposite Foam for Bone Defects	A. Forghani, L. Garber, C. Chen, R. Devireddy and D. Hayes
27	Investigation of the Molecular Mechanism of Tin Sulfide (SnS2) as a Lithium Ion Battery Electrode Material	K. Moyer, A. Hassan, C. Wick and R. Ramachandran
28	Ionic liquids in the Ordered Mesoporous Carbon CMK-5: Pore-pore Correlation Effects	X. He, J. Monk, R. Singh, L. Lorio and F. Hung

29	Lithiation Mechanism of RuO <sub>2</sub> , and its Potential Use as Lithium-Ion Battery Anode Material	A. Hassan, R. Ramachandran, C. Wick, A. Navulla and L. Meda
30	Metal Organic Frameworks as Vehicles for Drug Delivery	K. Taylor-Edinbyrd, T. Li and R. Kumar
31	Micellization of Cationic Linear Peptide Analogs Studied Using Molecular Dynamics Simulations	B. Novak and D. Moldovan
32	Molecular Dynamics Simulation Study of the Transport of DNA Mononucleotides through Nanoslits Driven by Electric Fields	K. Xia, B. Novak, D. Nikitopoulos, S. Soper and D. Moldovan
33	Monte Carlo study of a Spin Glass model with Correlated Disorder	K.M. Tam, J. Willard, J. Moreno and M. Jarrell
34	Multi-scale Theory in the Molecular Simulation of Electrolyte Solutions	W. Zhang, X. You and L.R. Pratt
35	Optimizing Growth Conditions of Zinc Sacrificial Layer for Micro-Origami Technology	R. Eskandari, B. Buchanan and L. Malkinski
36	Parallelizing Protein Docking Code to Accelerate Drug Discovery	B. Burkman, M. Brylinski and W. Feinstein
37	Periodic Anderson Model with Electron Phonon Interaction and its Antiferromagnetic Susceptibility	E. Li, P. Zhang, K.M. Tam, S. Yang, J. Moreno and M. Jarrell
38	Physical Properties of Superconducting Ca <sub>10</sub> Pt <sub>4</sub> As <sub>8</sub> (Fe <sub>2</sub> As <sub>2</sub> ) <sub>5</sub>	J. Pan, A. Karki and R. Jin
39	Quantum Chemistry Studies of Zn <sup>2+</sup> and Mg <sup>2+</sup> Ions in Aqueous Environments	L. Hartman, M. Soniat and S. Rick
40	Quantum Coherent Manipulation of Two-Level Systems in Superconducting Circuits	A. Burin, A. Maksymov and K. Osborn
41	Quantum Confinement Effect on Electron-phonon Interaction in Atomically Thin Nb <sub>3</sub> SiTe <sub>6</sub>	J. Hu, X. Liu, C.L. Yue, J.Y. Liu, H.W. Zhu, J. Wei, Z.Q. Mao, L. Antipina, Z.I. Popov, P.B. Sorokin, T.J. Liu, P.W. Adams, J. Heng and D. Natelson
42	Redeveloping and Optimizing the Interactive Chromatin Modeling Web Server Kernel	G. Kankanala, I. Sondh and T.C. Bishop
43	Sign-Learning Kink-Based Path Integral Calculations of Molecules H <sub>2</sub> O, N <sub>2</sub> , and F <sub>2</sub>	J. Baylis, X. Ma, F. Loffler, R. Hall, K. Kowalski, M. Jarrell and J. Moreno
44	Simulation of the Controlled Release of Molecules from Halloysite Nanotubes	D. Elumalai, M. McCoy, Y. Lvov, J. Tully and P. Derosa
45	Simulations of Ions in Non-Aqueous Solvents	A. Vuong, S. Wagstaff and S. Rick
46	Static and Dynamic Properties of Interacting Planar Magnetic Nanowire Arrays	S. Khanal, N. Vargas, M. Stokes, D. Adams and L. Spinu
47	Study of CO Adsorption and Dissociation on Metal clusters using DFT	S. Gyawali and D. Mainardi
48	Study of the Three-Dimensional Edwards-Anderson Model in an External Field with a Multi-spin Coding Parallel Tempering Monte Carlo Simulation	S. Feng, Y. Fang, K.M. Tam, J. Moreno, J. Ramanujam and M. Jarrell
49	Synthesis and Characterization of Dendronized Polymers based on Poly(Ethylene Glycol)	B. Myers and S. Grayson
50	Synthesis of Novel Amphiphilic Capping Ligands as an Organic Coating for Nanoparticulate Iron Oxide Imaging and Delivery Agents	D. Nilov, P. Kucheryavy, R. Komati, C. Mitchell, A. LeBeaud, A. Burin, V. Kolesnichenko and G. Goloverda
51	The Design and Synthesis of Nanosized Nickel Oxide on Stainless Steel	C. Arnold, A. Navulla and L. Meda
52	The Evaporation and Growth of Ruthenium Oxide Nanorods on Stainless Steel	L. Douglas, A. Navulla and L. Meda
53	The Origin of Excess Capacity in RuO <sub>2</sub>	A. Navulla and L. Meda
54	Towards Online Comparative Genomics of Mononucleosomes	V. Pereddy, P. Mahadasyam, M. Badar and T.C. Bishop
55	Typical Medium Dynamical Cluster Approximation Study of Disordered Superconductors	E. Siddiqui, C.E. Ekuma, H. Terletska, N.S. Vidyadhiraja, J. Moreno and M. Jarrell
56	Ultraviolet Radiation Effects on the Electrical Resistivity of some La(Ca/Sr)MnO Materials	W. Raziano, J. Franklin and L. Henry
57	Unifying Interactive Chromatin Model and Genome Browsing	K. Chitturi and T.C. Bishop
58	What is the Valence of Mn in (Ga, Mn)N?	R. Nelson, T. Berlijn, W. Ku, J. Moreno and M. Jarrell
59	Workflow Software for Keck & CAMD Tomography Systems	J. Yuan, B. Cormier and L. Butler

### Registered Attendee List

<b>Last Name</b>	<b>First Name</b>	<b>Affiliation</b>
Adams	Stephanie	Louisiana Tech University
Arnold	Corey	Xavier University of Louisiana
Ashbaugh	Henry	Tulane University
Badar	Mohammad	Louisiana Tech University
Bagayoko	Diola	Southern University and A&M College
Bhaskaran Nair	Kiran	Louisiana State University
Bishop	Thomas	Louisiana Tech University
Brylinski	Michael	Louisiana State University
Burkman	Brad	Louisiana School for Math, Science, and the Arts
Carpenter	Jenna	Louisiana Tech University
Chitturi	Komala Priya	Louisiana Tech University
Cormier	Braylon	Louisiana State University
Cruthirds	Rachel	Xavier University of Louisiana
D'Amour	Gene	Tulane University
Delone	Alysia	Louisiana Board of Regents
Derosa	Pedro	Louisiana Tech University
Ding	Yun	Louisiana State University
DiTusa	John	Louisiana State University
Douglas	Lacey	Xavier University of Louisiana
Dua	Sumeet	Louisiana Tech University
Dunn	Cindi	Office of Educational Innovation & Evaluation
Edwards Lange	Shelia	University of Washington
Elumalai	Divya	Louisiana Tech University
Fang	Ye	Louisiana State University
Fattah Hesary	Kasra	Louisiana State University
Gao	Feng	Southern University and A&M College
Gershey	Jim	Louisiana Board of Regents
Ghale	Kushal	Louisiana State University
Goloverda	Galina	Xavier University of Louisiana
Guice	Leslie	Louisiana Tech University
Gyawali	Suraj	Louisiana Tech University
Hasan	Md Rakib	Louisiana State University/CCT, CS
Hassan	Ayorinde	Louisiana Tech University
He	Xiaoxia	Louisiana State University
Hoehn	Jim Hoehn	EPSCoR/IDeA Fdn. (Retired)
Hu	Jin	Tulane University
Hung	Francisco	Louisiana State University
Jarrell	Mark	Louisiana State University
Jernigan	Susan	Louisiana Board of Regents
Jin	Rongying	Louisiana State University
Jones Crayton	DiOnetta	Massachusetts Institute of Technology

<b>Last Name</b>	<b>First Name</b>	<b>Affiliation</b>
Kankanala	Gyanadeep	Louisiana Tech University
Karimi	Roозbeh	Louisiana State University
Karnik	Mihir	Louisiana Tech University
Kennan	Sean	National Science Foundation
Khanal	Shankar	University of New Orleans
Khonsari	Michael	Louisiana Board of Regents
King	Amber	Louisiana Board of Regents
Kolesnichenko	Vladimir	Xavier University of Louisiana
Koppelman	David	Louisiana State University
Kumar	Revati	Louisiana State University
Lee	Shelley	Louisiana State University
Li	Xin (Shane)	Louisiana State University
Liman	James	Louisiana Tech University
Loeffler	Troy	Louisiana State University
Loffler	Frank	Louisiana State University
Mahadasyam	Parthasarathi	Louisiana Tech University
Maksymov	Andrii	Tulane University
Malozovsky	Yuriy	Southern University and A&M College
Mao	Zhiqiang	Tulane University
McKoy	B. Vincent	California Technical Institute
Meda	Lamartine	Xavier University of Louisiana
Moreno	Juana	Louisiana State University
Myers	Brittany	Tulane University
Nelson	Ryky	Louisiana State University
Nikitopoulos	Dimitris	Louisiana State University
Novak	Brian	Louisiana State University
Nwigboji	Ifeanyi	Southern University and A&M College
Oguntoye	Moses	Tulane University
Pan	Jiayun	Louisiana State University
Patton	Jessica	Louisiana Board of Regents
Pereddy	Venkat	Louisiana Tech University
Pesika	Noshir	Tulane University
Poobal	Karthik	Louisiana Board of Regents
Pratt	Lawrence	Tulane University
Ramachandran	Ramu	Louisiana Tech University
Ramanujam	J. Ram	Louisiana State University
Rick	Steve	University of New Orleans
Robinson	Anne	Tulane University
Ruscher	Janet	Tulane University
Saltzman	Alex	LA-SIGMA
Seetala	Naidu	Grambling State University
Sharma	Arjun	University of New Orleans

<b>Last Name</b>	<b>First Name</b>	<b>Affiliation</b>
Shelton	William	Louisiana State University
Shen	Yan	Louisiana State University
Shipman	Joshua	Tulane University
Silverman	Harold	Retired
Sinnott	Susan	University of Florida
Sissay	Adonay	Louisiana State University
Sklare	Samuel	Tulane University
Soto	Fernando	Louisiana Tech University
Spinu	Leonard	University of New Orleans
Stark	Wendi	Office of Educational Innovation & Evaluation
Sujon	Md Majedul Haque	Louisiana State University/CCT, CS
Taylor-Edinbyrd	Kiara	LA-SIGMA
Townsend	Leigh	Louisiana State University
Veronis	Georgios	Louisiana State University
Whaley	Clint	Louisiana State University/CCT, CS
Wick	Collin	Louisiana Tech University
Wilson	Zakiya	Louisiana State University
Xu	Ye	Louisiana State University
Yang	Shuxiang	Louisiana State University
You	Xinli	Tulane University
Yuan	Jumao	Louisiana State University
Zhao	Guanglin	Southern University and A&M College